A LANDSLIDE WARNING SYSTEM FOR A SOIL SLOPE ON OAHU

Wānana i ka Uahaneʻe ʻo Ulumawao

A DISSERTATION SUBMITTED TO THE GRADUATE DIVISION OF THE UNIVERSITY OF HAWAIʻI IN PARTIAL FULFILLEMENT OF THE REQUIREMENTS FOR THE DEGREE OF

DOCTOR OF PHILOSOPHY

IN

CIVIL ENGINEERING

MAY 2018

By

Melia K. Iwamoto

Dissertation Committee:

Phillip Ooi, Chairperson

Sayed Bateni

Horst Brandes

Aly El-Kadi

Thomas Giambelluca

Xiong Zhang (Missouri University of Science and Technology)

ACKNOWLEDGEMENTS

I would like to acknowledge the project sponsors, The Hawaii Department of Transportation and the Federal Highway Administration, specifically Brandon Hee and Herbert Chu of the Hawaii DOT, Geolabs for drilling the boreholes and installing the instruments, and Ryan Sugamoto at the UH Corrosion Lab for providing crucial meteorological data. I would also like to acknowledge Mitchell Pinkerton for his extensive help in installing field and lab equipment, as well as helping to troubleshoot the many and challenges experienced. Thank you to the undergraduate civil engineering students, Marica Otto, Wyatt Bartlet and John Nihi, who helped conduct some of the laboratory testing.

To Dr. Ooi, you have been an outstanding advisor these six and a half years, I truly could not have asked for a better one. I am forever indebted to you, first of all for the opportunities you have given me, but mostly for your patience, encouragement, and for creating a positive environment to work in.

Thank you to my family, especially my mom, dad, brother, and grandparents for keeping me grounded and my heart full. Thank you to my friends for all the laughs and for keeping me sane. Finally, thank you, Dev, for riding this Hawaiian rollercoaster ride with me.

Special thanks to: NHSEMP, Daniel Lipe, NSF Broadening Participation Grant, ARCS Foundation, Imi Na'auao Scholarship, East-West Center, Chi Epsilon, UH Graduate Student Organization, WRRC, UH Dept. of Civil Engineering, and the UH College of Engineering.

"Trust in the Lord with all your heart and lean not on your own understanding; in all your ways acknowledge Him and He will direct your path" – Proverbs 3:5-6

"E hana mua a pa'a ke kahua mamua o ke a'o ana aku ia ha'i" – Pukui 276

EXECUTIVE SUMMARY

A landslide warning system for a 40-foot-high cut soil slope on Kalaniana'ole Highway was developed by performing a soil investigation, laboratory tests, installing monitoring instruments, developing and calibrating a transient hydrological flow model, using the calibrated model to predict moisture/suction response during a design storm, inputting these moisture/suction predictions into a slope stability analysis and establishing threshold values for the monitoring instruments.

The geotechnical investigation and index testing showed that the slope consists of a uniform reddish-brown, stiff to very-stiff, highly overconsolidated elastic silt (MH). Saturated consolidation tests were performed to obtain the saturated compression curve and the saturated hydraulic conductivity, which was determined to be 10^{-6} cm/s. A saturated multi-stage consolidated-drained triaxial shear test was performed to obtain the Hvorslev true friction angle and true cohesion, which was 27° and 18 kPa, respectively. Pressure plate and vapor sorption analyser tests were performed to obtain the unconfined soil water characteristic curve (SWCC) and hydraulic conductivity function (HCF). Three constant water content isotropic compression (CWIC) tests were performed to obtain the Basic Barcelona Model (BBM) stiffness parameters and the porosity-dependent van Genuchten parameters. Constant water content triaxial shear tests (CWTS) were performed to obtain the BBM shear strength parameters, and the critical state friction angle which was estimated to be 37°. The BBM parameters were calibrated using the modified state-surface approach (Zhang and Lytton, 2009).

A 2D finite-element transient hydrological flow model was calibrated using the field measured suctions and water contents during a two-and-a-half-year period. A good fit between measured and predicted values for all sensors was obtained by modelling hysteresis and porosity-dependency in the SWCC and HCF. The calibrated model was then used to predict the slope response due to a 500-year design storm, and to establish landslide warning thresholds for the monitoring instruments. The predicted suctions and water contents during the design storm, and the porosity at each node estimated using the calibrated BBM stiffness parameters, were inserted into a slope stability analysis. The slope was deemed stable (FS_{min}~1.2) during a 500-year storm.

Amber and red thresholds were developed using Nicholson et al's (1999) traffic light approach for two tensiometers and two water content sensors based on the predicted suction and water content response during a 500-year storm and the maximum water contents and minimum suctions ever measured in the field. Proposed plans of action include: 1) cover the slope with a tarp or geomembrane to prevent further infiltration if the amber threshold is triggered, and 2) close the town-bound lane of Kalaniana'ole Highway if the red threshold is triggered.

Key findings include: (1) it is important for a transient hydrological flow model to account for SWCC and HCF hysteresis and porosity-dependency in order to predict field behaviour reliably; (2) Porosity-dependent SWCCs can be derived from constant water content isotropic compression tests along with the use of the Basic Barcelona Model stiffness parameters and a modified form of the van Genuchten (1980) equation; (3) Based on 2D slope stability analyses, the slope will survive a 500-year storm with a factor of safety ≈ 1.2.

TABLE OF CONTENTS

LIST OF FIGURES

LIST OF TABLES

1 INTRODUCTION

1.1 Landslides

Landslides and other mass movement of geomaterials cause approximately 25 to 50 deaths and US$1 - 2 billion worth of damage in the United States annually (Turner, 1996). They can be triggered naturally or by humans. Natural triggers include intense precipitation, earthquakes, undercutting of slope toe (e.g.; scour) and volcanic eruptions. Landslide abatement usually entails employing costly mitigation measures such as grading, excavation, drainage, pinning, retaining walls, etc. A less costly method to alleviate losses is to implement a monitoring and early landslide warning system. This type of system is especially suited towards slopes that are prone to rainfall-induced slides.

Researchers predict that global warming will cause an overall decrease in annual rainfall with an increase in frequency and intensity of tropical hurricanes in Hawaii (Murakami et al., 2013; Cai et al., 2015; Kossin et al., 2014). Occurrence of debris flows on the island of Oahu has been well-documented in a 1993 report by the U.S. Geological Survey (Peterson et al., 1993). Due to more recent rainfall, the island of Oahu, Hawaii has experienced numerous landslides along the state highways and elsewhere. This formed the State of Hawaii Department of Transportation's impetus to develop a site-specific landslide warning system for a precarious cut slope adjacent to a main thoroughfare just north of the Pali Highway.

A site-specific landslide warning system can be developed empirically, based on correlations between rainfall intensity/duration and previous slide occurrences or mechanistically, based on the principles of limit equilibrium (slope stability analysis; e.g. Eichenberger et al., 2013, Thiebes et al., 2014, Baum and Godt, 2010, and Kanjanakul et al., 2016) or based on a coupled flow-deformation numerical analysis. Since the mechanistic approaches are more rational, they form the focus of this work. The mechanistic approaches typically require:

1. A geotechnical investigation to characterize the soil;
2. Monitoring the in situ soil suction, water content, slope movement and rainfall;
3. A saturated-unsaturated transient flow model that has to be calibrated and then used to estimate the change in effective stresses during rain events. Influence of the antecedent moisture, rainfall intensity and duration, evapotranspiration, soil water characteristic curve (SWCC) and variation of hydraulic conductivity with water content or suction must be considered in the calibration process; and
4. An appropriate model (slope stability or numerical) for prediction and real time warning of rainfall-induced landslides.

1.2 Objectives

A precarious cut slope on the windward side of the island of Oahu, Hawaii was selected for this study and for development of a landslide warning system. This site is located on a road that is an extension of the Pali Highway into Kailua. It was selected because numerous slope failures have occurred along the Pali Highway since construction completion and because this slope is rather steep and barren.

The objectives of this research are as follows:

1. Perform laboratory tests to obtain the mechanical and hydraulic parameters necessary to model the slope response to rainfall and evaporation;
2. Obtain the BBM parameters for the slope material;
3. Calibrate a transient hydrological flow model to field-measured soil moisture and suctions;
4. Develop mechanistically-based landslide warning thresholds using the calibrated transient hydrological model to obtain moisture/suction response due to a design storm;
5. Establish threshold values and propose plans of actions if each threshold is exceeded; and
6. Perform a slope stability analysis of the slope due to a design storm event.

In order to achieve the objectives above, the following tasks were carried out:

1. Engage a drilling contractor to perform soil investigation, collect soil samples and install monitoring instruments at the slope site;
2. Install instruments such as tensiometers to measure in situ suction, water content sensors to measure water content, in-place inclinometers to measure lateral ground deflections and a rain gage to measure the rainfall at the slope to be investigated;
3. Conduct laboratory tests to measure saturated hydraulic conductivity, soil water characteristic curves, saturated and unsaturated shear strength and compressibility parameters for the in situ soil;
4. Investigate how the hydraulic conductivity, suction and shear strength vary as a function of degree of saturation (or water content);
5. Monitor rainfall and water content/suction in real time and calibrate the transient hydrological model;
6. Develop a saturated-unsaturated transient hydrological model using the geometry, in situ water contents/suction from Step 5, and laboratory test results from Step 4;
7. Use the calibrated transient hydrological model to predict pore pressure/suction in the slope during a design rainfall event. Input these pore pressure/suction values into a slope analysis.
8. Determine threshold values of these instruments to develop a real-time landslide warning system.

1.3 Outline

The outline of this report is as follows. Chapter 2 contains a review of the literature on elements pertinent to the development of a landslide warning system. In Chapter 3, details of the site, geology, historical landslides and geotechnical investigation are elucidated. Chapter 4 summarizes the various instrument types installed and their layout. Results of the laboratory tests and the resulting soil parameters are presented in Chapter 5. In Chapter 6, details of the transient hydrological model are discussed and the results summarized. A slope stability analysis assuming full saturation and assuming a 500-year storm is presented in Chapter 7 along with a methodology to develop threshold response values. Chapter 8 discusses the limitations of two finite element analysis software for analyzing unsaturated slopes. In Chapter 9, the report concludes with a summary of the pertinent findings along with some suggestions for future research. The following figure is a schematic of the outline the dissertation and how each chapter is related.

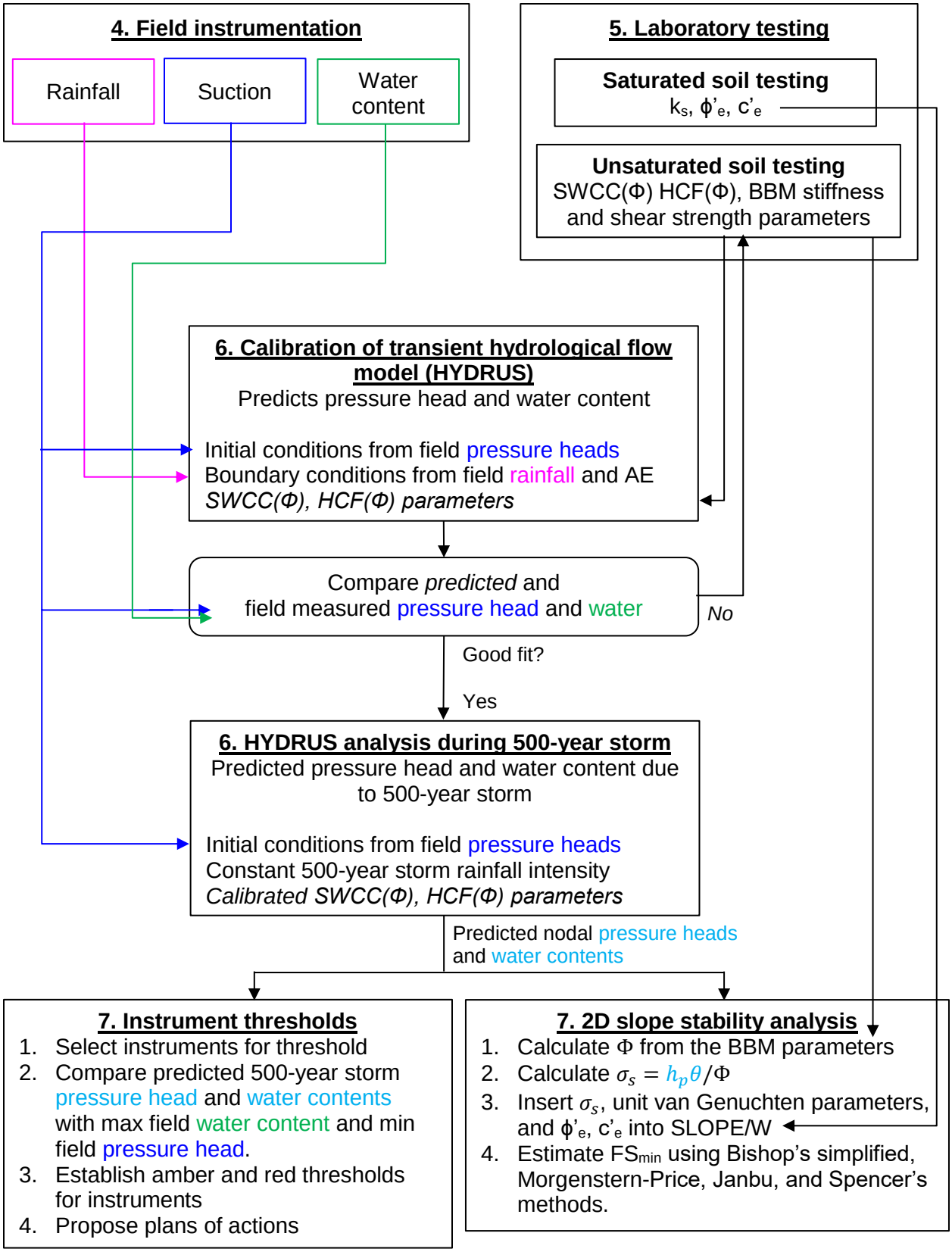

FIGURE 1.1 Flowchart showing organization of dissertation

2 LITERATURE REVIEW

In this chapter, only literature review of subjects pertinent to this research is provided. A topic deemed important and relevant to this research is constitutive modelling of partially saturated soils since this work involves unsaturated soil mechanics. Then, landslide warning systems that are based on limit equilibrium methods are reviewed followed by those based on numerical methods.

2.1 Constitutive Modeling of Partially Saturated Soils

Constitutive modelling of partially saturated soils has seen significant growth in the last three decades. Of these models, the Basic Barcelona Model (BBM) is probably the best known (Alonso et al., 1990). Several researchers have further advanced constitutive modeling of unsaturated soils to address some of the limitations of the BBM, however many of them follow the same framework. Therefore, a review of the BBM model can provide a general basis to understand constitutive modeling of unsaturated soils. Such a review is presented below. Some constitutive models have deviated from the general framework of the BBM to capture unsaturated soil behavior that is not possible to model using the BBM framework such as hysteresis, effective net mean stresses and undrained stress states. Detailed comparisons of constitutive models for unsaturated soils are available in the literature (Gens, 2006; Sheng, 2008; D'Onza et al., 2011).

The BBM is formulated using matric suction, *s*, as an additional independent stress state variable in addition to the Cambridge net mean stress (*p'*), deviatoric stress (*q*) and specific volume ($v = 1 + e$ defined as the volume of soil containing unit volume of soil grains), where in triaxial compression

$$p' = \frac{1}{3}(\sigma_1' + 2\sigma_3') \qquad (2.1)$$

$$q = \sigma_1 - \sigma_3 \qquad (2.2)$$

where σ_1 and σ_3 are the major and minor principal total stresses, respectively, σ_1' and σ_3' are the major and minor principal effective stresses, respectively. For convenience, the prime will be dropped from *p'* so that henceforth, *p* will automatically mean *p'*.

During virgin isotropic compression at constant *s*, v varies with *p* as follows:

$$v = N(s) - \lambda(s)\, ln\frac{p}{p^c} \qquad (2.3)$$

where *N*(*s*) = specific volume corresponding to a reference stress p^c and $\lambda(s)$ is the slope of the normal compression line (NCL) for a given value of suction. Therefore, Eq. 2.3 represents a family of constant suction NCLs that vary with suction. The "intercept" *N*(*s*) and slope $\lambda(s)$ are defined as follows:

$$N(s) = N(0) - \kappa_s\, ln\frac{s+p_a}{p_a} \qquad (2.4)$$

$$\lambda(s) = \lambda(0)[(1-r)\,exp(-\beta s) + 1] \qquad (2.5)$$

where $\lambda(0)$ = slope of the NCL when the soil is saturated (s = 0), $N(0)$ = specific volume corresponding to s = 0, r is a constant related to the stiffness of the soil [when $s \rightarrow \infty$, $r = \lambda(s\rightarrow\infty)/\lambda(0)$], β is a parameter that controls the rate of soil stiffness increase with suction, κ_s is the slope of the unload-reload line to define the elastic volumetric strains due to changes in suction and p_a = atmospheric pressure which is added to s to avoid having the natural logarithmic term be undefined when s = 0.

The BBM yield surface in p-q-s space is shown in Figure 2.1. When the soil is saturated, s = 0, the yield surface defaults to the Modified Cam Clay (MCC) ellipse. The BBM has three additional lines compared to the MCC. For isotropic compression, the model is characterized by two yield curves - loading collapse (LC) and suction increase (SI) curves. A third line is needed to capture the effects of the increase in shear strength due to the effects of suction; i.e.; suction causes the capillary cohesion to increase from 0 when the soil is saturated. Characteristics of these 3 lines are elucidated further below.

1. The size of the elastic domain increases as suction increases. The size of the elastic domain is limited by the loading collapse (LC) curve. The LC line allows a normally consolidated soil to support irreversible plastic strains and to harden when the suction increases as there will be an increase in stiffness with increasing suction. The equation for the LC line is given by (Alonso et al., 1990):

$$\frac{p_o}{p^c} = \left(\frac{p_o^*}{p^c}\right)^{\frac{\lambda(0)-\kappa}{\lambda(s)-\kappa}} \qquad (2.6)$$

   where p_o = preconsolidation pressure of the unsaturated soil, p_o^* = preconsolidation pressure of the soil when saturated and κ is the slope of the saturated unload-reload line which defines the volumetric elastic strains due to changes in net mean stress, p.

2. Under very high suctions, irreversible volumetric strains may occur as a consequence of suction increase due to drying. A suction increase (SI) line represents the yield curve when this occurs. Parameters associated with changes in suction and the SI yield curve include λ_s, which is the slope of the NCL due to changes in suction across virgin states and κ_s, which is the slope of the unload-reload line to define the elastic volumetric strains due to changes in suction.
3. A capillary cohesion varies linearly with suction as shown by the dashed line in Figure 2.1.

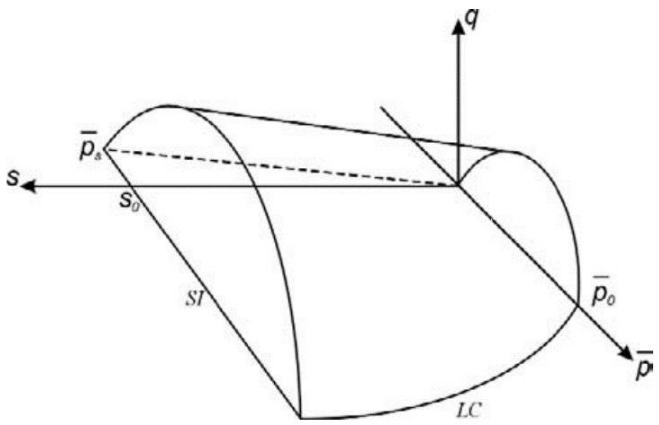

FIGURE 2.1 Basic Barcelona Model yield surface (after Laloui et al., 2008)

The BBM parameters can be measured by conducting the following tests:

1. Isotropic drained compression loading and unloading tests at several constant suction values to find p^c, p_o^*, $\lambda(0)$, κ, r and β;

2. Tests with a dry-wet cycle at a constant net mean stress to measure s_o, λ_s, and κ_s, where s_o is an initial reference suction variable that defines the initial position of the yield surface *SI*. Analogous to the preconsolidation pressure, s_o is the maximum past suction ever experienced by the soil. It is the value of suction at which the soil transitions from the elastic state to the virgin range when suction is increased; and

3. Drained shear strength tests at different suctions to provide G, M and k where G = shear modulus during elastic loading, k = slope of line on q-s plane that increases linearly with suction and M = slope of the critical state line.

The following are some limitations of the BBM:

1. The BBM uses straight lines to model the specific volume-ln p relationships. Use of straight lines implies a continuous increase of collapse strains upon wetting, which is unrealistic because collapse strains cannot increase indefinitely;

2. The elastic modulus is suction-independent, which is known to be untrue. This is deemed important in pavement geotechnics.

3. The loading collapse and suction increase yield curves are uncoupled. In more recent work (Zhang and Lytton, 2009), the expansion of one of the yield curves will lead to a coupled expansion of the other; and

4. The original BBM model does not model the coupled hydraulic and mechanical states during undrained loading; i.e.; it does not consider SWCC and HCF hysteresis nor does it consider the pressure dependency of the SWCC.

2.2 Limit-Equilibrium-Based Landslide Warning Systems

Limit equilibrium analysis of slopes to analyze their stability is ubiquitous amongst the geotechnical engineering profession. It has also been applied to develop landslide early warning systems for site-specific slopes. A summary of these warning systems is shown in Table 2-1. There are numerous publications on landslide warning systems for hypothetical slopes, slopes that do not have laboratory testing or monitoring instruments, slopes that do not consider transient flow seepage or slopes that do not consider suction in the stability model. These cases have been omitted. Only warning systems, or work toward establishing a warning system, for a site-specific, un-failed, real slope considering unsaturated soil behavior is included in Table 2.1. Information presented in Table 2-1 include laboratory tests performed to obtain the soil water characteristic curve (SWCC), whether scanning or hysteresis and pressure-dependency of the SWCC were considered, laboratory tests to obtain the shear strength parameters, software employed to model the transient seepage response of the slope due to rainfall, slope stability model utilized, instrument thresholds established and methodology to establish the thresholds.

Prediction of rainfall-induced slope failures consists of several necessary steps. Laboratory tests to obtain the soil's hydraulic characteristics and shear strength must be performed. The influence of suction on shear strength must be captured by using either Fredlund's ϕ^b (Fredlund et al., 1978) or by using Bishop's effective stress parameter, χ (Bishop, 1954). A software is needed to model the transient seepage occurring within the slope due to rainfall. Monitoring instruments are typically installed to measure real-time subsurface response to rainfall. The transient seepage model should be calibrated and used to predict the slope response due to a design storm scenario, the results of which can then be used to establish instrument thresholds. Thresholds can be established for rainfall intensity and duration that precedes slope failure. They can also be established for other types of instruments such as tensiometers, water content sensors and inclinometers.

Software that can be used to model the transient seepage response of a slope due to rainfall include: HYDRUS 2D/3D (Simunek et al., 2012), Seep/W (Geo-Slope International, 2012), CHASM (Lateh et al., 2008), Vadose/W (Geo-Slope International, 2014), and SVFlux (SoilVision Systems Ltd., 2018). There is a multitude of software available to analyze the stability of a slope, some of which include Slope/W (Geo-Slope International Ltd., 2015), CHASM, SVSlope (SoilVision Systems Ltd., 2018), STABL (Ensoft Inc., 2015), UTEXAS4 (Wright, 2004), STABGM (Duncan et al., 1985), etc. Common limit equilibrium procedures employed by these software to compute the most critical factor of safety include Ordinary Method of Slices, Bishop's simplified, Janbu, Morgenstern-Price, Spencer, Sarma, etc.

Table 2-1 Summary of site-specific limit-equilibrium-based landslide warning systems from the literature

Reference	SWCC Lab Tests	Shear Strength Lab Tests	Software for Transient Hydrological Calibration	Scanning Considered?	Pressure-Dependent SWCCs and HCFs?	Slope Stability Model	Instrument Thresholds Established	Methodology of Establishing Thresholds
Harris et al., (2016)	PP[1]	Back analyses + Literature	SEEP/W	No	No	Slope/W Morgenstern-Price	Rainfall	Artificial Neural Network
Eichenberger et al., (2013)	Suction-controlled PP[1]	Literature	Lagamine	No (hysteresis not observed in tests)	Yes	Infinite	Suction	Critical pore pressure parameter, r_u[2]
Thiebes et al., (2014)	None – obtained from SPAW model[3] using PSD[4]	Geotechnical database	CHASM	No	No	Bishop's simplified and Janbu	Rainfall, water content	*FS*[5] and groundwater levels
Kanjanakul et al., (2016)	N/A	Direct shear	SEEP/W	No	No	SLOPE/W Bishop's simplified	Rainfall and API[6]	*FS*[5]
Godt and McKenna, (2008)	Capillary-rise tests	Direct shear	TRIGRS	No	No	Infinite slope, Janbu	Rainfall	*FS*[5]

Notes: 1. PP = pressure plate

2. r_u = pore pressure ratio = $\frac{Vol.of\ sliding\ mass\ under\ water\ x\ Unit\ weight\ of\ water}{Vol.of\ sliding\ mass\ x\ Unit\ weight\ of\ soil}$

3. SPAW model = Soil-Plant-Air-Water model developed by Saxton and Rawls (2006) that contains a soil database filled with geotechnical and hydrological parameters
4. PSD = particle size distribution
5. FS = factor of safety
6. API = antecedent precipitation index

2.3 Landslide Warning Systems Based on Soil Volume Change and Stress-Deformation Behavior via Numerical Analysis

There are numerous numerical methods available to assess the stress-deformation behavior of an unsaturated soil slope due to rainfall. They include the finite element method (FEM), finite difference method, shear strength reduction technique, material point method, distinct element method, and enhanced limit method (Kulhawy, 1969). Finite element software available include: NOSAT (Alonso et al., 1996), CODE_BRIGHT (Olivella et al., 1996), SOFT (Xiong et al., 2014), ICFEP (Potts and Zdravkovic, 1999), ACMEG-TS (Francois and Laloui, 2008) and ABAQUS (2003). The enhanced limit method (Kulhawy, 1969) produces a global factor of safety along the slip surface based on stress distributions from a finite element model. The shear strength reduction technique uses finite elements to calculate the hydraulic and mechanical states, and shear strains at each node within the soil mass. It then calculates the factor of safety and deformations using a reduction of the shear strength parameters and the states of stresses from the FEM.

A thorough review of the literature did not yield a single reference of a landslide warning system that is based on numerical methods. Of the software mentioned above, none have yet been used to establish a landslide warning system for a real slope. One possible reason is because these computer programs are not able to model the scanning or hysteresis behavior of soil during drying and wetting cycles satisfactorily. Therefore, there is clearly room for growth and research in this area.

3 SITE DESCRIPTION

3.1 Location

The 12.2-m-high cut slope is adjacent to Kalaniana'ole Highway on the southeast side of the island of Oahu, Hawaii with Le Jardin Academy lying to the northeast as shown in Figure 3.1. The elevation view of the slope is shown in Figure 3.2, where it can be seen that the lower and upper portions of the compound slope are 55 and 63°, respectively.

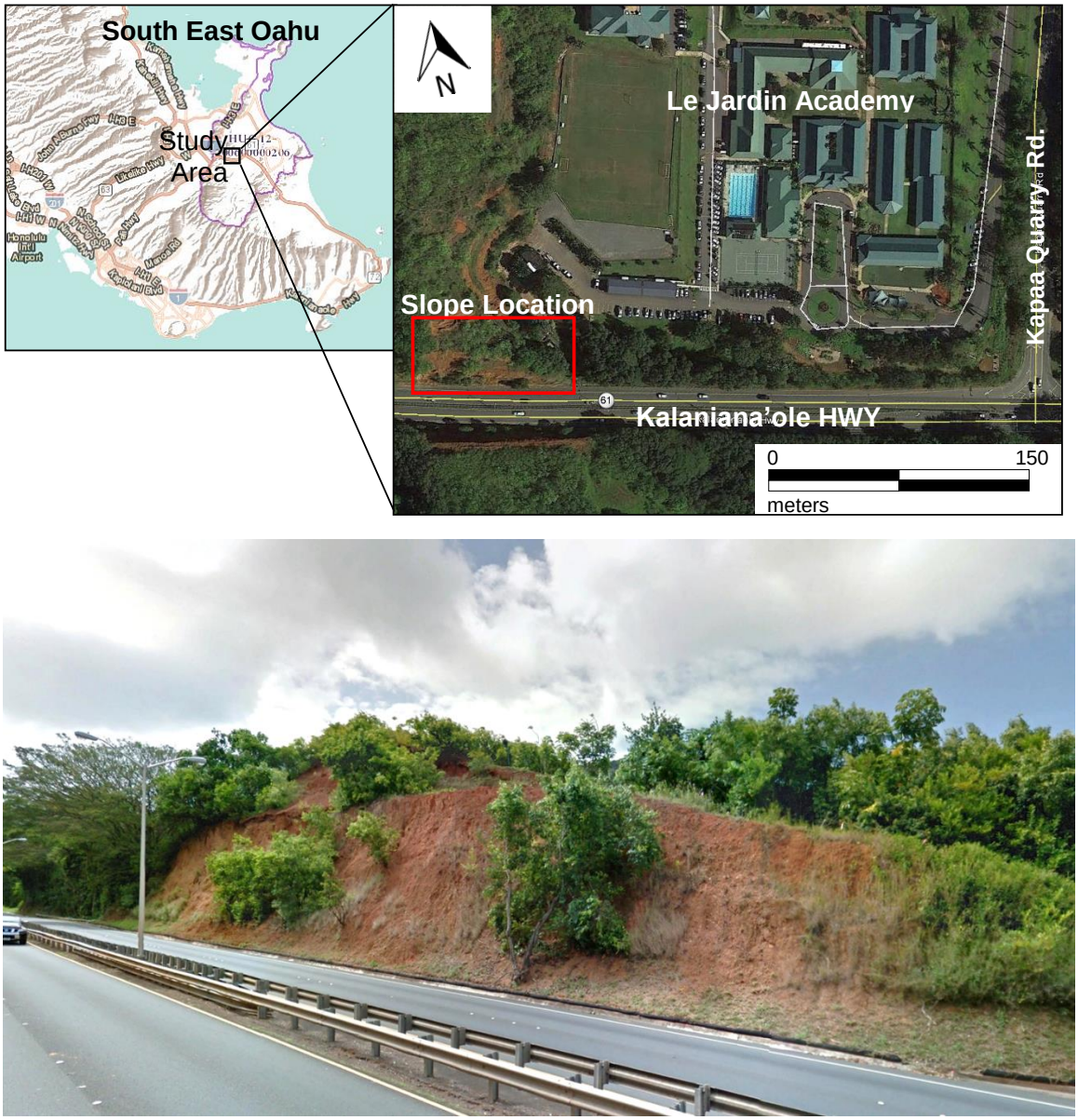

FIGURE 3.1 Location of cut slope on Kalaniana'ole Highway (Google maps, 2017)

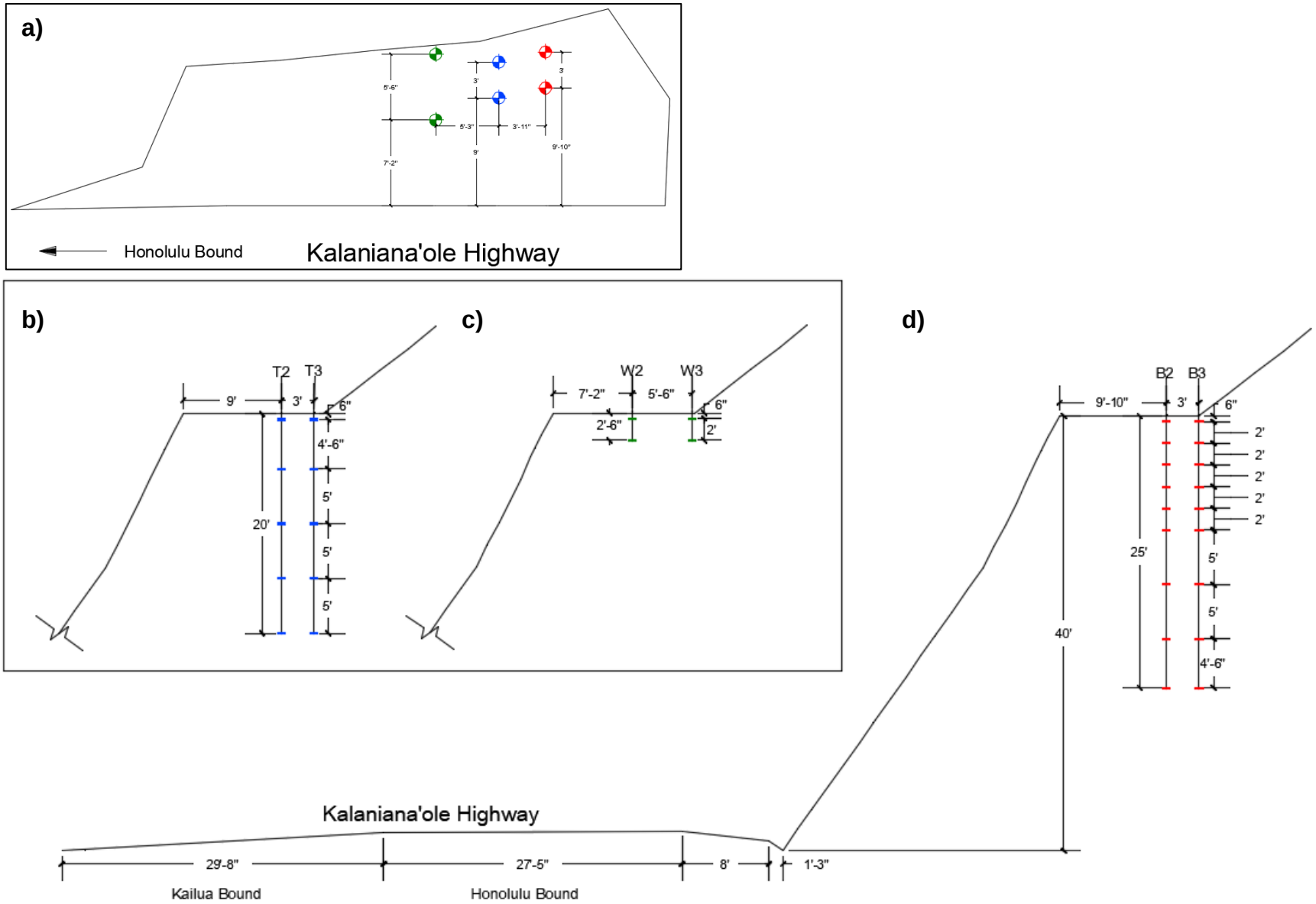

FIGURE 3.2 Instrument layout in plan (a) and profile view for (b) tensiometers (c) water content sensors, and (d) inclinometers

3.2 Geology and Prevailing Groundwater Conditions

The island of Oahu was formed by the extrusion of basaltic lava from the Waianae and Ko'olau shield volcanoes. The older Waianae Volcano is estimated to be middle to late Pliocene in age and forms the western third of Oahu, while the Ko'olau Volcano is estimated to be late Pliocene to early Pleistocene in age and accounts for about the eastern two thirds of Oahu. The Ko'olau and Waianae volcanos may have grown as separate islands but were eventually joined and saddled by the Leilehua Plateau (Hazlett and Hyndman, 1996). The Leilehua Plateau and the Waianae volcano braced the western flank of the Ko'olau volcano (Figure 3.3). A portion of the steep, unsupported eastern flank eventually slid into the ocean as more and more magma rose into the volcano. Known as the Nuuanu slide, this is one of the largest known slides on earth.

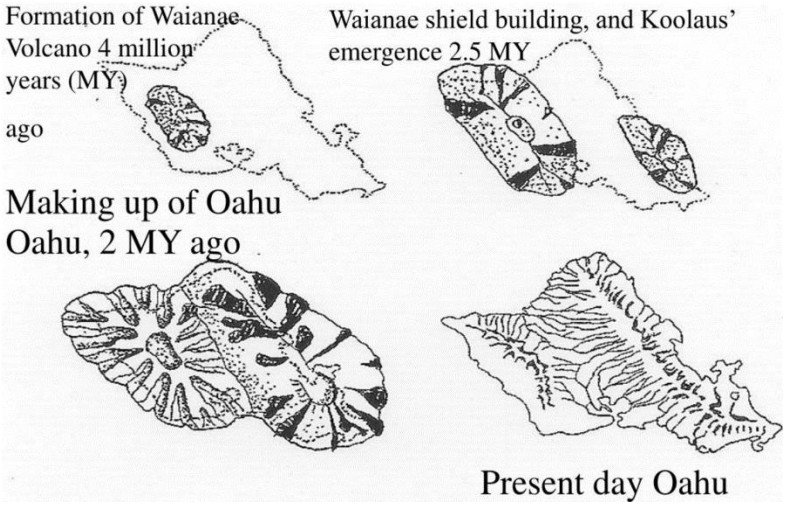

FIGURE 3.3 Formation of Oahu by coalescence of the Waianae and Ko'olau volcanoes (Carlquist, 1970)

The slope actually lies within the Ko'olau caldera (Figure 3.4), half of which is still standing while the other half has slid into the ocean (Figure 3.5). Rising hydrothermal fluids and gases emanating from the active volcano has caused intense decomposition of the basaltic lava and breccia, and over time, this material has weathered into a saprolite.

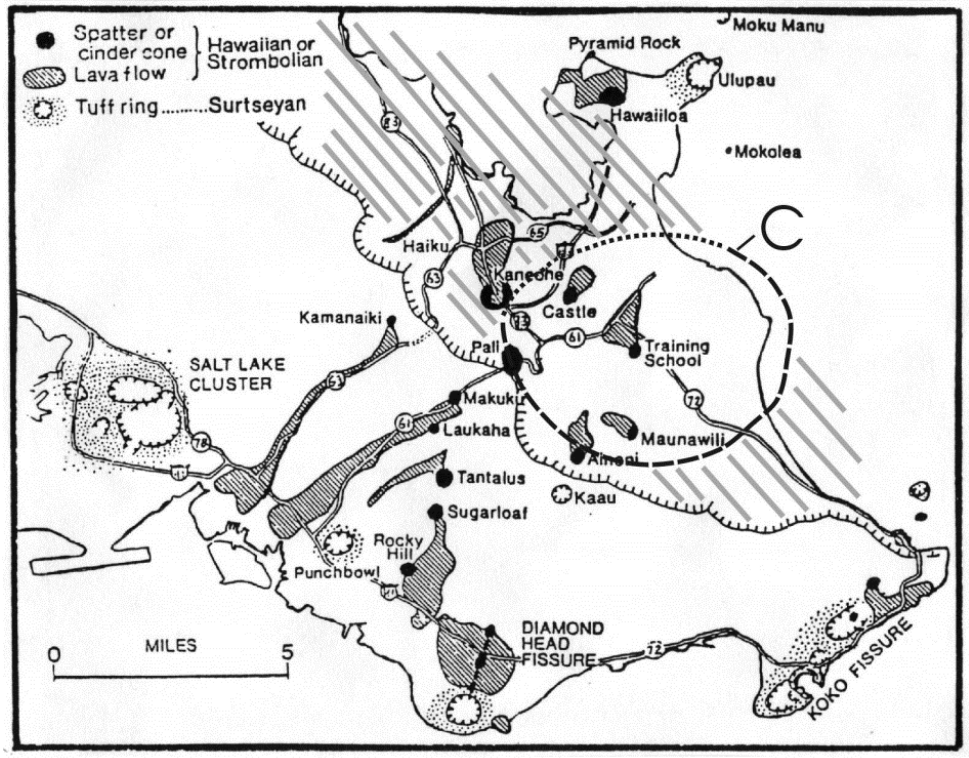

FIGURE 3.4 Slope location with respect to the Ko'olau caldera (Rowland and Garcia, 2004)

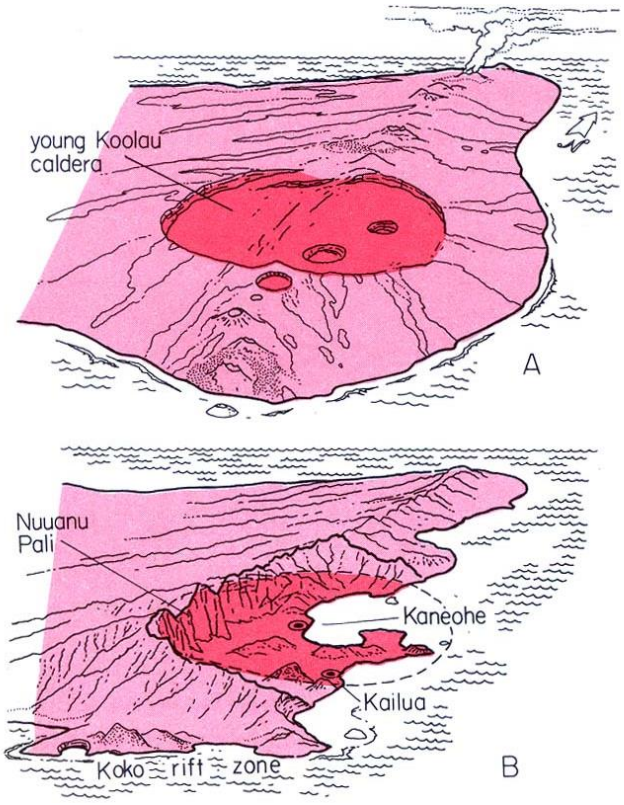

Collapse of the flank of Ko'olau caldera. A is before collapse; B is after collapse.

FIGURE 3.5 Collapse of the Ko'olau caldera (from Hazlett and Hyndman, 1996)

The slope crest lies about 50 m above mean sea level (MSL). Ground water table was not encountered in any of the borings drilled. However, according to Engott et al. (2015), the ground water table at this site is at about El. 5.8 m, which is 44.2 m below the slope crest.

3.3 Nearby Historical Landslides

Construction of the Pali Highway tunnel began in the mid-1950s and the tunnel was first opened for one-way traffic in 1957. A second tunnel was completed in 1961. The existing Pali Highway is actually the third roadway built along a route that runs roughly close to the old Pali Highway, which is now closed and mainly used by hikers.

The current Pali Highway lies southeast of the slope site. Since completion in the late 1950s, it has experienced a number of landslides, many of which have been documented by Torikai and Wilson (1992) and Macdonald et al. (1983). Table 3.1 documents some of the slope failures in the vicinity of Pali/Kalaniana'ole Highway since construction completion of the Pali Highway tunnel while figures 3.6 through 3.13 contain illustrations of a couple of listed in Table 3.1 plus some other more recent slides.

Table 3-1 Landslides in the vicinity of Pali/Kalaniana'ole Highway (from Torikai and Wilson, 1992 and Macdonald et al., 1983)

Date	Slide Location	Source
3/6/1958	Rock slide at entrance to Kailua-side tunnel of Pali Highway, Honolulu-bound. 6 inches of mud at exit of Kailua-side tunnel, Honolulu-bound.	Honolulu Star Bulletin
11/13/1965	High bank gave way on north side of excavation for Kailua Drive-in Theater, which is the site of Le Jardin Academy. Hundreds of tons of mud poured over parking area of theater.	Macdonald et al., (1983)
11/13/1965	Large landslide on Kailua-side of Pali tunnels, just above hairpin turn; 15 feet of mud and boulders, covering three lanes, 60 feet wide. Debris slid down 90 feet over a 120 foot high terraced embankment (Figure 3.6)	Cavaliero, E.,and McMurray, T., 1965
11/14/1965	Second, larger slide on Pali Highway; covered 4 lanes up to 15 feet above road surface. Occurred as crews were clearing area of earlier slide	Honolulu Star Bulletin
11/16/1965	Third and largest slide of this storm on Pali Highway, near hairpin turn on Kailua-side dumps 8000 cubic yards of mud and jagged rock on top of two earlier slides. Occurred as helicopter hovered over slide area	Honolulu Star Bulletin
August 1967	A fourth slide took place at the same Pali Highway location as the above three November 1965 slides (Figure 3.7)	Macdonald et al., (1983)
2/1/1969	Rocks on Pali Highway near upper truck ramp	OCDA
5/12/1977	Landslide blocking one Honolulu-bound lane, one block east of Pali Highway and Kamehameha Highway	OCDA
10/31/1978	Boulders on road at Pali Highway and Kamehameha Highway	OCDA
1/8/1980	Landslide at Kalaniana'ole/Kamehameha/Pali Highways junction blocking one lane	OCDA
1/21/1982	Landslide at junction of Auloa Road and Pali Highway	OCDA
1/21/1982	Mudslide on Pali Highway at same site, Honolulu bound, fronting Kailua Drive-In (Note: Kailua Drive-in currently does not exist)	OCDA
2/14/1985	Mudslides blocking one lane on Kalaniana'ole Highway at Kailua Drive-In	OCDA
2/14/1985	Small landslide between Pali Highway and Auloa Road	OCDA
12/31/1987	Mudslide at Kalaniana'ole and Kamehameha Highways	OCDA
1/1/1988	Mudslides on Pali and Kalanianaole Highways	Honolulu Star Bulletin
3/19/1991	Landslide on Kalaniana'ole Highway, past Kailua Drive-In	OCDA
3/23/1991	Mudslide, Kailua side of Pali between Kailua Drive-In and Maunawili Junction, Honolulu-bound	OCDA
5/20/2003	Landslide at Castle Junction	Honolulu Star Bulletin
6/2/2003	Fallen debris at Castle Junction	Honolulu Star Bulletin

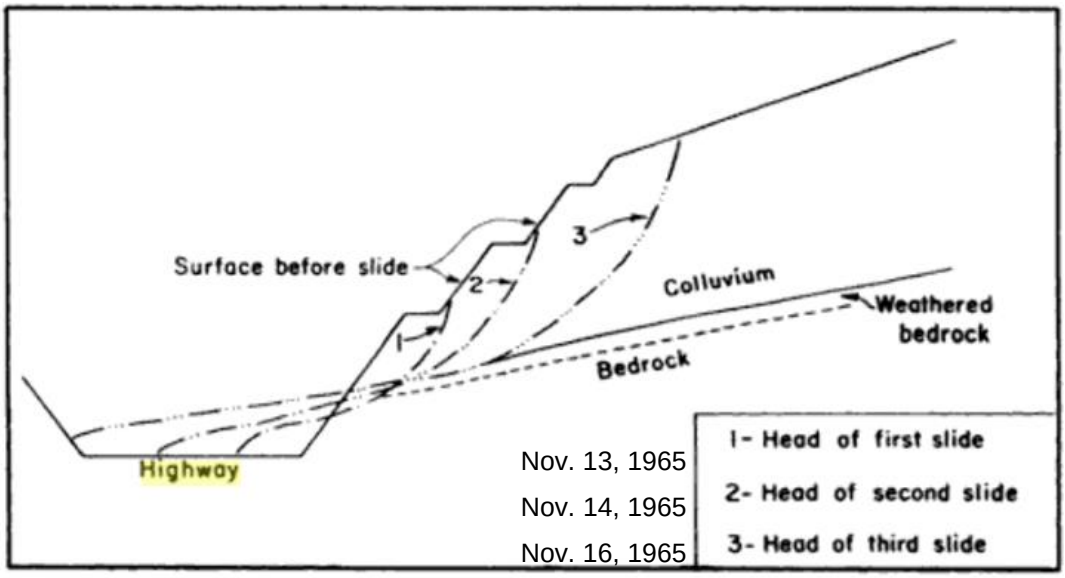

FIGURE 3.6 Cross sections of November 1965 landslides on Pali Highway (from Macdonald et al., 1983)

FIGURE 3.7 August 1967 landslide on Pali Highway at the same location as above (from Macdonald et al., 1983)

FIGURE 3.8 May 20, 2003 Castle Junction slide (Honolulu Star Bulletin, 2003)

FIGURE 3.9 November 1, 2006 landslide on Pali Highway (Honolulu Star Bulletin, 2006)

FIGURE 3.10 February 28, 2011 landslide on Pali Highway (Honolulu Star Advertiser, 2011)

FIGURE 3.11 February 2014 landslide on Pali Highway

FIGURE 3.12 September 28, 2015 mudslide on Pali Highway (KITV4 News, 2015)

(a)

(b)

FIGURE 3.13 July 25, 2016 landslide on Honolulu-bound side of Pali Highway due to Tropical storm Darby (a) before and (b) after covering with a geotextile

Two maps summarizing some of these slides are shown in figs. 3.14 and 3.15. Figure 3.14 from Deb and El-Kadi (2009) presents slides occurring before 2006. Figure 3.15 illustrates slope failures taken from a NASA landslide database which records globally occurring landslides from 2006 to present.

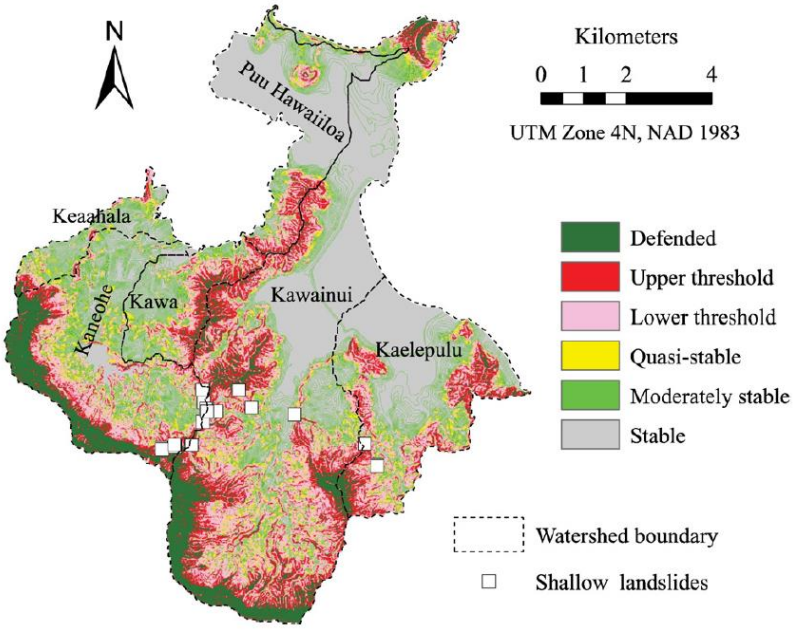

FIGURE 3.14 Locations of rainfall-induced shallow landslides from 1940 – 2006 (Deb and El-Kadi, 2009)

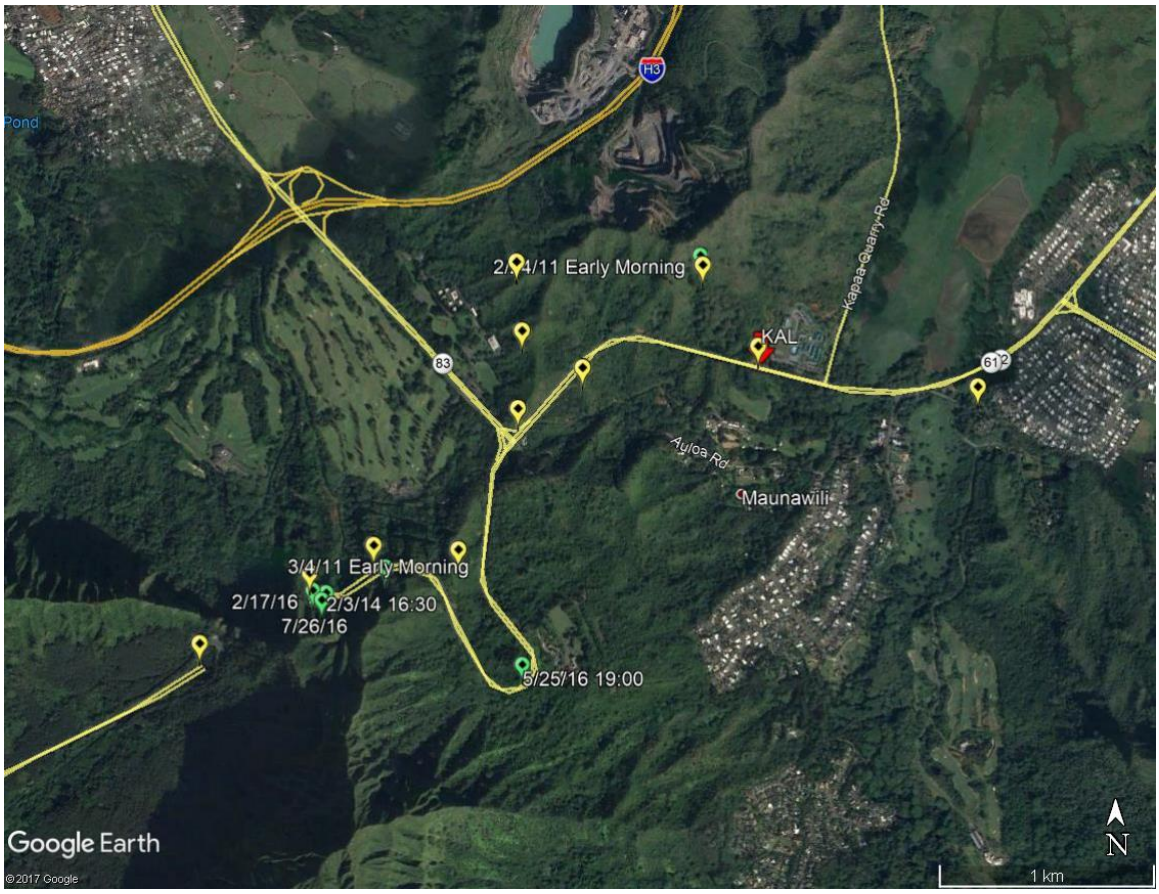

FIGURE 3.15 Map summarizing the locations of recent landslides (20011 – present) on Pali Highway and its vicinity (from Kirschbaum et al., 2010)

3.4 Geotechnical Investigation

Two borings, B2 and B3, were drilled by Geolabs, Inc. to a depth of 7.6 m (25 ft) with continuous sampling alternating between California and split-spoon samplers over the depth of boring (Figure 3.2). For safety reasons, the boreholes were drilled at a 3-m-setback from the slope crest. Inclinometer casings were then inserted into the boreholes and grouted in place after reaching the bottom of the borings. In-place inclinometers were then installed inside the casings in borings B2 and B3. Additional boreholes were drilled nearby to install tensiometers (T2 and T3 in boreholes drilled to a depth of 6.1 m or 20 ft) and water content sensors (W2 and W3 in boreholes drilled to a depth of 0.76 m or 2.5 ft). However, no samples were retrieved from these holes.

Split spoon samples were used for index testing to measure the soil grain size distribution, Atterberg limits, water content and specific gravity. Soil specimens from the California samplers were utilized for shear and stiffness tests as well as tests to obtain the soil-water characteristic curves (SWCC).

3.4.1 Split Spoon Samplers from Standard Penetration Test

Standard penetration tests (SPT) were conducted using a safety hammer, which has an energy efficiency of 60%, and which has an energy correction factor of 1.0. From the split spoon samplers, the soil was observed to consist of a red-brown stiff to very stiff (standard penetration test or SPT blow counts varying from 11 to 31) uniform elastic silt (MH) or saprolite with more than 90% fines. Figure 3.16 presents the SPT blow counts corrected for overburden plotted versus depth. The average corrected blow count over the depth of both borings B2 and B3 is approximately 26 blows/ft.

3.4.2 Modified California Samplers

Modified California samplers were used to obtain “undisturbed” samples by Geolabs, Inc. because Shelby tubes would have likely crimped when pushed into such stiff soils and because Pitcher samplers were not available at the time of drilling. The modified California sampler is a thick-wall, ring-lined split barrel sampler that is driven into the soil using a 64-kg (140-lb) SPT hammer falling 76 cm (30 inches). Strictly, samples from the modified California Sampler are technically “disturbed” due to the large area ratio of the sampler (sampler wall area/sample cross sectional area) and due to hammer advancement of the sampler. However, this was the only option provided by the driller to obtain soil samples for strength and stiffness testing. To reduce the effects of disturbance, the outer portion of the modified California samples were trimmed down from a diameter of 2.8 inches to 2.4 inches for strength testing, and to 2.5 inches for consolidation testing.

Approximately half the modified California soil samples were tested at the University of Hawaii and the other half were provided to Prof. Xiong Zhang of Missouri University of Science and Technology to perform constant water content consolidation and constant water content direct shear tests for estimating the Basic Barcelona model (BBM) soil parameters. Simultaneously and independently, the BBM parameters were determined as part of this work by running isotropic compression and constant water content triaxial tests on unsaturated soil specimens to enable a comparison of the parameters from both approaches to be made.

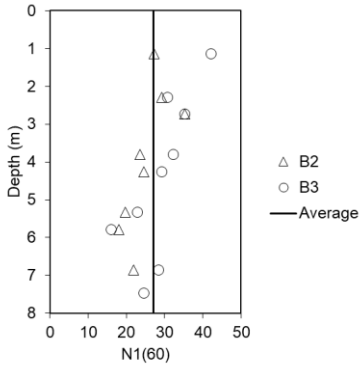

FIGURE 3.16 SPT blow counts versus depth

4 INSTRUMENTATION

4.1 Instrumentation Types, Layout and Installation

The following instruments were installed at the slope. The layout of the instruments is shown in Figure 3.2.

Table 4-1 Instrument, purpose, type, location and depth

Instrument	Purpose	Make, model and accuracy	Location	Depth
In-place inclinometer	To measure lateral deflection of the slope	Geokon MEMs 6150-4 (±0.05 mm/m)	B2 and B3	≤ 7.62 m (25 ft)
Tensiometer	To measure soil suction	Decagon MPS-6 (±10% accuracy)	T2 and T3	≤ 6.1 m (20 ft)
Water content sensor	To measure soil water content	Decagon GS-3 (±3% accuracy)	W2 and W3	≤ 0.76 m (2.5 ft)
Rain gage	To measure precipitation	Campbell Scientific TE525WS-L tipping rain bucket (±1% accuracy)	Above ground	N/A

Prior to installation of the in-place inclinometers, a casing was first inserted into the borehole and the annular space grouted (Figure 4.1). The string of in-place inclinometers was then assembled and lowered into the casing and the hole capped off. The bottom of the inclinometer casing is embedded 7.6 m (25 ft) below the slope crest, which is below the sliding surfaces of most rainfall-induced landslides (usually between 2 and 4 m deep according to Eichenberger et al., 2010). The bottom of the inclinometer casing was deemed relatively immobile and can be considered as a point of fixity for reference purposes.

Five tensiometers were installed each in boreholes T2 and T3 at depths of 0.15 m (0.5 ft), 1.52 m (5 ft), 3.05 m (10 ft), 4.57 m (15 ft) and 6.1 m (20 ft). The tensiometers were first attached to a sacrificial PVC pipe (Figure 4.2) and then the whole assembly was lowered into the borehole. The volume immediately surrounding each tensiometer was backfilled with silica fines but the volume in between adjacent tensiometers was backfilled with bentonite cement grout to prevent flow continuity along the borehole depth. The measurable suction for the Decagon MPS-6 tensiometers ranges from 9 to 100,000 kPa.

FIGURE 4.1 Installation of inclinometer casing

(a) (b)

FIGURE 4.2 (a) Decagon MPS-6 tensiometer and (b) tensiometer/PVC assembly lowered into borehole

Water content sensors were installed in the walls of the W-series boreholes at depths of 0.15 m (0.5 ft) and 0.76 m (2.5 ft corresponding to an arm's length). Having to insert the 3 needle sensor prongs

(Figure 4.3a) horizontally into the borehole wall (Figure 4.3b) precluded them from being installed at larger depths because an installation tool was not available at that time. After installation, the boreholes were grouted with bentonite cement grout.

(a) (b) (c)

FIGURE 4.3 (a) Decagon GS-3 water content sensor, (b) water content sensors affixed to the borehole wall, and (c) hand auger used to drill water content sensor borehole

The wires from all instruments were connected to two Geokon 16-channel multiplexers, which in turn was wired to a GEOKON Micro-1000 datalogger. The datalogger was programmed to collect readings every 4 hours. Data was downloaded via a cellular phone modem housed in the datalogger. The whole system was powered by a 12V battery charged by a solar panel during the day. A rain gage was housed separately from the datalogger and solar panel to minimize obstruction when collecting precipitation (Figure 4.4).

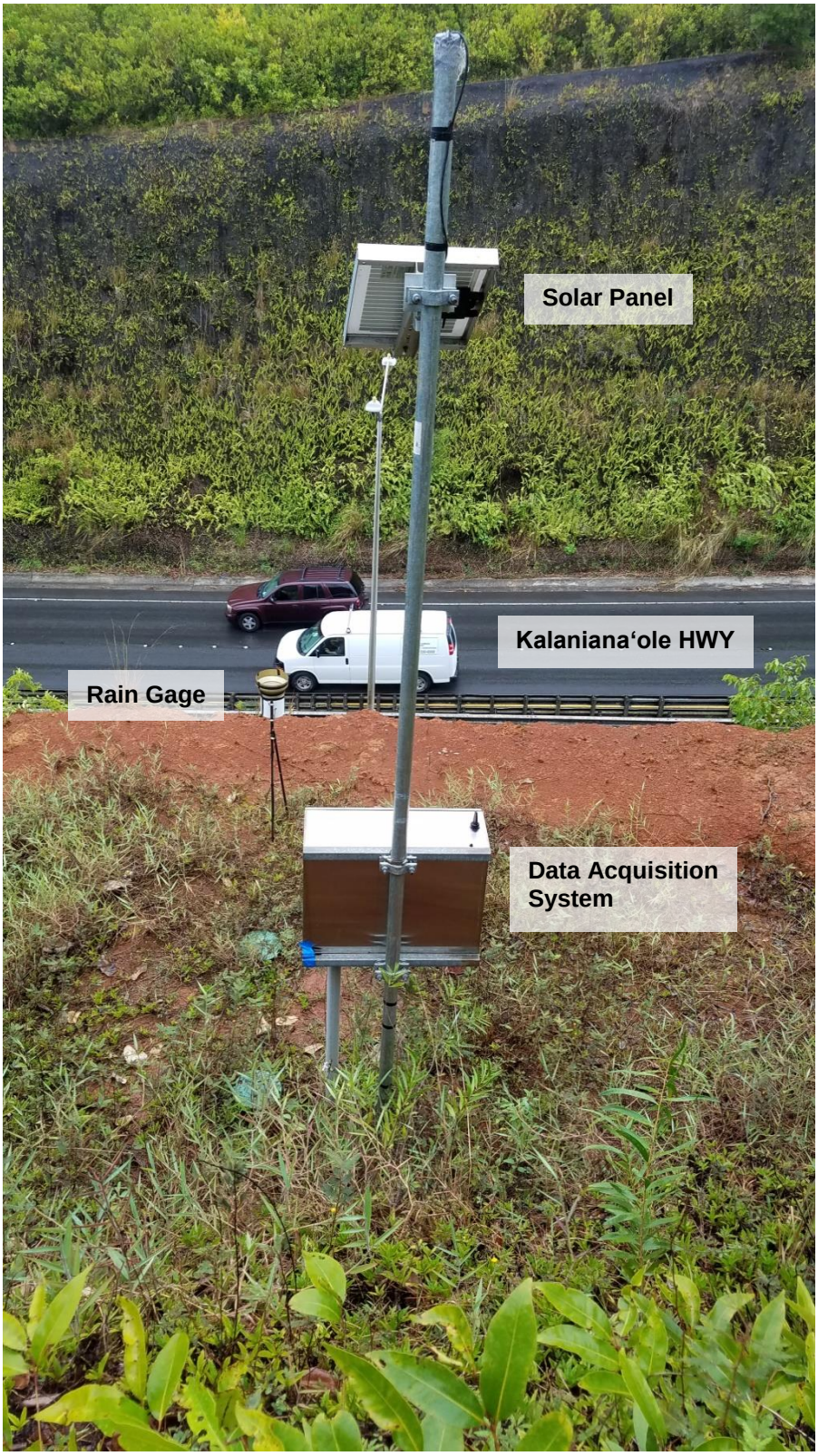
Solar Panel
Kalaniana‘ole HWY
Rain Gage
Data Acquisition System

(a)

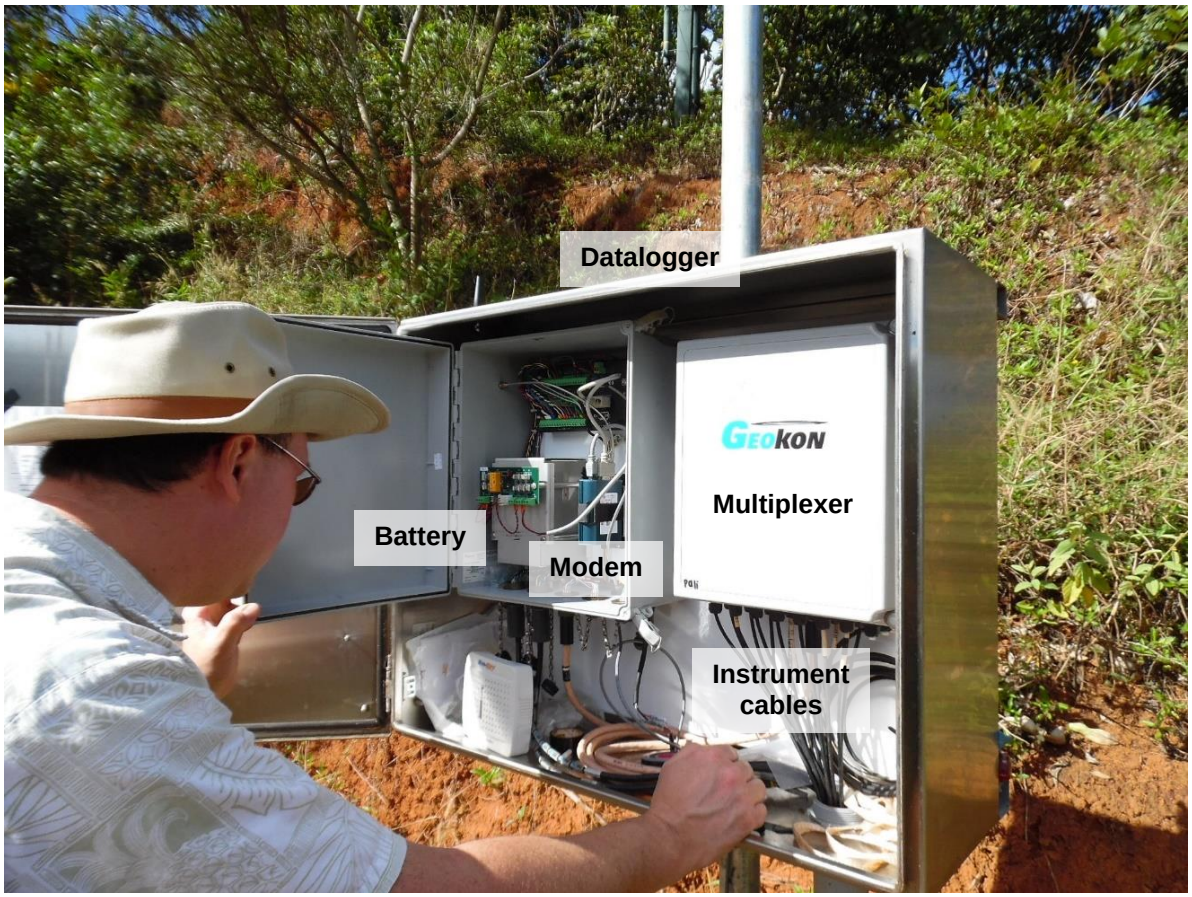

(b)

FIGURE 4.4 (a) Datalogger, solar panel and rain gage and (b) interior of the datalogger

4.2 Results

This section presents the results from the monitoring instruments.

4.2.1 Precipitation

Due to limited resources, only a rain gage was installed at the slope site rather than a comprehensive weather station that would provide all the data necessary to estimate potential evaporation. The rainfall record over the entire monitoring period is shown in Figure 4.5.

There exists a gap in all the instrument data from 12/2/2016 to 1/27/2017 due to the following: (a) the 12V battery in the datalogger had to be replaced; and (b) damage of the tensiometer cables in Borings T2 and T3. Bees built a hive inside the circular valve box covering the top of the inclinometer casing in Boring B3 (Figure 4.6), which is believed to have attracted rodents that chewed on the cables within the PVC conduit routing the tensiometer and water content sensor cables to the data acquisition system. The cables were subsequently spliced after engaging a beekeeper to dispose the hive.

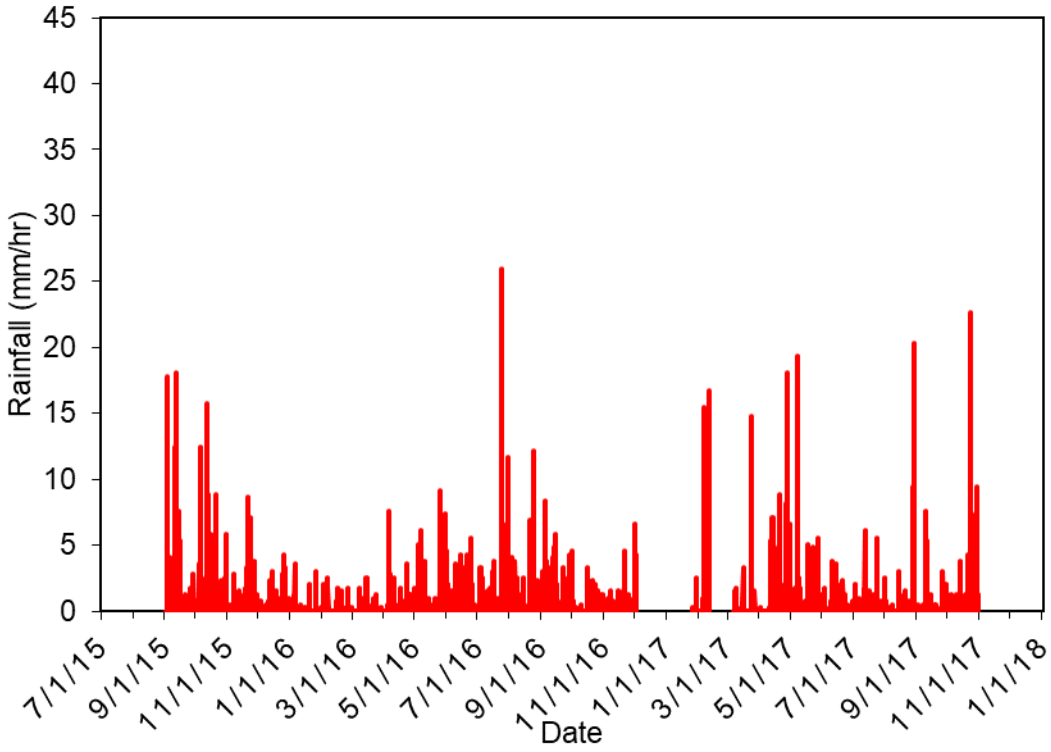

FIGURE 4.5 Rainfall record at the slope site

FIGURE 4.6 Bee hive at inclinometer Boring B3

There were two other problematic events that required the rain gage data to be corrected: (a) when the rain gage was clogged (7/1/2015 to 9/2/2015 and 11/1/2017 to 1/1/2018); and (b) when the higher solar panel and the lower rain gage were initially installed on the same pole, where the former may have obstructed precipitation from entering the latter (9/2/2015 to 12/2/2016). The rain gage was subsequently relocated to stand alone as shown in Figure 4.4a.

To correct the rainfall record during these problematic events, data from 5 nearby rain gages were collected and averaged using an inverse-distance-weighting (IDW) averaging method. These 5 gages are located at Kailua Fire Station (KFS), Luluku (LUL), Maunawili (MAU), St. Stephens Seminary (STV), and Olomana Fire Station (OFS) (Figure 4.1). Their coordinates, distance from the slope, dates used to calculate the IDW average, and source of the data are shown in Table 4-2.

Table 4-2 Rain gages used to calculate the inverse-distance-weighting average rainfall at the slope site

Station	Latitude	Longitude	Distance (m)	Dates Used	Source
KFS	21.39580	-157.73990	3654	7/1/15 - 9/30/15	NOAA NCEI (2018)
LUL	21.38750	-157.80940	4236	7/1/15 - 9/30/15	NOAA NCEI (2018)
MAU	21.35080	-157.76670	3045	7/1/15-1/1/18	NOAA NCEI (2018) and Horel (2002)
STV	21.37430	-157.79385	1955	9/30/15-1/1/18	Horel (2002)
OFS	21.37750	-157.75083	2544	9/30/15-1/1/18	Horel (2002)

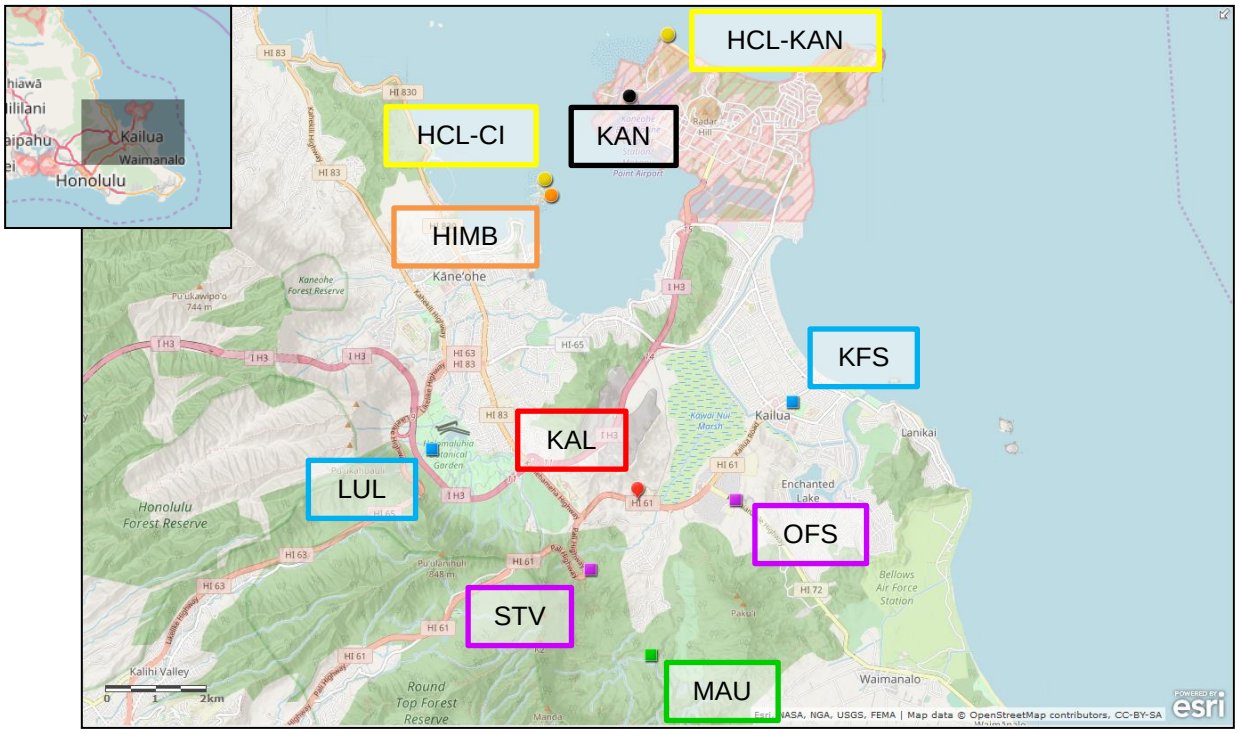

FIGURE 4.7 Location of rain gage and meteorological sites

These problematic rainfall records were adjusted using a double-mass curve. The double mass curve can be used to compare the data for a single station (in this case the rain gage at the slope site being researched denoted as KAL) with that of a pattern composed of data from several other stations in the area (KFS, LUL, MAU, STV and OFS). According to the double mass curve method, a graph of the cumulative precipitation at KAL versus the cumulative IDW precipitation from KFS, LUL, MAU, STV and OFS should be a straight line. Using this concept, the cumulative IDW rainfall is plotted versus the cumulative measured rainfall (Figure 4.8) to populate the missing or problematic KAL data summarized in Table 4-3. The last line of Table 4-3 without an event number is considered the most reliable. The corrected rainfall, KALcorr, was calculated by multiplying the cumulative KAL by the slope of the most reliable data (0.921) divided by the slope during which the corrected rainfall is being calculated (Figure 4.9).

Table 4-3 Problematic or missing rainfall data along with period when the rain gage worked well (last row)

Event	Description	Start Date and Time	End Date and Time	Slope
1	Gage clogged	7/1/15 0:00	9/2/15 9:00	1
2	Rain gage shared same pole as solar panel	9/2/15 9:00	12/2/16 23:00	0.6904
3	Power outage	12/2/16 23:00	1/27/17 14:00	1
4	Gage clogged	11/1/17 0:00	1/1/18 0:00	1
	When gage worked well	1/27/17 1400	11/1/17 000	0.921

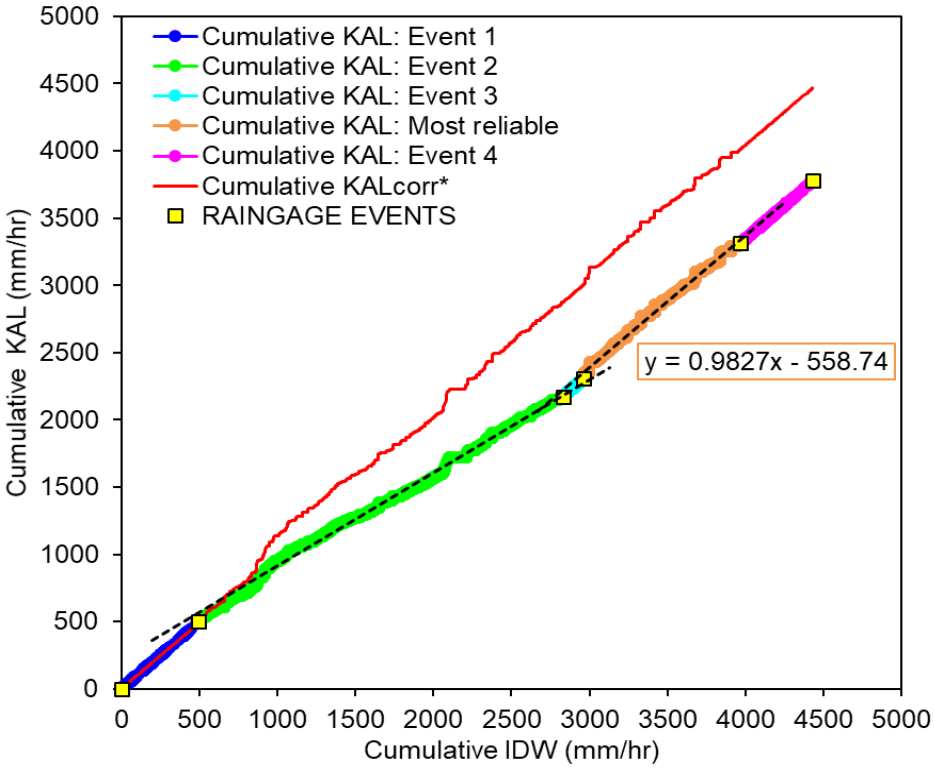

FIGURE 4.8 Double-mass curve

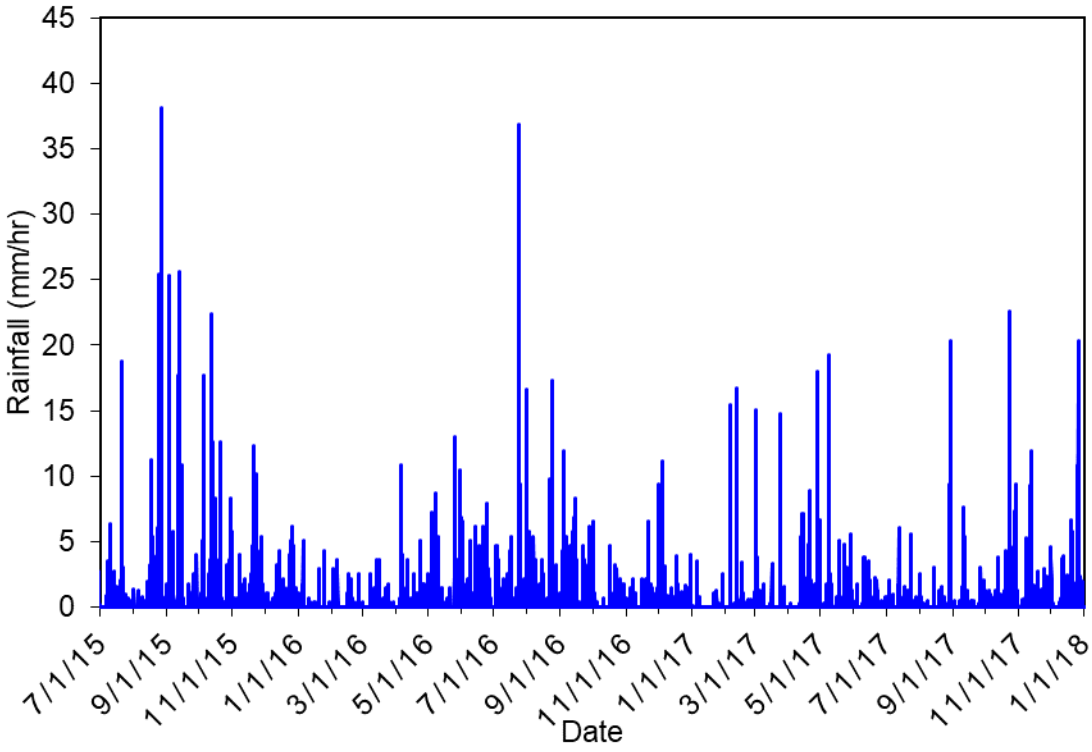

FIGURE 4.9 Corrected and adjusted rainfall data

4.2.2 Inclinometer

Ground deflections at the slope site (Figure 4.10) were minimal (< 2 mm or 0.08 inch at the ground surface) during the monitoring period. Deflections decreased with increasing depth. This amount of deflection is probably within the tolerance error of the inclinometer. For all intents and purposes, the lateral deflections are considered negligible during the period of this study.

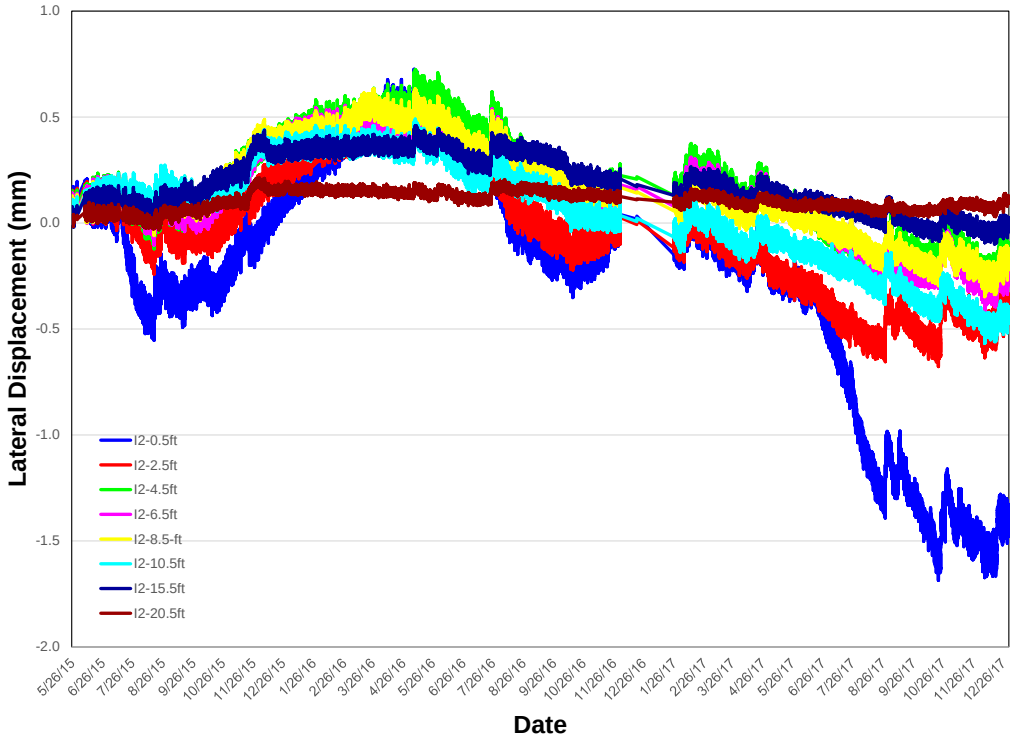

(a)

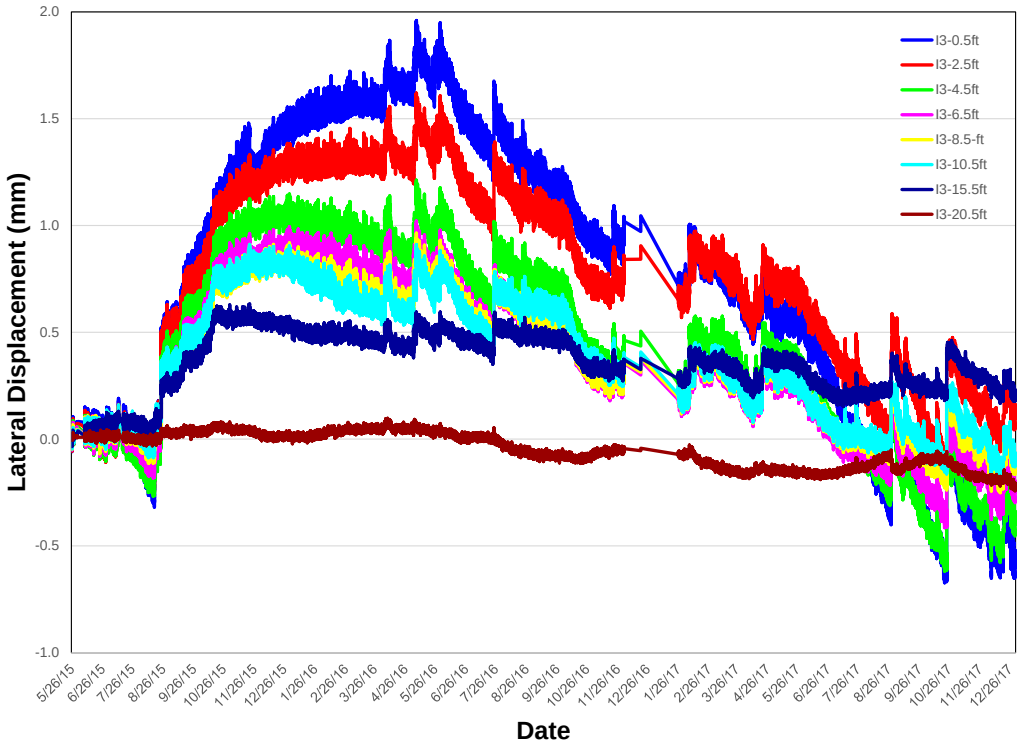

(b)

FIGURE 4.10 Inclinometer deflections in borings (a) B2 and (b) B3

4.2.3 Tensiometer and Water Content Sensor

Suction is plotted versus time for the shallower (≤ 1.5 m or 5 ft deep) tensiometers in Figure 4.11a and the deeper (≥ 3 m or 10 ft) tensiometers in Figure 4.11b. From Figure 4.11, it is interesting to note that suctions are affected by precipitation mostly at shallow depths (< 1.5 m or 5 ft). Beyond this depth, the suctions are fairly constant (Figure 4.11b). The suction and water content sensor readings are plotted in juxtaposition to show the influence of one on the other in Figure 4.12. The precipitation versus time plot can be compared to Figure 4.12 to further corroborate the increase/decrease in moisture trends. The fact that when suction decreases, water content increases illustrates that the instruments are responding in a logical fashion.

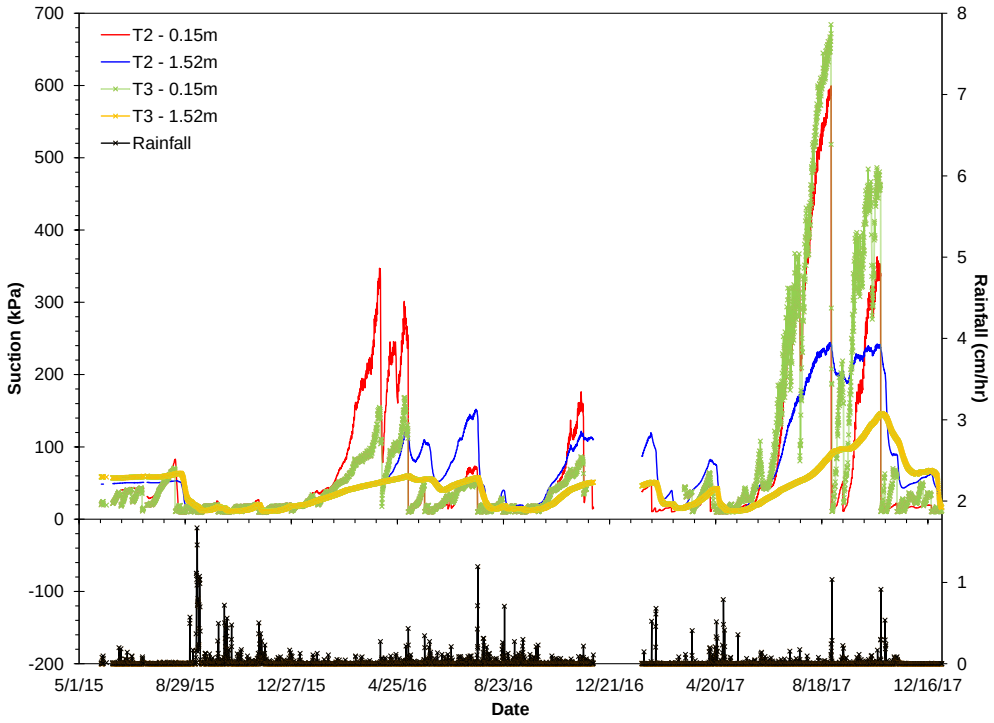

(a)

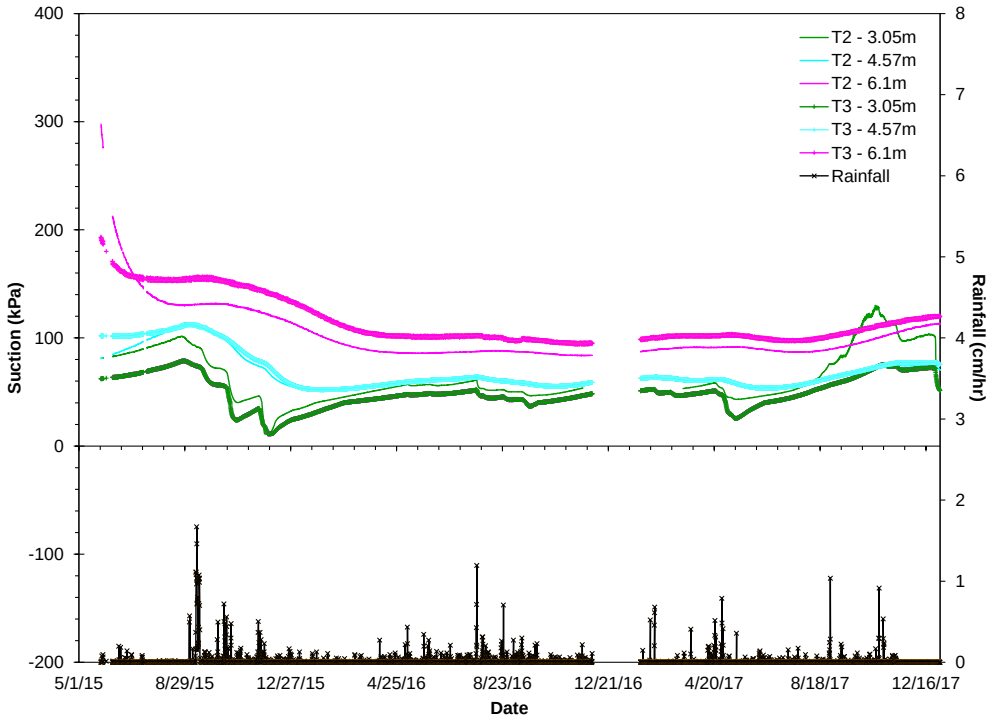

(b)

FIGURE 4.11 Suction versus time for (a) shallow (≤ 1.5 m or 5 ft deep) tensiometers and (b) deeper (≥ 3 m or 10 ft) tensiometers

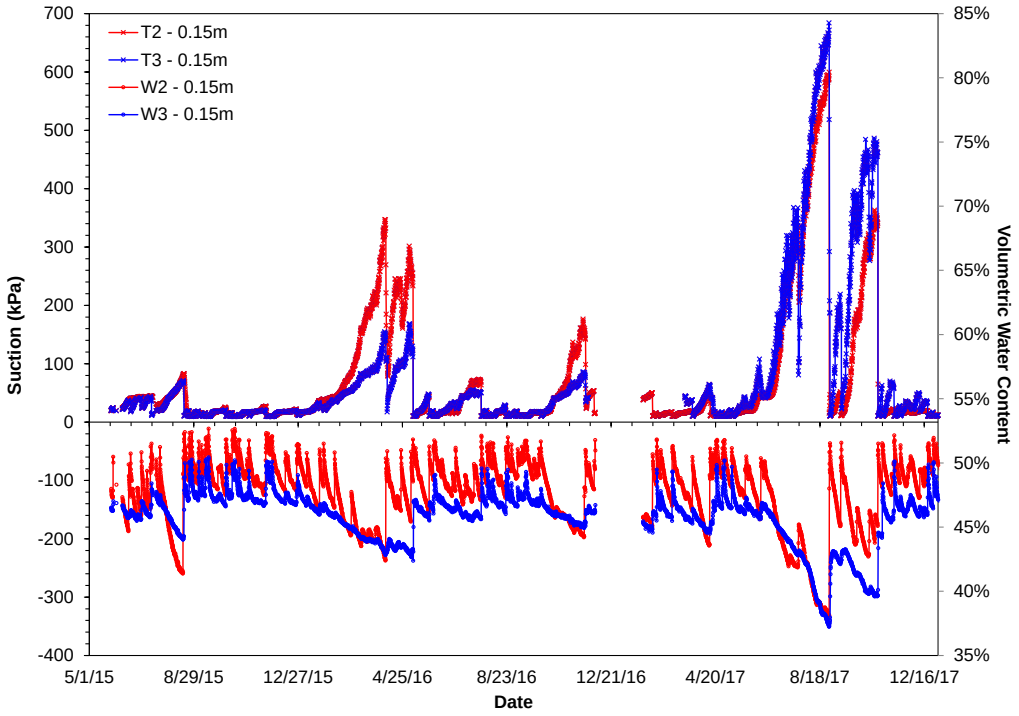

(a)

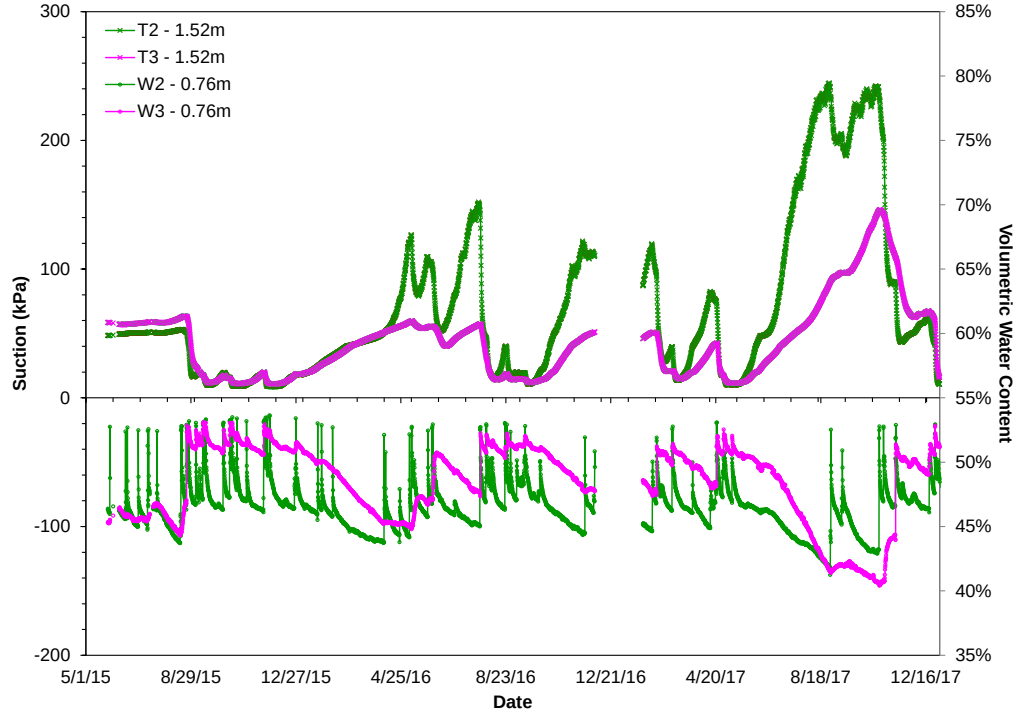

(b)

FIGURE 4.12 Suction and water content versus time for (a) 0.15 m or 0.5 ft deep tensiometers and (b) 1.5 m or 5 ft deep tensiometers

5 LABORATORY TESTING

Laboratory tests were conducted on soil samples collected in borings B2 and B3, a copy of the boring logs are shown in Appendix A. Index test results are presented in Section 5.1 followed by the non-index test results for the saturated and unsaturated soil in sections 5.2 and 5.3, respectively.

5.1 Index Testing

Index tests performed include grain size analysis, Atterberg limits, natural water content and specific gravity, the results of which are summarized in the following sub-sections.

5.1.1 Grain Size Analysis

The grain size curves for the soil (Figure 5.1) indicate that the soil is fine-grained.

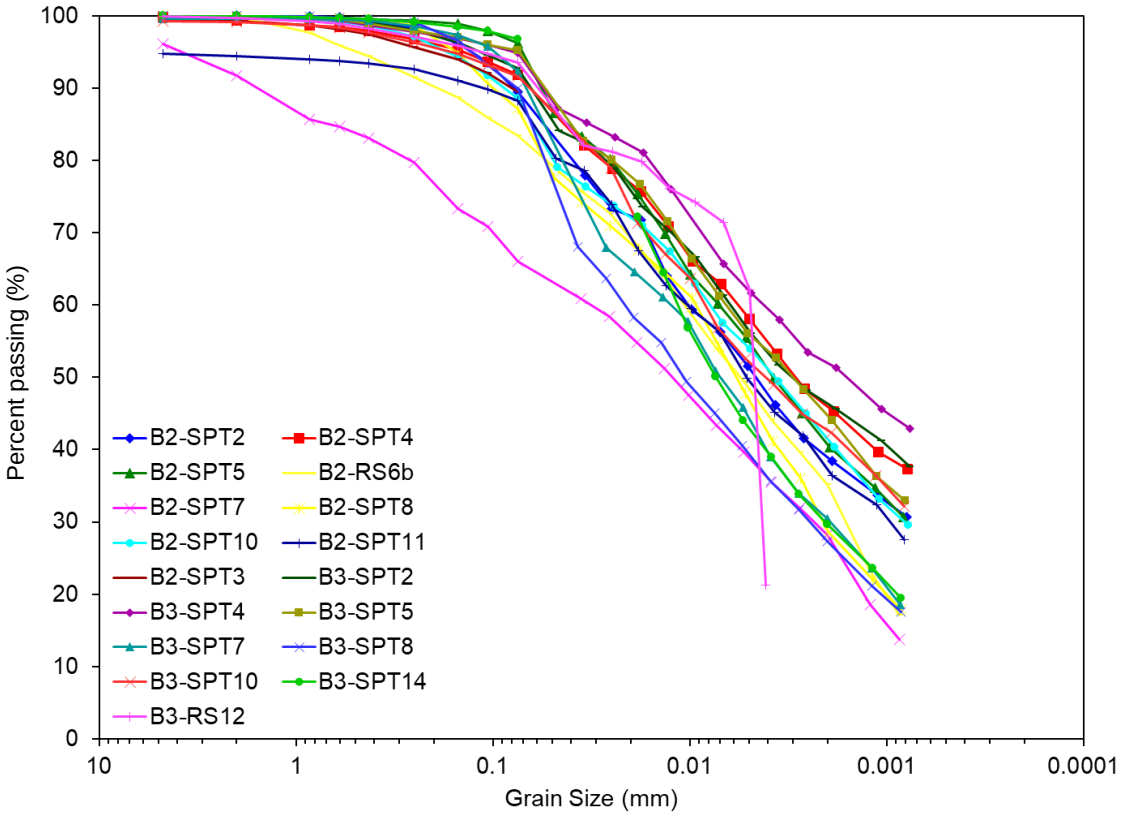

FIGURE 5.1 Grain size curves

5.1.2 *Atterberg Limits and Natural Water Contents*

When plotted on a plasticity chart, the Atterberg limits indicate that all soil samples classify as high plasticity silt (MH) based on the Unified Soil Classification System (Figure 5.2). The water contents are plotted alongside the respective plastic and liquid limit versus depth values in Figure 5.3.

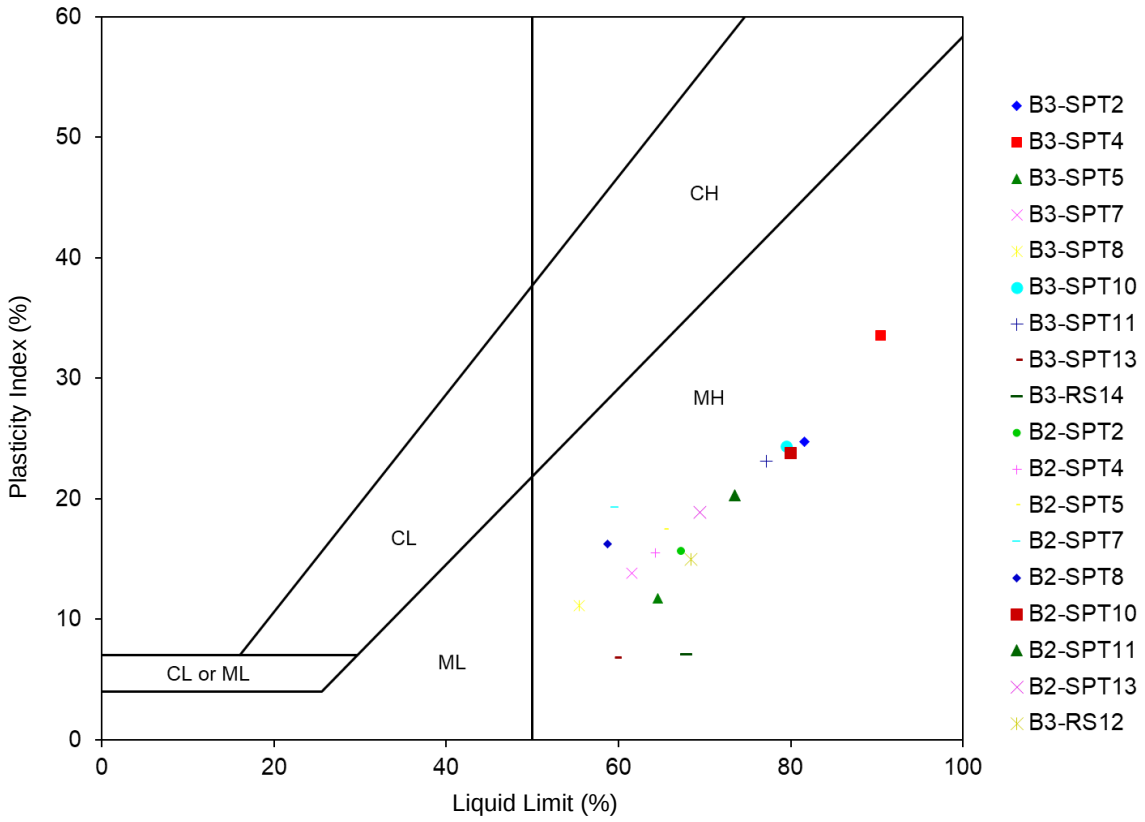

FIGURE 5.2 Plasticity chart

Liquidity indices ($LI = \frac{w - PL}{PI}$) ranged from -2.4 to +0.1 with an average of -0.7. The liquidity index provides an indication of the soil's consistency and sensitivity. If LI approaches unity, the soil is close to the liquid limit, which is an indication that the soil is sensitive. On the other hand, if LI ≈ 0, the natural water content is close to the plastic limit. This indicates that the soil sensitivity (undisturbed strength divided by remoulded strength) is low and the soil consistency may be relatively stiff. This is corroborated by the SPT blow counts of 11 to 31, which are indicative of a stiff to very stiff soil. Overall, it can be concluded that the saprolite is most likely heavily overconsolidated since the natural water contents are predominantly less than the corresponding plastic limits.

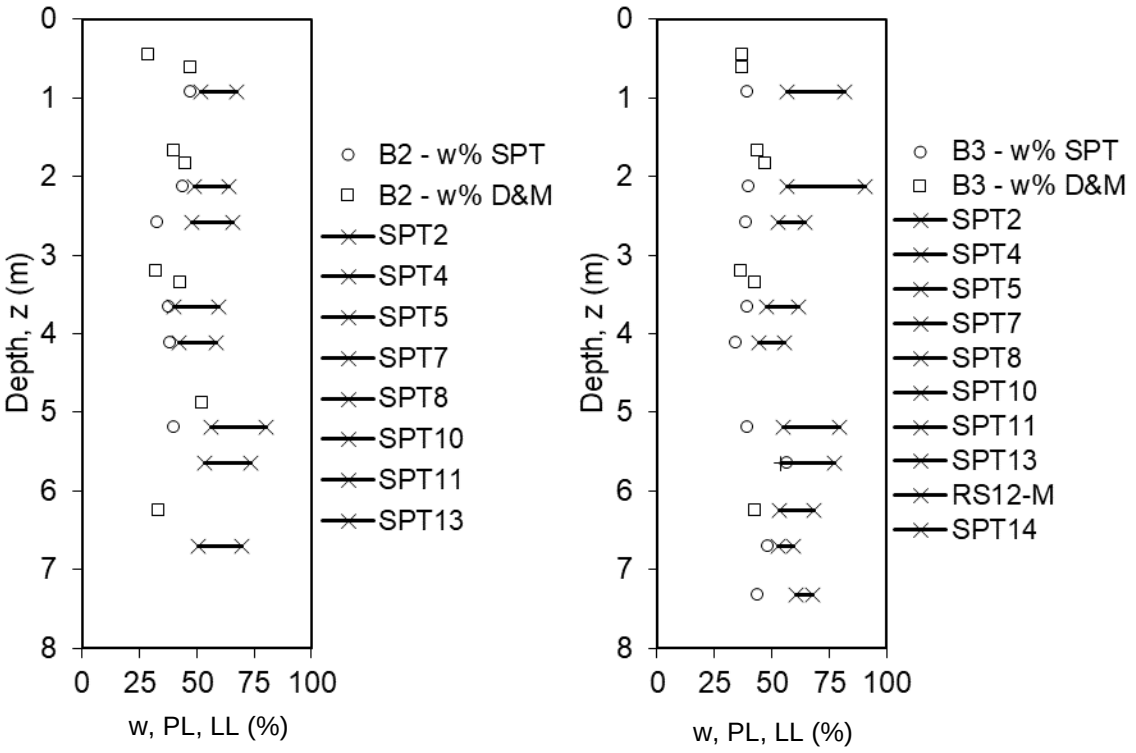

FIGURE 5.3 Natural water content and Atterberg limits vs depth for borings B2 and B3

The natural water content over the depth of both borings averaged approximately 41% (Figure 5.4). There does not appear to be much variation in the water content with depth.

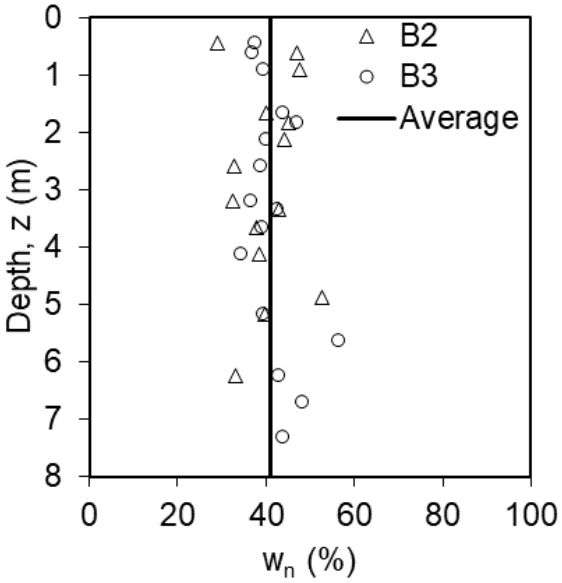

FIGURE 5.4 Natural water content vs depth for soils in borings B2 and B3

5.1.3 Specific Gravity

The specific gravity of the soil was measured in accordance with ASTM Standard D854-98 using a pycnometer, the results of which are summarized in Figure 5.5. The average specific gravity was about 2.9 for all soil samples tested.

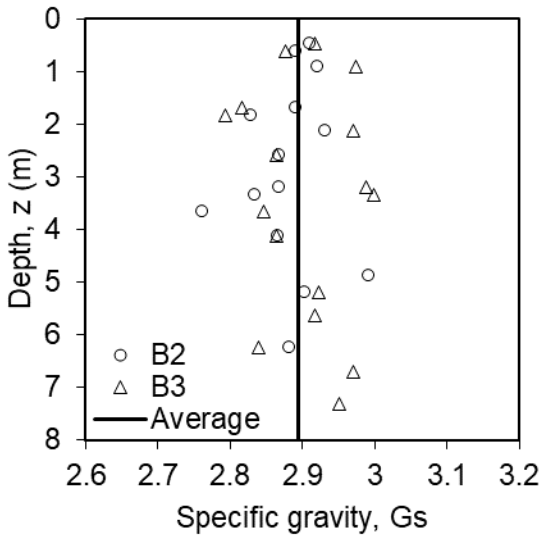

FIGURE 5.5 Specific gravity vs depth for soils in borings B2 and B3

5.2 Saturated Soil Testing

One 1D consolidation test and one multi-stage consolidated drained triaxial test were conducted on soil samples B3-1 (0.3 to 0.76 m or 1 to 2.5 ft depth) and B2-1 (0.3 to 0.76 m or 1 to 2.5 ft depth), respectively.

5.2.1 Consolidation Test

A 1D consolidation test was conducted on a soil sample in its saturated state using a Geocomp Loadtrac II loading frame and a 55.7 kN (12,500 lbf) load cell to estimate the saturated hydraulic conductivity, preconsolidation pressure and compressibility parameters. Results of this test are presented in Figure 5.6 through 5.8. From Figure 5.6, it can be seen that the soil has a preconsolidation pressure of ≈ 160 kPa corresponding to an overconsolidation ratio (*OCR*) ≈ 20. This high *OCR* is consistent with the SPT blow counts and negative values of liquidity indices.

From measured values of coefficient of consolidation (c_v was estimated using both Taylor's (1948) $\sqrt{t}$ and Casagrande and Fadum's (1940) log t methods in Figure 5.7) and coefficients of volume compressibility (m_v), the hydraulic conductivity of the soil when overconsolidated is about 10^{-6} cm/s (Figure 5.8).

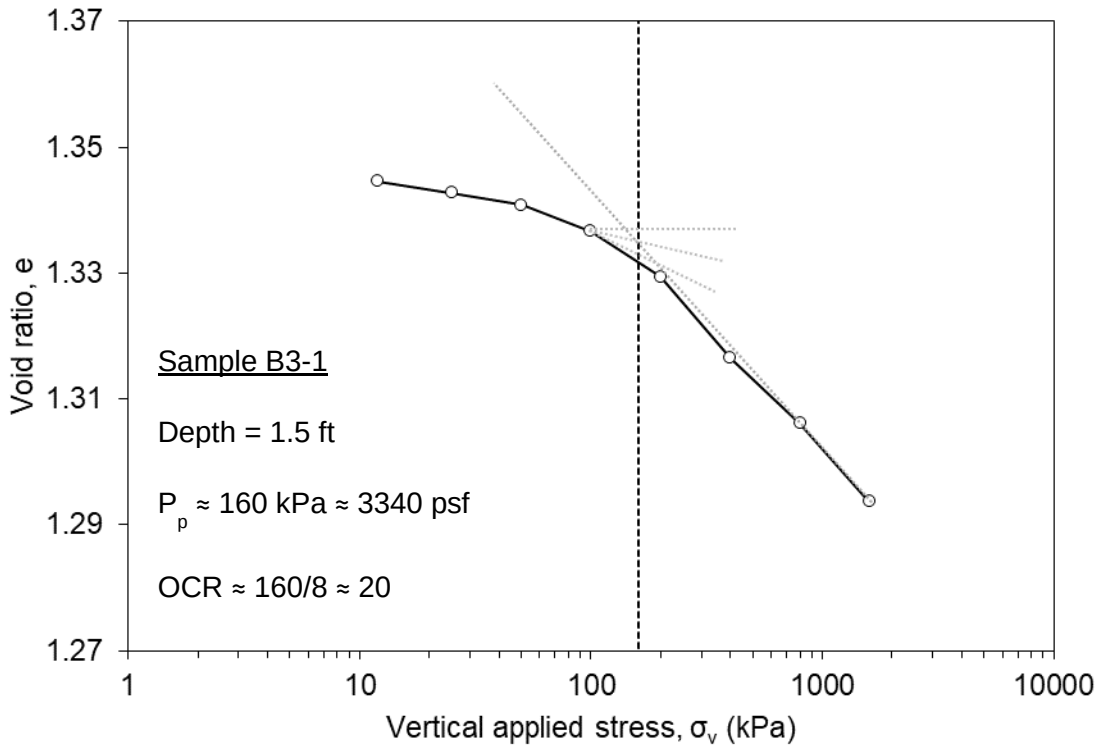

FIGURE 5.6 Consolidation test results on Sample B3-1

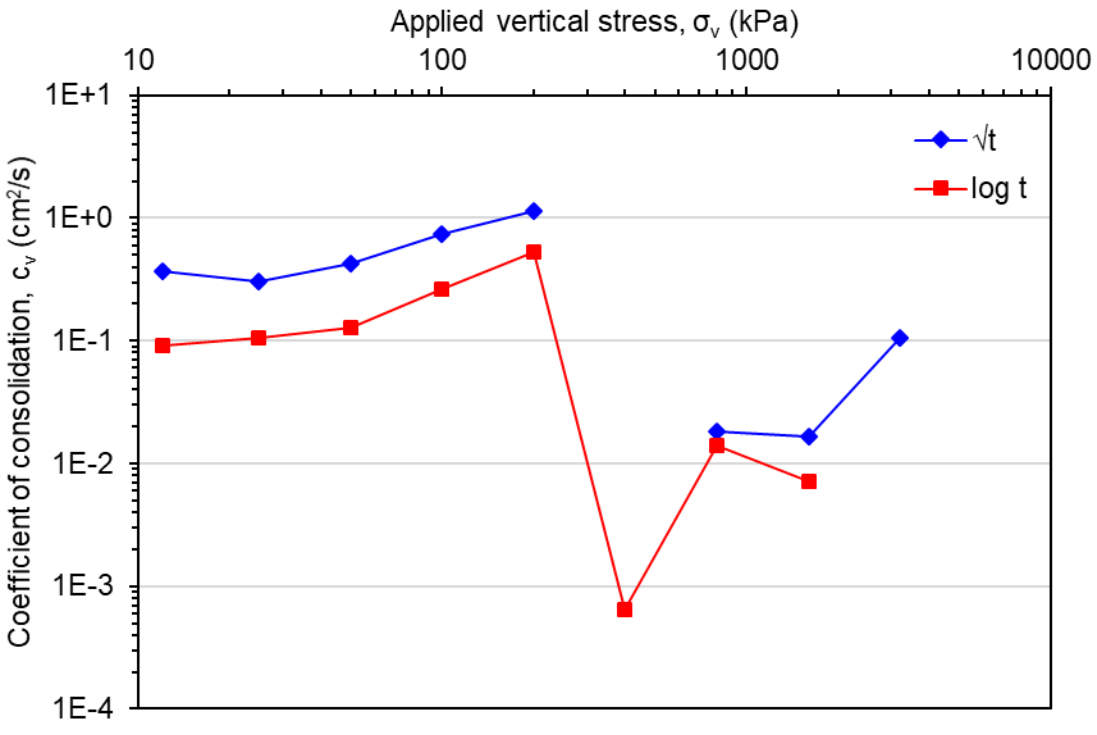

FIGURE 5.7 Coefficient of consolidation versus pressure (Sample B3-1)

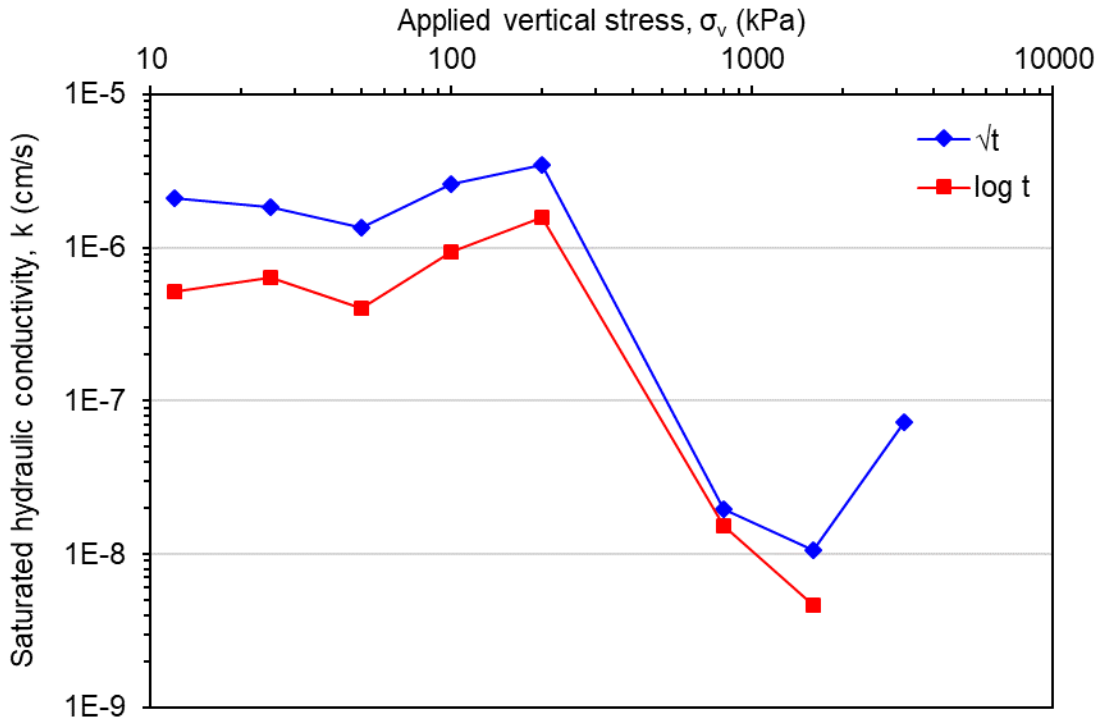

FIGURE 5.8 Hydraulic conductivity versus pressure (Sample B3-1)

5.2.2 Multi-stage Consolidated Drained Triaxial Test

Due to a limited number of samples, a multi-stage consolidated drained triaxial test was performed on one sample to obtain the saturated shear strength parameters. The sample was first saturated by increasing the confining stress ($\Delta\sigma_3$) with the drainage valve closed and then measuring the change in pore pressure (Δu). The ratio $\Delta u/\Delta\sigma_3$ = Skempton's pore pressure parameter, B, was then calculated. This was repeated until a *B*-value of 0.98 was attained, at which point the sample can be considered saturated.

The confining stress was then increased to 15 kPa, 30 kPa and 50 kPa, and the sample was sheared at each confining stress in a drained fashion whereby excess pore pressures were allowed to dissipate (Figure 5.9). At confining stresses of 15 and 30 kPa, peak deviator stresses occurred at axial strains of 1.37% and 2.13%, respectively. The axial strains were limited to 2.5% before increasing the confining stress during the first two stages. At the last stage (σ_3 = 50 kPa), the test was run to larger axial strains (about 5.7%). The axial strain at failure was 3.29% for the 50 kPa confining stress. The failed specimen is shown in Figure 5.10.

Since the sample was consolidated to 3 different values of confining stress prior to shearing, this implies that the *OCR*s are different at each confining stress. Therefore, Hvorslev's (1937) shear strength theory was used to discern meaningful shear strength parameters from such a test.

Based on companion direct shear and consolidation test results, Hvorslev showed that the shear strength can be separated into two components, one that is a function of the effective normal stress at failure (ϕ'_e or Hvorslev's true ϕ) and another that is dependent on the water content at failure (c'_e or Hvorslev's true c). To obtain these strength parameters, the equivalent consolidation pressure (σ'_e) must first be obtained at each normal stress. σ'_e is the normal stress that corresponds to the void ratio on the virgin compression curve. When the normalized failure shear stress (τ_f/σ'_e) is plotted versus the normalized normal stress (σ'_f/σ'_e), Hvorslev noticed that the tests for all soils plotted on a straight line as follows.

$$\frac{\tau_f}{\sigma'_e} = \frac{c'_e}{\sigma'_e} + \frac{\sigma'_f}{\sigma'_e}\tan\phi'_e \tag{5.1}$$

For this research, CD triaxial tests were run instead of direct shear tests. Bishop and Henkel (1962) suggested that the corresponding equation for CD tests is as follows:

$$\frac{(\sigma'_1 - \sigma'_3)_f}{2\sigma'_e} = \frac{c'_e}{\sigma'_e}\frac{\cos\phi'_e}{1-\sin\phi'_e} + \frac{\sigma'_{3f}}{\sigma'_e}\frac{\sin\phi'_e}{1-\sin\phi'_e} \tag{5.2}$$

where σ_1' and σ_3' are the major and minor principal effective stresses, respectively and the subscript "f" denotes values at failure. If the soil was tested in direct shear, σ'_e would simply be obtained from the void-ratio vs log vertical stress plot from a 1D consolidation test (Figure 5.6) because in both direct shear and consolidation tests, no lateral straining of the soil occurs. Since the lateral restraint in a CD triaxial and consolidation tests are different, the consolidation test results were replotted in terms of void ratio versus the log of mean effective normal stress, p', instead of the vertical stress so that the equivalent stress is based on the mean effective normal stress, which is defined as follows:

$$p' = \sigma'_1\frac{1+2K_o}{3} \tag{5.3}$$

where σ'_1 = applied vertical stress and K_o = at-rest lateral earth pressure coefficient estimated using the expression proposed by Schmidt (1966) as follows:

$$K_o = (1-\sin\phi'_e)OCR^{\sin\phi'_e} \tag{5.4}$$

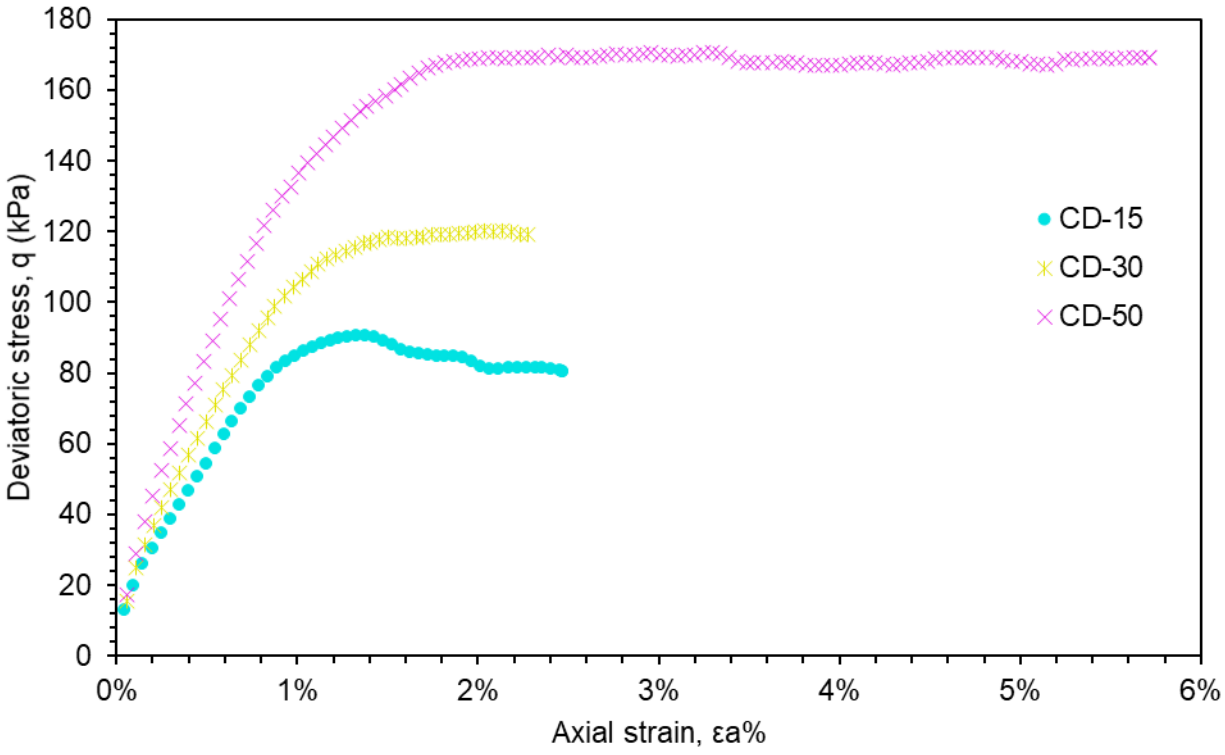

(a)

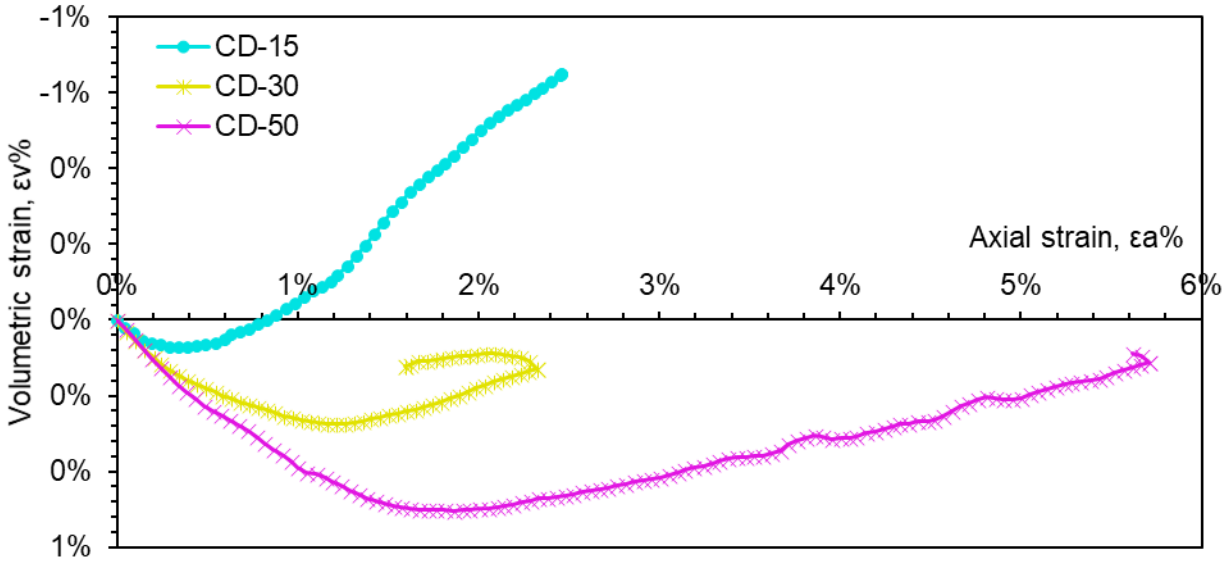

(b)

FIGURE 5.9 (a) Deviator stress vs axial strain and (b) volume change curves for Sample B2-1

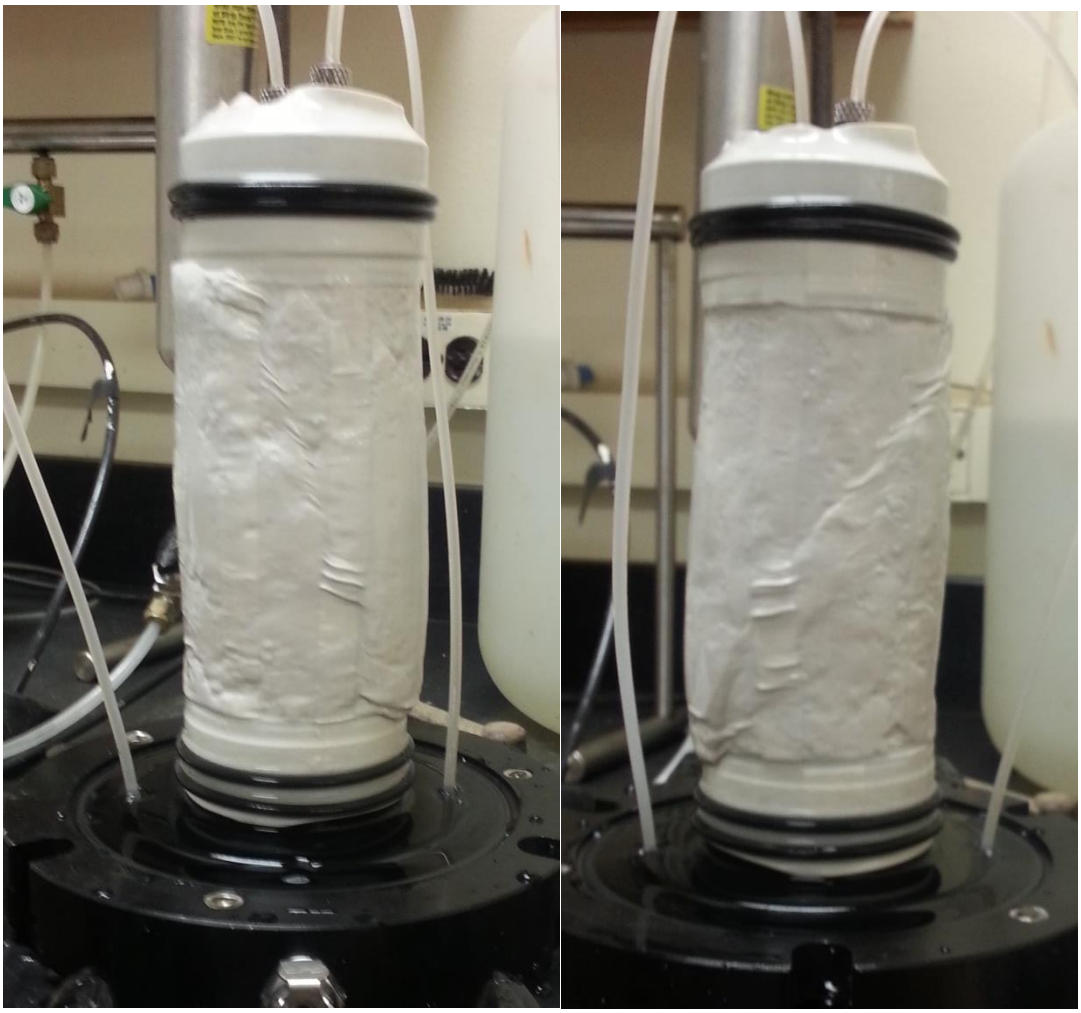

FIGURE 5.10 Shear plane in multi-stage CD triaxial specimen

Hence, Equation 5.2 can be rewritten as follows:

$$\frac{(\sigma_1^{'}-\sigma_3^{'})_f}{2p_e^{'}}=\frac{c_e^{'}}{p_e^{'}}\frac{\cos\phi_e^{'}}{1-\sin\phi_e^{'}}+\frac{\sigma_{3f}^{'}}{p_e^{'}}\frac{\sin\phi_e^{'}}{1-\sin\phi_e^{'}} \qquad (5.5)$$

In the multi-stage CD test, $p' = \sigma'_3$ since the soil is isotropically consolidated. Therefore, a trial and error process is needed to estimate ϕ'_e as follows:

1. Guess ϕ'_e so that p' and K_o can be estimated using equations 5.3 and 5.4.
2. Plot Figure 5.11 to estimate the void ratio on the recompression line based on the value of p' at each confining stress.
3. Use the void ratio from Step 2 to estimate p'_e on the normally consolidated line.

4. Plot $\frac{(\sigma_1^{'}-\sigma_3^{'})_f}{2p_e^{'}}$ vs $\frac{\sigma_{3f}^{'}}{p_e^{'}}$ as shown in Figure 5.11 to obtain ϕ'_e and the intercept, $\frac{c_e^{'}}{p_e^{'}}\frac{\cos\phi_e^{'}}{1-\sin\phi_e^{'}}$.

5. Iterate to find the final value of ϕ'_e, which is obtained when the guessed and calculated values of ϕ'_e match (≈ 28°).

The final values of void ratio, water content, p'_e and c'_e at each of the 3 confining stresses are summarized in Table 5.1. Hvorslev's true c'_e varies with water content as shown in Figure 5.12. The values of ϕ'_e and $c'_e(w)$ are then used in slope stability analyses needed for development of the landslide warning system.

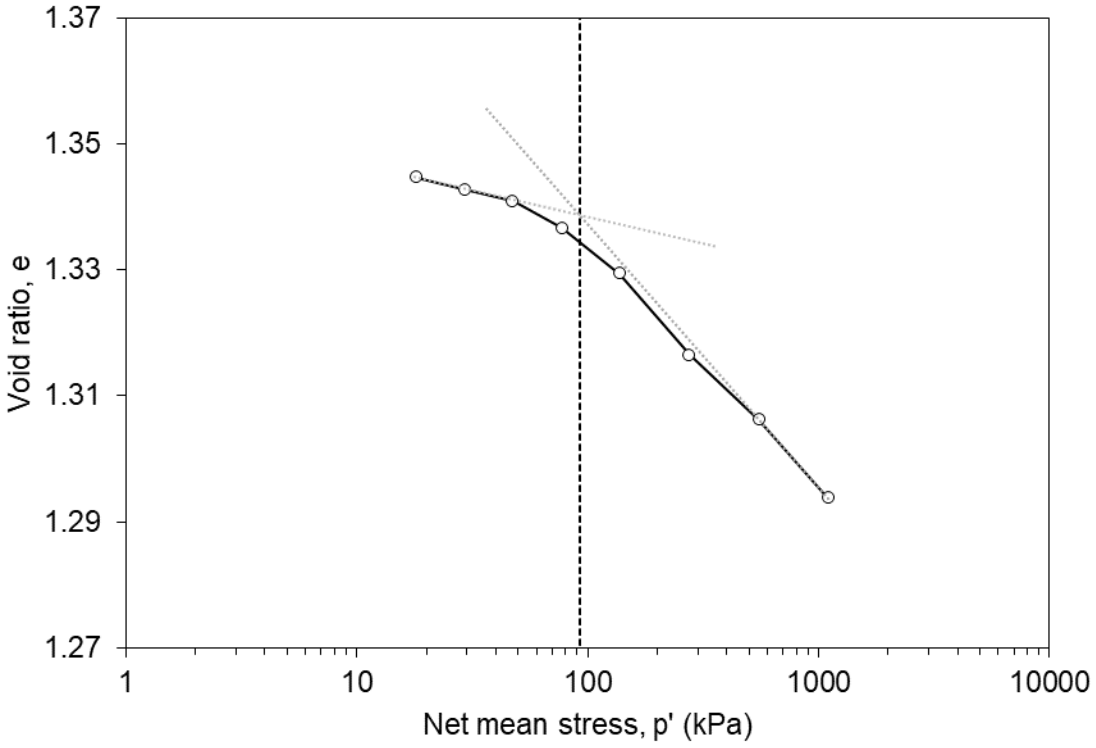

FIGURE 5.11 Consolidation test results replotted in terms of void ratio vs mean stress

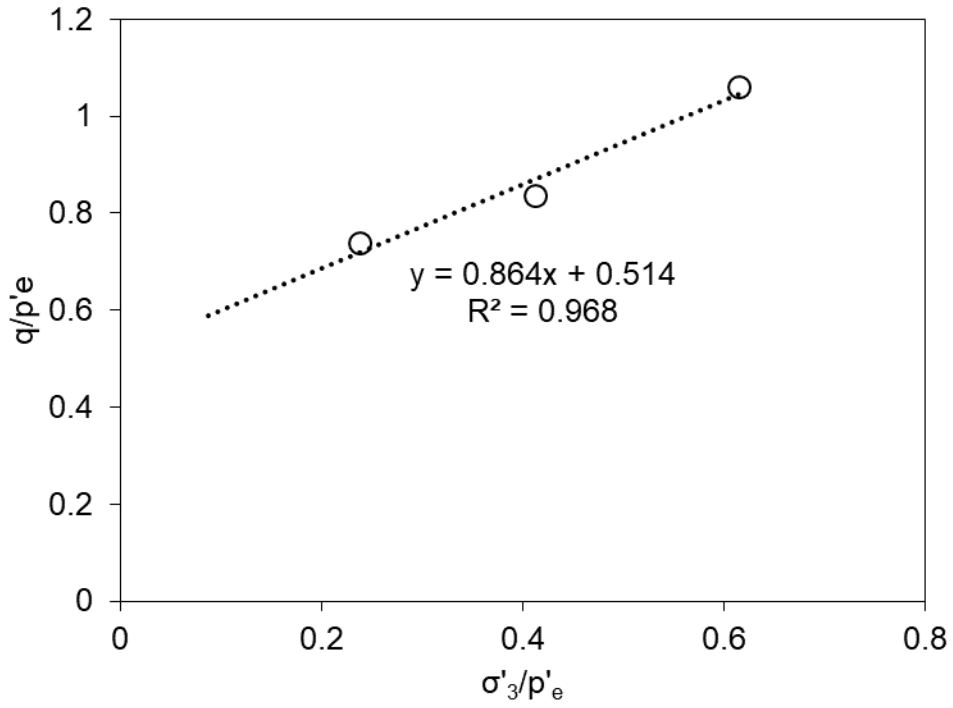

FIGURE 5.12 Consolidation test results replotted in terms of void ratio vs mean stress

Table 5-1 Summary of void ratio, p'_e, water content and c'_e for the CD test

Confining Stress, $\sigma'_3 = p'$ (kPa)	*Void Ratio*, *e*	*Water Content*, *w* (%)	p'_e (kPa)	c'_e (kPa)
15	1.345	46.5	61.6	19.2
30	1.343	46.4	72.0	22.4
50	1.341	46.3	80.6	25.1

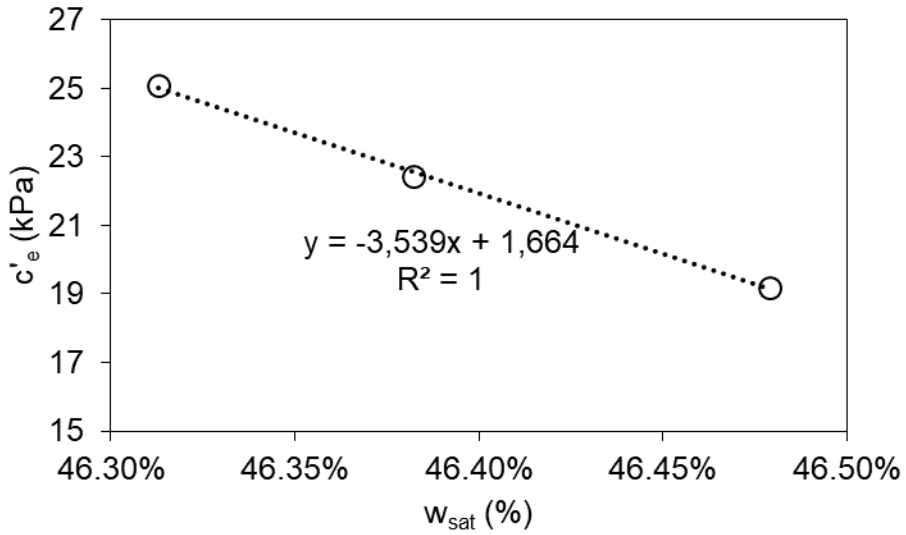

FIGURE 5.13 Hvorslev's c'_e as a function of water content

To determine the value of cohesion to use, it is necessary to look at the variation of water content of the soil when it is saturated with depth. This value of water content can be obtained by dividing the in situ void ratio by the specific gravity, and the in-situ void ratios can be obtained from unit weight measurements of the modified California samples. A plot of the water content of the soil if it were saturated (w_{sat}) versus depth (Figure 5.14) indicates an average value of about 46.5%. Figure 5.14 also indicates that w_{sat} is fairly constant with depth. This suggests that a value of c'_e of 18 kPa may be reasonable for this site.

It is possible that the soil sample may have failed at a confining stress of 15 kPa because of softening as seen in the stress-strain curve at that confining stress (Figure 5.9a) even though the strains only reached a maximum of 2.5%. Nevertheless, the shear strengths obtained from this test should be on the conservative side. In contrast, Prof. Xiong Zhang's constant water content direct shear tests (Appendix B) yielded friction angle and cohesion values of 25.8° and 35.5 kPa, respectively (compared to 28° and 18 kPa). In their tests, they attached a tensiometer that was placed in a pre-drilled hole that extended to near the failure surface of the direct shear specimen. It is not known how much of a reinforcing effect the tensiometer had on the direct shear specimens and to what extent the tensiometer affected the shear strength parameters.

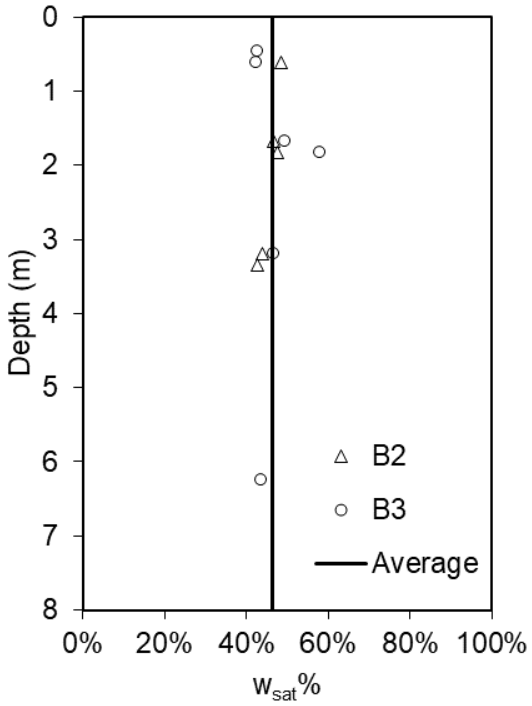

FIGURE 5.14 Variation of water content of the soil if it were saturated with depth

5.3 Unsaturated Soil Testing

This sub-section summarizes the results of tests conducted to obtain the soil-water characteristic curve, the hydraulic conductivity function and the Basic Barcelona model (BBM) parameters.

5.3.1 Soil Water Characteristic Curve and Hydraulic Conductivity Function

The soil-water characteristic curve (SWCC) was estimated by running a pressure plate (PP) test (apparatus manufactured by Soilmoisture Equipment Corp.). The PP apparatus (Figure 5.15) has a porous ceramic plate with an air-entry value of 500 kPa. This means that it is useful for deriving the portion of the SWCC in the lower suction range (< 500 kPa). To obtain the portion of the SWCC at higher suctions (6,000 to 600,000 kPa), a Decagon Devices' (now owned by Meter Environment) Aqua Lab Vapour Sorption Analyser (VSA - Figure 5.16) was used.

The pressure plate apparatus was used to test a specimen obtained from a modified California sampler. The VSA is unique in the sense that unlike the pressure plate, the soil sample does not have to be "undisturbed." This can be explained as follows. Because the VSA only measures suction in the very dry range, the water in the soil exists only at the particle surface and not in the capillary pore spaces. A disturbed soil will have a different soil structure than an undisturbed one. This will change the capillary spaces, but since all the water is associated with those at the particle surface, it will not affect the isotherm in the VSA.

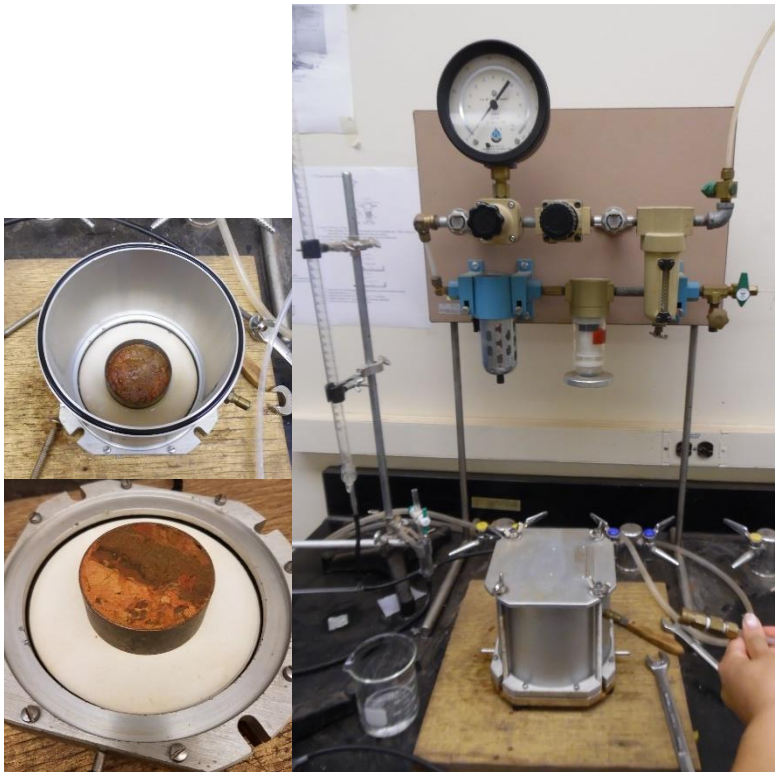

FIGURE 5.15 Soilmoisture Equipment Corp. pressure plate apparatus having a porous ceramic plate with an air-entry value of 500 kPa

FIGURE 5.16 Decagon Devices' Aqua Lab Vapor Sorption Analyzer

One important consideration is that the SWCC is pressure dependent (Ng & Pang, 2000; Gallipoli et al., 2003; Sun et al., 2007; Khalili et al., 2008; Nuth & Laloui, 2008; Sheng & Zhou, 2011). Since the pressure plate and VSA are conducted in the lab under atmospheric pressure, the resulting SWCC is only

valid for very shallow soils. Nevertheless, these results render the SWCC a very useful yardstick for the response of surficial soils to precipitation and evaporation. Pressure dependent SWCC's can be derived from the results of constant water content isotropic compression tests. They are presented in Section 5.1.2.

The resulting drying and wetting branches of the SWCC conducted on an "undisturbed" sample (B2-6 from a depth of 3.05 m or 10 ft) in a PP apparatus are shown in Figure 5.17. Two cycles of drying and wetting were performed in the PP test. According to Likos et al. (2014), the first wetting and second drying cycles form the main wetting and drying curves of the SWCC, respectively while the second wetting cycle represents a scanning curve that runs from the drying curve to the wetting curve. Based on readings in the 0.15-m-deep tensiometer, the field-measured suctions never exceeded 700 kPa thus rendering the VSA data irrelevant.

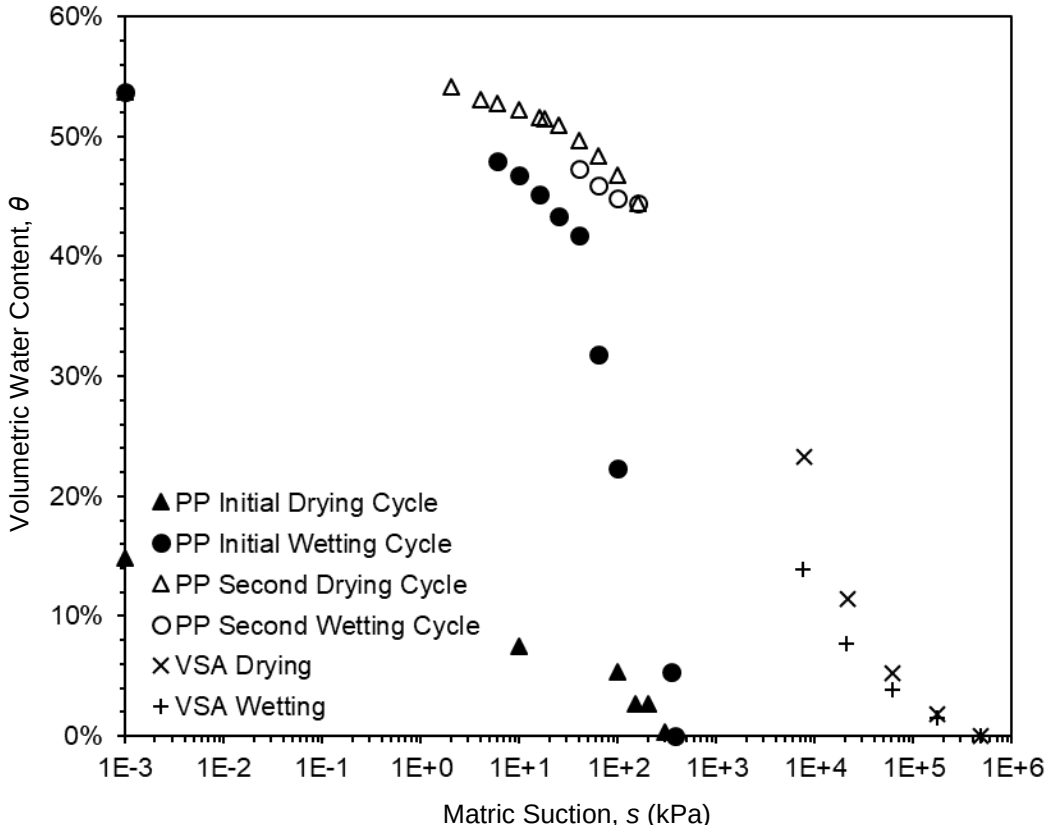

FIGURE 5.17 Laboratory measured soil-water characteristic curve

It is well known that the hydraulic conductivity of soil decreases with decreasing saturation. Measuring the unsaturated hydraulic conductivity at different degrees of saturation is a tedious and time-consuming proposition. Known as the hydraulic conductivity function (HCF), the variation of unsaturated soil hydraulic conductivity (k) with suction (s) can be alternatively obtained using the SWCC data together with a statistical approach proposed by Kunze et al. (1968) as follows:

$$k(\psi)_i = \frac{1}{k_s}\frac{T_s^2\gamma_w}{2\mu_w}\frac{\theta_s^2}{N^2}\sum_{j=1}^{m}\left\{(2j+1-2i)\psi_j^{-2}\right\} \quad (5.5)$$

where i = interval number which increases as the volumetric water content decreases, T_s = surface tension of water = 0.072 N/m, γ_w = unit weight of water, θ_s = volumetric water content at 100% saturation, k_s = saturated hydraulic conductivity (from consolidation test, $k_s \approx 10^{-6}$ cm/s), μ_w = absolute viscosity of water = $8.62\text{x}10^{-4}$ N-s/m^2, N = total number of intervals computed between saturated volumetric water content and zero volumetric water content, j = counter from 1 to m, m = total number of intervals between the saturated volumetric water content and the lowest volumetric water content on the experimental SWCC and ψ_j = matric suction corresponding to the j^{th} interval. Based on the SWCC data, the resulting HCF is shown in Figure 5.18 in terms of the relative hydraulic conductivity (k_{rel}) which is defined as the hydraulic conductivity of the soil at a given degree of saturation divided by the saturated hydraulic conductivity, and is a number between 0 and 1.

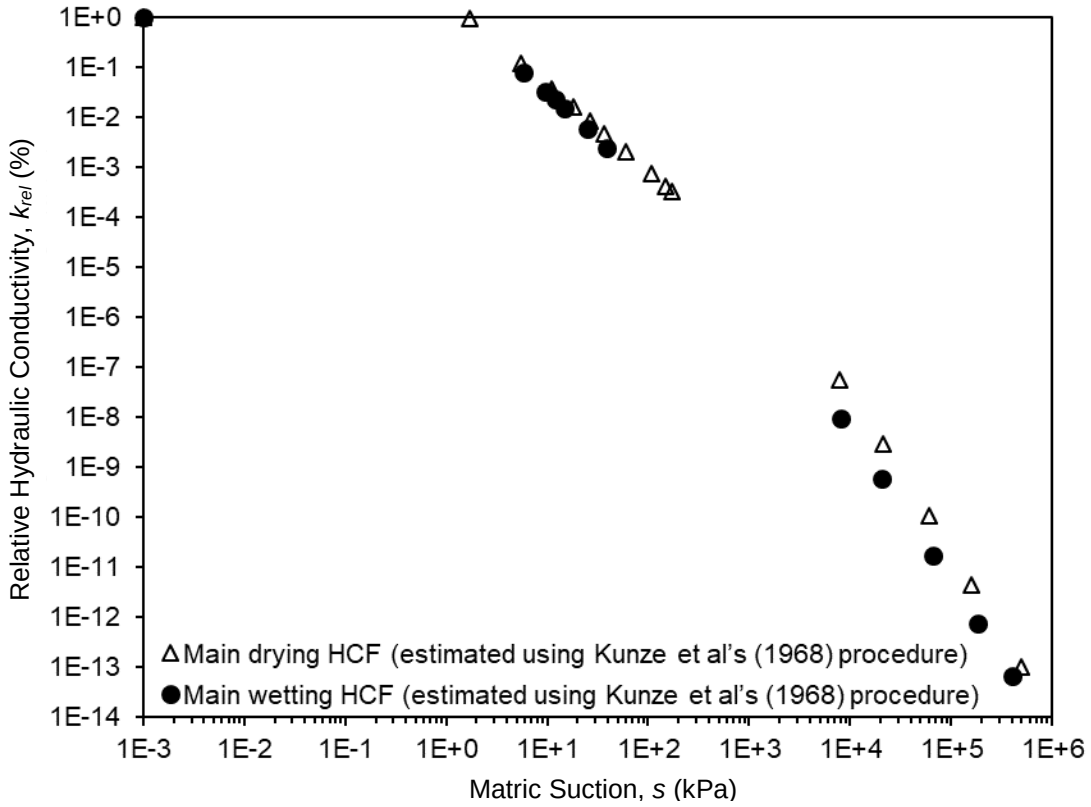

FIGURE 5.18 Hydraulic conductivity function derived from the SWCC using Kunze et al.'s (1968) procedure

At shallow depths, the suction can vary considerably due to climactic effects. When the suction is high, the soil's hydraulic conductivity is low. If it reaches a point low enough that it can be considered "impermeable," it is easy to see why perched water tables can readily form during a downpour resulting in

the development of positive pore water pressures in slopes. Naturally, the elevated pore pressures are the main culprit for triggering rainfall-induced landslides.

5.3.2 Triaxial Test

Triaxial tests were conducted on three unsaturated soil samples extruded from modified California samplers using a GDS triaxial automated system. When testing unsaturated soil, the biggest challenge is in quantifying the volume change in the soil. The GDS equipment uses a Hong Kong University of Science and Technology (HKUST) system for measuring soil volume change whereby the basic principle is "to record the differential pressure between the water inside an open-ended, bottle-shaped inner cell and the water inside a reference tube using a differential pressure transducer" (Ng and Menzies, 2007). The inner cell is sealed onto the pedestal of the outer cell, a schematic of which is shown in Figure 5.19 and pictures of the GDS triaxial equipment are shown in Figure 5.20.

Each sample was subjected to constant water content isotropic compression (CWIC) to obtain stiffness parameters (Section 5.3.2.1) and constant water content triaxial shear (CWTS) tests to obtain strength parameters (Section 5.3.2.2). The parameters obtained from these tests are compared in Section 5.3.2.3 to those obtained by Prof. Xiong Zhang and Dr. Lin Li, who used constant water content oedometer and constant water content direct shear tests (Appendix B).

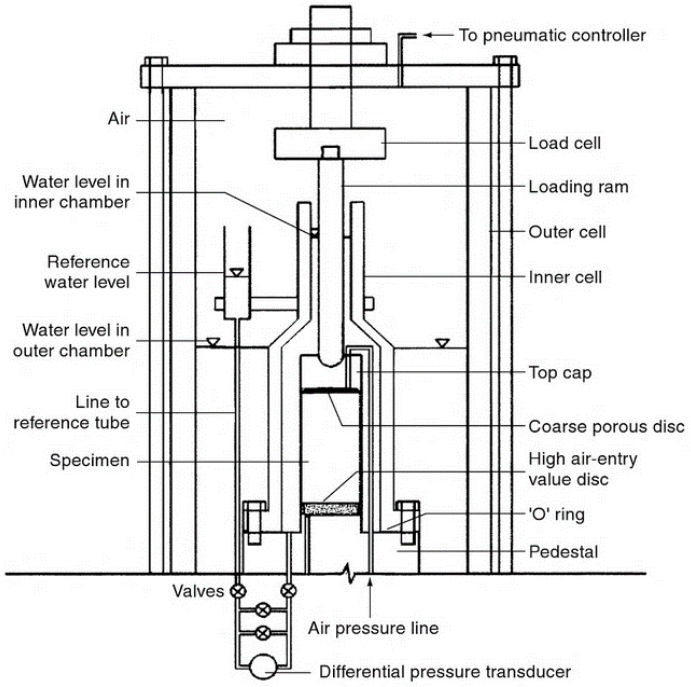

FIGURE 5.19 Schematic of HKUST double wall volume change measurement system in a triaxial cell for unsaturated soil testing (from Ng and Menzies, 2007)

FIGURE 5.20 GDS triaxial apparatus with HKUST double wall volume change measurement system

FIGURE 5.21 Photos of sheared specimen from tests (a) CWCU-1, (b) CWCU-2, and (c) CWCU-3

5.3.2.1 **Constant Water Content Isotropic Compression Tests**

An idealized stress path for a soil subjected to CWIC test is shown in Figure 5.22 (Zhang, 2016). This test differs from the more conventional suction-controlled isotropic compression test (SCIC) reported in the literature by Wheeler and Sivakumar 1995; Cui and Delage 1996; Rampino et al. 1999; Sharma 1998; Hoyos 1998; Blatz and Graham 2003; Thu et al. 2007, in which both the pore water and pore air pressures are drained (i.e.; suction is controlled). Zhang (2016) indicated that the limitations of SCIC tests include longer testing times and deviation of actual stress paths from the idealized ones (Figure 5.23). Advantages of CWIC tests are: (1) unlike pore water pressure, pore-air pressure is instantaneously distributed throughout the sample which significantly reduces testing time and which eliminates the deviation of actual stress paths from the idealized ones; (2) BBM stiffness parameters can be deduced from less tests and types of stress paths; and (3) undrained pore water pressure conditions more closely resemble rapid rainfall-induced slope failures (Rahardjo et al., 2004 and Thu, 2006).

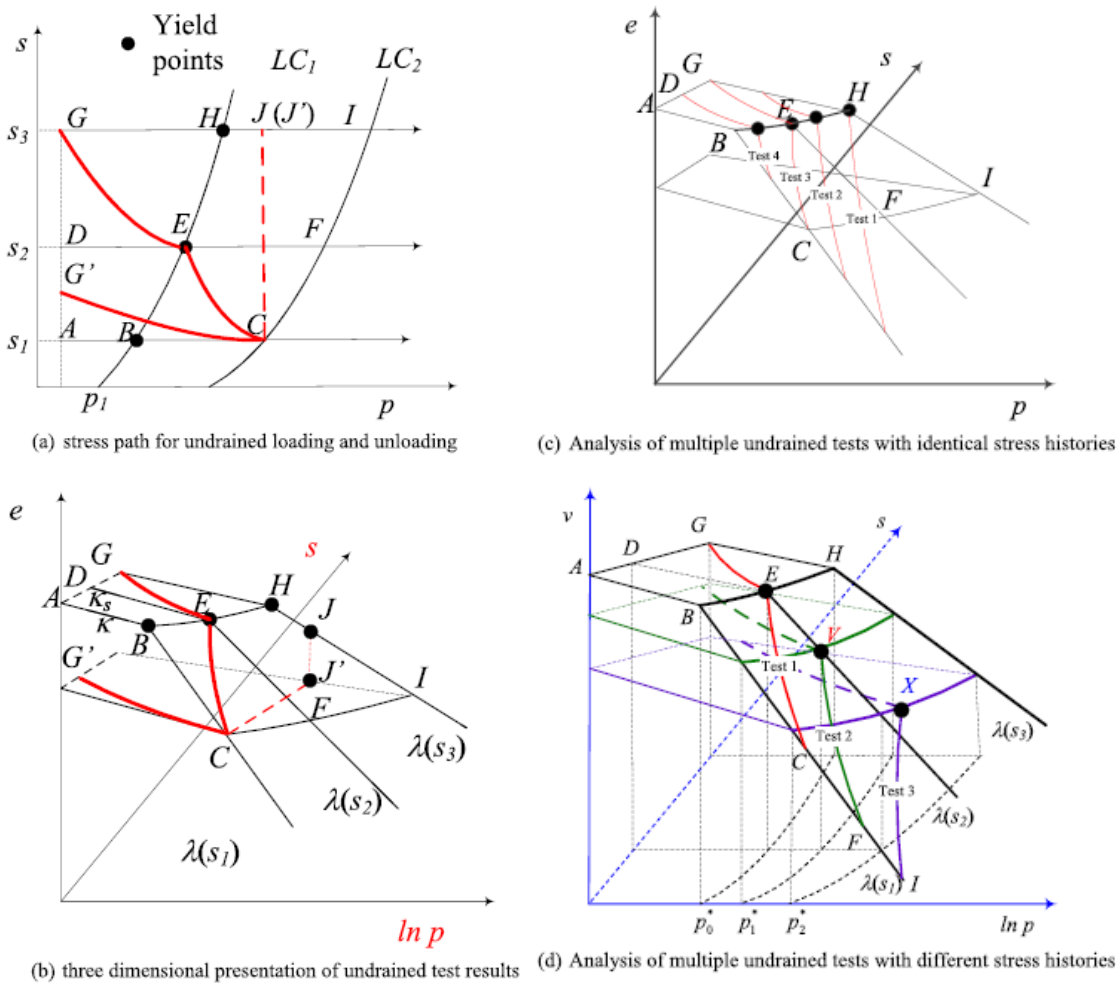

FIGURE 5.22 Idealized stress paths for undrained constant water content isotropic compression (CWIC) tests (from Zhang, 2016)

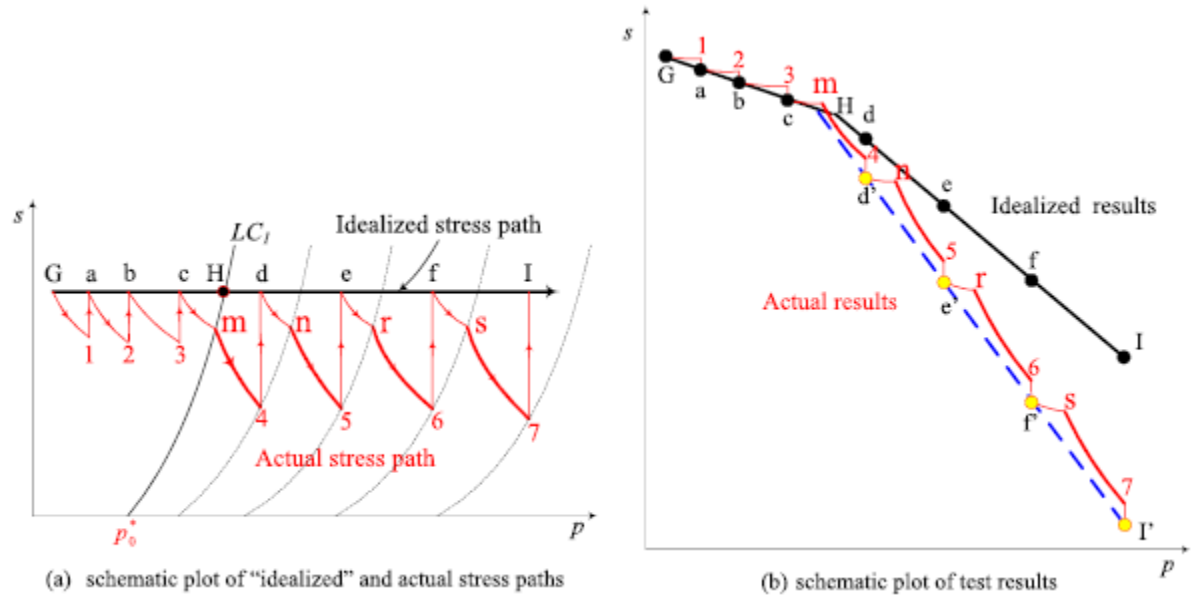

FIGURE 5.23 Idealized versus actual stress paths for suction-controlled isotropic compression (SCIC) tests (from Zhang, 2016)

In SCIC tests, two of the stress-state variables, *p* and *s*, are controlled and the void ratio is determined by measuring the volume change. In CWIC tests, only water content and net mean stress are controlled, and suction and volume change (which yields void ratio) are measured. Due to the highly coupled hydraulic and mechanical states during CWIC testing, they are not commonly performed (Casini et al., 2013 and Li, 2015).

Zhang and Lytton (2009a, b and c) developed a modified state surface approach (MSSA), which adopts the same stress space as the BBM (Alonso et al., 1990). Because the BBM remains one of the most fundamental models for unsaturated soils, the MSSA is based on the same framework and can be used to obtain BBM stiffness parameters from CWIC tests. This section presents the testing procedure, results, and calibrated BBM parameters from three CWIC tests.

5.3.2.1.1 **Procedure**

The GDS apparatus consists of a high air entry disk (HAED) that is mounted on the triaxial cell base pedestal (Figure 5.20a) to allow for pore pressure measurement via the axis-translation technique (Hilf, 1956). When the HAED is saturated, it allows liquid to flow through its pores but it restricts air flow. If the differential pressure between the pore air pressure at the top of the HAED (u_a) and the pore water pressure at the bottom of the HAED (u_w) reaches its air entry value (-15 bars), air begins to enter the pores of the HAED. When the pore water pressure beneath the HAED is more than 1 bar larger than the pore air pressure at the top of the HAED, cavitation will occur. Cavitation can be avoided by increasing the pore air pressure in the sample as opposed to applying a negative pore water pressure. Pore water

pressure can be either controlled (drained test) or measured (undrained test) once equilibrium is reached. The resulting suction is calculated as pore air pressure minus pore water pressure.

Once the HAED was saturated, the sample was mounted on the pedestal (Figure 5.20b), covered by placing the inner cell and sealing the top with tape, and then allowed to equalize with the HAED. The sample was then subjected to a drying stage after recording the initial suction value. For tests CWIC-1 and 2, suction was increased via air-drying. The sample was exposed to atmospheric lab conditions for one-hour a day and covered by Saran wrap the rest of the time to avoid rapid drying, which can cause surface cracks that will establish an irreversible differential suction profile within the specimen. After the desired suction value was achieved, the GDS apparatus was assembled (Figure 5.20c-e) and the isotropic compression stage commenced. The suction prior to isotropic compression for the three test samples are shown in Table 5-2.

For test CWCIC-3, the GDS apparatus was assembled immediately after the sample was mounted. Suction was increased via the axis-translation technique while maintaining a nominal confining stress of 10 kPa, following the procedure described in JGS 0527-1998 (1998). Volume change was measured during this stage. The suction increased from 42.9 kPa to 60 kPa prior to isotropic compression.

Table 5-2. Initial specimen conditions prior to constant water content isotropic compression

Test	Sample	D_0 (mm)	H_0 (mm)	s_0 (kPa)	e_0	S_0	Water content
CWIC-1	B3-1-B	58.35	136.9	15.7	1.286	86%	38.4%
CWIC-2	B3-6-M	61.13	127.7	25.7	1.365	91.5%	44.3%
CWIC-3	B3-3-M	61.00	126.7	42.9	1.348	89.7%	43.7%

During the CWIC tests, pore water pressure was measured (undrained), and pore air pressure was controlled (drained). Cell pressure was instantaneously applied at varying user-defined increments to capture the yield point and to avoid sudden saturation. Cell pressure was maintained until the pore water pressure and volume change equalized. An unload/reload cycle was performed in tests 1 and 3. All samples were unloaded to achieve a prescribed level of preconsolidation prior to shear.

5.3.2.1.2 **Results**

Figure 5.24a shows the *p*-*s* stress paths for all tests. Also shown on Figure 5.11 is the location of the saturated yield point, P_0^* = 92 kPa, obtained from the 1D consolidation test. Figure 5.24b and c show specific volume and saturation versus net mean stress, where saturation is obtained by dividing the product of water content and specific gravity (constants) by the current void ratio. From Figure 5.24b, the yield points for tests CWIC-1, 2, and 3 were estimated to be 265, 113, and 67 kPa, respectively. Figures 5.24d and e show the specific volume and saturation versus matric suction, respectively.

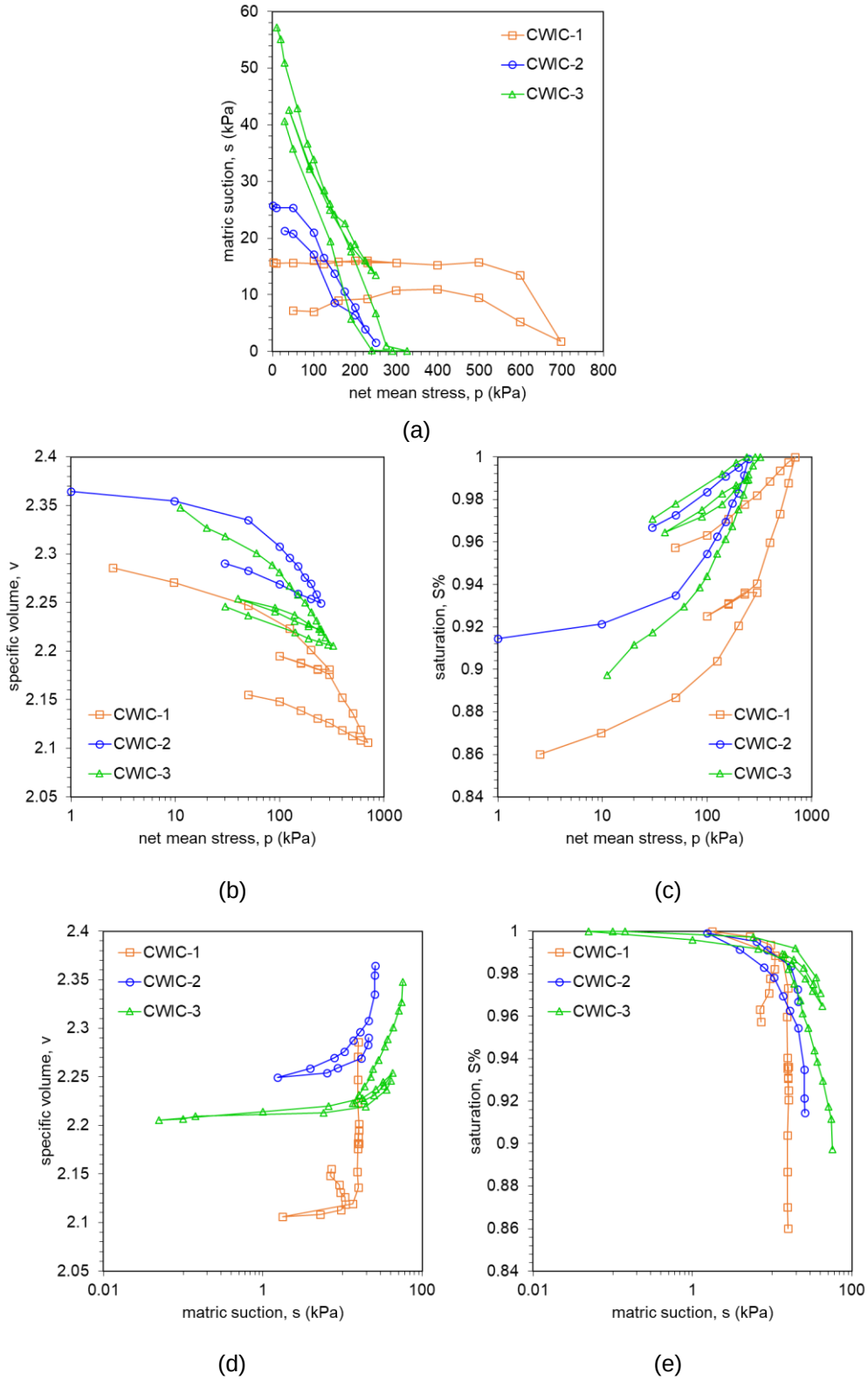

FIGURE 5.24 Constant water content isotropic compression test results of (a) measured stress paths, (b) specific volume versus net mean stress, (c) saturation versus net mean stress, (d) specific volume versus matric suction, and (e) saturation versus matric suction

5.3.2.1.3 **BBM stiffness parameters**

The MSSA developed by Zhang and Lytton (2009) re-expressed the BBM model using 3-dimensional surfaces. One advantage of the MSSA is its capability to model soils with different stress histories (FIGURE 5.22). During recompression, the stress path follows the elastic surface until it reaches the yield curve, irrespective of stress history (P_0, s_0, v_0). The elastic surface is inclined at an angle κ in the ln p - v plane and κ_s in the ln s - v plane but is unfixed and allowed to shift vertically along the void ratio (or specific volume) axis. Once the LC yield curve is reached, the stress path falls on the plastic collapse surface. This surface is fixed in the ln p - ln s - v space. The elastic surface and the plastic collapsible surface can be mathematically expressed as:

$$v^e = C_1 - \kappa \ln p - \kappa_s \ln(s + p_{at})\ elastic\ surface \tag{5.1}$$

$$v = N(0) - \kappa_s \ln\left(\frac{s+p_{at}}{p_{at}}\right) - \lambda(s) \ln\left(\frac{p}{p^c}\right)\ plastic\ collapsible\ surface \tag{5.2}$$

where C_1 is a constant, $\lambda(s)$ is the slope of the NCL line and is a function of suction = $\lambda(0)[(1 - r)\exp(-\beta s) + r]$; r = parameter controlling the slope of the virgin compression line, β = parameter controlling the slope of the virgin compression line for $s \neq 0$, $\lambda(0)$ = slope of the virgin compression line associated with the mean net stress at saturation ($s = 0$); p^c is a reference stress where the LC curve is a vertical line, and $N(0)$ = intercept of the saturated NCL line when p = 1 kPa. A third plastic expanse surface that models plastic deformation during drying also exists. However, this surface is not applicable to the tests performed because the suction values during testing never exceeded the initial suction values established at the start of the tests.

BBM parameters $N(0)$, κ, κ_s, $\lambda(0)$, β, r, and p^c were calibrated using ordinary least squares regression of the predicted specific volume (calculated from equations 5.1 and 5.2) and the measured values shown in Figure 5.24. The calibrated parameters are displayed in Table 5-3. Figure 5.25 shows a comparison between measured and predicted specific volumes with a coefficient of determination of 98.4%.

Table 5-3. Calibrated BBM stiffness parameters

Parameter	Unit	Best fit
κ	-	0.0181
κ_s	-	0.0039
$N(0)$	-	1.90
$\lambda(0)$	-	0.13
r	-	0.01
β	MPa^{-1}	6.22
p^c	MPa	3.33
p_{at}	MPa	0.1013
R^2		98.4%

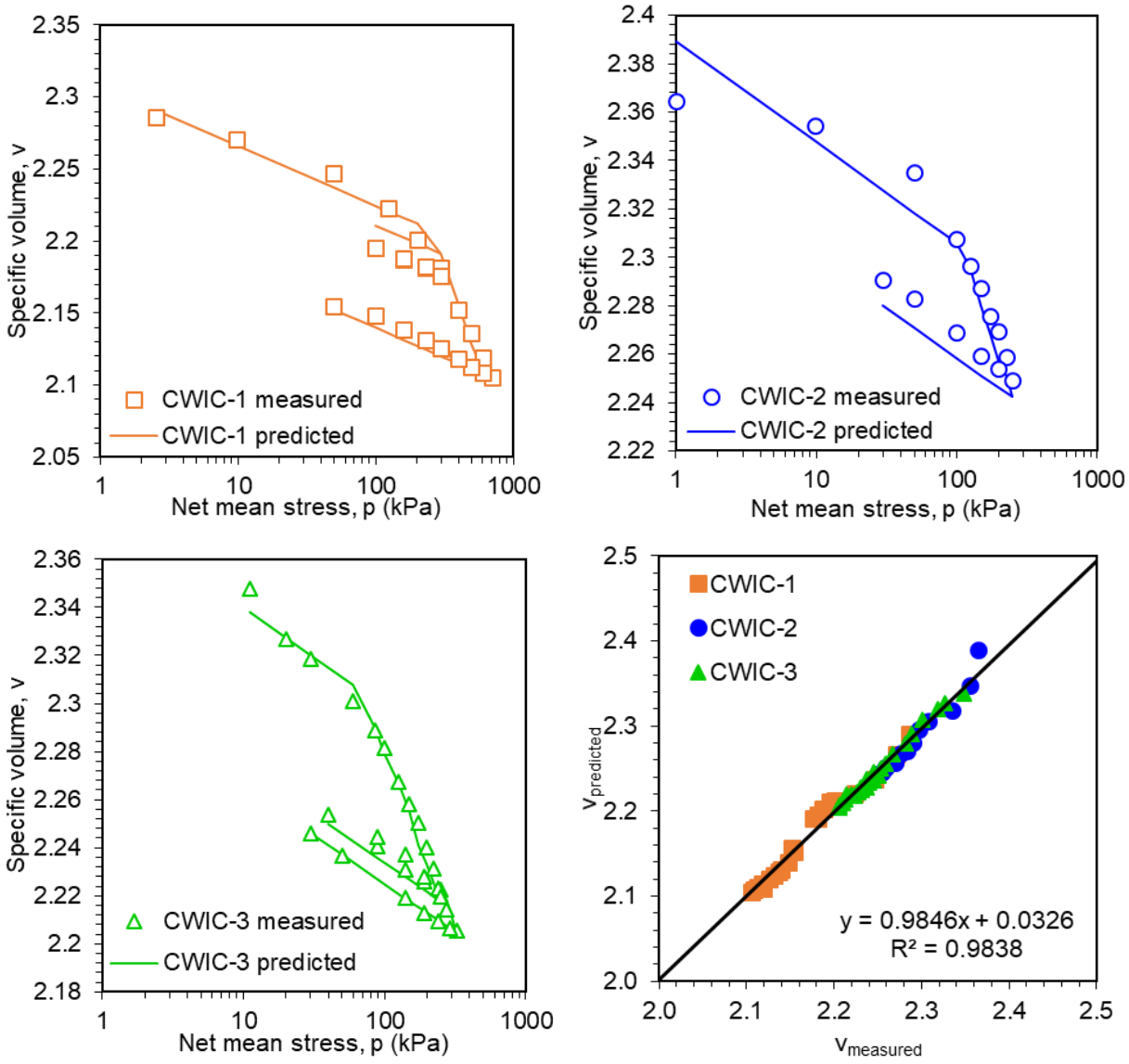

FIGURE 5.25 Comparisons of predicted and experimental results for CWIC tests

Figure 5.26 presents the LC yield curves for the CWIC tests and the 1D consolidation test. The LC yield curve is expressed as:

$$\frac{p_0}{p^c} = \left(\frac{P_0^*}{p^c}\right)^{\frac{\lambda(0)-\kappa}{\lambda(s)-\kappa}} \tag{5.3}$$

where p_0 is the yield stress along the LC yield curve under unsaturated conditions ($s > 0$), P_0^* is the yield stress along the LC curve under saturated conditions ($s = 0$), $\lambda(s) = \lambda(0)[(1 - r)\exp(-\beta s) + r]$, s is the matric suction, and $\lambda(0)$, κ, β, and p^c are previously defined BBM parameters. The shape of the predicted LC curves is classified as Type 3 (Zhang, 2015). This shape was first deemed illogical by Alonso et al., (1990) because there was little experimental evidence showing that this type of yield curve exists. More

recently, undrained isotropic compression tests performed by Sun et al., (2008), Thu et al., (2007) and Zhang and Lytton (2009b) (Figure 5.27) and Sheng et al., (2008) (Figure 5.28) provided the missing experimental evidence. In 2009, Zhang and Lytton (2009) theoretically proved that the Type 3 LC yield curve is applicable to expansive soils.

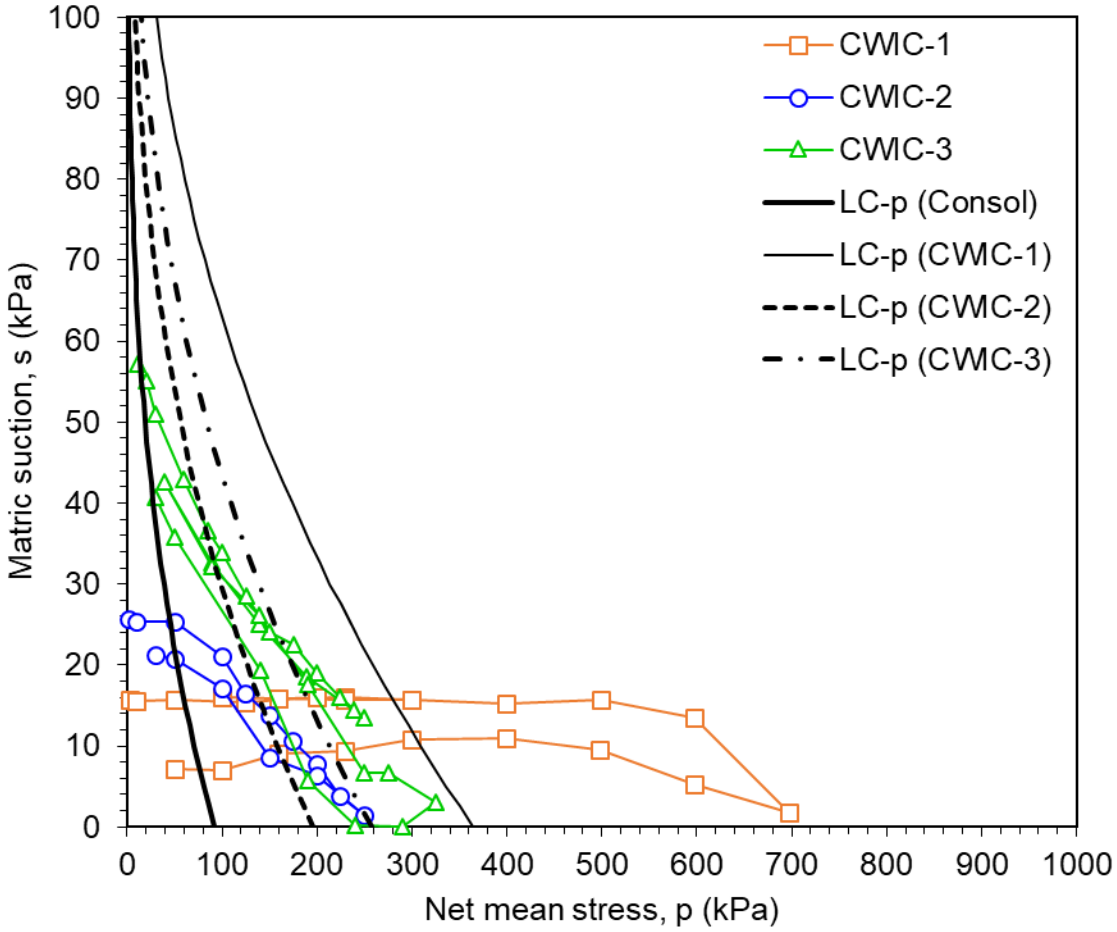

FIGURE 5.26 Predicted loading collapse yield curves for oedometer and CWIC tests

Figure 5.26 shows that the yield mean net stress generally decreases with increasing suction.

The location of the SI curve has not been experimentally determined in this research. Therefore, two scenarios are presented assuming two different locations of the SI curve. First, assume the SI curve runs close to the maximum past suction (say 80 kPa since maximum measured field suction = 79 kPa – see Table 7-3) as shown in Figure 5.29. If a soil is initially within the elastic region, has a net mean stress greater than p_0 (which is the value of p at the intersection of the LC and SI yield curves = 14 kPa) and is dried at constant net mean stress, it will experience plastic collapse at suctions greater than that on the LC yield curve. This soil will not collapse due to wetting. This can be best illustrated by Sample CWIC-2 from a depth of 3.3 m (10 ft), which is in close proximity to a tensiometer in Boring T3 at the same depth.

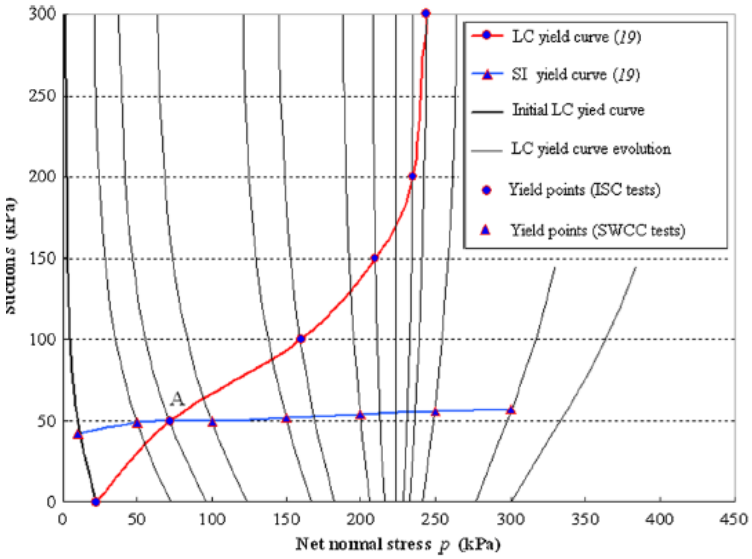

FIGURE 5.27 LC evolution of a MH Malaysian silt (Thu et al., 2007) exhibiting three types of LC yield curves (Zhang and Lytton, 2009)

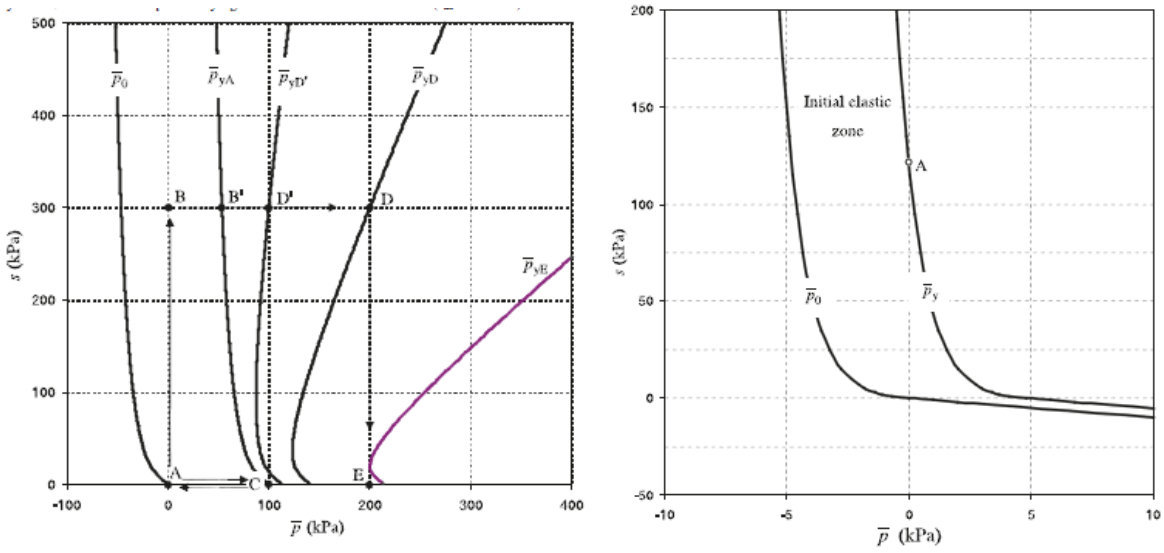

FIGURE 5.28 Type 3 yield curve for Pearl clay (Sheng et al., 2008)

The soil is initially at a net mean stress of 50 kPa (Point A), which is within the elastic region. Under a constant net mean stress, the stress path will run from A→B, which is located on the LC yield curve. Upon further drying, the soil follows path B→C where it undergo irreversible plastic strains (Equation 5-2).

A second scenario is if the SI yield curve is omitted (Figure 5.30) and the LC yield curve extends until it intersects with the *s* axis. In the case of CWIC-2, the LC yield curve approaches the *s* axis at about *s* = 100 kPa. This type of yield curve has previously been shown by Zhang and Lytton (2009b) to exist for a high-plasticity compacted clay based on Brackley's (1975) data (Figure 5.31).

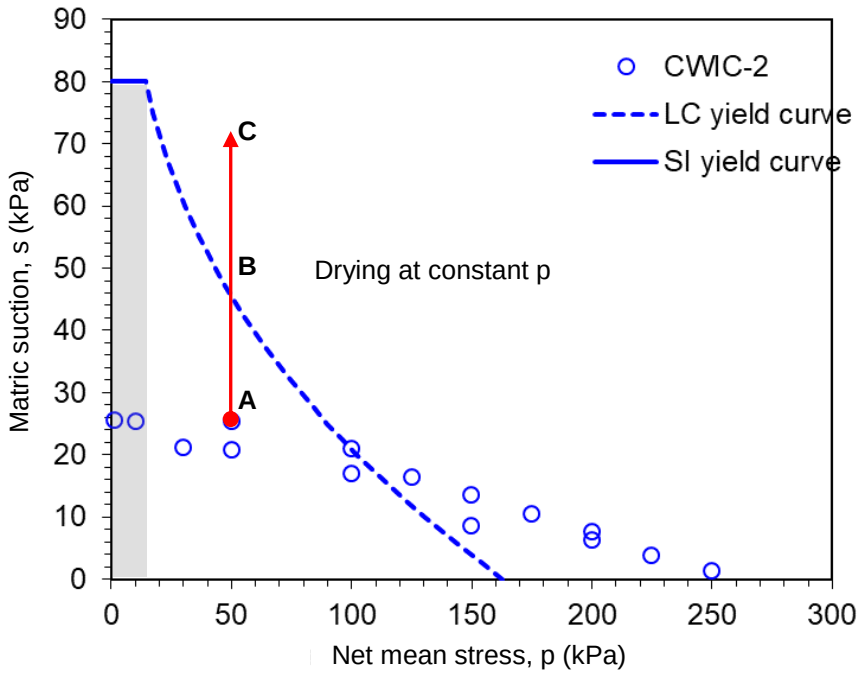

FIGURE 5.29 LC and hypothetical SI yield curves for CWIC-2

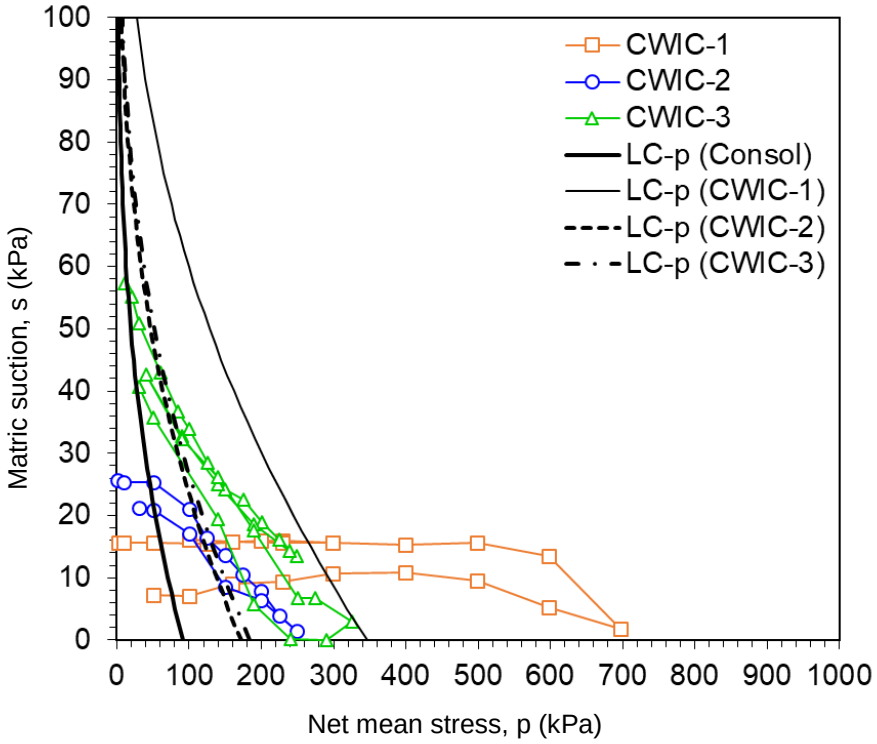

(a)

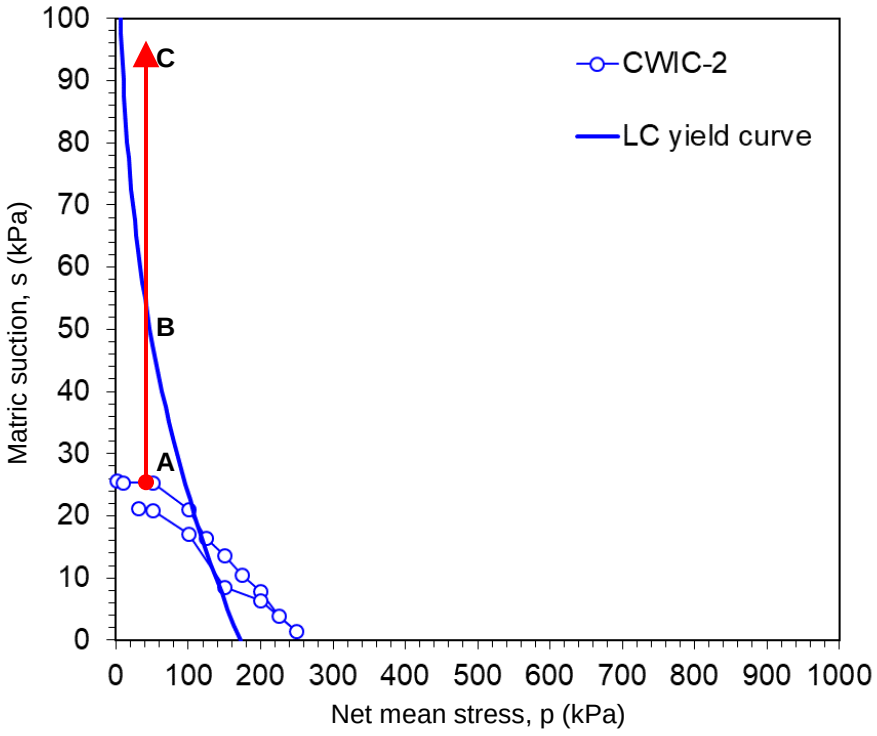

(b)

FIGURE 5.30 LC yield curves at high suctions for (a) all tests and (b) CWIC-2

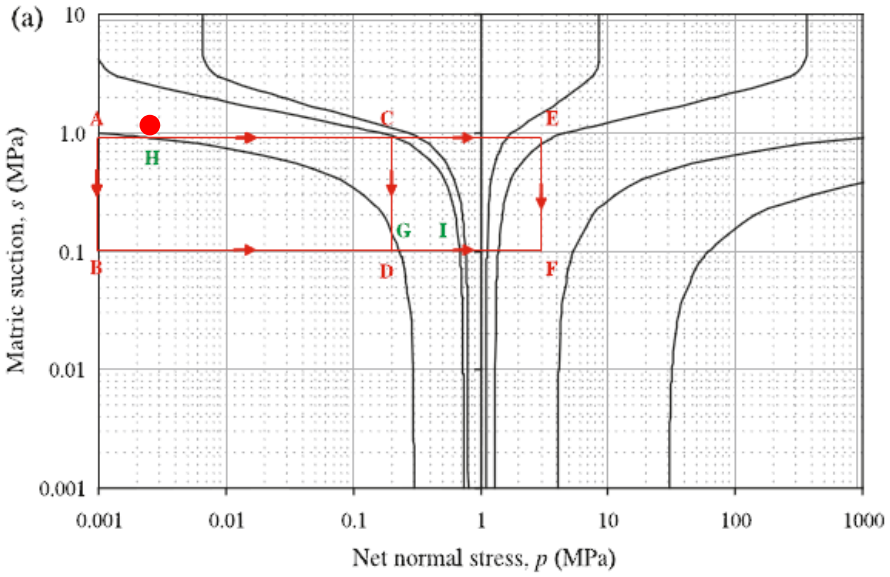

FIGURE 5.31 Evolution of LC yield curves for high-plasticity compacted clay (Zhang and Lytton, 2009b)

5.3.2.1.4 **Porosity-Dependent SWCC**

Porosity-dependent SWCC can be incorporated in coupled hydro-mechanical models either by expressing the individual SWCC parameters such as the air entry suction as a function of confining stress (Gallipoli et al., 2003; Huang et al., 1998; Nuth and Laloui, 2008; Cabarkapa and Cuccovillo, 2006; Hu et al., 2013; and UPC, 2017), or by expressing the SWCC as a function of the soil stress state (Sun et al, 2008; Masin, 2010; Mbonimpa et al., 2006; and Zhou et al., 2012). In HYDRUS, which is the software used for the transient hydrological flow model in Chapter 6, hysteretic behavior is only available for the van Genuchten model (1980). Therefore, only hydraulic models that express the van Genuchten parameters as a function of stress state are considered. Hu et al., (2013) derived a relationship between the air entry suction and void ratio, which varies with pressure. D'onza et al. (2011) and UPC (2017) expressed two of the van Genuchten parameters, P and λ, as a function of porosity.

$$S_e = \frac{S - S_r}{S_l - S_r} = \left[1 + \left(\frac{s}{P}\right)^{\frac{\lambda}{1-\lambda}}\right]^{-\lambda} \tag{5.4}$$

$$P = P_0 \exp[a(\Phi_0 - \Phi)]$$

$$\lambda = \lambda_0 \exp[b(\Phi_0 - \Phi)]$$

where S_r is the residual saturation, S_l is the maximum saturation, s is the matric suction (kPa), P and λ are the van Genuchten parameters, Φ is the porosity, P_0 and λ_0 are the van Genuchten parameters at a reference porosity, Φ_0 and a and b are fitting parameters. Sometimes, the van Genuchten equation is more commonly expressed in terms of α and n instead of P and λ. However, the two pairs of parameters are related as follows:

$$P = \frac{g}{\alpha} \tag{5.5}$$

$$\lambda = m = 1 - \frac{1}{n}$$

where g is acceleration due to gravity.

CWIC data was used to obtain the porosity-dependent van Genuchten parameters (P_0, λ_0, a, b and Φ_0). The porosity can be calculated from the specific volume ($\Phi = (\nu - 1)/\nu$). The specific volume can be estimated using the BBM (equations 5.1 and 5.2) and inserted into Equation 5.4 to predict the degree of saturation during isotropic compression. Data points during the loading stage were used to calibrate the main wetting branch of the porosity-dependent SWCC since suction decreases during compression. Conversely, data points during the unloading stage were used to calibrate the main drying branch of the porosity-dependent SWCC. The parameters λ_0 and b were assumed to be equal for both drying and wetting. The model parameters (a_d, a_w, P_0^d, P_0^w, b, λ_0 and Φ_0) were calibrated by performing ordinary least squares regression of the measured and predicted saturation and are presented in Table 5-4.

Figure 5.32 show the predicted versus measured saturation versus matric suction curves. The resulting coefficient of determination was 0.958 (Figure 5.32d) based on CWIC tests 2 and 3 data. Using the parameters in Table 5-4 and Equation 5.3, the porosity-dependent SWCCs are plotted in Figure 5.33.

Table 5-4 Calibrated porosity-dependent van Genuchten parameters

Parameter	Unit	Drying Branch	Wetting Branch
Φ_0	-	80.13%	80.13%
P_0	kPa	3.32	0.003
λ_0	-	0.13	0.13
a	-	14.4	41.36
b	-	-0.01	-0.01

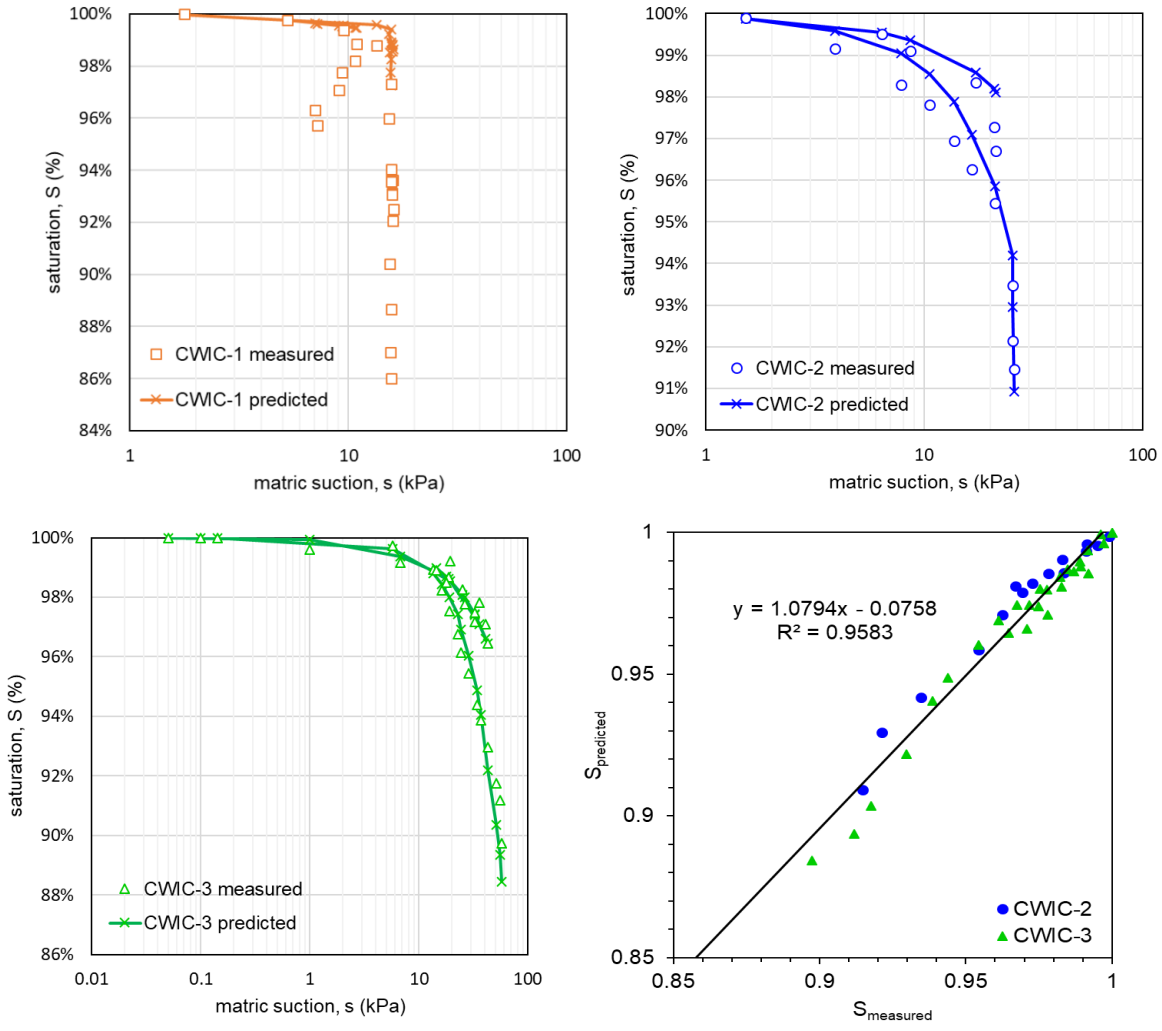

FIGURE 5.32 Predicted versus measured saturation versus suction curves for CWIC- (a) 1; (b) 2; (c) 3 and (d) predicted versus measured saturation for CWIC tests 2 and 3

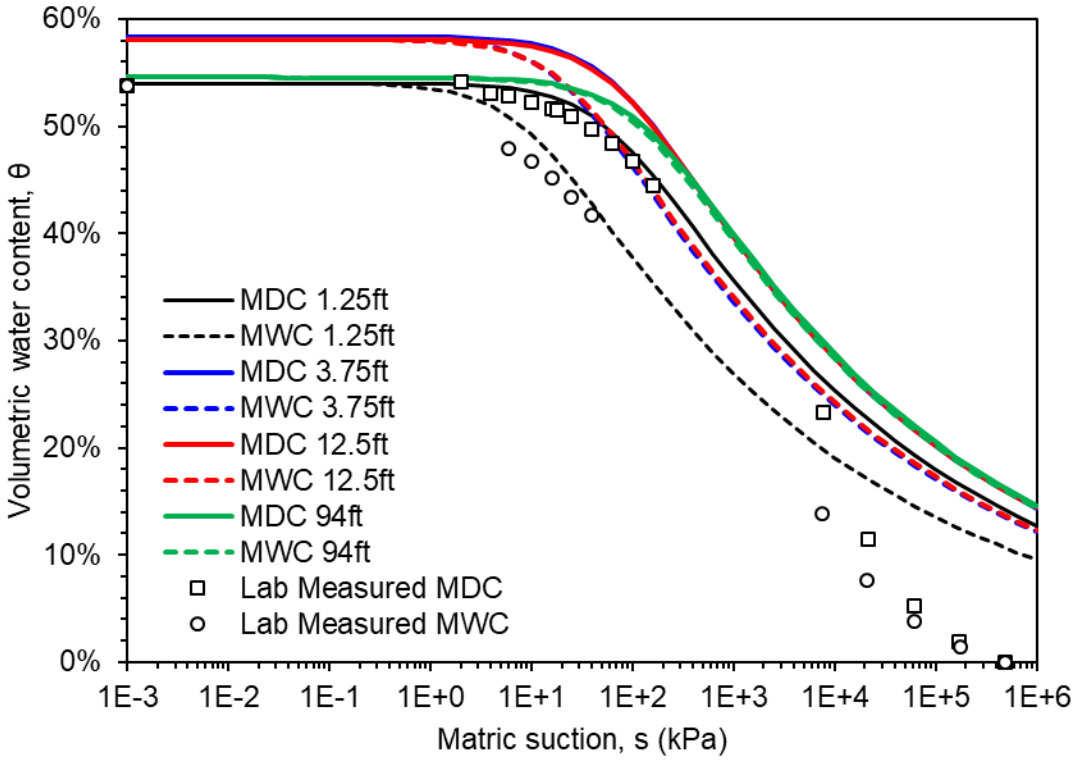

FIGURE 5.33 Predicted porosity-dependent SWCC

5.3.2.2 **Constant Water Content Triaxial Shear Tests**

Constant water content shear tests have been performed under triaxial (Bishop et al., 1960; Bishop and Donald, 1961; Satija, 1978; Georgetti and Vilar, 2011; Ma et al., 2013; Rahardjo et al., 2004; Thu et al., 2006) and direct shear (Tarantino, 2009; Ng and Chiu, 2001; Maswoswe, 1985). Rahardjo et al. (2004) performed CD and CWTS tests on reconstituted residual silt and found that shear strengths obtained from both tests show good agreement. Georgetti and Vilar (2011) observed that CWTS deviator stress-strain curves more closely resemble those from saturated CD tests rather than saturated CU tests.

The next section presents the results of three CWTS tests alongside those for the multi-stage CD triaxial tests for comparison purposes.

5.3.2.2.1 **Procedure**

Constant water content triaxial shear (CWTS) tests were performed to obtain the BBM shear parameters (G, k, and M). The pore-water was undrained and pore-air drained during shearing. An unload-reload stage was performed during tests 2 and 3 to obtain the elastic shear modulus, G. Table 5-5 summarizes the initial specimen conditions before shearing.

The samples were sheared at constant cell and pore-air pressure at a rate of 0.01%/min in accordance with JGS-0527-1998 (1998). The same shearing rate was also adopted by Ma et al. (2013), Rahardjo et al. (2004), Thu et al. (2006) and Maleki and Bayat (2012). Thu et al. (2006) measured

suction at three sample heights during constant water content shearing of a compacted silt and concluded that a constant rate of strain of ~0.01%/min produced small differences between suctions measured at the base plate and at ¼, ½ and ¾ of the sample height from the base plate.

Table 5-5 Initial conditions of specimen before shearing

Test	Sample	D_0 (mm)	H_0 (mm)	w	p_0(kPa)	s_0 (kPa)	OCR_0
CD-15	B2-1-B	59.4	124.6	sat	15	0	6
CD-30	B2-1-B	58.9	126.6	sat	30	0	3
CD-50	B2-1-B	58.7	128.4	sat	50	0	2
CWC-1	B3-1-B	57.3	136.6	38.4%	50	44	14
CWC-2	B3-6-M	60.2	127.7	44.3%	30	21	5
CWC-3	B3-3-M	59.3	125.8	43.7%	30	40	11

5.3.2.2.2 **Results**

Table 5-6 summarizes the results of the CWTS tests. Deviatoric stress versus axial strain plots are shown in Figure 5.34a. All tests exhibited post-peak strain softening. For tests conducted at the same confining stress {= 50 kPa for CD-50 and CWC-1} and {= 30 kPa for CD-30, CWC-2 and CWC-3}, the peak deviatoric stress increased with increasing suction.

The samples were loaded to large strains towards critical state. For tests conducted at the same confining stress of 30 and 50 kPa, the deviatoric stress at critical state decreased with increasing suction. This indicates that one or both tests did not reach critical state yet.

Volume change curves are shown in Figure 5.34b. For the CWTS tests at the same confining stress of 30 kPa, the amount of dilation increased with increasing suction and *OCR*.

Suction versus axial strain curves are shown in Figure 5.34c. Suctions did not change significantly during shearing. The maximum suction difference during tests 1, 2, and 3 were 3.5 kPa, 1.3 kPa, and 6.9 kPa, respectively. The suction response during shear was different for all tests. With CWC-1, suctions initially increased to a peak of 45.1 kPa then decreased until the peak deviator stress was reached. The suction then gradually increased for the remainder of the test. With CWC-2, there was no significant change in suction throughout despite there being two unload-reload cycles. With CWC-3, the suction initially decreased during shear and increased during the unload-reload cycle. During reloading, the suction decreased until the peak deviatoric stress was reached and then gradually increased for the remainder of the test. Thu et al., (2007) performed CWTS and CD tests on a MH Malaysian silt and found that the suction response decreased as the initial suction value decreased. Our test data are consistent with those results.

Table 5-6 Peak and critical state results for saturated and unsaturated triaxial shear tests

Test	p_0 (kPa)	Peak				Critical state			
		p (kPa)	s(kPa)	q (kPa)	ε_a	p (kPa)	s (kPa)	q (kPa)	ε_a
CD-15	15	45	0	91	1.4%	[1]	[1]	[1]	[1]
CD-30	**30**	70	0	120.5	2.1%	[1]	[1]	[1]	[1]
CD-50	**50**	107	0	171	3.3%	106	0	170	5.7%
CWC-1	**50**	189	42	411	2.6%	99	42.6	142	13.3%
CWC-2	**30**	108	21.5	236	6.2%	83	21	162	17.4%
CWC-3	**30**	120	40	269	3.3%	75	43	135	21.2%

Note: 1. First two stages of the multi-stage CD triaxial test did not reach critical state.

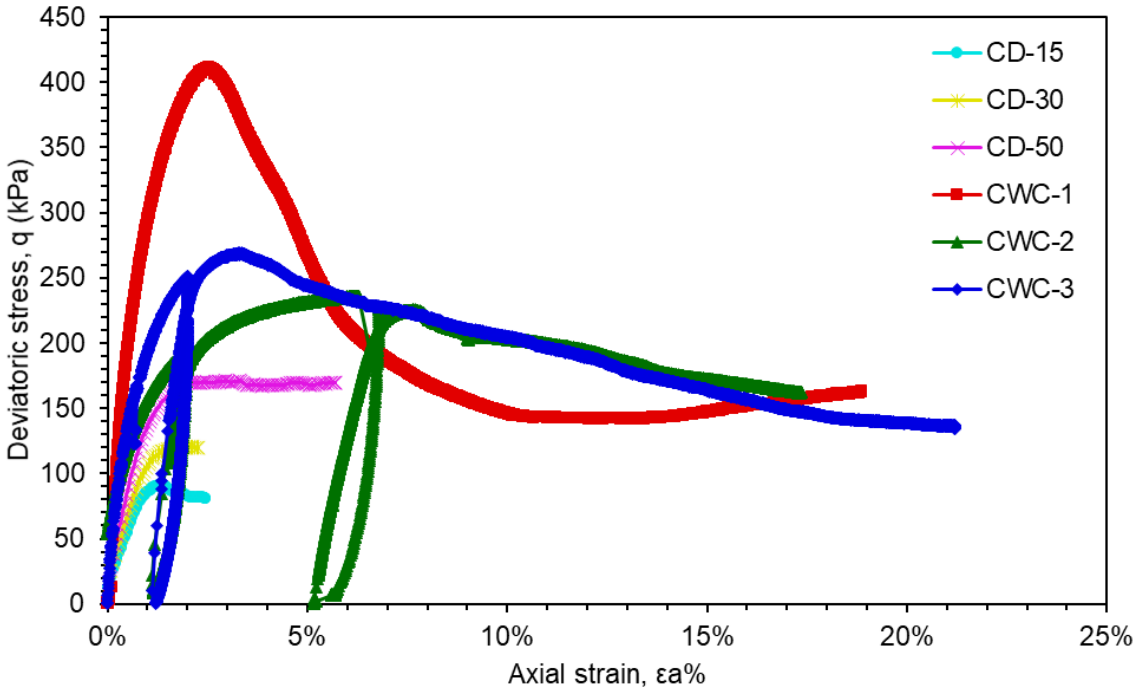

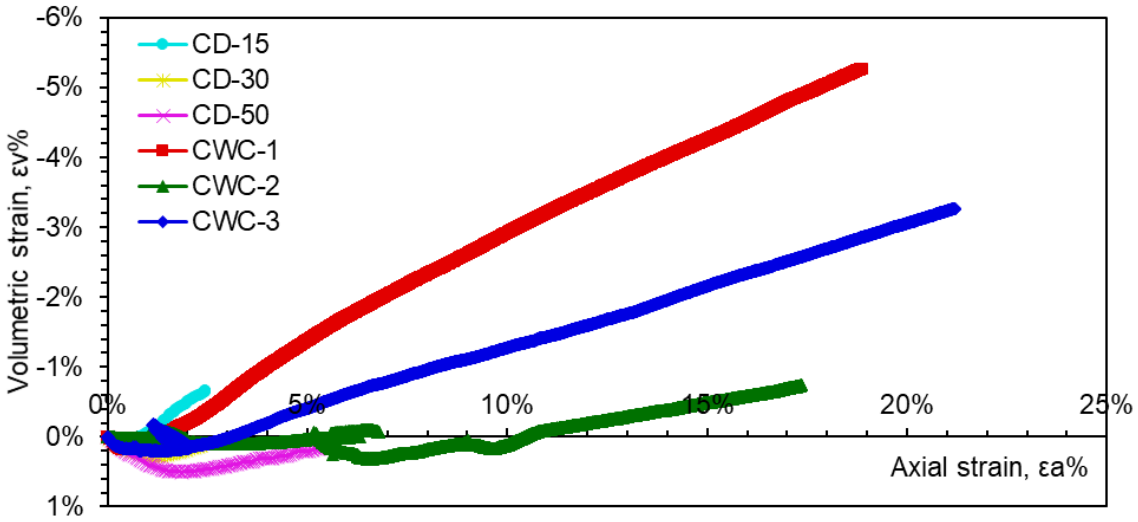

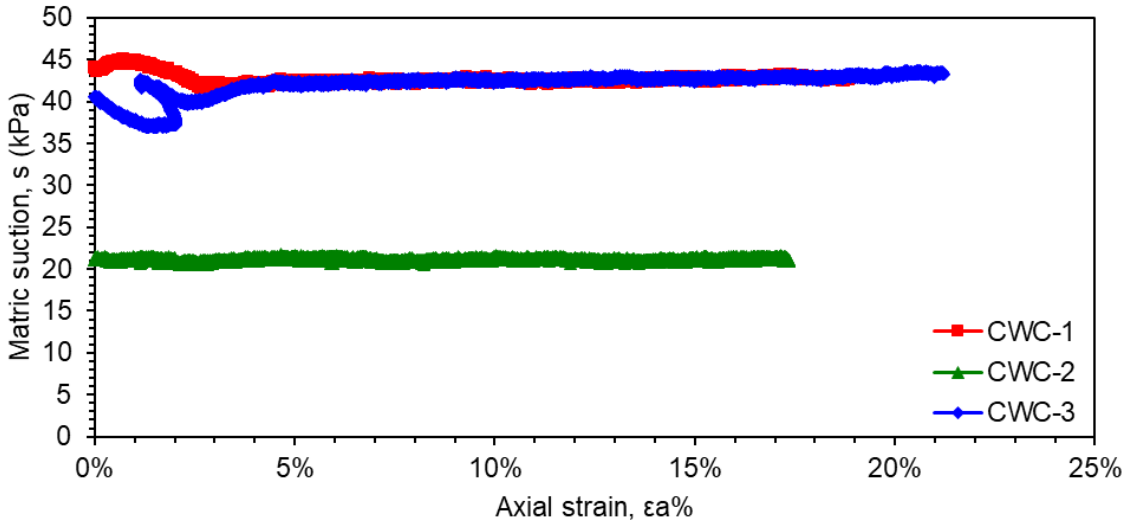

FIGURE 5.34 CWTS test results (a) deviatoric stress versus axial strain, (b) volumetric versus axial strain, and (c) matric suction versus axial strain

5.3.2.2.3 **BBM Shear Strength Parameters**

The shear modulus, *G*, can be calculated from the unload-reload portion of CWC-2 and 3 and the elastic regions of CD-15, -30, -50, and CWC-1. However, in reality, the shear modulus is pressure dependent as shown in the following expression,

$$G = \frac{3p(1-2\mu)(1+e_0)}{2\kappa(1+\mu)} \tag{5.6}$$

where μ = Poisson's ratio, e_0 = initial void ratio, κ = slope of the unload-reload line and is different for saturated versus unsaturated soil and *p* = mean net pressure within the soil. Since *G* is not needed for this research and since it is pressure dependent, no value will be reported herein.

Figure 5.35 shows the CWTS and CD test results in *p*-*q* space. From this plot, the BBM shear parameters (*M* and *k*) can be determined. A limitation of the multi-stage CD triaxial test performed on the saturated sample is that post-peak strains are small for all stages except the final stage. Therefore, the σ_c = 15 kPa and 30 kPa CD test results could not be used to obtain BBM shear parameters. The critical states of the σ_c = 50 kPa multi-stage CD triaxial test on the saturated sample (henceforth denoted as CD50), and the three CWTS tests were used to obtain BBM parameters *M* and *k*.

From Fig. 5.36, it can be seen that samples CD-50 and CWC-1 have reached critical state. Normalized *q*/*p* values appear to be still decreasing with increasing strain for samples CWC-2 and -3 although CWC-3 appears close to plateauing.

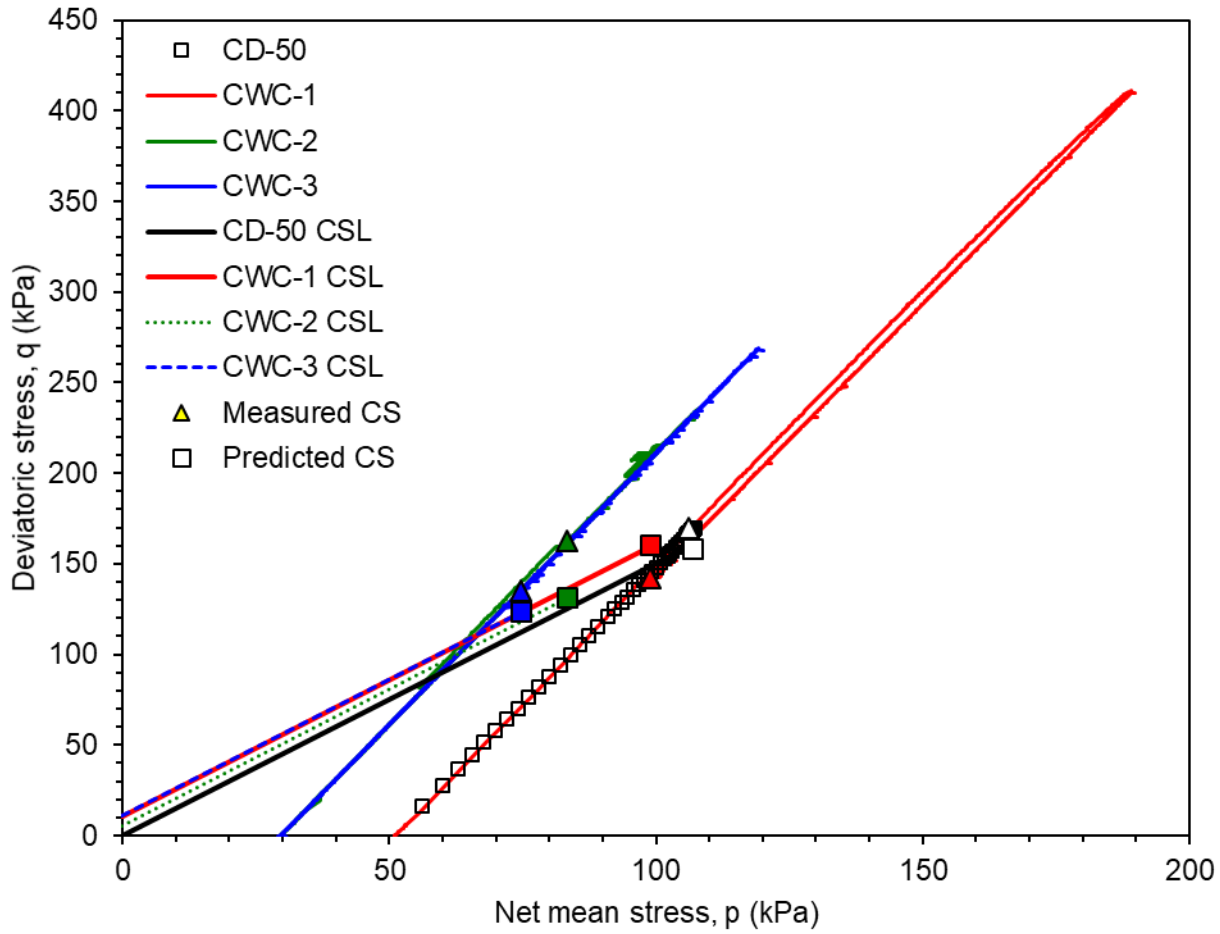

FIGURE 5.35 Stress paths and measured critical states for CD50, and the CWC tests

Ordinary least-squares regression was used to fit the data at critical state for tests CD-50, CWC-1, and -3 to a plane expressed by the equation:

$$q = M(p + ks) \tag{5.7}$$

where M and k are the BBM shear parameters estimated to be 1.51 and 0.17, respectively. CWC-2 was omitted from the regression because it does not appear to have reached critical state yet. A criterion was imposed such that $q_{predicted\ CWC\text{-}1} \geq q_{predicted\ CD50}$. The resulting critical state failure plane can then be expressed by the following equation,

$$q = 1.51(p + 0.17s) \tag{5.8}$$

A coefficient of determination of 42% was obtained between the measured and predicted failure deviatoric stresses. The parameter, M is related to the critical state friction angle as follows

$$M = \frac{6 \sin \phi'_{cs}}{3 - \sin \phi'_{cs}} \tag{5.9}$$

Based on the estimated value of *M*, the critical state friction angle was calculated to be 37°.

Figure 5.37a shows the *p*-*q* stress paths for the CD and CWTS tests and their respective critical state lines. Figure 5.37b shows the stress paths in *p*-*q*-*s* space with the critical state failure plane described by Equation 5.8.

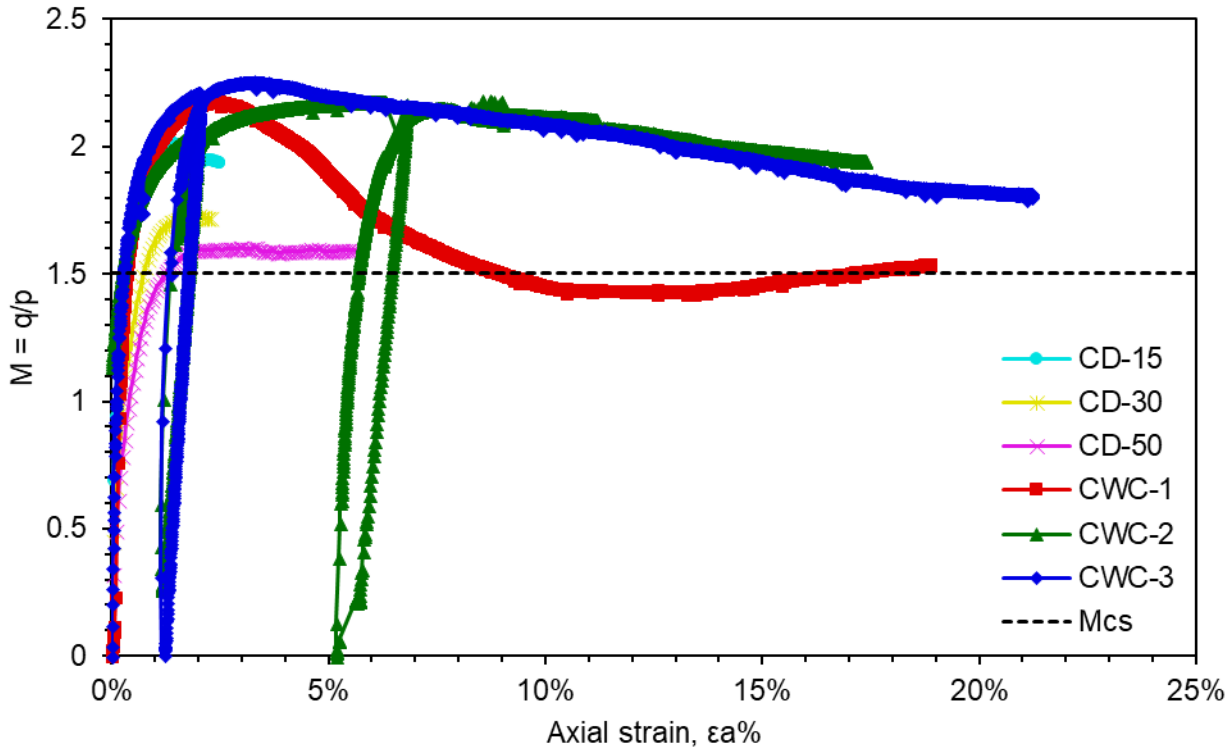

FIGURE 5.36 Normalized deviator stress versus axial strain

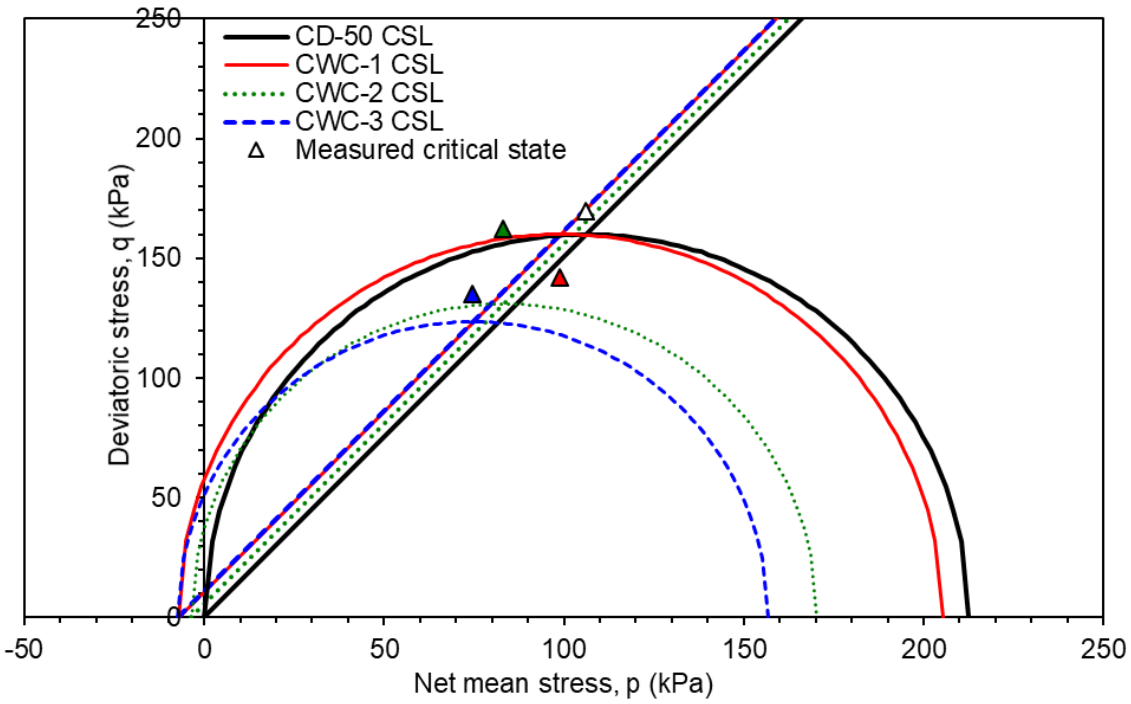

(a)

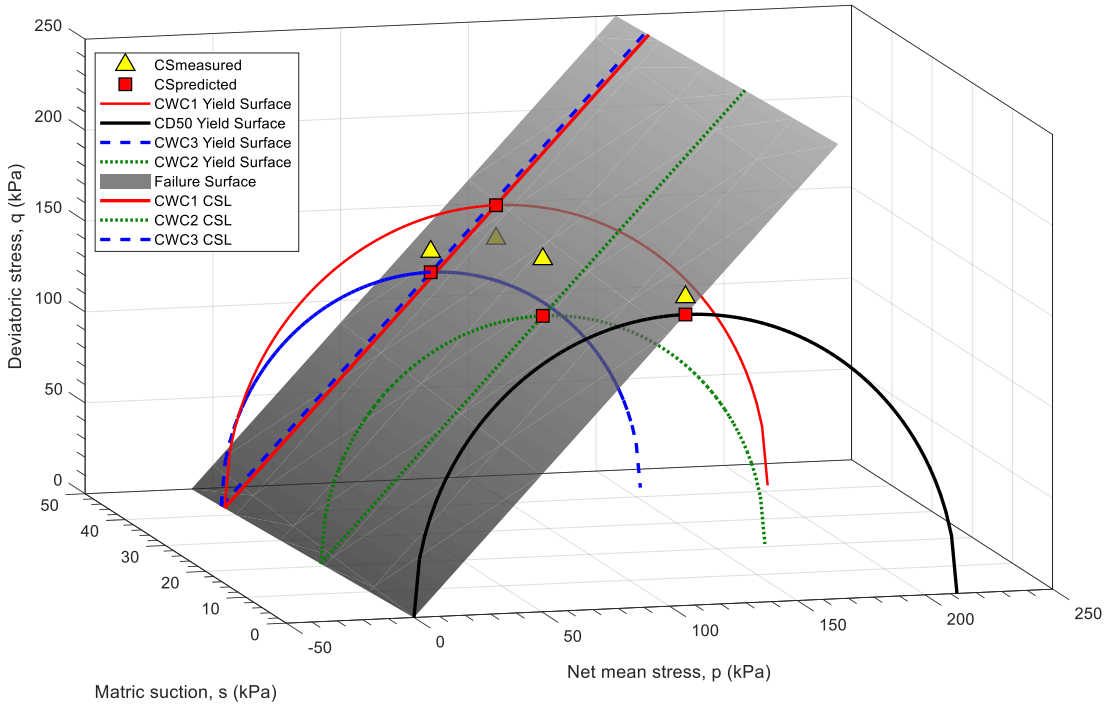

(b)

FIGURE 5.37 Predicted CSL and failure planes in q-p-s space

5.3.2.3 **Comparison of BBM Parameters Obtained with those from Prof. Zhang and Dr. Li's Constant Water Content Oedometer and Constant Water Content Direct Shear Tests**

Constant water content oedometer (CWK_0C) and constant water content direct shear (CWDS) tests on soil samples from this slope were carried out by Professor Xiong Zhang and Dr. Lin Li. Details of the test description, procedure, analysis and results can be found in Appendix B. Table 5-8 provides a summary of the tests performed in this study (UH) and by Professor Zhang and Dr. Li. Sections 5.3.2.3.1 and 5.3.2.3.2 compare the BBM stiffness and strength parameters, respectively.

Table 5-7 Summary of tests performed and parameters obtained

Group	Test	w%	Stress path	Stiffness	Shear	Strength	Porosity-Dependent SWCC
UH	CD-15, 30, 50	Sat	CD shear	-	G, M, k	ϕ'_e, c'_e, ϕ'_{cs}	-
	CWIC-1	38.4	CWC isotropic compression	$N(0)$, κ, κ_s, $\lambda(0)$, β, r, p^c	-	-	-
	CWIC-2	44.3					a^d, a^w, $P_0{}^w$, $P_0{}^d$, b, λ_0, Φ_0
	CWIC-3	43.7					
	CWTS-1	38.4	CWTS shear	-	G, M, k	ϕ'_{cs}	-
	CWTS-2	44.3					
	CWTS-3	43.7					
Zhang	CWK_0C-1	35.81	$CWCK_0$ compression	$N(0)$, κ, κ_s, $\lambda(0)$, β, r, p^c	M, k, α	ϕ', c', ϕ_b, ϕ'_{cs}	-
	CWK_0C-2	46.04					
	CWK_0C-3	34.23					
	CWK_0C-3	29.84					
	CWK_0C-4	33.56					
	CWK_0C-5	30.09					
	CWK_0C-6	26.19					
	CWK_0C-7	34.64					
	CWDS-1	30.21	$CWCK_0$ shear				
	CWDS-2	29.10					
	CWDS-3	35.81					
	~~CWDS-4~~	~~38.34~~					
	CWDS-5	41.38					
	CWDS-6	41.23					
	CWDS-7	44.23					
	CWDS-8	32					
	CWDS-9	32.43					
	CWDS-10	33.72					

5.3.2.3.1 **Stiffness Parameters**

Table 5-9 compares BBM stiffness parameters from CWIC tests (UH) with those from CWK_0C tests by Zhang and Li. Zhang and Li derived the BBM parameters using an incremental form of equations 5-1 and 5-2. The constants C_1 and $N(0)$ are not applicable when using the incremental form, therefore Zhang and Li provided $N(0)$ values for each test rather than a single value. To test the validity of Zhang and Li's BBM stiffness parameters, $N(0)$ was allowed to vary for each CWIC test performed in this research and Zhang and Li's stiffness parameters [κ, κ_s, $\lambda(0)$, β, r, and p^c] were utilized to check goodness of fit of the CWIC test results. Figure 5.32 shows that Zhang and Li's parameters reasonably predict the CWIC tests

in this research as long as $N(0)$ is allowed to vary for each test. However, the parameter $N(0)$ is a constant when the BBM is used to model stress states other than those experienced during testing. Thus, for modelling field situations, $N(0)$ must be a determined value.

Table 5-8 Calibrated BBM stiffness parameters obtained from this research and by Zhang and Li

Parameter	Unit	UH	Zhang and Li
κ	-	0.0181	0.0147
κ_s	-	0.0039	0.0066
$N(0)$	-	1.90	Varies
$\lambda(0)$	-	0.13	0.075
r	-	0.01	0.158
β	MPa^{-1}	6.22	3.812
p^c	MPa	3.33	0.046

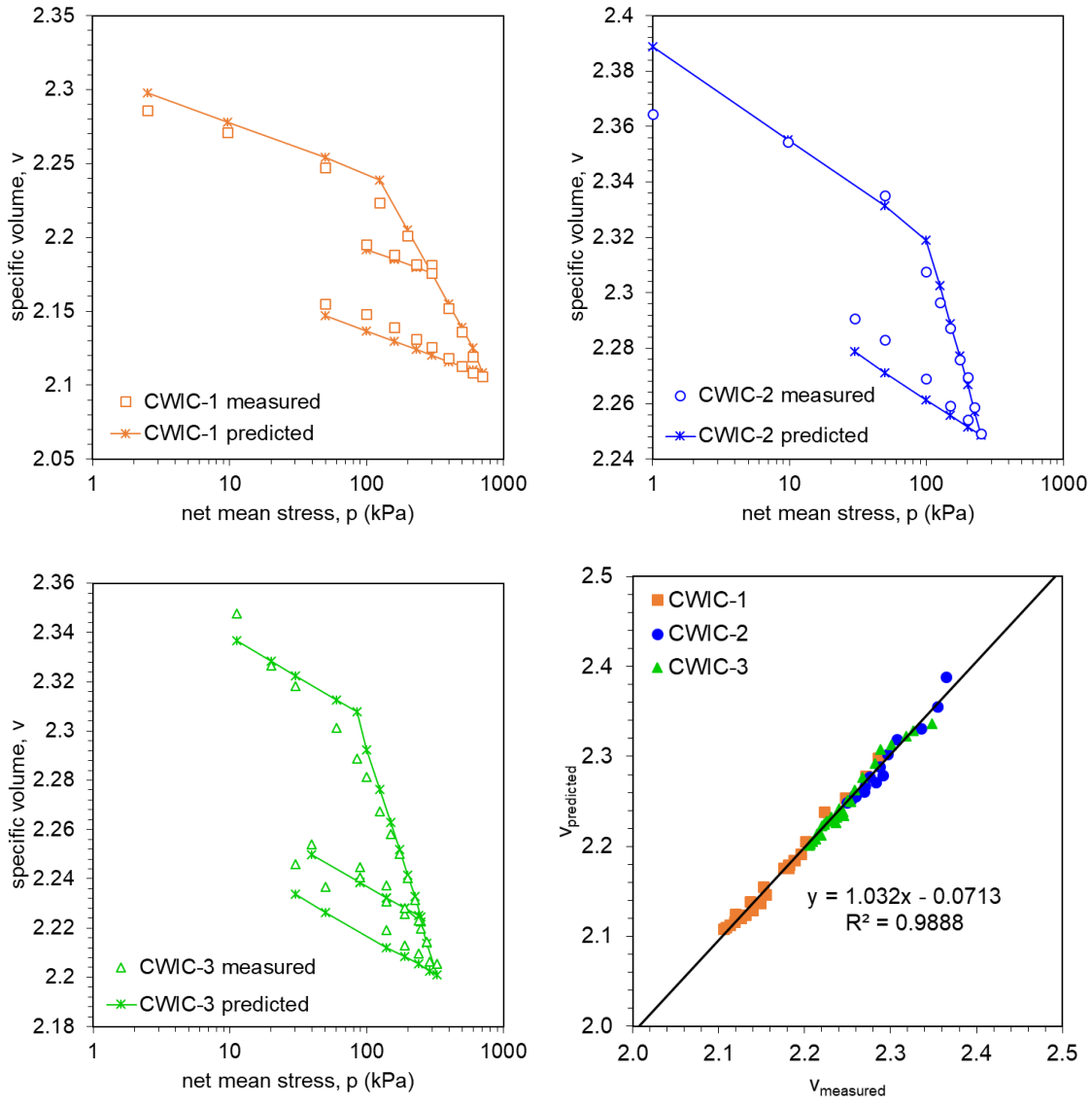

FIGURE 5.38 CWIC tests reinterpreted using Zhang and Li's parameters and allowing N(0) to vary for each test

The LC yield curves determined for the test samples in this research (Figure 5.31) are of the Type 3 variety where the mean net stress decreases with increasing suction (Zhang, 2015) whereas Zhang and Li's curves shown in Figure 4.16 of Appendix B (reproduced in Figure 5.39) are Type 1 where the mean net stress increases with increasing suction and they are also non-convex. Type 2 LC yield curves are vertical and they occur when p_o^* = preconsolidation pressure of the soil when saturated = p^c. When $p_o^* > p^c$, it generally implies that the soil is collapsible (p^c = 46 kPa according to Zhang and Li and = 3.33 MPa according to this research) whereas when $p_o^* < p^c$, the soil is generally expansive in nature. Types 1, 2 and 3 curves can be generated by changing the value of p_o^*. These three curve types are shown in Figure 5.37 based on p^c = 3.33 MPa. It should be noted that the dash-lined LC yield curves shown in Figure 5.39b are an extrapolation using the BBM stiffness parameters. Additionally, the LC yield curve

extension into suction ranges larger than 40 kPa are extrapolations as well. The water content and suction ranges of the CWIC testing program are for the low suction ranges in comparison to the CWOD tests performed by Zhang and Li. Idealy, the CWIC testing program would have been performed to cover suction and net mean stress ranges expected in the field however due to limitations of the GDS pneumatic controller, larger suctions values could not be imposed.

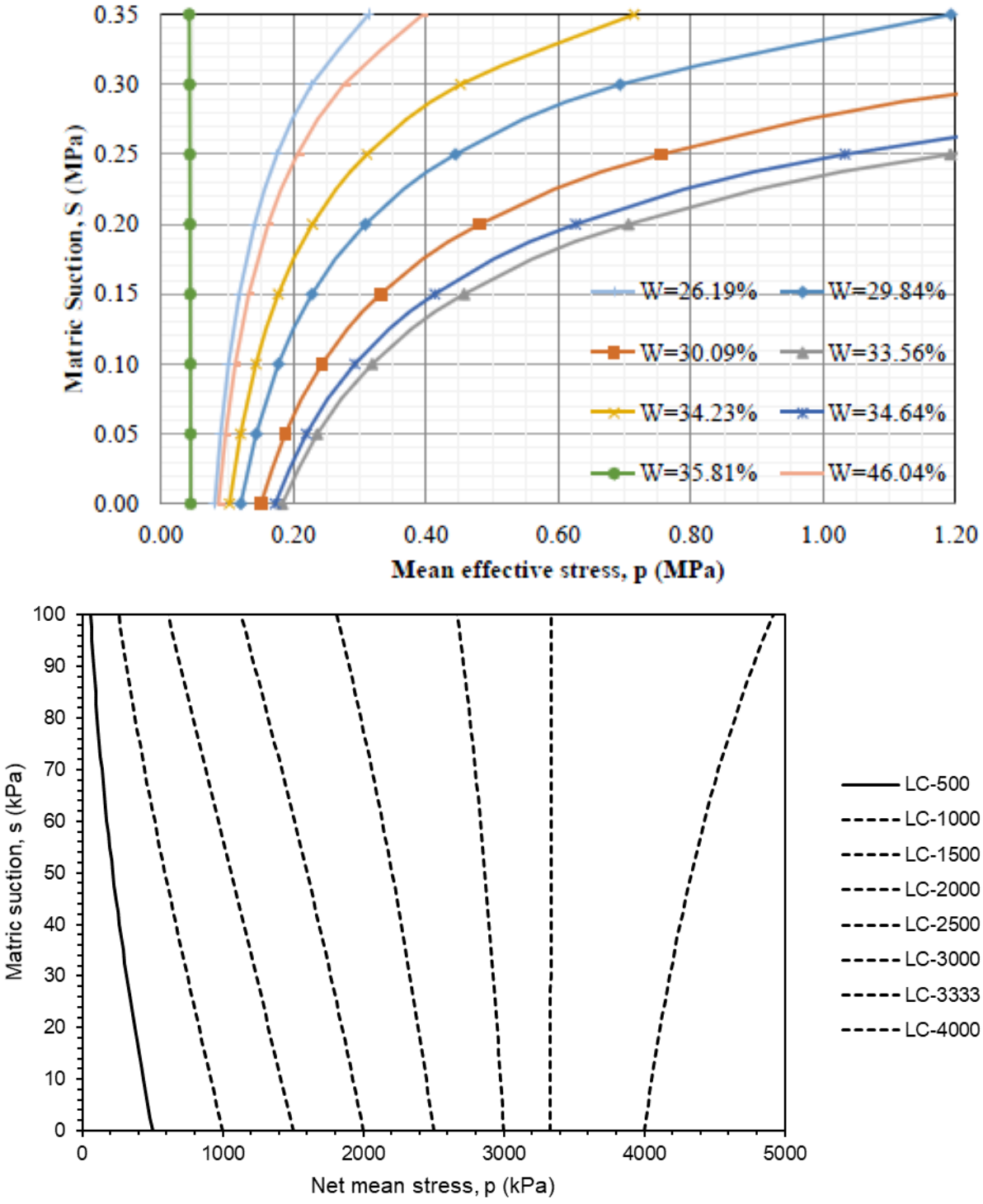

FIGURE 5.39 LC yield curves produced by (a) Zhang and Li and (b) UH

5.3.2.3.2 **Shear Strength Parameters**

The BBM contains 10 parameters to model unsaturated soil behaviour. Three of those, *G*, *M*, and *k* are for modelling the soil behaviour during shear (Table 5-10). Zhang and Li did not report the elastic shear modulus, *G*, as a BBM parameter in Appendix B. They assumed a Poisson's ratio of 0.35, which theoretically can be used to estimate *G* for any value of *p* and e_o in accordance with Equation 5.6.

Zhang and Li also estimated the parameter α which is defined as follows.

$$\alpha = \frac{M(M-9)(M-3)}{9(6-M)}\left\{\frac{1}{1-\frac{\kappa}{\lambda(0)}}\right\} \tag{5.10}$$

Figure 5.40a shows the predicted BBM failure planes in *q*-*p*-*s* space predicted by Zhang and Li compared to that from this research. The plane with colour contours is from this study while the uncontoured plane is predicted by Zhang and Li. The planes intersect at a net mean stress to suction ratio of 1.55.

At a depth of 4m, the net mean stress is approximately 60 kPa and the planes intersect at a suction of 46 kPa (Figure 5-30b). Therefore, below a depth of 4m, the UH BBM parameters predict higher strengths than Zhang and Li's parameters up until a suction of 46 kPa. Once the suction exceeds 39 kPa, the Zhang and Li parameters predict higher shear strengths than the UH parameters.

The peak and critical shear strength parameters can be compared in Table 5-9. The shear strength parameters at peak are strictly not BBM parameters. Also, the parameters are not expected to be the same. Rowe (1969) showed that the shear strength parameters in direct shear will differ from those in a triaxial test because of the different boundary conditions. However, the parameters are too far apart with the percent difference shown in the last column.

Table 5-9 Shear strength parameters obtained by the UH team and Zhang and Li

Parameter	Unit	UH	Zhang and Li	Percent Difference
G	MPa	Varies with *p*	-	-
M	-	1.51	1.13	75%
k	-	0.17	0.74	440%
μ	-	0.329	0.35 (assumed)	106%
α	-	-	0.802	-
φ_{cs}	-	37	28.38	-23.3%
φ_{peak}	-	27.6	25.84	-6.4%
c_{peak}	kPa	18.2	35.47	+195%

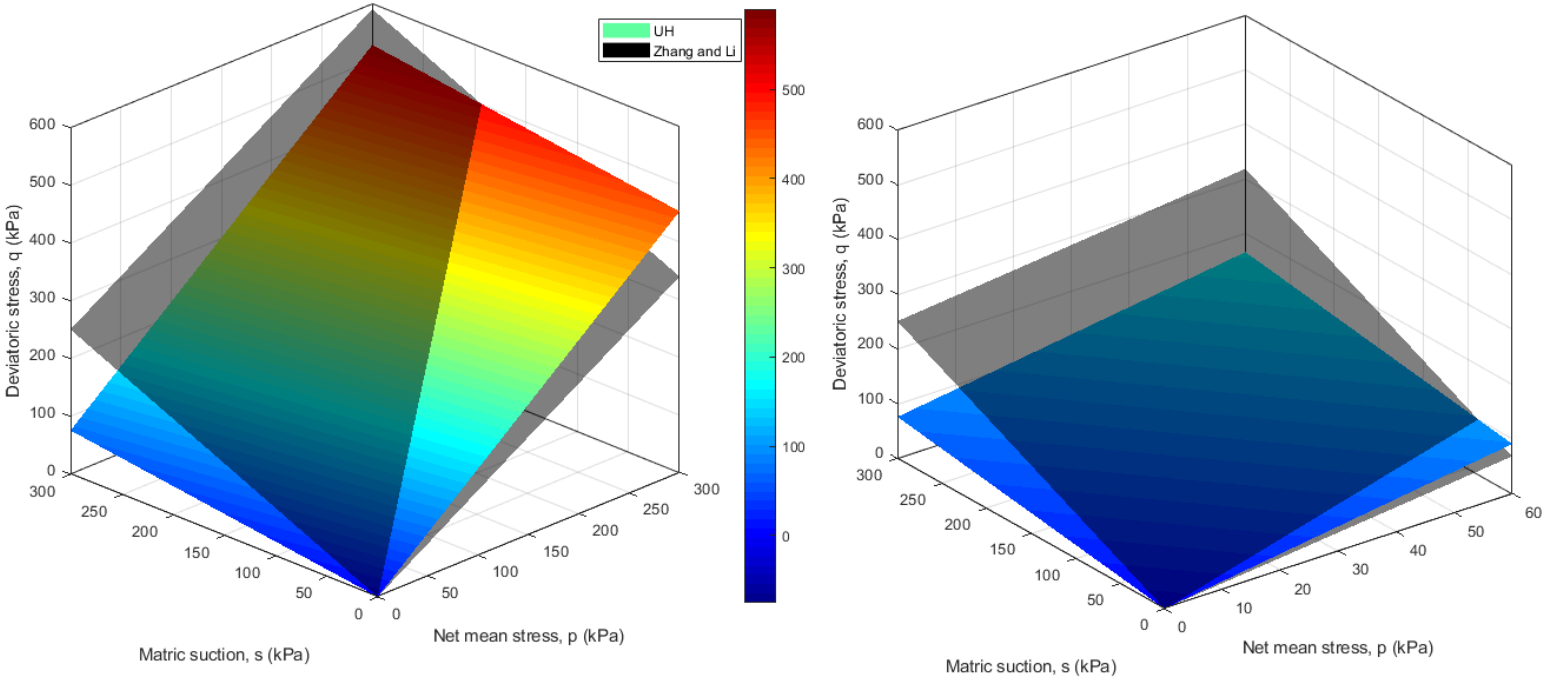

FIGURE 5.40 Comparison of q-p-s failure planes determined by Zhang and Li with those from this research

6 TRANSIENT HYDROLOGICAL FLOW MODEL

A saturated-unsaturated transient hydrological flow model was developed and calibrated for the purpose of estimating the suctions/pore water pressures in the soil slope during the design storm. As explained in Chapter 1, this model is an integral part of the landslide warning system. It has to be first calibrated to determine the appropriate parameters to use. Calibration is achieved by adjusting the model parameters to match the laboratory measured and calculated SWCC and HCF, and to match calculated and field-measured suctions and water contents. Once the model is calibrated, then it can be used to predict the pore pressures during a storm with a prescribed design return period. Return periods in transportation infrastructure design is typically based on a 100-year event. However, the return period can be justifiably increased depending on the importance of structure and consequence of failure. This slope has been in existence for many decades and may have already survived a 100-year if not higher storm. In fact, during the approximately two and a half years of monitoring, the slope experienced a storm with a 200-year return period on 10/15/2015. Since this slope abuts Kalaniana'ole Highway and since the consequence of failure is "high", it was decided to investigate the effects of a storm with a 500-year return period (= 1/500 or 0.2% annual probability of occurrence) to facilitate selection of threshold values for use in the development of a landslide warning system. Elements of this model are presented below.

6.1 Water Balance

A soil's shear strength is governed by the shear strength parameters and the pore water pressure in the soil. The pore water pressure can be positive if the soil is below the ground water table or negative if it is above the ground water table. Since the ground water table at this site is purportedly more than 40 m below the slope crest, the slope is not subject to ground water recharge from below, and water can only enter the slope naturally in the form of precipitation. A systems analysis of the water balance at the site requires that the precipitation (P), runoff (R), actual evapotranspiration (AET) and surface infiltration (SI) satisfy the following:

$$P = R + AET + SI \tag{6.1}$$

In addition, the slope is relatively barren and for all intents and purposes, transpiration can be deemed negligible; i.e.; $AET \approx AE$ = actual evaporation. Runoff is automatically calculated based on the slope geometry. Thus, only the effects of precipitation and actual evaporation need be applied to the top boundaries (ground surface) for the model to estimate SI. The method adopted for estimating AE is explained in the following section.

6.2 Actual Evaporation

While the precipitation is directly measured, actual evaporation must be estimated. Actual evaporation is calculated by HYDRUS using a mathematical scheme that mimics the stages of evaporation rather than by modelling vapor flow. The following is a summary of the mathematical scheme. Actual evaporation, which is a function of relative humidity and potential evaporation, can be estimated using the following relationship (Campbell ,1985):

$$AE = \frac{W_s - W_a}{1 - W_a} PE$$

where W_s is the relative humidity of the soil, W_a is the relative humidity of the atmosphere, and *PE* is the potential evaporation. The relative humidity of the soil is related to suction using the following relationship (Edlefson and Anderson, 1943),

$$W_S = \exp\left(\frac{M_w s}{TR\rho_w}\right)$$

where M_w is the molecular mass of water (0.018 kg/mol), *s* is the soil suction at the surface (Pa), *T* is the temperature (K), and ρ_w is the mass density of water (998 kg/m^3). There are three stages of evaporation when the soil dries from an initially saturated state; the first stage is when *AE* = *PE* and flow occurs mainly in the liquid phase, the second is when *AE* rapidly decreases from *PE* and this is when flow occurs in both liquid and vapor phases, the third stage is when the rate of decrease of *AE* starts to level off, during which flow occurs mainly in the vapor phase. Rassam and Williams (1999) showed that the maximum rate of change between stages one and two occur at a pressure head of -300 m (i.e. $W_s \approx$ 97.8%).

HYDRUS mimics the above evaporation stages by using a user-defined minimum pressure head, $h_{crit}A$, that initiates stage 2 when the boundary pressure head exceeds this value. The value of $h_{crit}A$ = -300 m was experimentally shown to trigger stage 2 by Wilson et al. (1997) regardless of soil type. An $h_{crit}A$ = -1000 m was proposed for silty soil by Simunek et al. (2006). In this research, a value of $h_{crit}A$ = -300 m (Wilson et al., 1997) was used.

Therefore, the required input for HYDRUS is $h_{crit}A$ and the potential evaporation which can be estimated with the aid of the following:

1. global solar radiation (from Hihara and Sugamoto, 2017);
2. wind speed (from Hihara and Sugamoto, 2017);
3. air temperature (from Hihara and Sugamoto, 2017);
4. relative humidity (from Hihara and Sugamoto, 2017);
5. cloud factor (from NOAA, Lott et al., 2001); and

6. albedo (from Giambelluca et al., 2014)

and utilizing Kohler and Parmele's (1967) modification of Penman's (1948) equation (as shown in Dingman, 2008). After a process of trial and error involving several other methods of estimating *PE*, it was found that this method worked best for this site and their expression for *PE* is as follows:

$$PE = \frac{\Delta\left(K + L^{'} - G\right) + \gamma^{'} K_E \rho_w v_a e_a^* (1 - W_a)}{\rho_w \lambda_v \left(\Delta + \gamma^{'}\right)} \tag{6.2}$$

where

Δ = slope of saturation vapour-temperature curve = $\frac{2508.3}{(T_a+237.3)^2} \exp\left(\frac{17.3T_a}{T_a+237.3}\right)$ [kPaK^{-1}] (6.3)

K = net shortwave radiation $= (1 - \alpha)K_{global}$ (6.4)

L' = adjusted net longwave radiation $= \varepsilon_s \sigma (1 - \varepsilon_{at})(T_a + 273.2)^4$ (after Kohler and Parmele, 1967 as shown in Dingman, 2008) (6.5)

G = soil heat flux = *0.2(K+L')* (after Fuchs and Hadas, 1972, Idso et al., 1975 and Novak and Black, 1983) (6.6)

γ' = adjusted psychrometric constant $= \frac{c_a p_a}{0.622\lambda_v} + \frac{4\varepsilon_s \sigma (T_a+273.2)^3}{K_E \rho_w \lambda_v v_a}$ (after Kohler and Parmele, 1967 as shown in Dingman, 2008) (6.7)

K_E = atmospheric constant $= \frac{0.622\rho_a}{p_a \rho_w} \frac{V^2}{\left[\ln\left(\frac{zm}{z_0}\right)\right]^2}$ (6.8)

ρ_w = mass density of water [kgm^{-3}]

v_a = measured wind speed [ms^{-1}]

e_a* = saturation vapour pressure [kPa] = $0.611 \exp\left(\frac{17.3T_a}{T_a+237.3}\right)$ (after Monteith and Unsworth, 2008) (6.9)

W_a = measured relative humidity

λ_v = latent heat of vaporization [Jkg^{-1}] = $2.5 \times 10^6 - 2370T_a$ (6.10)

T_a = measured air temperature [°C]

α = albedo (site-specific monthly values taken from Giambelluca et al., 2014)

K_{global} = measured global solar radiation [Wm^{-2}]

ε_s = soil emissivity = $\min(0.9 + 0.18\theta; 1)$ (after van Bavel and Hillel, 1976) (6.11)

σ = Stefan-Boltzmann constant = 5.67×10^{-8} Wm^{-2}K^{-4}

ε_{at} = atmospheric emissivity = $1.72\left(\frac{W_a e_a^*}{T_a+273.2}\right)^{1/7}$ (after Brutsaert, 1975 as shown in Dingman, 2008)

(6.12)

c_a = heat capacity of air = 1×10^{-3} MJkg^{-1}K^{-1}

$p_a(z)$ = atmospheric air pressure at elevation, z [kPa] = $101.32\left(\frac{293-0.0065z}{293}\right)^{5.26}$ (after Burman et al., 1987)

(6.13)

ρ_a = mass density of air = $\frac{p_a}{0.288T_a}$ kgm^{-3}

V = von Karman constant typically = 0.4 (after Dingman, 1980)

z_m = height at which air temperature, relative humidity, and wind speed were measured = 2 m

z_0 = roughness height = 1.1 x 10^{-3} m for bare soil (after Chow et al., 1988)

θ = measured volumetric water content near the surface

The calculated *PE* is shown in Figure 6.1a.

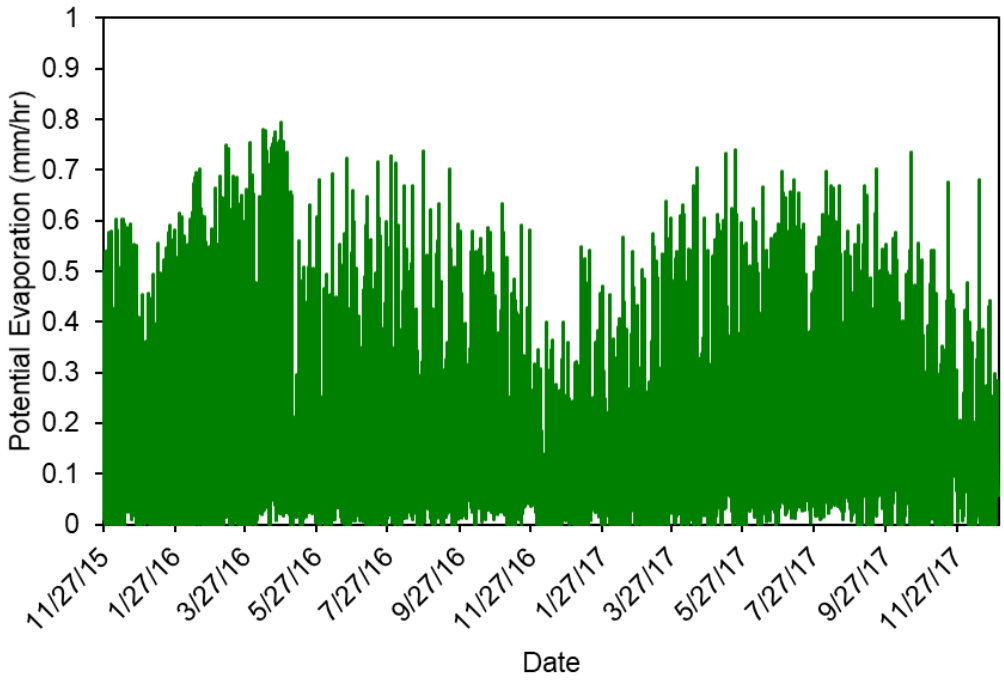

(a)

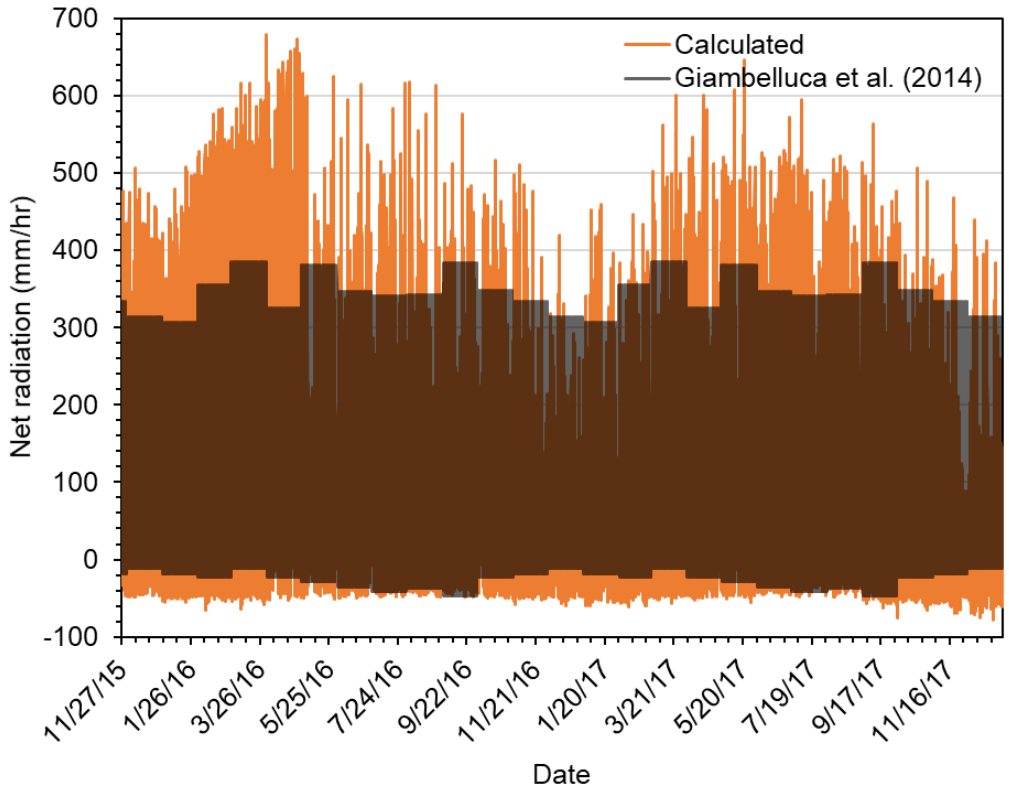

(b)

FIGURE 6.1 (a) Potential evaporation estimated using Kohler and Parmele's (1967) modification of Penman's (1948) equation and (b) estimated net radiation using equations 6.4, 6.5 and 6.6 = K+L'-G compared with net radiation reported by Giambelluca et al. (2014) at the slope site

Giambelluca et al. (2014) provided estimates of monthly, monthly-hourly, and annual-hourly evapotranspiration maps for Hawaii. The calculated net radiation = $K + L' - G$ is compared to the monthly-hourly net radiation at the slope site from Giambelluca et al. (2014) in Figure 6.1b. The calculated shortwave radiation is subject to errors due to the presence of trees and other vegetation in other areas of the slope, however an R^2 of 71.2% was estimated between the calculated and Giambelluca et al. (2014) values.

It should be noted that global solar radiation, wind speed, air temperature and relative humidity were obtained from Hihara and Sugamoto (2017), who are with the University of Hawaii's Department of Mechanical Engineering, and their data cannot be readily accessible by the general public. Alternatively, a similar set of such data can be downloaded from a weather station on Coconut Island (Hawaii Institute of Marine Biology). However, it was found that for the period of this research, the Coconut Island data is sporadic with missing gaps. This is why, the Hihara and Sugamoto (2017) data was adopted for this study.

6.3 Governing Differential Equation for Saturated-Unsaturated Transient Flow

The governing differential equation for the problem of water flow through an isotropic unsaturated soil is Richards's equation (1931), which is based partially on Darcy's law and is given as follows:

$$\frac{\partial}{\partial x}\left(k\frac{\partial h}{\partial x}\right)+\frac{\partial}{\partial y}\left(k\frac{\partial h}{\partial y}+1\right)=\frac{\partial \theta}{\partial t} \quad (6.14)$$

where k = unsaturated soil hydraulic conductivity, θ = volumetric water content, h = pressure head (m) and x and y are Cartesian coordinates in the x- and y-directions, respectively. The pressure head is the primary unknown in Eq. 6.14. Note k, θ and h are all functions of matric suction.

Solving Equation 6.14 will yield the pressure head (which can be converted to matric suction) and the volumetric water content at any (x, y) coordinate in the domain. It should be noted that this analysis completely ignores the effects of enthalpy (thermodynamic quantity equivalent to the total heat content of a system) in the porous media. This may be reasonable for Hawaii where the temperature extremes are not significantly different and where the soil temperature is fairly constant. In addition, the effects of temperature and solar radiation are embodied in the estimate for potential evaporation.

6.4 Geometry

Both 1D and 2D models of the slope were analysed to estimate the effects of precipitation, runoff, potential evaporation and surface infiltration on the pressure head, which will affect the pore water pressures, effective stresses and strength of the soil in the slope.

6.4.1 1D Model

A 1D model was analysed as a first approximation. It was deemed reasonable to analyse the slope crest as a 1D model because the 4-m-wide crest ledge is nearly horizontal (i.e.; assume surface runoff due to rain falling on the ledge is negligible; i.e.; R = 0, meaning that the precipitation on the ledge undergoes evaporation and surface infiltration only) and because the instruments are set back at a fairly long distance from the slope crest. As seen from the mesh in Figure 6.2, more elements were provided at shallow depths, which is the area of interest.

Even though a rectangle is strictly a 2D model, the analysis is effectively 1D due to the use of the following boundary conditions:

1. Top boundary – assume atmospheric conditions where precipitation (Figure 4.5) and potential evaporation (Figure 6.1) are defined on an hourly basis.
2. Bottom boundary – assume a constant head of 5.8 m at El. 0 (Engott et al., 2015).
3. Left and right boundaries – no flux.

The antecedent pressure heads from tensiometer data were input as initial conditions over the top 6.1 m. From a depth of 6.1 m to El. 0, the pressure heads were obtained by linear interpolation.

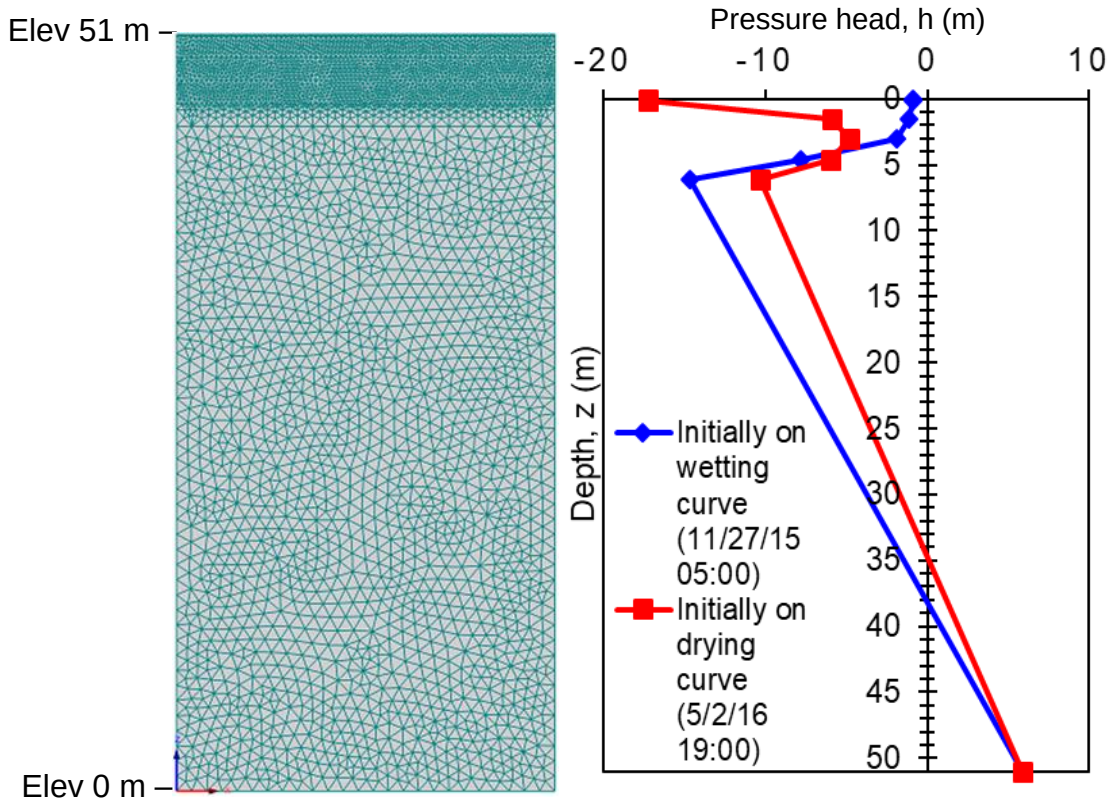

FIGURE 6.2 1D finite element mesh for saturated-unsaturated transient flow model and initial pressure head profile

6.4.2 2D Model

The mesh for a 2D model is shown in Figure 6.3. The initial pressure head profile (Figure 6.4) below the ground surface generally mimics the values in the 1D model (Figure 6.2) over the top 6.1 m. The initial heads were then linearly interpolated from a depth of 6.1 m to El. 0, which has a head of 5.8 m. In Figure 6.4, the deeper head contours appear jagged probably because of an inadequate kriging routine in HYDRUS, the software used to solve Richards's equation in this work. However, these anomalies are not critical because they lie outside the area of interest (top 4 m).

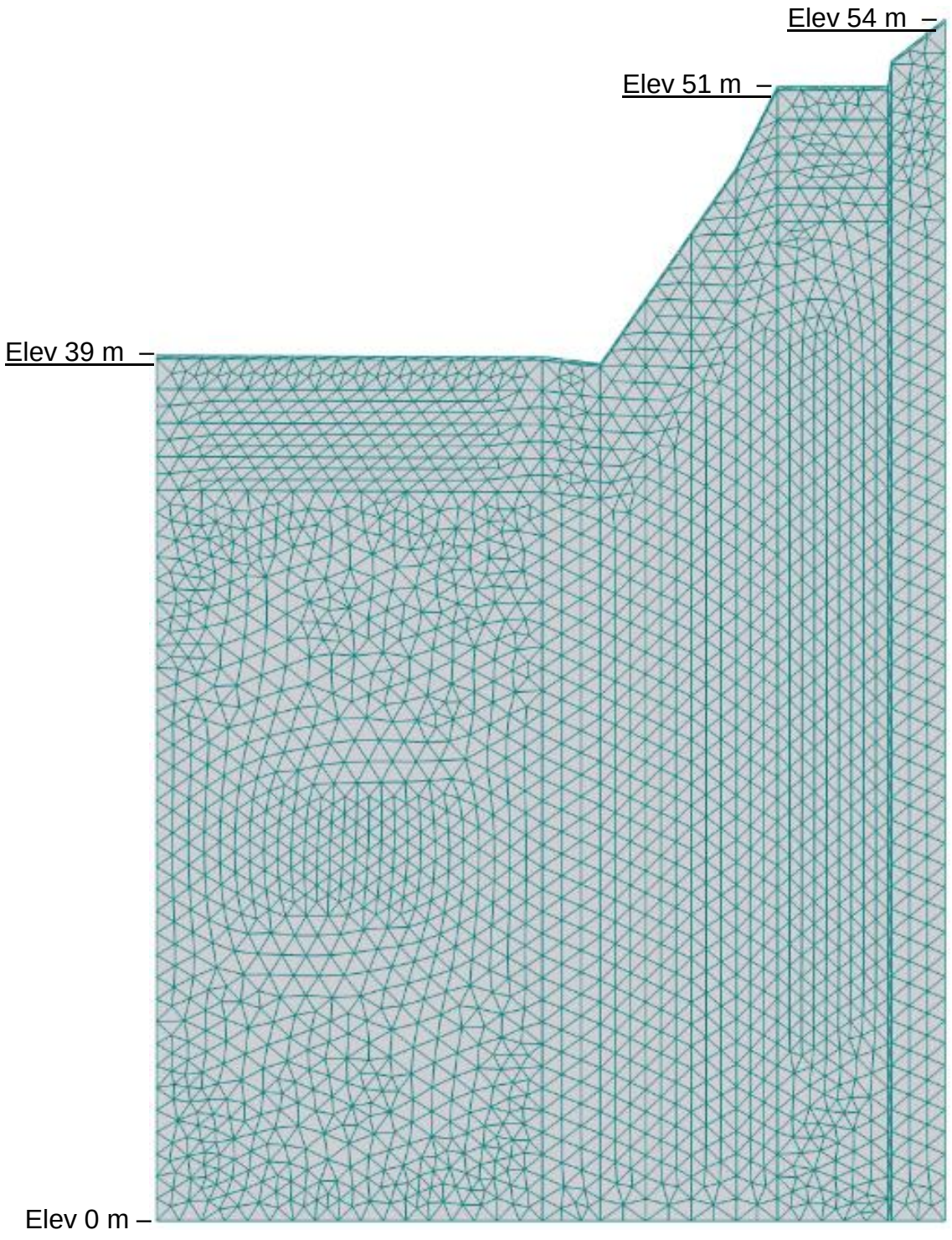

FIGURE 6.3 2D finite element mesh for saturated-unsaturated transient flow model

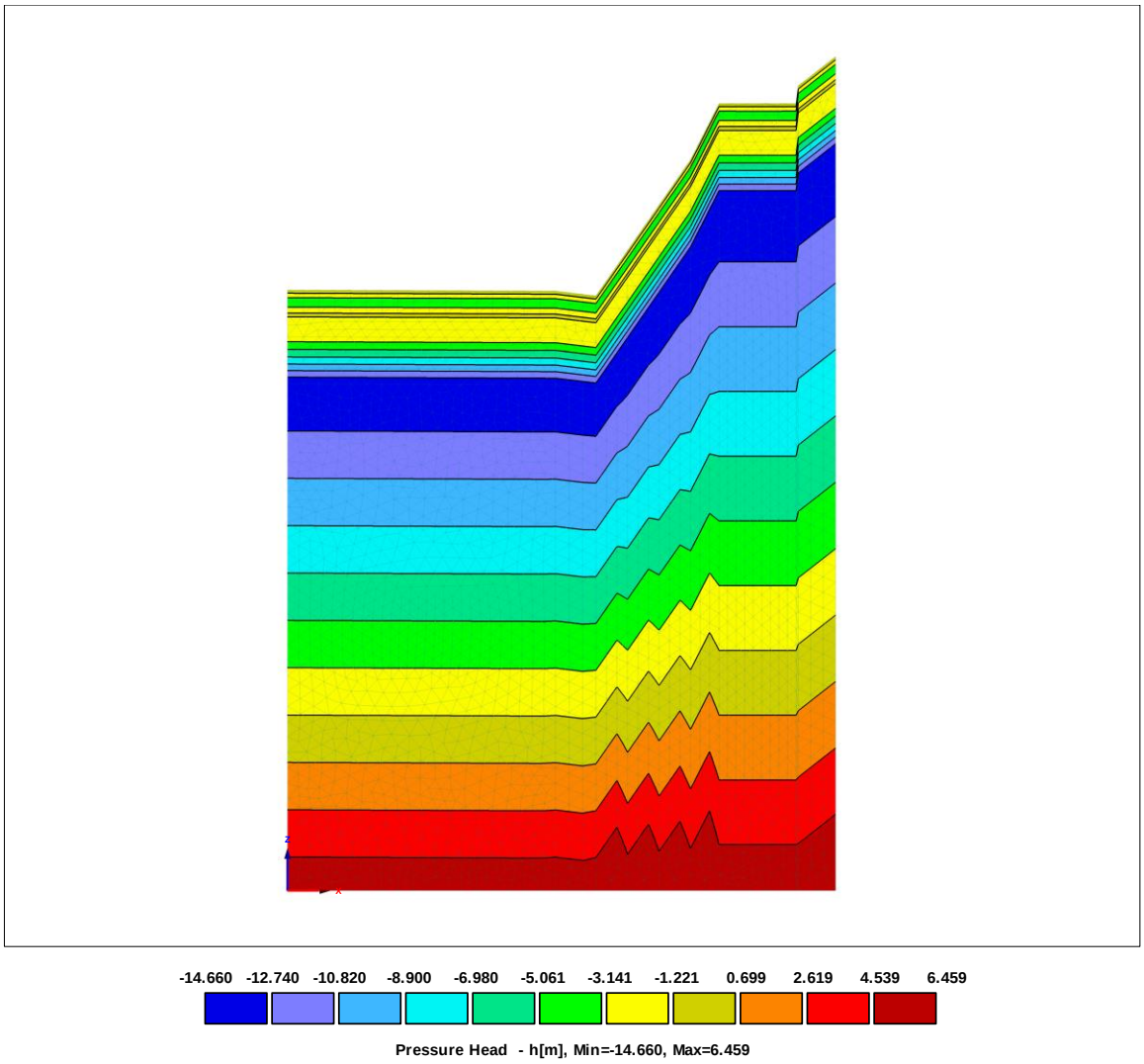

FIGURE 6.4 Initial pressure head contours for 2D finite element analysis of saturated-unsaturated transient flow

The boundary conditions are essentially identical to the 1D analysis as follows:

1. Top boundary – assume atmospheric conditions where precipitation (Figure 4.5) and potential evaporation (Figure 6.1) are defined on an hourly basis.
2. Bottom boundary – assume a constant head of 5.8 m at El. 0 (Engott et al., 2015).
3. Left and right boundaries – no flux.

6.5 Model Calibration

Steps in the calibration process are summarized in Figure 6.5. To the author's knowledge, HYDRUS (Simunek et al., 2006) is the only commercial software that allows for hysteresis in the SWCC and HCF. If say a soil starts off at a point on the drying curve of the SWCC prior to a rain event, then when the soil is wetted, the suction path will run along a scanning curve between the main drying and

main wetting branches. This is a fundamentally important behaviour that needs to be captured when calibrating the model.

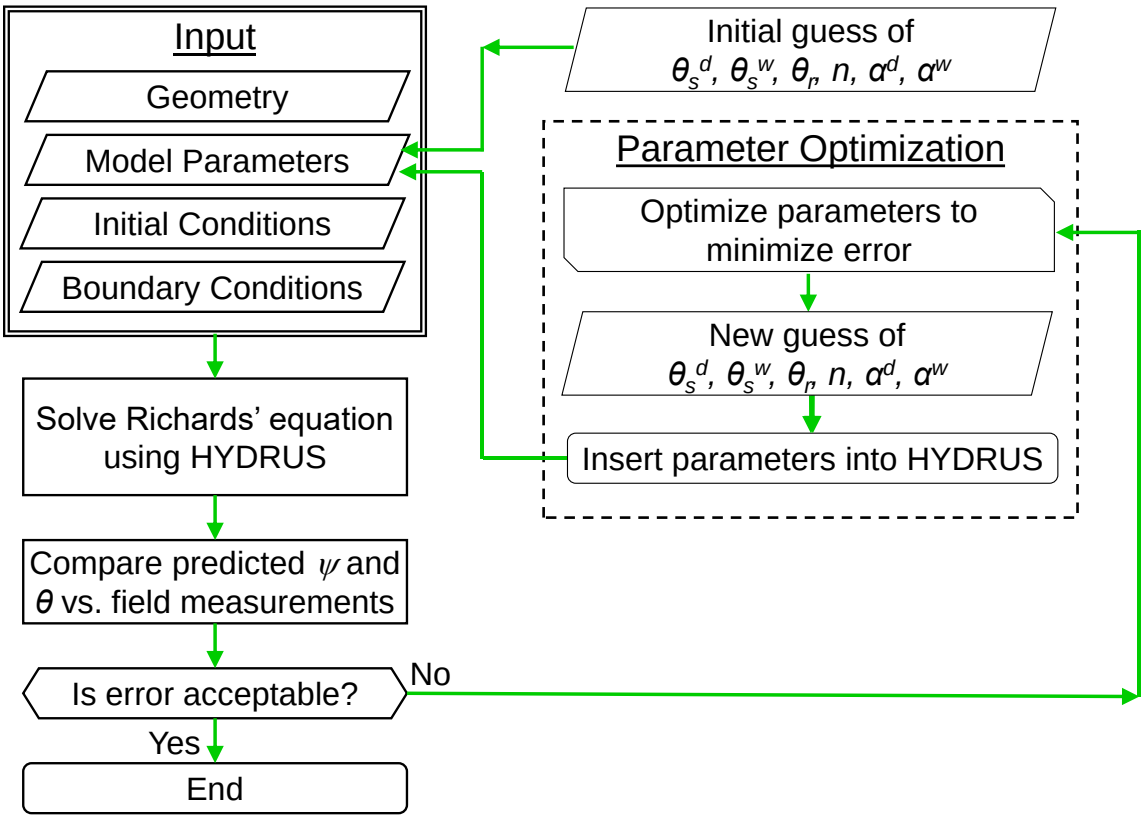

FIGURE 6.5 Flow chart for calibration process

Before discussing the calibration steps, the van Genuchten models for the SWCC and HCF are first presented. The van Genuchten (1980) equation that is applicable to both the main drying and main wetting branches of the SWCC is as follows:

$$\theta(h) = \theta_r + \frac{\theta_s - \theta_r}{[1+(\alpha\psi)^n]^m} \tag{6.15}$$

where θ = volumetric water content, θ_r = residual volumetric water content, θ_s = saturated volumetric water content, ψ = matric suction, α and n are van Genuchten parameters and m = 1 - 1/n. The physical meaning of α and n are as follows: α is a measure of the matric suction at which the pore fluid begins to leave a drying soil and in fact it is the inverse of the air entry pressure, whereas the parameter n is an indicator of the pore size distribution of the soil. The reader is referred to the HYDRUS manual (Simunek et al., 2006) for the mathematical formulation of the scanning curves.

Also, the van Genuchten equation in terms of relative hydraulic conductivity (k_{rel}) that is applicable to both the main drying and main wetting branches of the HCF is as follows:

$$K_{rel} = \frac{K(h)}{K_s} = \frac{\left[1-|\alpha h|^{n-1}(1+|\alpha h|^n)^{\frac{1}{n}-1}\right]^2}{(1+|\alpha h|^n)^{\frac{1}{2}\left(1-\frac{1}{n}\right)}} \quad (6.16)$$

where k = hydraulic conductivity of the unsaturated soil, k_s = hydraulic conductivity of the saturated soil and all other parameters have been previously defined. HYDRUS restricts θ_r and n to be the same for drying and wetting; i.e.; $\theta_{rd} = \theta_{rw}$ and $n_d = n_w$. Other restrictions include $\alpha_d \leq \alpha_w$, $k_{sw} \leq k_{sd}$, $\theta_{sw} \leq \theta_{sd}$ and $n > 1$. Since the saturated hydraulic conductivity was measured from a consolidation test, $k_{sw} = k_{sd} \approx 10^{-6}$ cm/s was used unless otherwise noted. This leaves the following 6 parameters to be determined to fully define the drying and wetting SWCC and HCF: α_d, α_w, θ_{sd}, θ_{sw}, θ_r and n.

The saturated-unsaturated transient flow model was calibrated by optimizing these 6 parameters so that:

1. The lab-measured and van Genuchten volumetric water contents on the drying and wetting branches of the SWCC match closely;
2. The lab-measured and van Genuchten relative permeabilities on the drying and wetting branches of the HCF curves match closely; and
3. The field-measured and HYDRUS matric suction and water contents match closely. Initial attention is paid to matching the water content sensor and tensiometer at a depth of 0.5 ft utilizing the same SWCC and HCF constant throughout the entire slope. Eventually, the goal is for HYDRUS to match the responses of all water content sensors and tensiometers.

The first two matches can be achieved relatively easily but for all 3 to match requires a process of trial and error as shown in Figure 6.5. As discussed previously, the wetting and drying episodes in the field usually run along the scanning curves. So in essence, the calibration process involves finding 6 parameters that gives the optimum drying and wetting curves for the lab SWCC and HCF and the scanning curves for the field.

Based on the HYDRUS results at a depth of 0.5 ft, the calibrated van Genuchten parameters for the soil at this site are summarized in Table 5-1 below:

Table 6-1 Calibrated van Genuchten parameters

Parameter	Unit	Best-fit
θ_{sd}	-	52.25%
θ_{sw}	-	52.25%
θ_r	-	0
α_d	m^{-1}	0.14
α_w	m^{-1}	1
$n_d = n_w$	-	1.15

Before discussing the field results, a comparative discussion of the lab-measured versus van Genuchten SWCC and HCF curves is first warranted. From Figure 5.16, the parameters were selected

such that the van Genuchten SWCC fits the PP data well but the accuracy was sacrificed for the VSA data. This is deemed reasonable because the field-measured suctions were all less than 7 bars while the lowest suction measured using the VSA was 75 bars. The data points in Figure 5.17 represent the HCF that was derived by applying the analytical method of Kunze et al. (1968) on the SWCC data while the solid lines represent the HCF using the van Genuchten model. Overall, the van Genuchten HCF fit is quite reasonable.

6.5.1 1D Results

Figure 6.6 compares the field-measured and calculated matric suction vs time and volumetric water content vs time. Calculated values were derived using HYDRUS assuming the following 3 scenarios:

1. Use of SWCC and HCF along the drying branch only with no scanning allowed;
2. Use of SWCC and HCF along the wetting branch only with no scanning allowed; and
3. Use of SWCC and HCF with scanning allowed.

Figure 6.6 shows the importance of scanning between the drying and wetting branches. Tsai (2010) showed that it is important to consider hysteresis in the SWCC when modeling rainfall-induced landslides based on a case history in Taiwan. He demonstrated that using the main drying branch alone led to an underestimation of the factor of safety against landslide occurrence. When no scanning is allowed, the drying branch will over-predict suctions and volumetric water contents while the wetting branch has a tendency to under-predict especially the volumetric water contents. However, the analysis that allows scanning offers the most reasonable agreement with the field measured values overall in terms of both matric suction and volumetric water content. The reason for this can be best illustrated with the aid of the volumetric water content-suction path (henceforth referred to as the field suction path) taken by the soil during the various drying-wetting events (see Figure 6.7). The field suction path can be constructed by plotting the field response of a tensiometer and the corresponding water content sensor at the same depth (0.15 m in this case). For best visual effect, it should be superimposed on the lab SWCC main wetting and main drying curves. In early May 2016, the soil was initially very dry (θ = 0.45 in Figure 6.6b) and the suctions were high (s = 160 kPa in Figure 6.6a). A rainfall episode then caused the suctions to drop dramatically (from 160 kPa to 9 kPa, which is the lowest suction measurable by the tensiometer). Subsequent drying-wetting events caused the field SWCC to scan rather than travel along the main drying or main wetting branches as seen by the black circular symbols. The green lines in Figure 6.7 represent the field suction paths calculated by HYDRUS if scanning is allowed, while the red and blue lines represent the HYDRUS-calculated field suction paths for the main drying and main wetting SWCC branches, respectively if scanning is disallowed. Therefore, these results confirm that:

1. A field suction path can be drawn by plotting tensiometer and the corresponding water content sensor readings over several drying-wetting events;

2. The field suction path usually runs along a scanning curve except during periods of heavy rain or extreme drought when the field suction path could join up and run along the wetting or drying branches, respectively. It should be noted that in Figure 6.7, excursions of the field suction path did occur beyond the wetting branch during a rain event. This is probably because the backfill around the top tensiometer is silica sand, which is more permeable than the native soil. It is probable that the tensiometer reacted to the presence of water quicker than the water content sensor, which has three prongs embedded in the native MH soil. However, the other deeper tensiometer readings should correctly reflect the suctions in the native soil instead of the silica sand because these tensiometers are surrounded by the native soil, whose suction governs the value measured;
3. It is important for a saturated-unsaturated transient flow model to allow for scanning in order to predict field behavior reliably;
4. If scanning is not allowed, the calculated field suction path will run along the main drying or main wetting branches only depending on which is specified. Doing so will result in over-estimated suctions and water contents when the SWCC and HCF are specified for the drying branch only. Conversely, use of the wetting branch only will yield under-predicted suctions and water contents; and
5. HYDRUS allows the user to begin an analysis on one of either the main drying branch (i.e.; during a period of extreme drought) or the main wetting branch (i.e.; during a period of extreme rain). It will not allow an analysis to begin on a scanning curve. Hence, the starting point was chosen at the end of a drought period when using the main drying branch in the analysis. Conversely, the analysis was started after a period of heavy rain when analyzing using the main wetting branch.

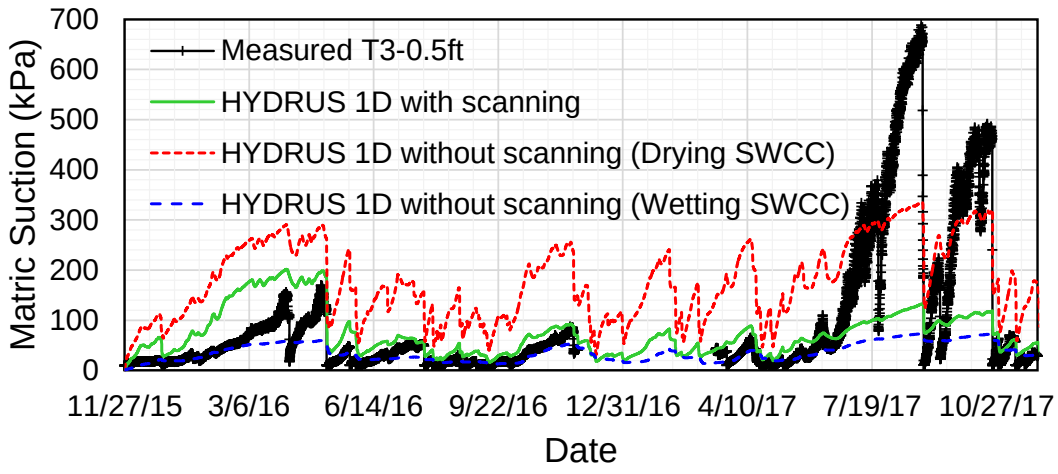

(a)

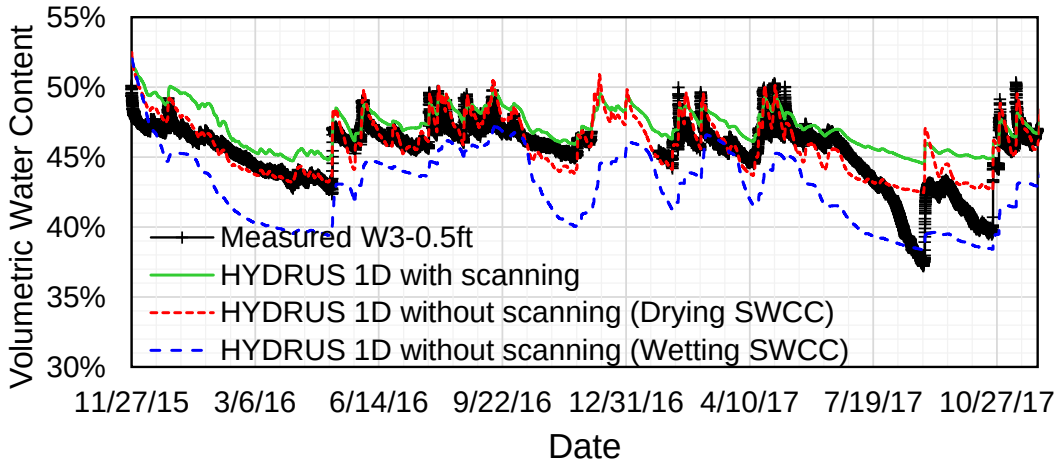

(b)

FIGURE 6.6 Measured vs 1D HYDRUS-derived assuming a constant SWCC and HCF throughout (a) matric suction vs time and (b) volumetric water content vs time at depth of 0.15 m (0.5 ft)

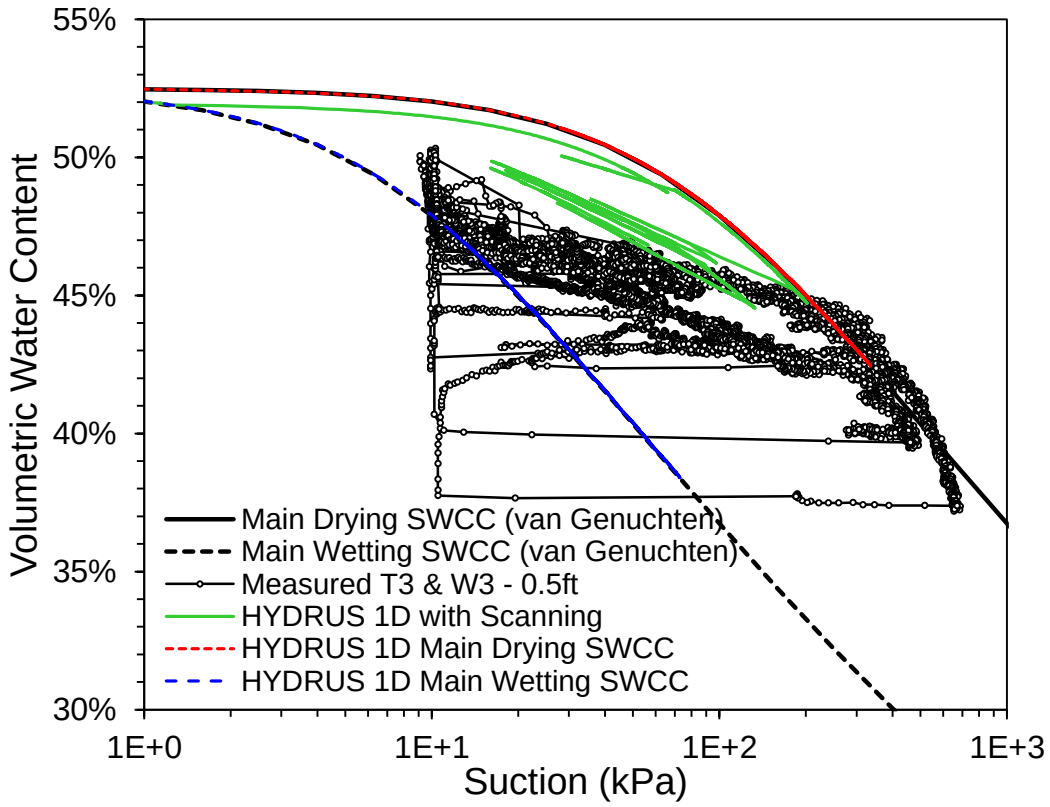

FIGURE 6.7 Measured vs 1D HYDRUS-derived field stress paths along the scanning portion of the SWCC at depth of 0.15 m (0.5 ft) assuming a constant SWCC and HCF throughout

Only instruments from W3 and T3 are considered in this research because these readings make more sense than those from W2 and T2. With W2 and T2, the field suction path at 0.15 m (0.5 ft) plotted to the right of the main drying branch of the SWCC instead of the left. Also, the correlation coefficients between the measured and calculated water content and suction at the W2 and T2 instruments are less than those at W3 and T3.

The volumetric water content and suctions calculated at other depths are also compared to measured values in Figs. 6.8 through 6.12. Despite having a good match at a depth of 0.15 m (0.5 ft), it was observed that the calculated values at larger depths did not match the measured field values as well. In fact, the calculated values at larger depths are not as "reactive" as the field values. At first, it was thought that this may have been due to the presence of desiccation cracks in the surficial soils allowing moisture to infiltrate deeper quicker. To create a response in the calculated values at larger depths, the saturated hydraulic conductivity of the soil below a depth of 0.15 m was artificially increased from 10^{-6} cm/s to 10^{-4} cm/s. Despite the increase in calculated response, the calculated values are still not as reactive as the field-measured values at larger depths.

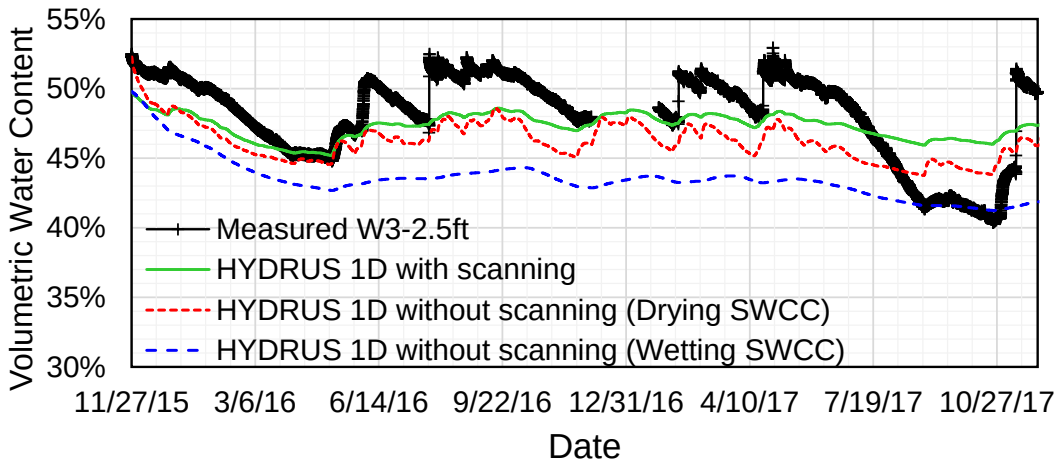

FIGURE 6.8 Measured vs 1D HYDRUS-derived volumetric water content vs time at depth of 0.76 m (2.5 ft) assuming a constant SWCC and HCF throughout

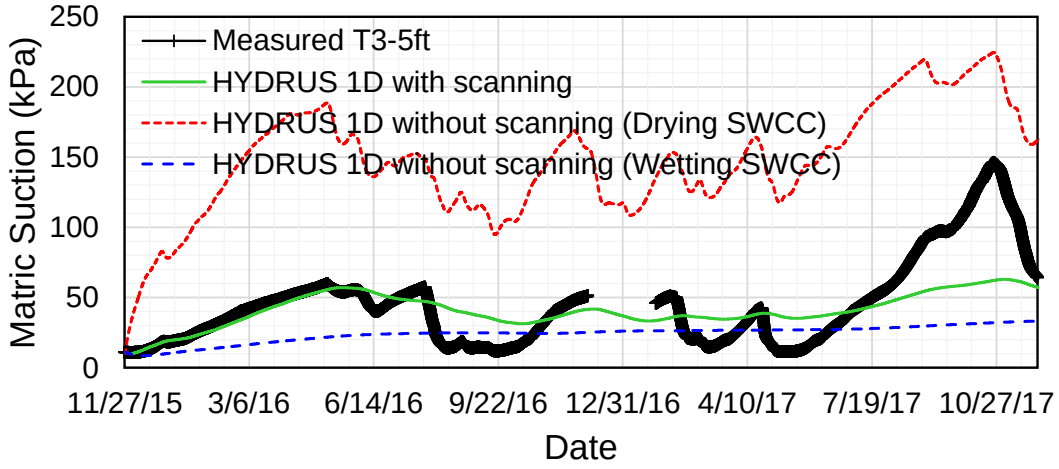

FIGURE 6.9 Measured vs 1D HYDRUS-derived matric suction vs time at depth of 1.52 m (5 ft) assuming a constant SWCC and HCF throughout

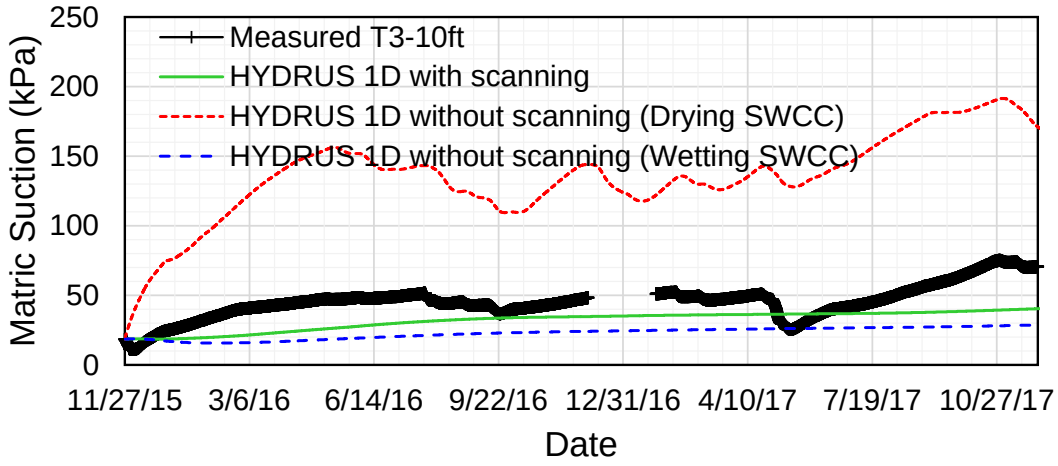

FIGURE 6.10 Measured vs 1D HYDRUS-derived matric suction vs time at depth of 3.05 m (10 ft) assuming a constant SWCC and HCF throughout slope geometry

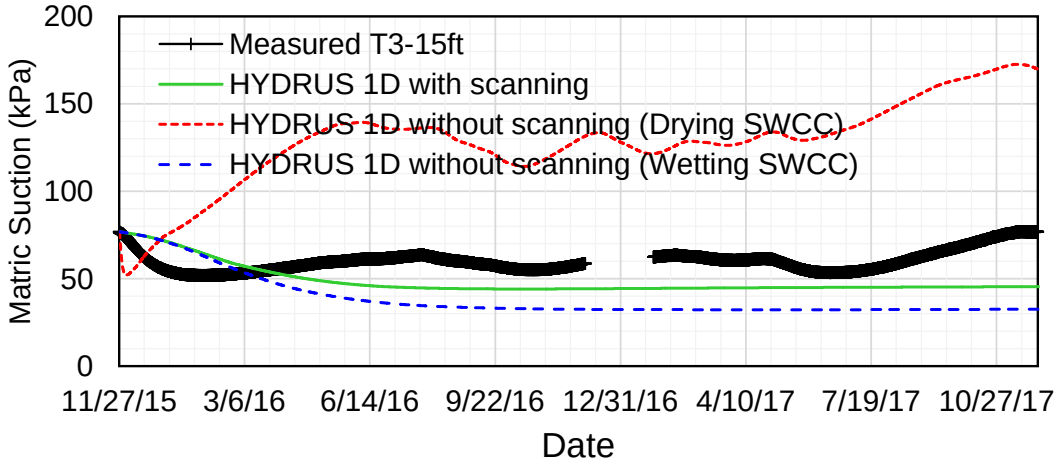

FIGURE 6.11 Measured vs 1D HYDRUS-derived matric suction vs time at depth of 4.57 m (15 ft) assuming a constant SWCC and HCF throughout

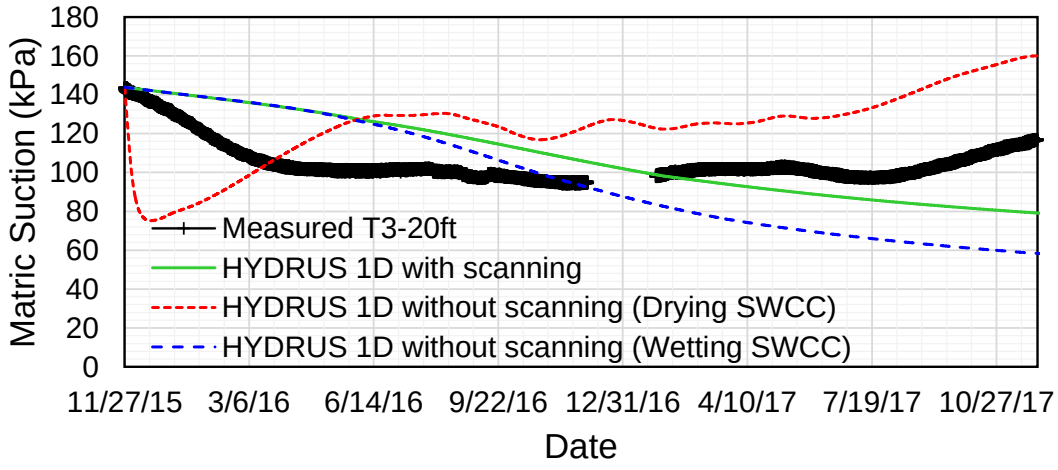

FIGURE 6.12 Measured vs 1D HYDRUS-derived matric suction vs time at depth of 6.1 m (20 ft) assuming a constant SWCC and HCF throughout

6.5.2 2D Results

The 2D geometry allows runoff to occur that is neglected in the 1D analysis. Now recognizing the importance of scanning, the first part of this section presents 2D analysis results using a single SWCC applied to the entire soil slope. However, as it will be shown, use of a porosity- or pressure-dependent SWCC is critical to achieve a good match between the calculated results and measured field data. The pressure-dependent SWCC was determined earlier using BBM stiffness parameters and the van Genuchten model with parameters that are expressed as a function of porosity as discussed in Section (5.1.4.2.1). Therefore, the second part of this section presents the calibration results using porosity-dependent SWCC.

6.5.2.1 **2D Calibration with Porosity-Independent SWCC**

HYDRUS-calculated suctions and volumetric water content versus time for the 2D slope geometry are compared with the 1D results at a depth of 0.15 m in Figs. 6.13a and 6.13b, respectively for the case where scanning is permitted. Correlation coefficients between the calculated and measured suction and volumetric water content values are shown in Table 6.1.

Table 6-2 Correlation coefficients between calculated and measured suctions and volumetric water contents

Depth (m)	Analysis	Suction	Volumetric Water Content
0.15	1D	0.430	0.805
	2D	0.807	0.762
0.76	1D	-	0.807
	2D	-	0.909
1.52	1D	0.791	-
	2D	0.876	-
3.05	1D	0.648	-
	2D	0.659	-
4.57	1D	0.157	-
	2D	0.109	-
6.10	1D	0.426	-
	2D	0.378	-

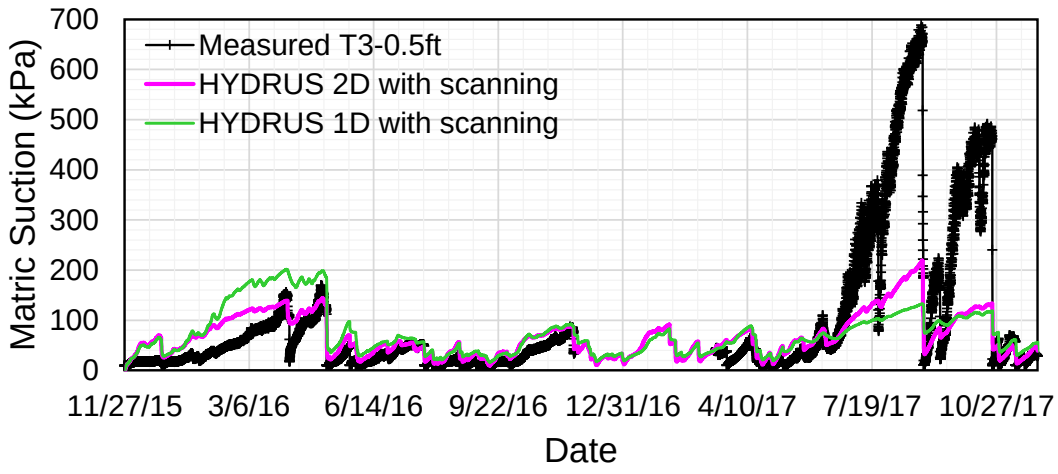

(a)

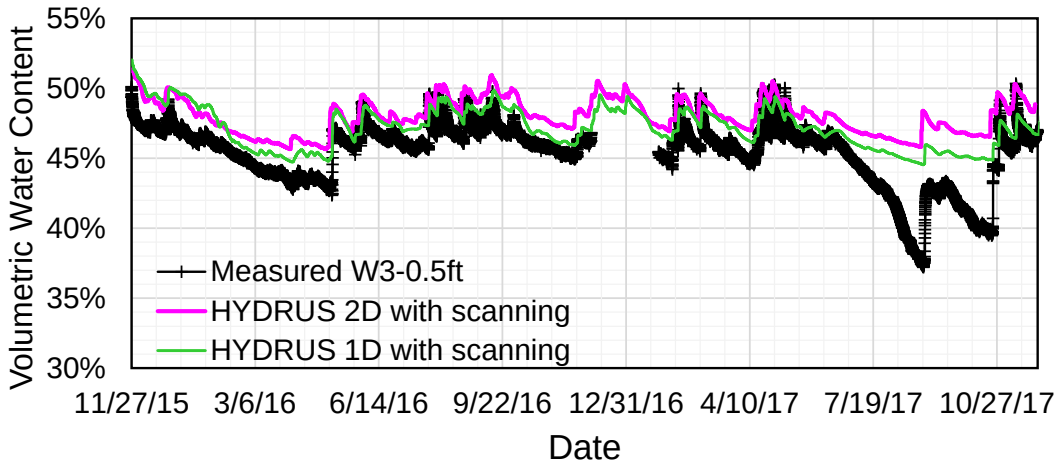

(b)

FIGURE 6.13 Measured vs 2D HYDRUS-derived (a) matric suction vs time and (b) volumetric water content vs time at a depth of 0.15 m (0.5 ft) assuming a constant SWCC and HCF throughout slope geometry

Based on the 0.15-m correlation coefficients alone, it can be seen that the 2D analysis results in a significant improvement in the volumetric water content prediction over the 1D analysis whereas the 1D and 2D suctions are both reasonably well correlated. Including results at other depths, the 2D analysis is overall better at 4 sensor locations while the 1D is better at 3. These results suggest that the 1D analysis is not unreasonable. However, the advantage of performing the 2D analysis is that it is more rational and also the 2D analysis allows for suction contours to be generated throughout the slope geometry for use in slope stability analysis (Chapter 7).

Figure 6.14 presents a comparison of the field suction path with those calculated from both 1D and 2D HYDRUS analyses. As expected, the 1D and 2D HYDRUS-derived scanning curves are very similar. The 2D scanning curves do contain excursions beyond the lab SWCC main drying branch. This is probably because of an aberration in the scanning algorithm and is not a real property of the soil. The scanning algorithm utilizes a scaled version of the main drying and wetting curves whereby it assigns a fictitious θ_s for the drying scanning curve and a fictitious θ_r for the scanning wetting curve that can cause these excursions to occur.

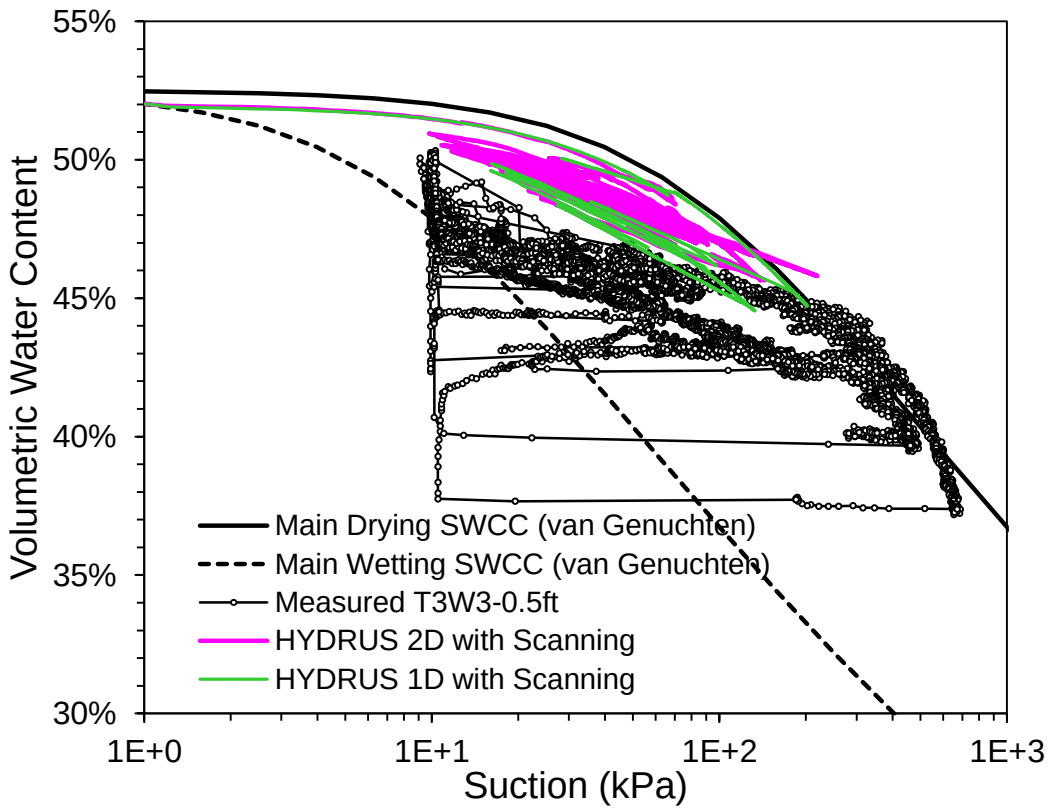

FIGURE 6.14 Measured vs 2D HYDRUS-derived field stress paths along the scanning portion of the SWCC assuming a constant SWCC and HCF throughout slope geometry

The volumetric water content and suctions calculated at other depths are also compared to measured values in Figs. 6.15 through 6.19.

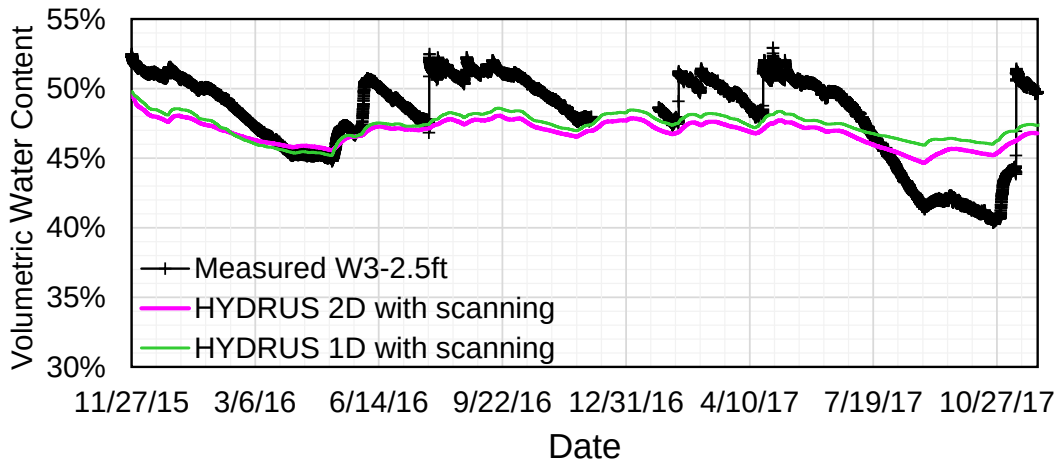

FIGURE 6.15 Measured vs 1D and 2D HYDRUS-derived volumetric water content vs time at depth of 0.76 m (2.5 ft) assuming a constant SWCC and HCF throughout slope geometry

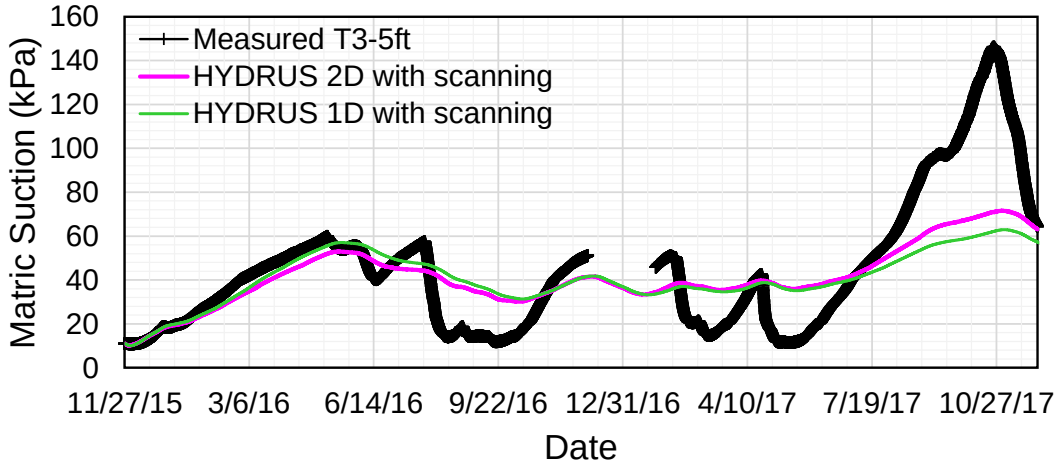

FIGURE 6.16 Measured vs 1D and 2D HYDRUS-derived matric suction vs time at depth of 1.52 m (5 ft) assuming a constant SWCC and HCF throughout slope geometry

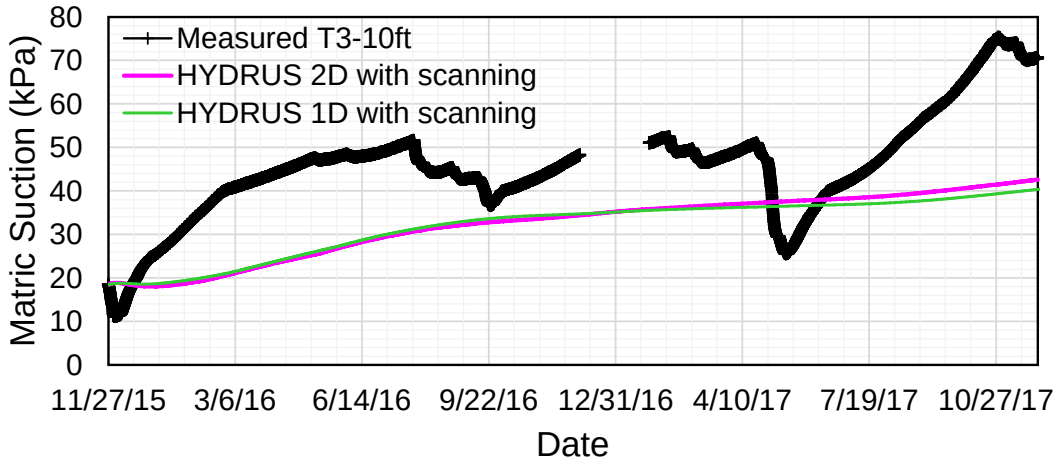

FIGURE 6.17 Measured vs 1D and 2D HYDRUS-derived matric suction vs time at depth of 3.05 m (10 ft) assuming a constant SWCC and HCF throughout slope geometry

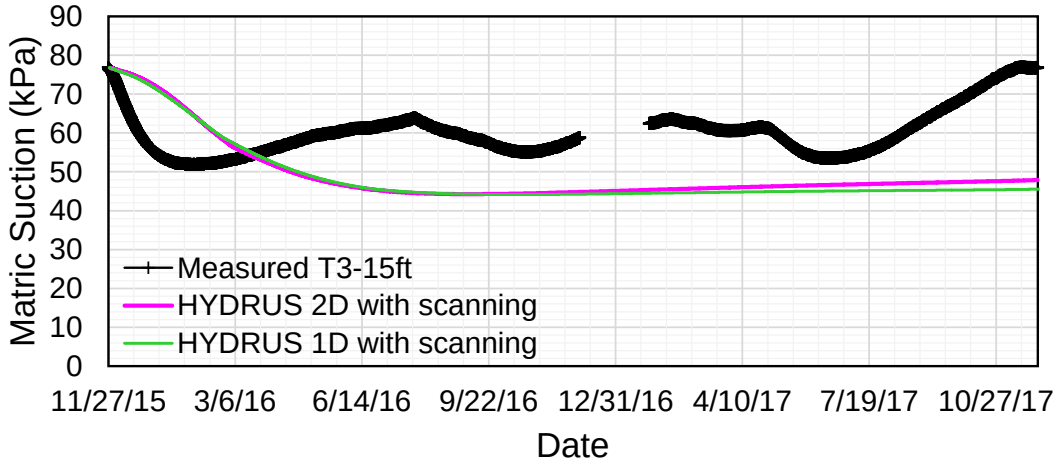

FIGURE 6.18 Measured vs 1D and 2D HYDRUS-derived matric suction vs time at depth of 4.57 m (15 ft) assuming a constant SWCC and HCF throughout slope geometry

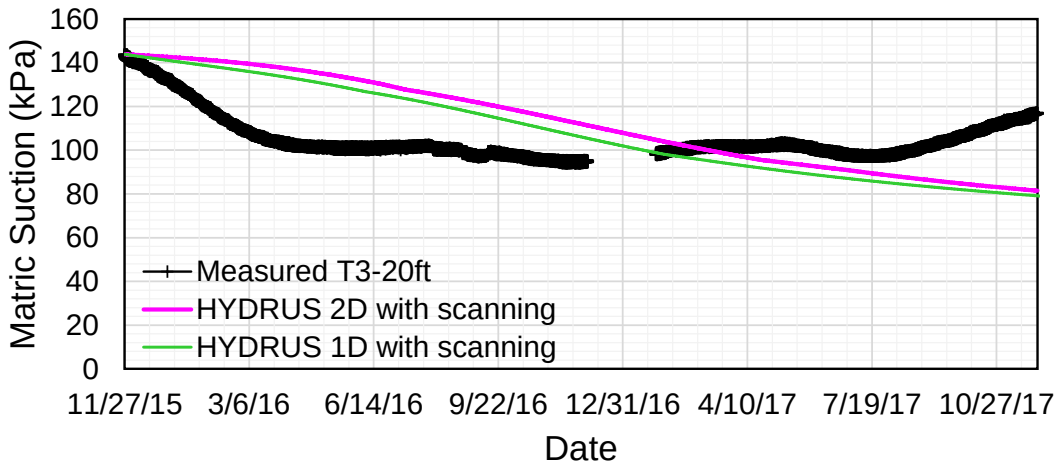

FIGURE 6.19 Measured vs 1D and 2D HYDRUS-derived matric suction vs time at depth of 6.1 m (20 ft) assuming a constant SWCC and HCF throughout slope geometry

6.5.2.2 **2D Calibration using Porosity- or Pressure-Dependent SWCC**

Once again, while the predictions at 0.5 ft are reasonably good, the same cannot be said for the predictions at larger depths. This can be explained as follows. In reality, the SWCC is affected by confining stress (Ng and Pang, 2000; Assouline, 2006). As seen in Figure 6.20, increasing confining stress has a tendency to "squash" or "pancake" the SWCC. This implies that the soil at larger depths tend to have larger changes in suction for the same change in water content as the shallower soils. The SWCC obtained via laboratory testing (Figure 5.16) was derived under zero confinement and thus are applicable only to surficial soils (say at 0.15 m or 0.5 ft).

To estimate pressure-dependent SWCCs, specialized equipment such as a modified pressure plate is needed (e.g.; Figure 6.21), which is not available at the University of Hawaii. However, it is possible to use the results of the isotropic compression triaxial tests to discern points on the SWCC for different confining stresses by selecting points at equal void ratios.

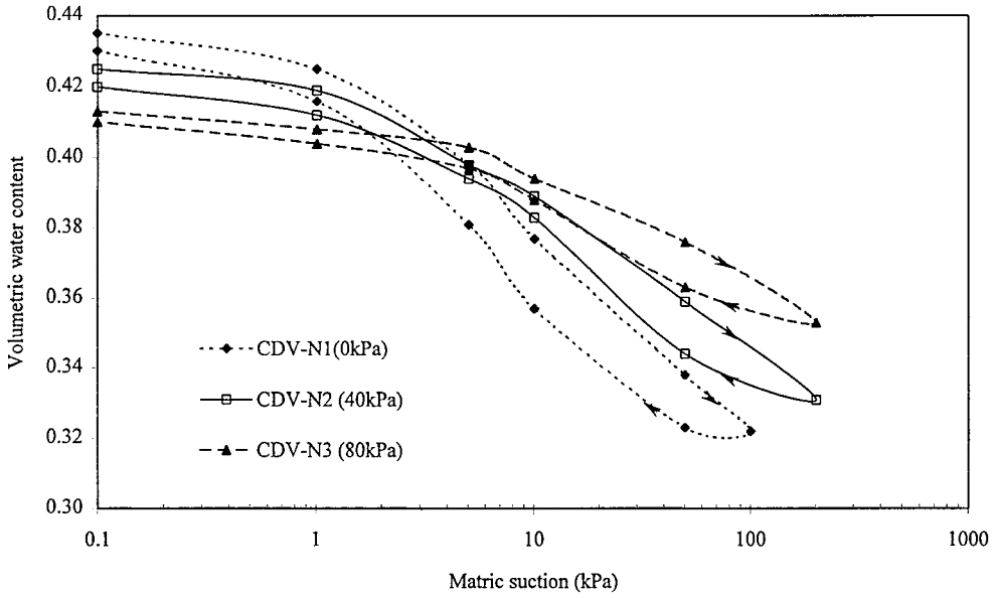

FIGURE 6.20 Effect of confining stress on SWCC (after Ng and Pang, 2000)

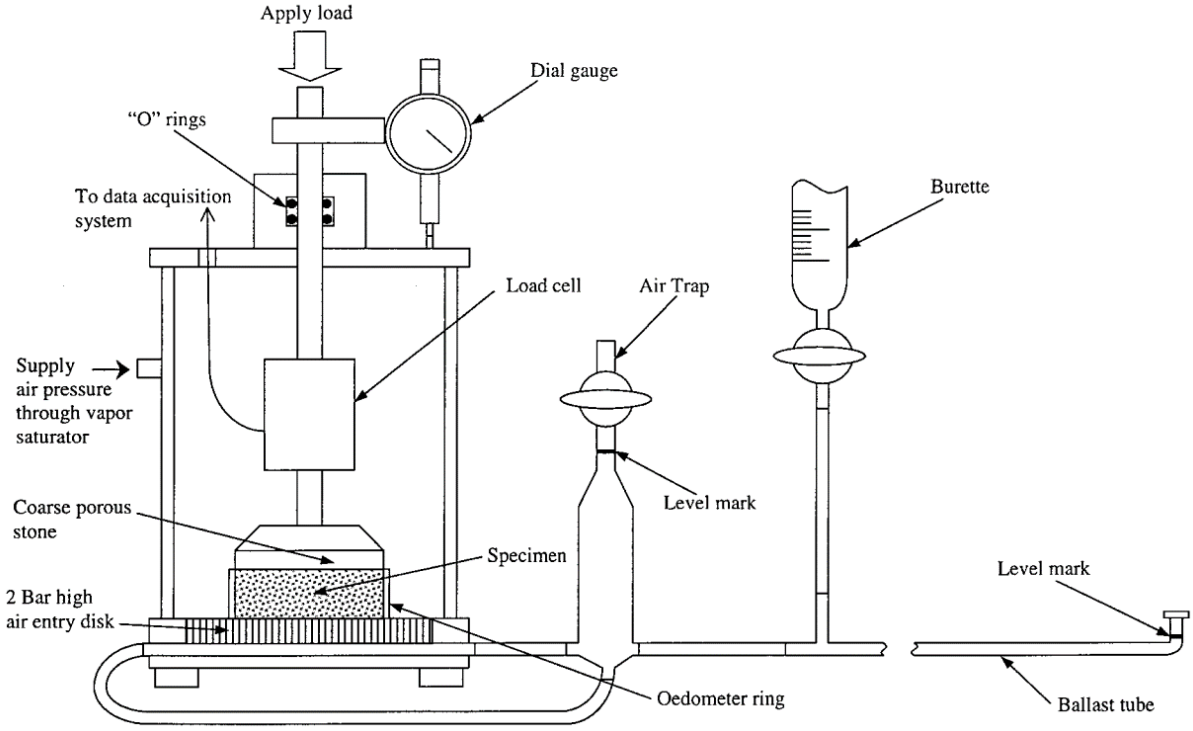

FIGURE 6.21 Schematic of modified pressure plate apparatus that is capable of measuring SWCC under variable confining stress (after Ng and Pang, 2000)

Pressure-dependent SWCC can be modelled using the van Genuchten equation with its parameters expressed as functions of porosity (which is a function of pressure). The description of the model and calibration of parameters are found in section 1.4.2.1.3. The model is restated below. When the residual saturation is zero, as was determined for this soil, saturation, *S*, is expressed as

$$S = [1 + (\alpha h)^n]^{-\left(1-\frac{1}{n}\right)} = \left[1 + \left(\frac{s}{P}\right)^{\frac{1}{1-\lambda}}\right]^{-\lambda} \quad (6.18)$$

where h = pressure head (m), s = suction (kPa) = gh, $\alpha = g/P$ and $\lambda = 1 - 1/n$. HYDRUS uses the first form of equation 6.18 which expresses the van Genuchten equation in terms of pressure head, h, and parameters α and n. The authors of the Code Bright (a finite element software for unsaturated soils) Manual at the Universitat Politecnica de Catalunya (UPC, 2017) suggested that P and λ can be expressed in terms of the soil porosity, Φ as follows:

$$P = P_o \exp\left[a\left(\Phi_o - \Phi\right)\right] \quad (6.19)$$

$$\lambda = \lambda_o \exp\left[b\left(\Phi_o - \Phi\right)\right] \quad (6.20)$$

where P_o, λ_o, Φ_o, a and b are constants. Since Φ is a function of pressure, equations 6.18, 6.19 and 6.20 can be used as a model for the pressure-dependent SWCC. Separate values of P_o, λ_o, Φ_o, a and b for the drying and wetting portions of the isotropic compression tests were discerned by ordinary least-squares (OLS) regression analysis. The resulting constants are summarized in Table 6.2.

Table 6-3 Hydraulic parameters for drying and wetting portions of the SWCC

Parameters	Drying	Wetting
P_o	3.32	0.00299
λ_o	0.129	0.129
Φ_o	0.8013	0.8013
a	14.4	41.4
b	-0.01	-0.01

With the model constants in Table 6.2, the SWCC and HCF can be derived for the soil at any depth (Figure 6.24). The slope was divided into 4 layers (Figure 6.25). At the mid-depth of each layer, the mean stress p' was calculated, from which the porosity and van Genuchten parameters shown in Table 6.3 can be derived using Table 6.2 and assuming $\theta_r = 0$.

Table 6-4 Slope layers, resulting van Genuchten parameters and saturated hydraulic conductivity

Layer	Depth Range (m{ft})	p (kPa)	Φ	θ_s^d	θ_s^w	α^d	α^w	n^d	n^w	k_s (cm/s)
1	0 – 0.76 {0 – 2.5}	12.7	0.54	0.54	0.54	0.15	1	1.15	1.15	10^{-6}
2	0.76 – 1.52 {2.5 – 5}	25.6	0.584	0.584	0.584	0.129	0.405	1.15	1.15	5×10^{-3}
3	1.52 – 6.1 {5 – 20}	58.5	0.581	0.581	0.581	0.124	0.364	1.15	1.15	10^{-4}
4	6.1 - 51 {20 - 167}	349	0.546	0.546	0.546	0.074	0.083	1.15	1.15	10^{-5}

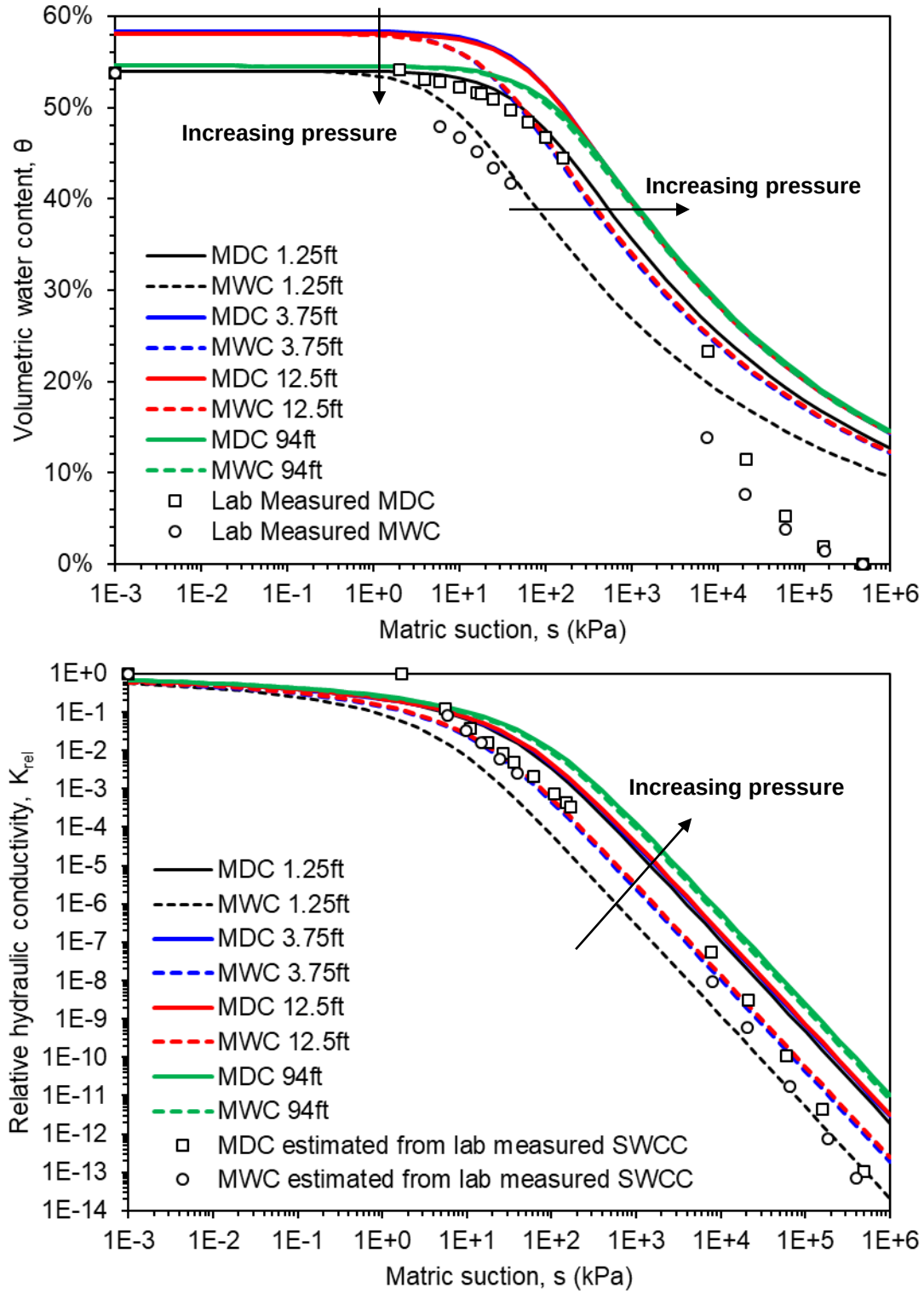

FIGURE 6.22 Pressure-dependent SWCC and HCF using the Universitat Politecnica de Catalunya-modified (UPC, 2017) version of the van Genuchten model

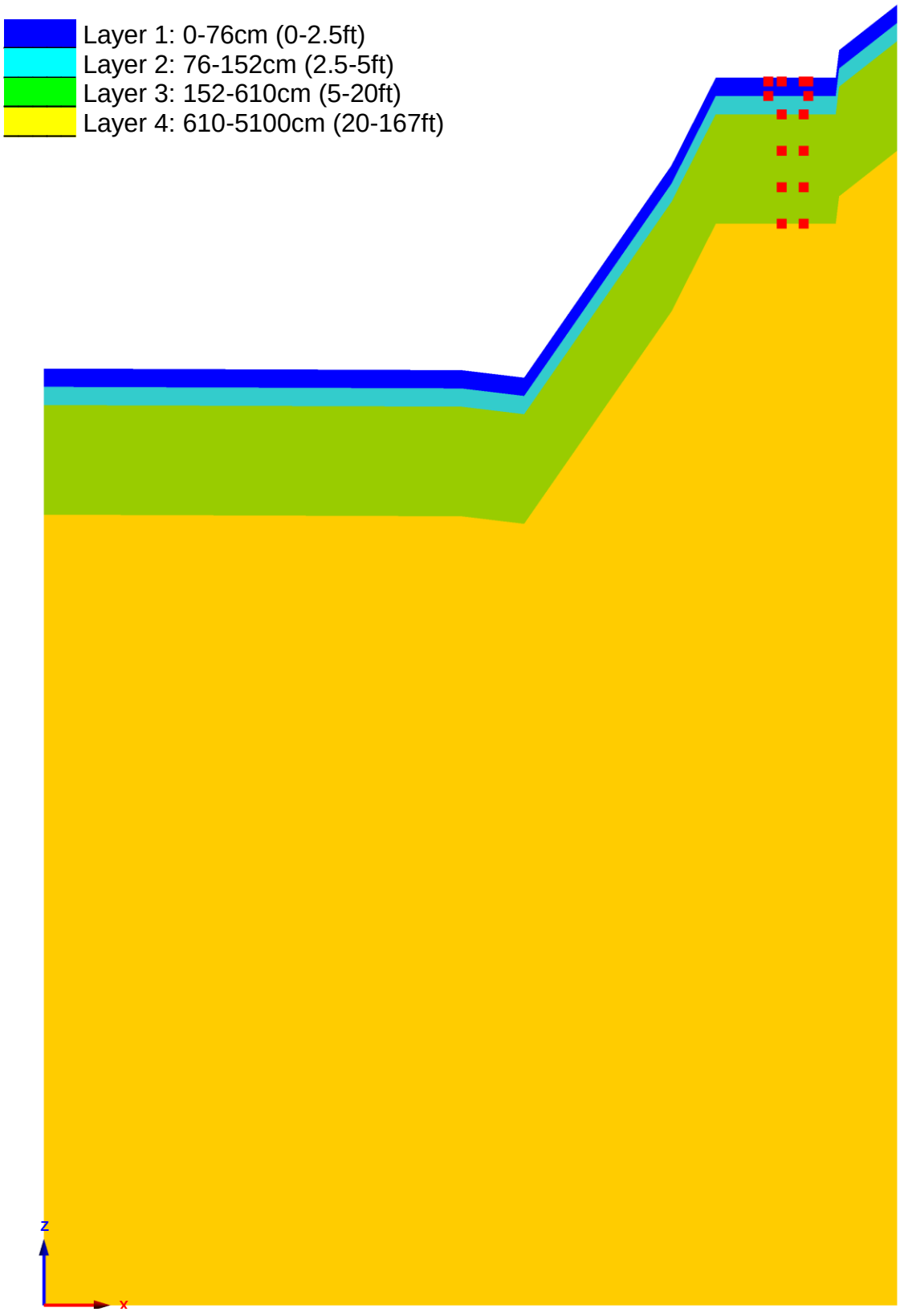

FIGURE 6.23 Slope model in HYDRUS showing the 4 layers

This 4-layer model was then utilized to rerun HYDRUS. Presented in Figure 6.26 through 6.31, the agreement between measured and predicted responses is much improved from before. Now, it can be seen that the soils at larger depths are more reactive. To optimize the match, k_s values for the 3 lower layers had to be increased to the values shown in Table 6.3. Justification for these higher values can be attributed to the fact that desiccation cracks may allow water to infiltrate quicker into the soil.

By no means perfect, the fits are reasonably good. This is the best that can be obtained with the limited time and resources available, and this model and parameters in Table 6.3 was then utilized to determine the pore water pressure/suction profile in the slope after a design storm, which is taken to be a 500-year storm.

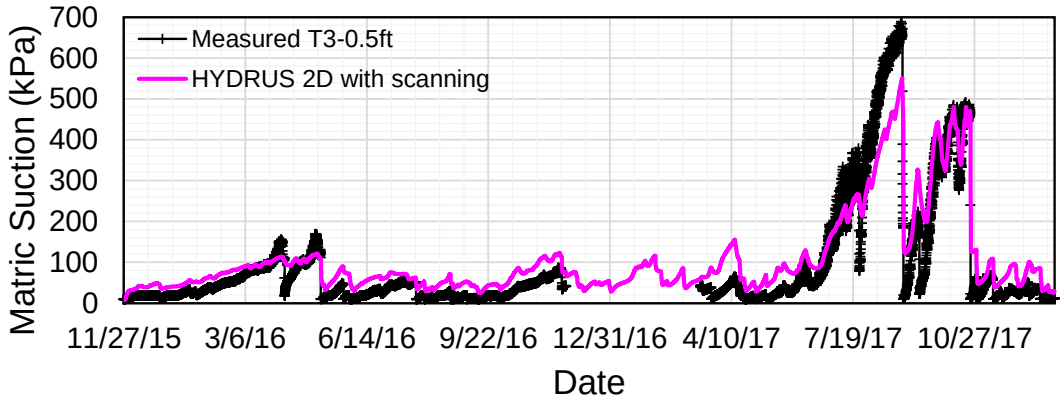

(a)

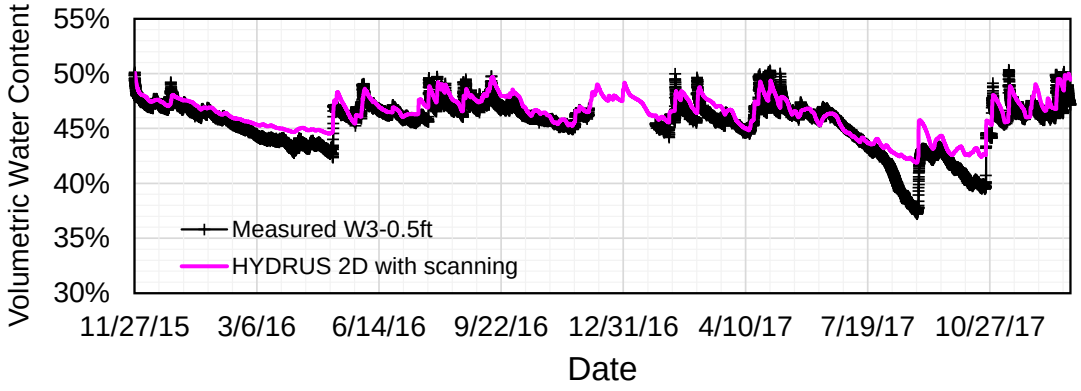

(b)

FIGURE 6.24 Measured vs 2D HYDRUS-derived (a) matric suction vs time and (b) volumetric water content vs time at a depth of 0.15 m (0.5 ft) using a pressure-dependent SWCC and HCF throughout slope geometry

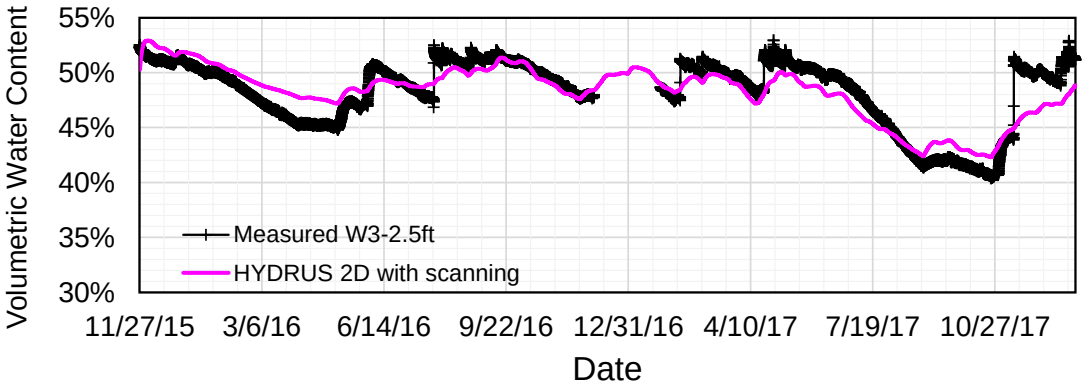

FIGURE 6.25 Measured vs 1D and 2D HYDRUS-derived volumetric water content vs time at depth of 0.76 m (2.5 ft) using a pressure-dependent SWCC and HCF throughout slope geometry

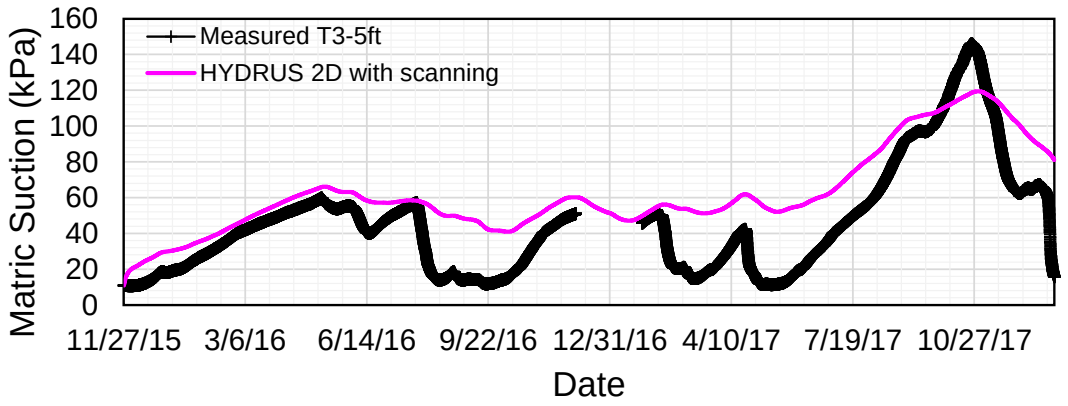

FIGURE 6.26 Measured vs 1D and 2D HYDRUS-derived matric suction vs time at depth of 1.52 m (5 ft) using a pressure-dependent SWCC and HCF throughout slope geometry

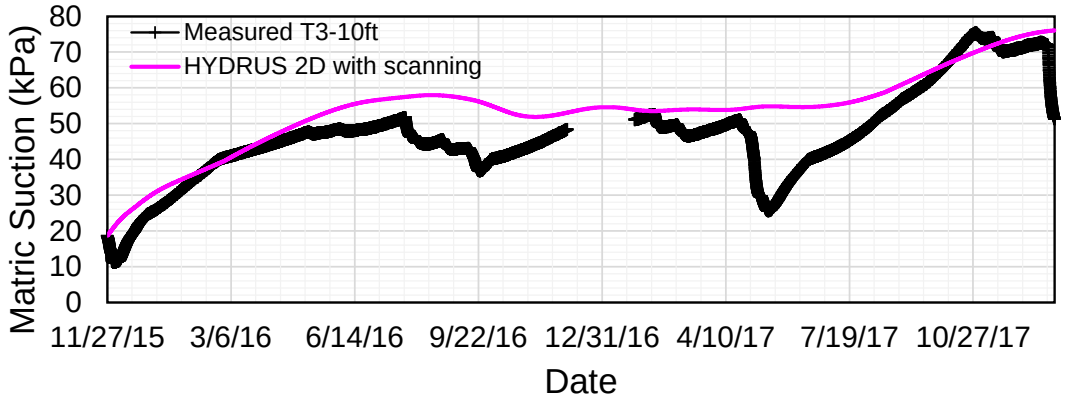

FIGURE 6.27 Measured vs 1D and 2D HYDRUS-derived matric suction vs time at depth of 3.05 m (10 ft) using a pressure-dependent SWCC and HCF throughout slope geometry

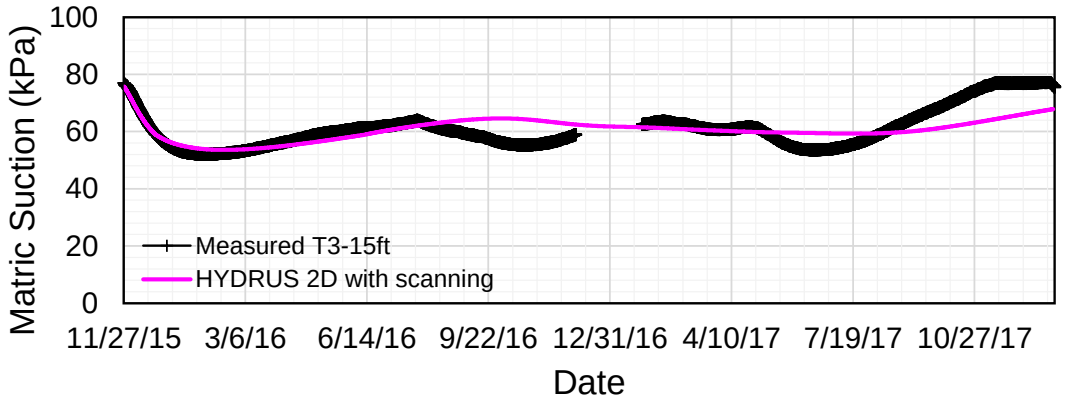

FIGURE 6.28 Measured vs 1D and 2D HYDRUS-derived matric suction vs time at depth of 4.57 m (15 ft) using a pressure-dependent SWCC and HCF throughout slope geometry

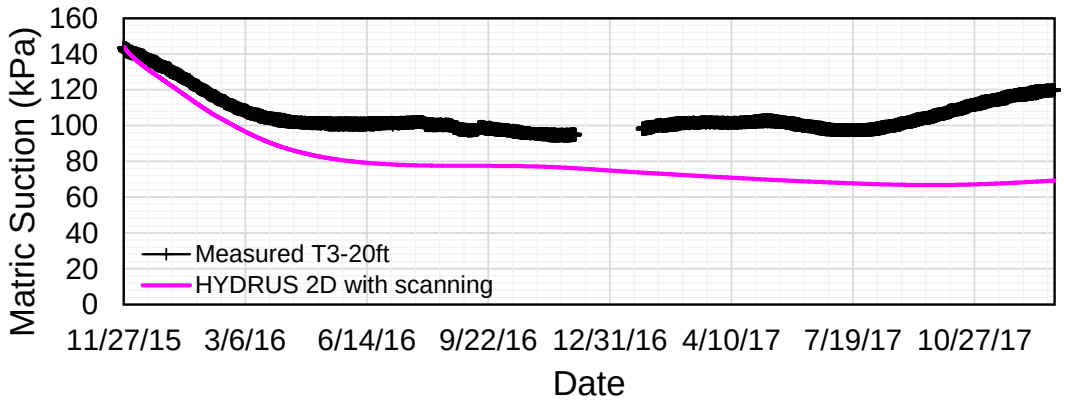

FIGURE 6.29 Measured vs 1D and 2D HYDRUS-derived matric suction vs time at depth of 6.1 m (20 ft) using a pressure-dependent SWCC and HCF throughout slope geometry

To validate that HYDRUS is calculating reasonable values of actual evaporation (*AE*), the boundary pressure head (which is a measure of the moisture of the soil at the ground surface) from HYDRUS is plotted versus the ratio of the actual (from HYDRUS) to the potential evaporation (*AE*/*PE*) as shown in Figure 6.30. In this figure, the three distinct stages of evaporation are evident when the surficial soil dries from an initially saturated stage as described in Section 6.2. When the boundary pressure head is 0 (soil is wet), *AE*/*PE* = 1. This is akin to the first stage of evaporation. Then *AE* decreases rapidly from *PE* with small changes in pressure head. This is akin to the second stage of evaporation. In the last stage, the rate of decrease of *AE* starts to level off. This is representative of the third stage of evaporation. All three stages are correctly and well represented during the 2.5-year calibration period. The HYDRUS results of boundary pressure head versus AE/PE were fitted using a hyperbolic best-fit line. The resulting coefficient of determination (R^2) is 0.692 (Figure 6.30).

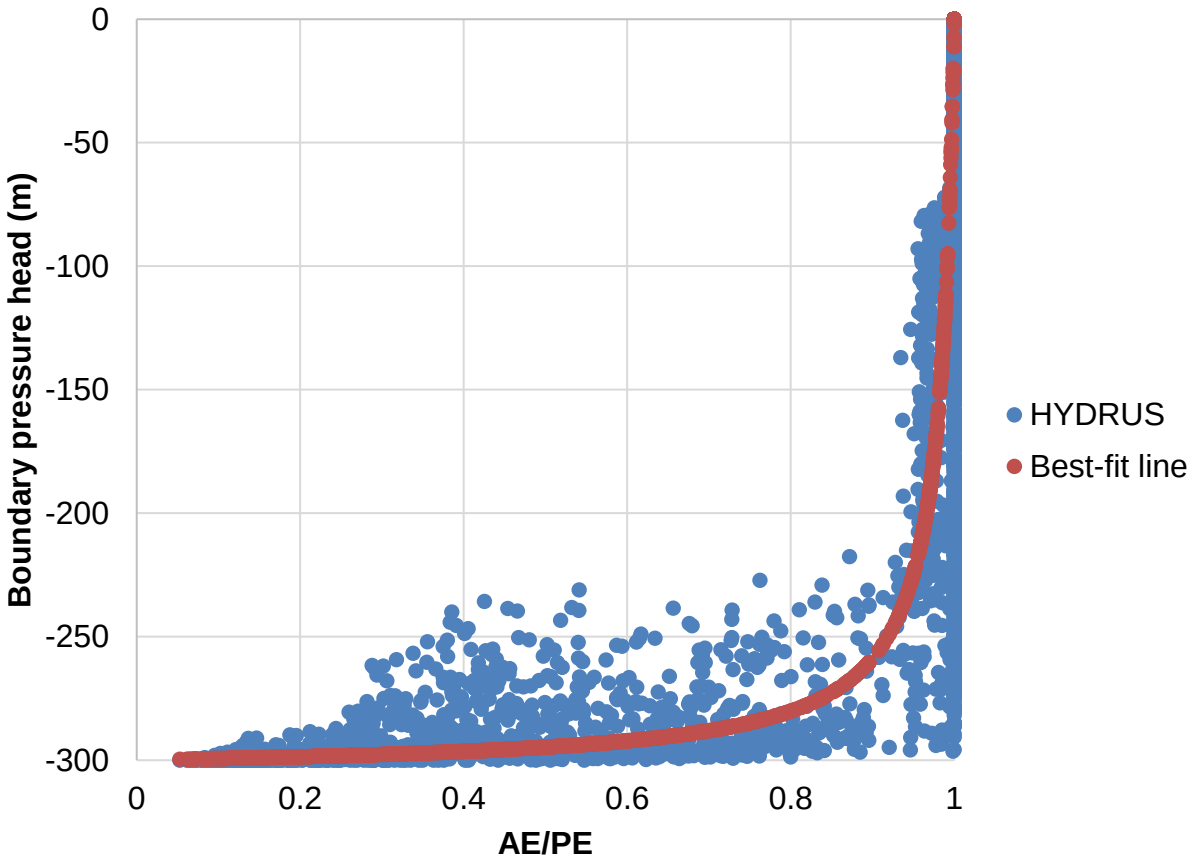

FIGURE 6.30 Boundary pressure head versus ratio of actual to potential evaporation

6.6 Transient Flow Analysis during a Storm with a 500-year Return Period

The 500-year-return period precipitation intensity vs duration frequency curve (IDF) for the site was downloaded from NOAA's National Weather Service precipitation frequency data server (2018) and is plotted in Figure 6.31. IDF curves can also be downloaded from the same website for 3 (Pali Golf Course, Maunawili, and Kailua Fire Station) of the 5 rain gages utilized to correct precipitation for periods of missing data (Section 4.2.1). The inverse-distance weighting average was then used to calculate the IDF curve for the slope site (IDW Average).

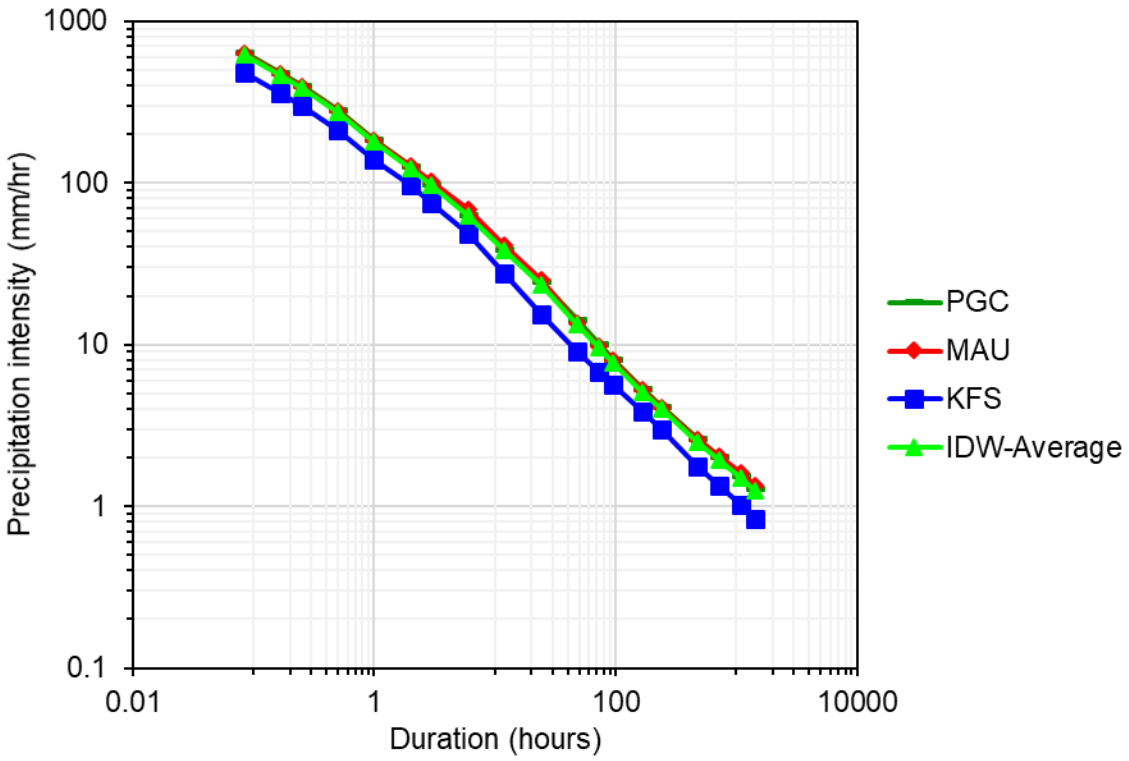

FIGURE 6.31 Precipitation intensity vs duration curve for a 500-year-return period storm at the slope site

The 5-minute (622 mm/hr) and 60-day (1.25 mm/hr) values of precipitation intensity were then applied to the 2D slope mesh in HYDRUS resulting in the suction contour plots of Figs. 6.11 and 6.12, respectively. It was found that the longer duration low intensity storms are most critical when analysing slope stability. Storms with durations between 5-minute and 60 days are not presented in this report.

Baum and Godt (2010) discussed the importance of seasonal pre-storm (antecedent) rainfall for slopes in areas that subject seasonal wetting and drying cycles on the slope. They stated that antecedent precipitation is less significant for humid areas with evenly distributed rainfall throughout the year, specifically the Ko'olau range of Oahu. In contrast, Kanajanakul (2016), Rahardjo et al., (2007), and Zhang et al., (2016) showed the importance of antecedent rainfall for slopes in Southeast Asia. The Kalaniana'ole Highway slope is situated closer to the coast and is sparsely vegetated. Therefore, the effects of pre-storm moisture conditions on slope stability have been investigated.

Two initial conditions were considered; one starting at a relatively dry time (May 2, 2015 19:00) and the other at a relatively wet time (November 27, 2015 05:00) of the monitoring period. These same initial conditions along a vertical through the slope crest were used for calibrating the 1D model. The initially wet condition for calibrating the 2D model was previously shown in Figure 6.4 and is reshown here in Figure 6.32a along with the initially dry condition in Figure 6.32b.

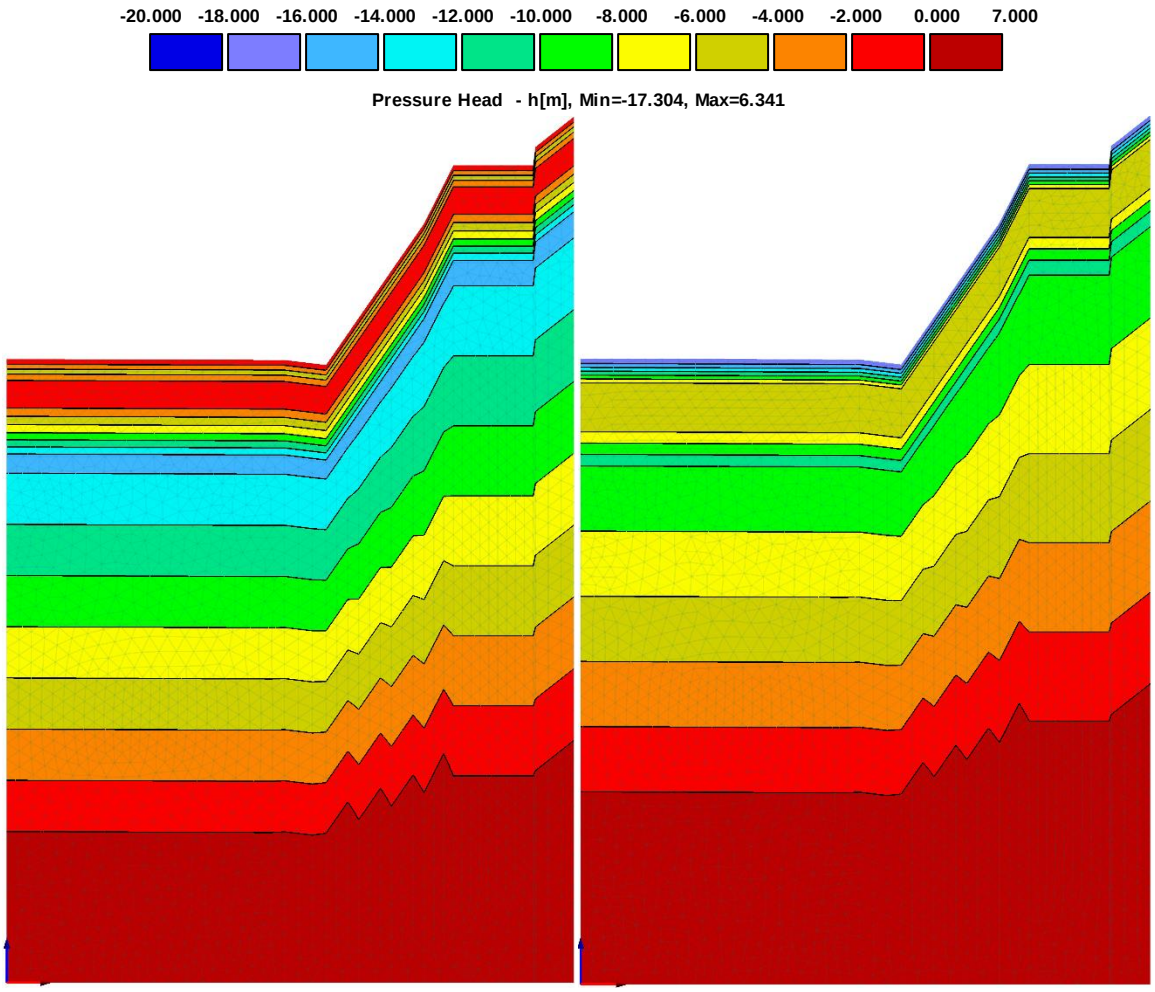

(a) (b)

FIGURE 6.32 Initial conditions for (a) a relatively wet period (November 27, 2015) and (b) a relatively dry period (May 2, 2015)

The 500-year design storm could occur when the ground is already saturated to begin with or when the ground is dry. When the initial conditions are wet to begin with, it would mean that the design storm's actual return period is higher than 500-years. Nevertheless, both sets of initial conditions are indeed possible and were utilized to provide good insight into what may occur in the field.

The HYDRUS analyses were extended for another 60 days beyond the end of the 500-year storm as the moisture was still making its way into the soil after the rain event. During the 60-day extension, it was assumed that the precipitation ceased and there was no evaporation (conservative). Figs. 6.33 and 6.34 represent the suction contours at the end of the storm through 3 days after the end of the storm. Suction contour plots at any point in time can be generated and utilized to perform stability analyses of the slope, as described in Chapter 7. The results of these analyses also form the bases of selection of threshold values for the landslide warning system.

The suctions within the initially dry slope are noticeably lower than within the initially wet slope. In fact, the dark red contour represents a pressure head greater than 0, or saturated conditions. Therefore, saturated conditions have occurred within the initially dry slope and not the initially wet slope. An explanation is provided below.

The SWCC predicted at sensor locations are shown in Figure 6.35. As can be seen, a scanning path was not followed when the initially dry slope was subjected to the 500-year 60-day duration rainfall. As discussed previously, the field SWCC paths exhibit scanning which must be captured by the model or else the suctions and water contents will be over-predicted. It was hypothesized that shorter duration, lower intensity, lower return-period rainfalls are necessary to trigger a scanning path. Zhang et al., (2016) found that the minimum factor of safety will occur before the end of a storm if the rainfall follows an advanced (green) or normal (red) pattern as shown in Figure 6.36. Variable rainfall patterns like those proposed by Ng et al (2010), that more closely resemble real rainfall patterns, should be but were not investigated as they are hypothetical scenarios that fall outside the scope of work.

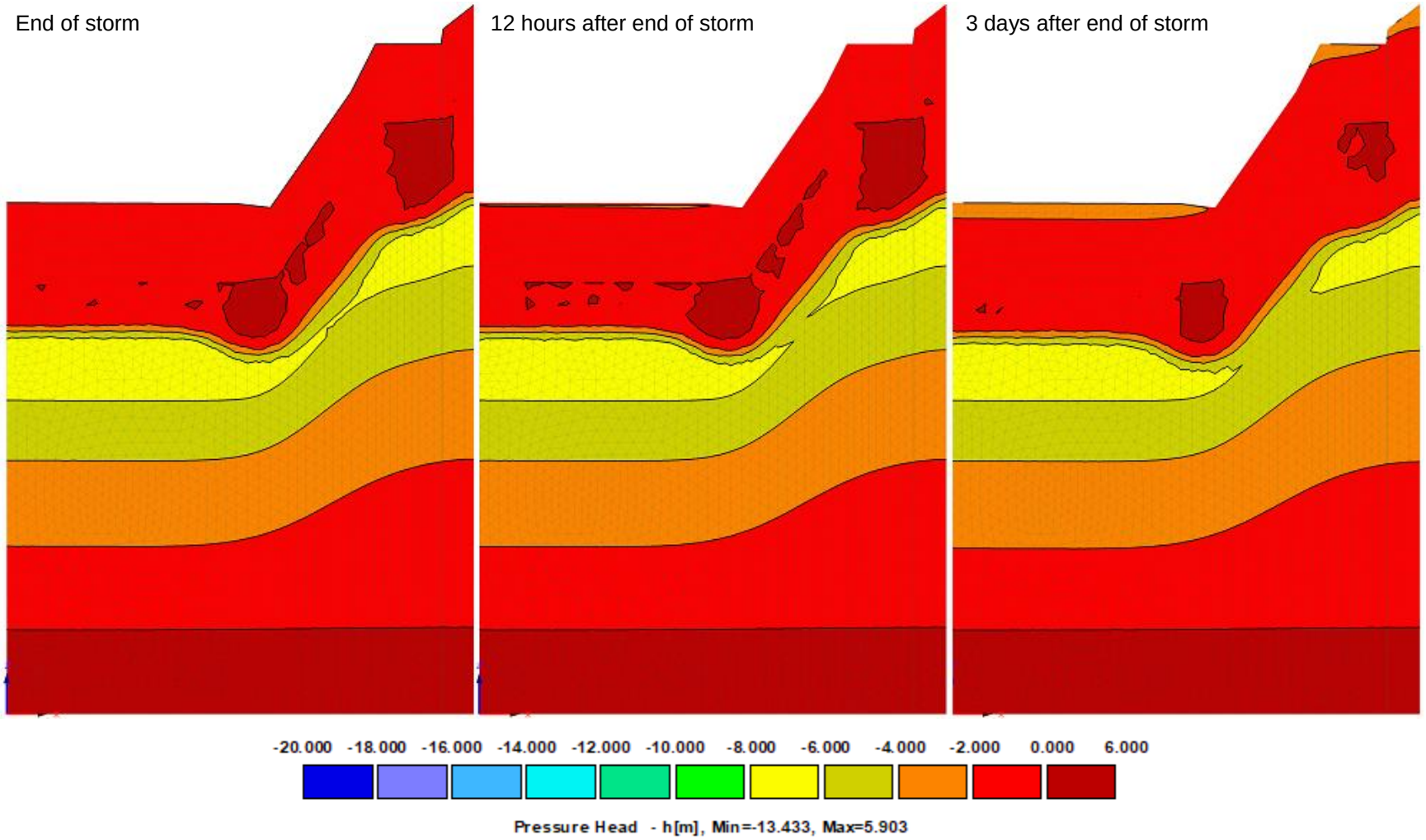

FIGURE 6.33 Suction contours for an initially dry slope during a 60-day duration 500-year return period storm

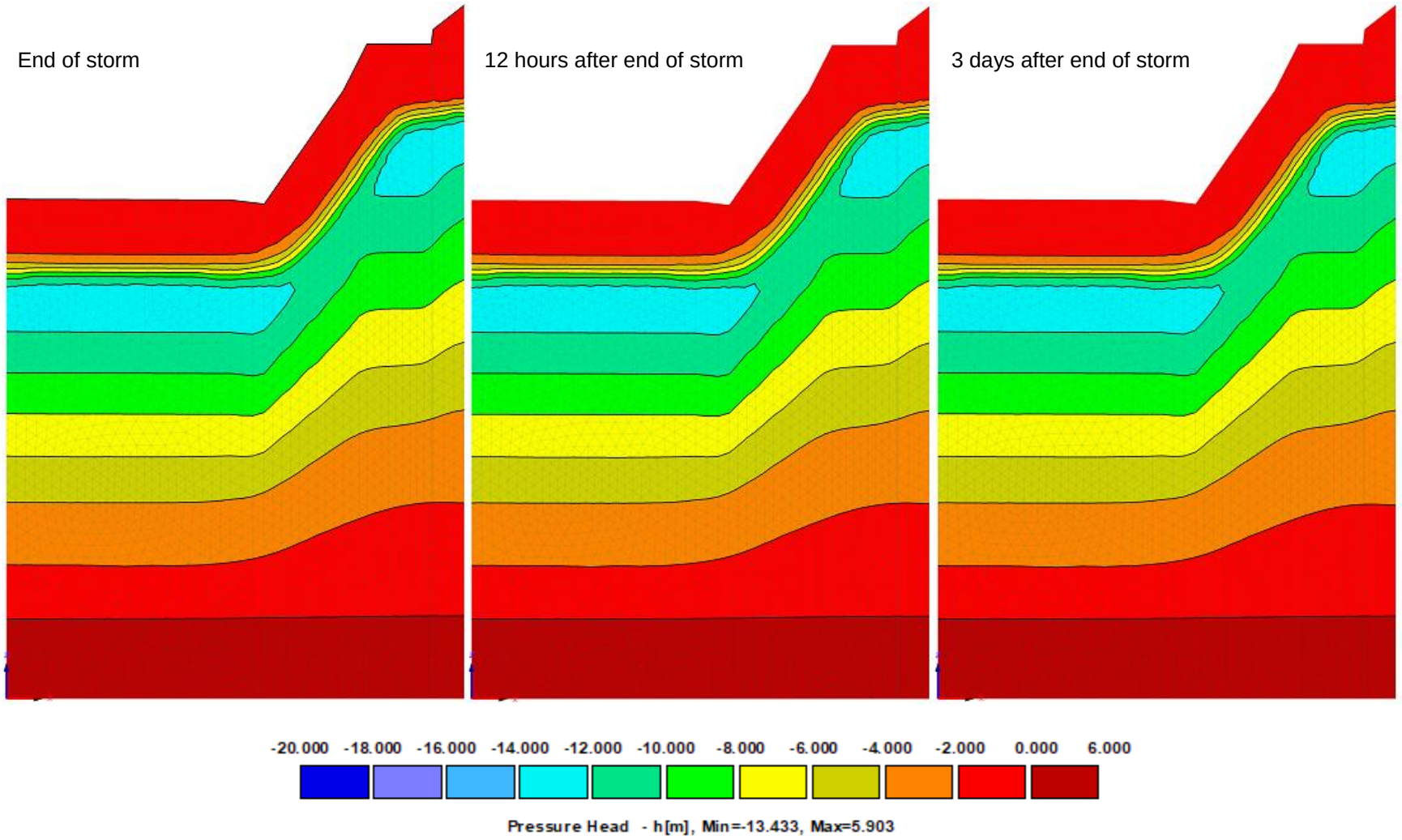

FIGURE 6.34 Suction contours for an initially wet slope during a 60-day duration 500-year return period storm

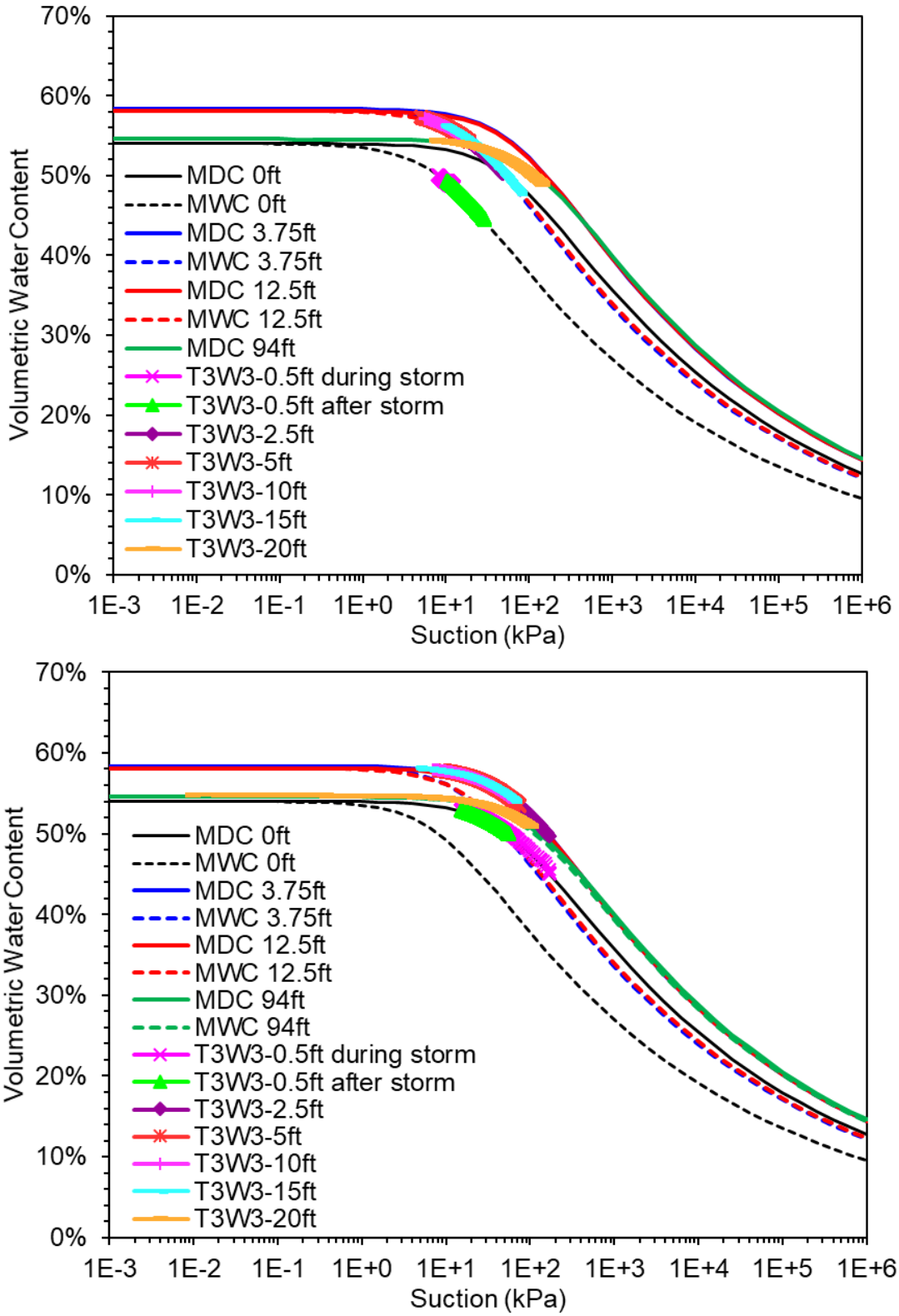

FIGURE 6.35 Predicted suctions at sensor locations during a 500 year, 60 day storm fir initially wet and initially dry conditions

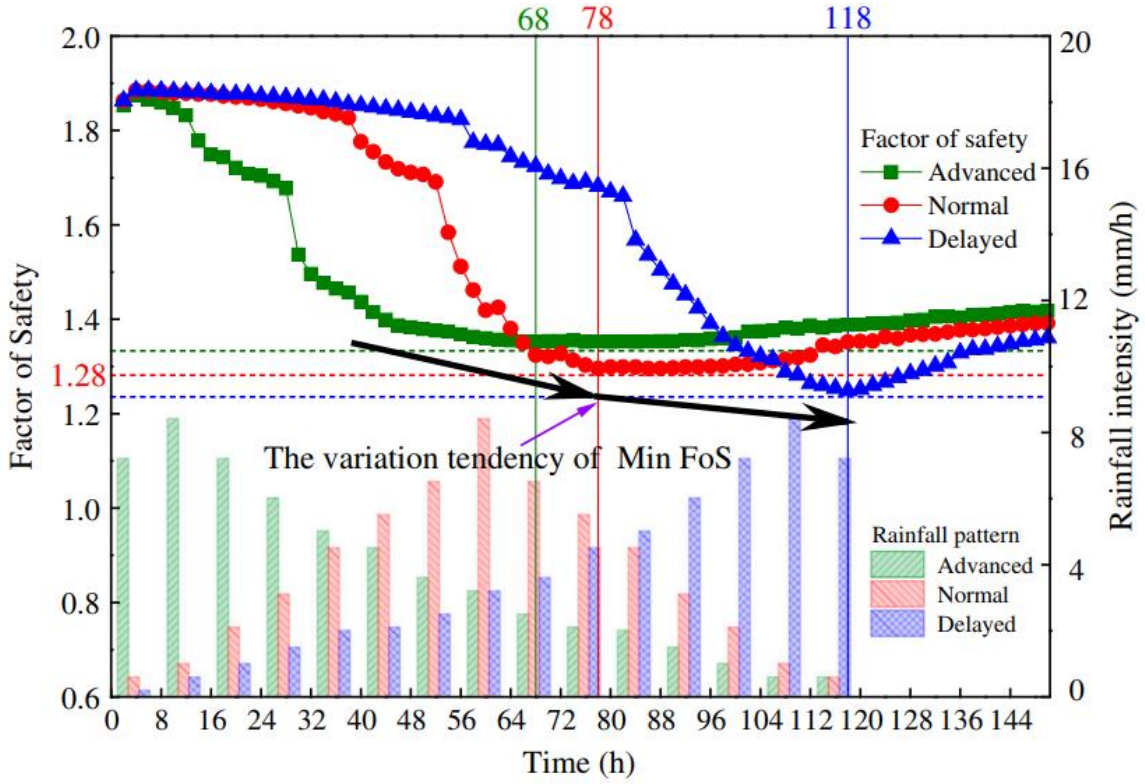

FIGURE 6.36 Effects of variable rainfall patterns on delayed response of the minimum factor of safety (from Zhang et al., 2016)

7 SLOPE STABILITY ANALYSIS

Infinite slope analysis is useful to analyze slope failures where the slip surface runs roughly parallel to the slope face and is long in comparison to its depth. Even though the slope is not infinitely long, an infinite slope analysis provides a useful index to investigate the sensitivity of the various factors that affect the margin of safety. Only the steepest (63°) portion of the compound slope is analyzed since the 55° portion will be less critical.

First, the slope was analyzed assuming a fully saturated infinite slope. This was followed by a 2D analysis of the actual slope geometry assuming full saturation. The results of the infinite slope analysis were then compared to the 2D slope analysis for the saturated case. Analyses of the unsaturated infinite and 2D slope were then performed utilizing the suctions estimated for the 500-year storm.

7.1 Infinite Slope Analysis Assuming Full Saturation

The factor of safety for a saturated, infinite slope with an inclination of α with respect to the horizontal can be written as:

$$FS = \frac{c' + \left(\gamma_{sat} z \cos^2 \alpha - u_w\right) \tan \phi'}{\gamma_{sat} z \cos \alpha \sin \alpha}$$

$$FS = \frac{2c'}{\gamma_{sat} z \sin 2\alpha} + \frac{\tan \phi'}{\tan \alpha} - \frac{u_w}{\gamma_{sat} z}\left(\tan \alpha + \cot \alpha\right) \tan \phi' \qquad (7.1)$$

where c' and ϕ' are the effective cohesion and angle of internal friction of the soil, respectively, γ_{sat} is the saturated soil unit weight, u_w is the pore water pressure and z is the depth of the sliding surface. The expression for factor of safety can be thought of as having three separate components: (1) a cohesion term; (2) a frictional term; and (3) a pore water pressure term. The pore water pressure influences the soil shear strength. Its magnitude is a function of the seepage inclination with respect to the horizontal, θ (Figure 7.1) as follows:

$$u_w = \frac{\gamma_w z}{1 + \tan \theta \tan \alpha} \qquad (7.2)$$

It can be seen from Equations 7.1 and 7.2 that the factor of safety is a minimum when θ = 0° or the seepage is horizontal. Horizontal seepage can only occur when there is a sink (e.g.; pumping well). Since no is sink present, it is unlikely that seepage will be horizontal. However, both horizontal seepage

(i.e.; $\theta = 0$) and seepage parallel to the slope (i.e.; $\theta = \alpha$) are analysed with the former representing a lower bound. Their respective expressions for factor of safety are:

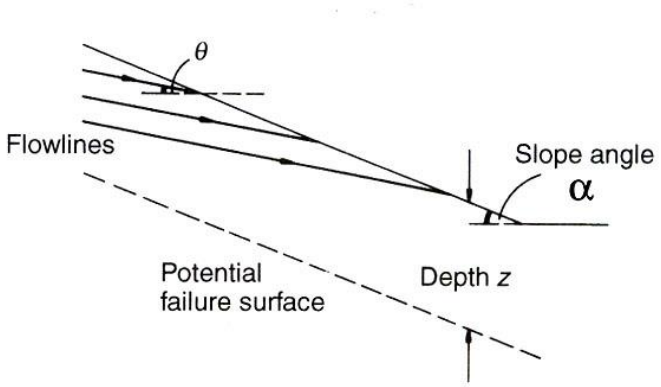

FIGURE 7.1 Infinite slope with seepage at an inclination of θ to the horizontal (after Powrie, 1997)

$$FS = \frac{2c'}{\gamma_{sat} z \sin 2\alpha} + \frac{\tan\phi'}{\tan\alpha} - \frac{\gamma_w}{\gamma_{sat}}\left(\tan\alpha + \cot\alpha\right)\tan\phi' \qquad (7.3)$$

$$FS = \frac{2c'}{\gamma_{sat} z \sin 2\alpha} + \frac{\gamma_b \tan\phi'}{\gamma_{sat} \tan\alpha} \qquad (7.4)$$

where γ_b = soil buoyant unit weight. Figure 7.2 presents the factor of safety for a 63° infinite slope with both horizontal seepage and seepage parallel to the slope and utilizing Hvorslev's true $\phi'_e \approx 28°$ and $c'_e \approx$ 18 kPa. The factor of safety varies with depth since the cohesion term is a function of z. When the factor of safety is 1.0, the critical depths were 1.7 m and 2.9 m, respectively indicating that the horizontal seepage case has a shallower critical depth than the seepage parallel to slope scenario.

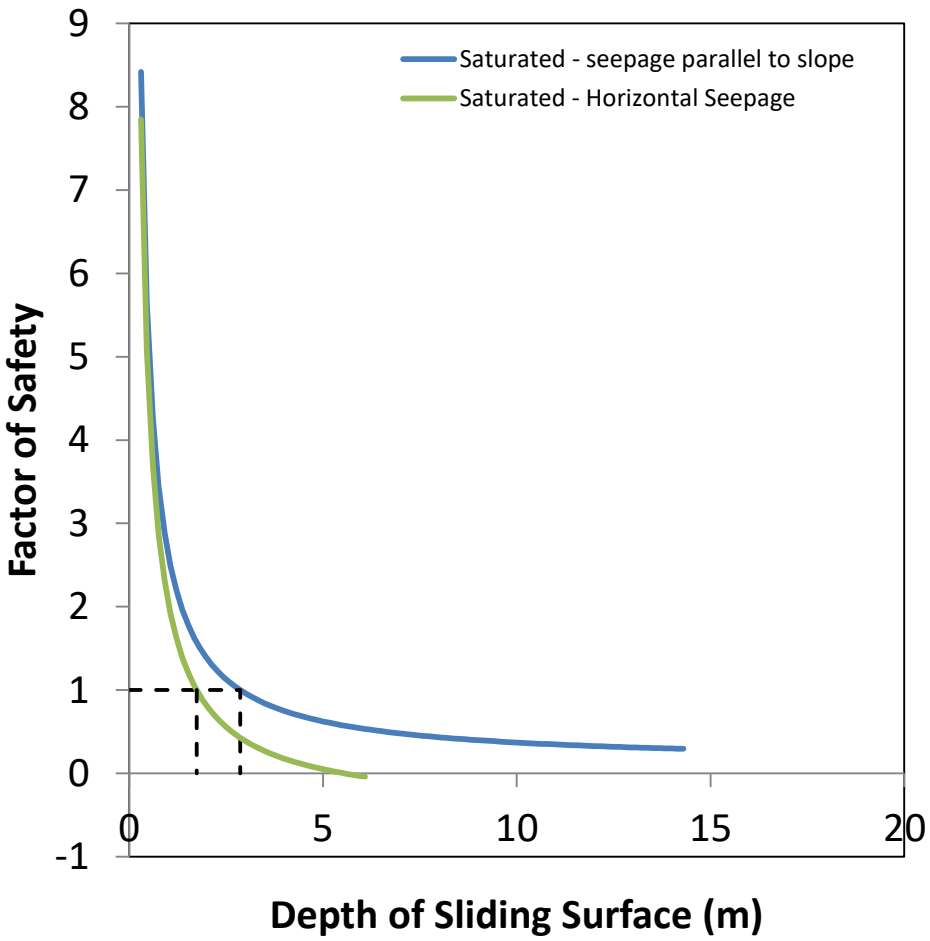

FIGURE 7.2 Factor of safety assuming 63° infinite slope with seepage parallel to slope

7.2 2D Slope Stability Analysis Assuming Full Saturation

As a comparison to the infinite slope analysis, the 2D factor of safety for the slope when entirely saturated was calculated using the method of slices with the aid of the search routines in SLOPE/W (Geo-slope International, Ltd., 2012). The factors of safety using Bishop's simplified (1955), Morgenstern-Price's (1965), Spencer's (1967) and Sarma's (1973) methods were calculated to be 0.520, 0.530, 0.493 and 0.522, respectively (see Figs. 7.3, 7.4, 7.5 and 7.6, respectively). Bishop's simplified method satisfies overall moment equilibrium and force equilibrium only in the vertical direction. Even though it does not satisfy force equilibrium in the horizontal direction, it is commonly used in the geotechnical profession because it is known to be reasonable if the limitations are recognized and overcome. The last three methods satisfy all conditions of equilibrium and therefore, should provide factors of safety accurate to within ±5% for any condition (Duncan and Wright, 2005).

When entirely saturated, the factors of safety indicate that the slope is unstable. However in reality, the slope is still standing and is unsaturated. This demonstrates the importance of suction in keeping this slope stable since suction increases the soil shear strength and also the factor of safety of the slope under normal ambient unsaturated soil conditions.

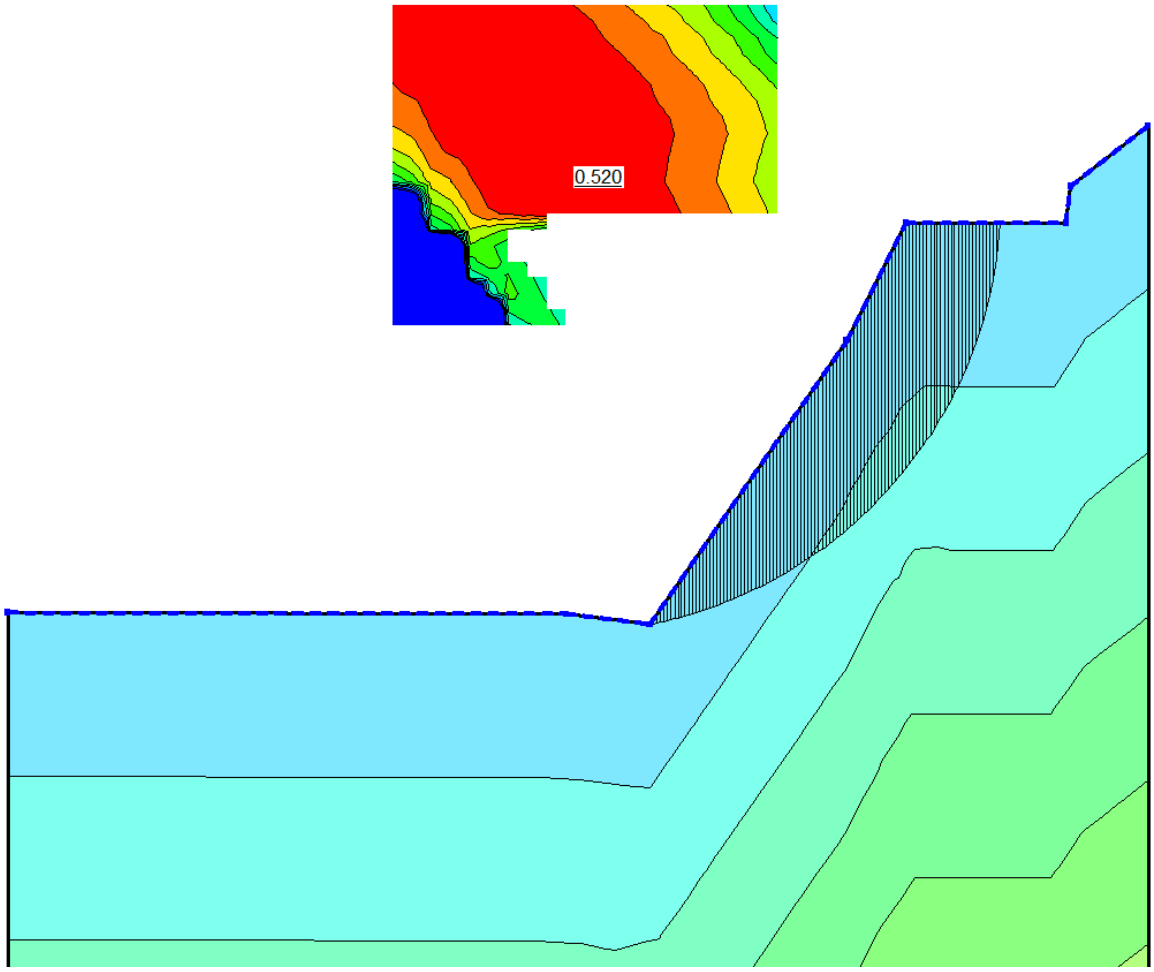

FIGURE 7.3 2D factor of safety using Bishop's simplified method from SLOPE/W assuming a fully saturated slope

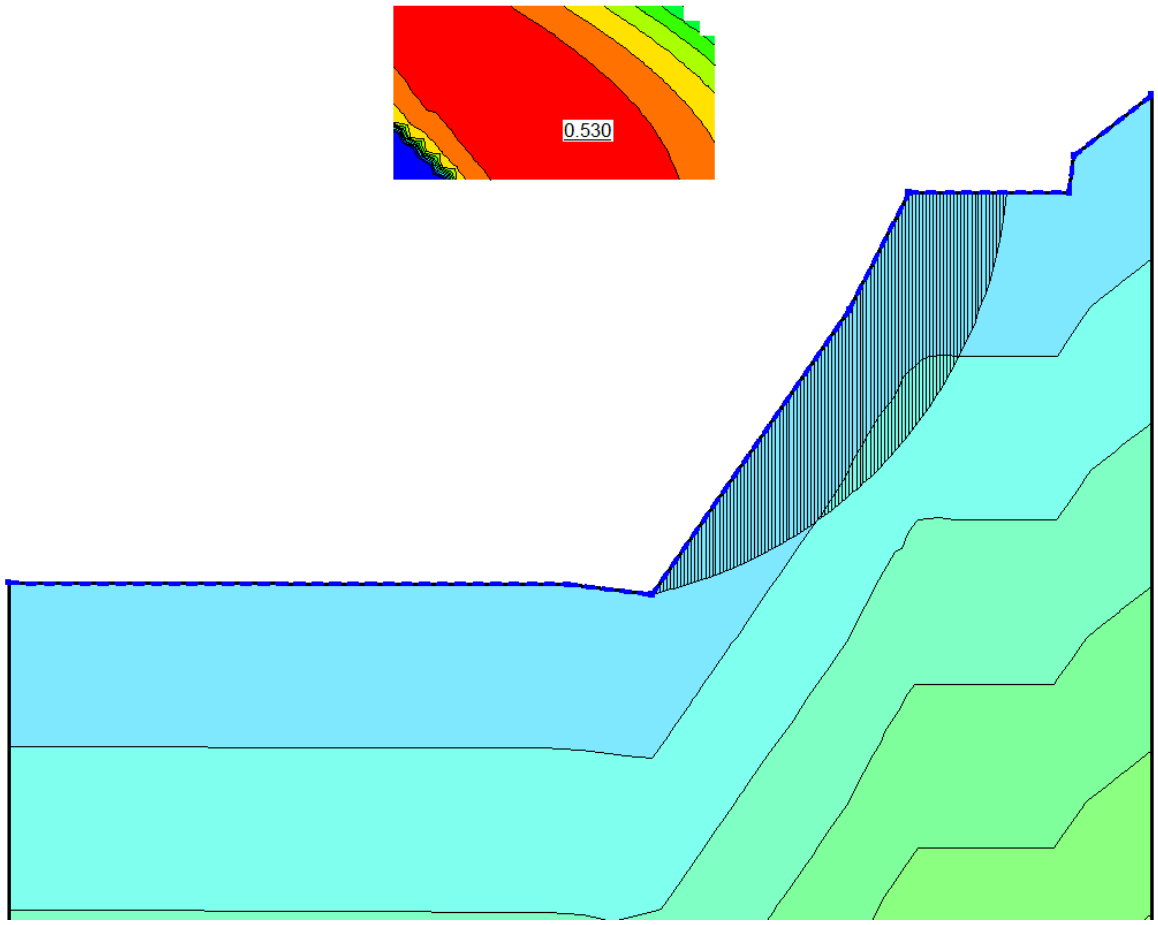

FIGURE 7.4 2D factor of safety using Morgenstern-Price's method from SLOPE/W assuming a fully saturated slope

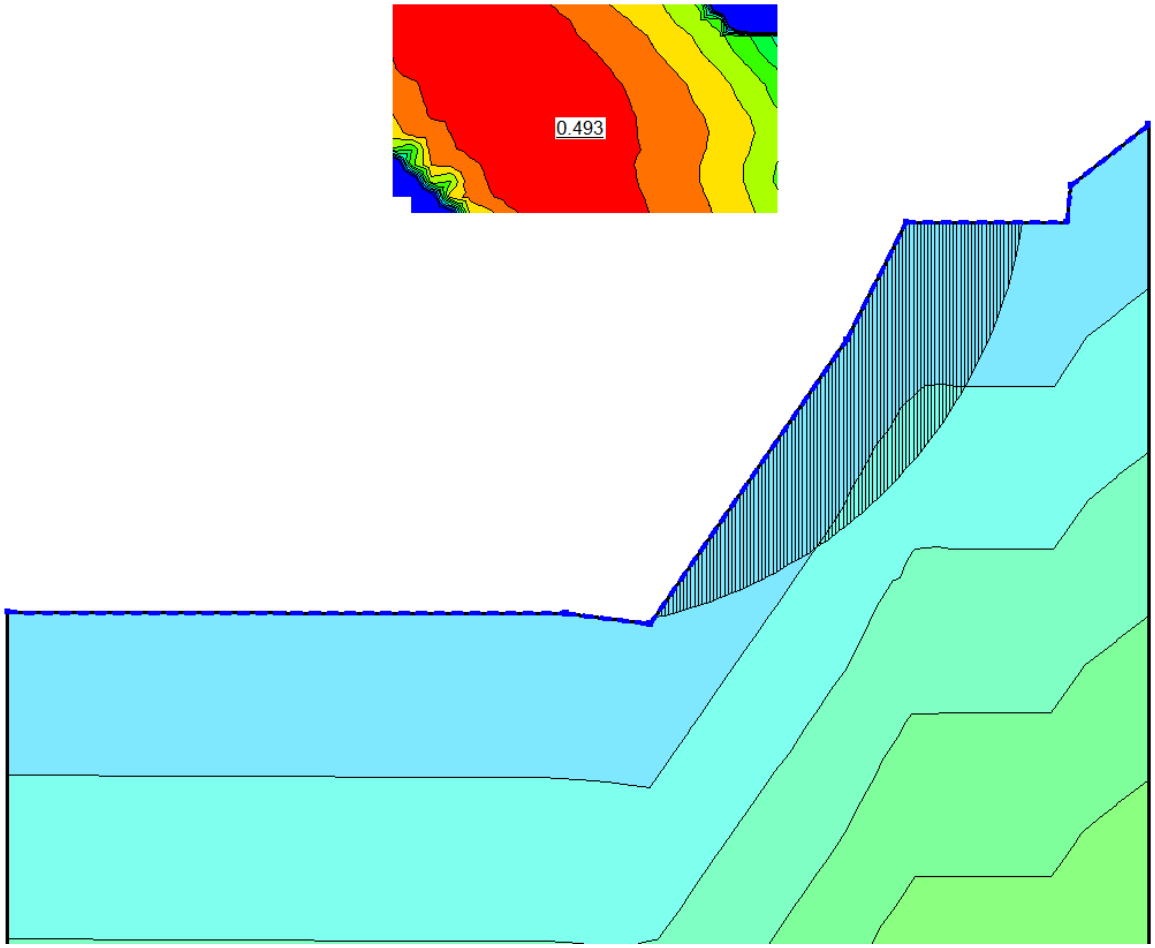

FIGURE 7.5 2D factor of safety using Spencer's method from SLOPE/W assuming a fully saturated slope

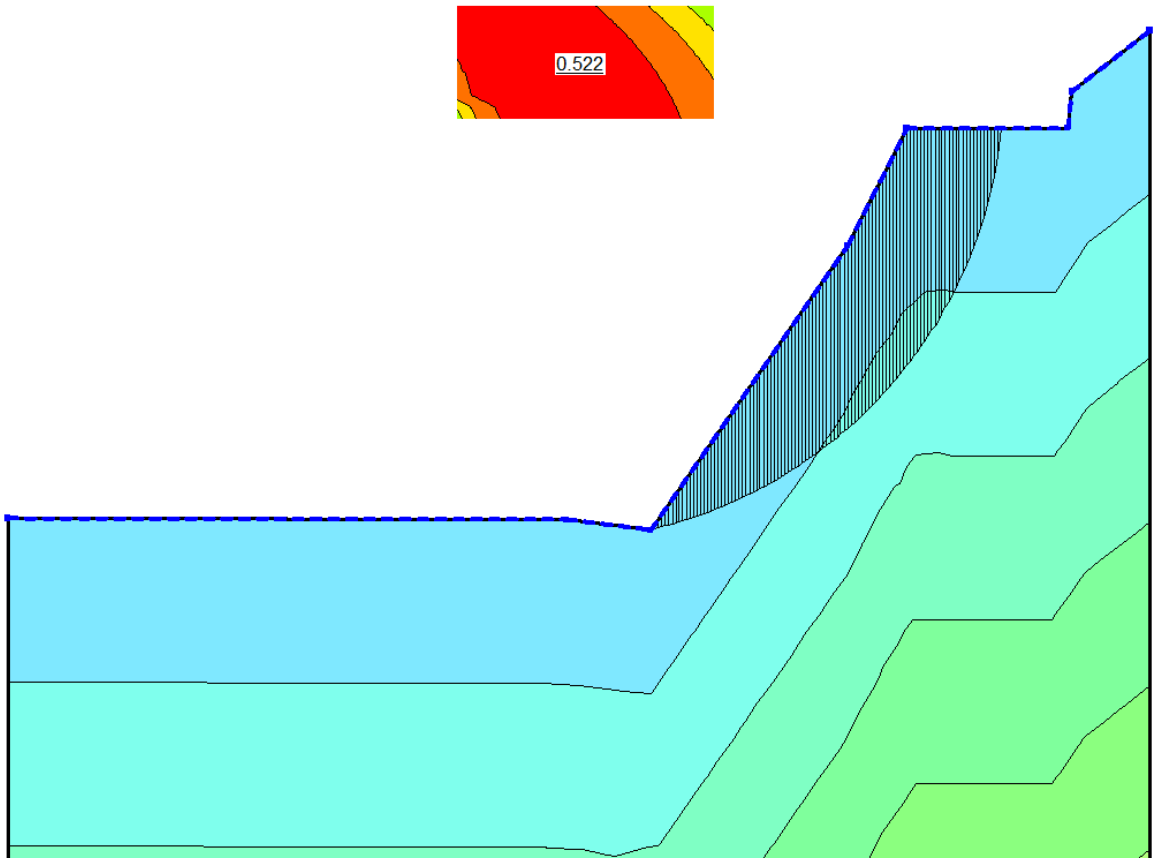

FIGURE 7.6 2D factor of safety using Sarma's method from SLOPE/W assuming a fully saturated slope

7.3 Infinite Slope Stability Analysis During 500-year Storm

An infinite slope stability analysis was conducted at several depths and during several points in time after the 500-year storm using values of suction from Figs. 6.33 and 6.34. The factor of safety for an unsaturated slope can be calculated as follows (Lu and Godt, 2013):

$$FS = \frac{2c'}{\gamma z \sin 2\alpha} + \frac{\tan\phi'}{\tan\alpha} - \frac{\sigma^s}{\gamma z}\left(\tan\alpha + \cot\alpha\right)\tan\phi \qquad (7.5)$$

where σ^s = suction stress (in units consistent with γz) at the depth of the sliding plane, z. Equation 7.5 is similar to Equation 7.1 with σ^s replacing u_w. The background behind the suction stress and how it can be estimated is described below.

In 1954, Bishop (1954) proposed an expression for the effective stress, σ', of unsaturated soil as follows:

$$\sigma' = \sigma - u_a + \chi(u_a - u_w) \tag{7.6}$$

where σ = total stress, u_a = pore air pressure, u_w = pore water pressure and χ = Bishop's effective stress parameter = 0 when the soil is dry and unity when the soil is saturated. According to Bishop's equation, as a soil moistens, suction decreases leading to a decrease in effective stress which usually implies an increase in volume. Jennings and Burland (1962) criticized Bishop's equation saying that it cannot adequately explain the behavior of collapsing soils since such soils undergo a decrease in volume upon wetting. However, this criticism was made assuming a linear elastic framework. Non-recoverable deformations such as collapse can be modelled with an effective stress framework if a yield surface is defined as a function of suction. Such work has been reported in the literature by Kohgo et al. (1993), Modaressi and Abou-Berk (1994), Bolzon et al. (1996), Loret and Khalili (2000) and Khalili and Loret (2001).

Another issue with Bishop's equation has been the problem associated with estimating χ. Bishop (1954) initially suggested $\chi = S$, where S = degree of saturation. As seen in Figure 7.7, Gens (1996) showed that $\chi \neq S$ and there is considerable variation in this relationship depending on soil type.

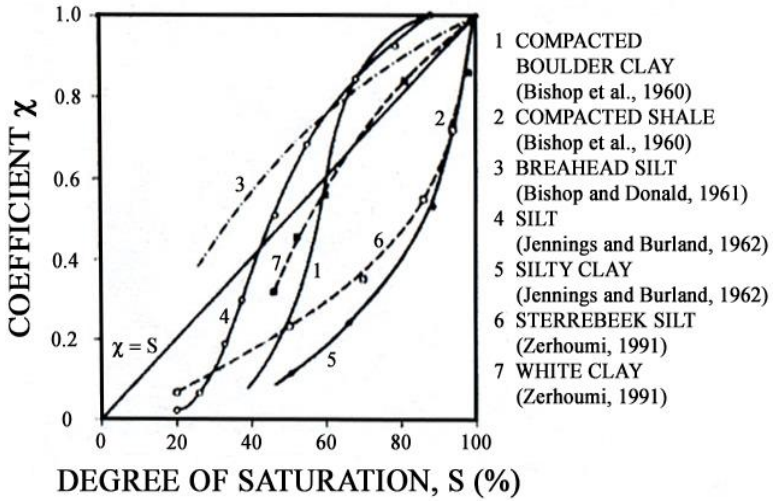

FIGURE 7.7 Variation of χ with degree of saturation for various soils (Gens 1996)

Khalili and Khabbaz (1998) and Khalili et al. (2004) experimentally showed that χ is related to suction if it is normalized by its air entry value (Figure 7.8). This relationship can be mathematically approximated as follows:

$$\chi = \begin{cases} \left(\frac{s}{s_e}\right)^{-0.55}, & if\ s \geq s_e \\ 1, & if\ s < s_e \end{cases} \tag{7.1}$$

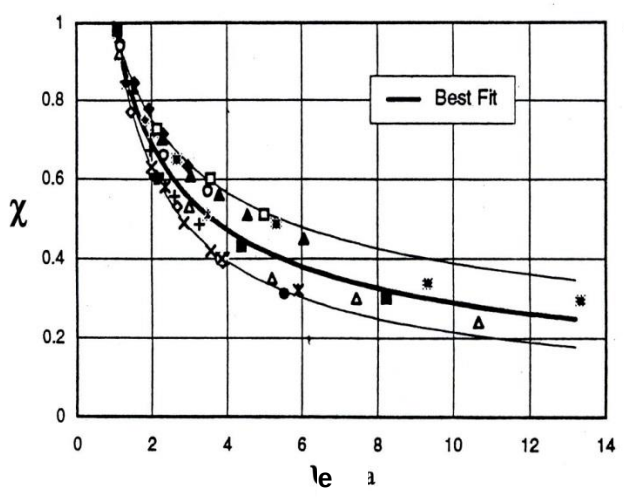

FIGURE 7.8 χ versus matric suction normalized with the air entry value (Khalili & Khabbaz, 1998)

In 2010, Lu et al. (2010) proposed a simple way to estimate χ by introducing the concept of suction stress, σ^s, into the effective stress equation whereby they rewrote Equation 7.6 as:

$$\sigma' = \sigma - u_a - \sigma^s \qquad (7.2)$$

They then argued that the suction stress is related to the matric suction, $s = u_a - u_w$, as follows:

$$\sigma^s = -S_e s = -\frac{\theta-\theta_r}{\theta_s-\theta_r}(u_a - u_w) \qquad (7.3)$$

where S_e = equivalent degree of saturation which is akin to Bishop's (1954) effective stress parameter, χ, for unsaturated soils, θ = volumetric water content, θ_r = residual volumetric water content and θ_s = saturated volumetric water content. σ^s can be calculated using Equation 7.9 and substituted into Equation 7.5 to calculate the infinite slope factor of safety.

By combining Equation 7.9 and van Genuchten's model (Eq. 6.15), S_e can be related to the van Genuchten SWCC as follows:

$$S_e = \frac{1}{[1+(\alpha h)^n]^m} \qquad (7.4)$$

where α and n are van Genuchten model parameters and $m = 1 - 1/n$. Therefore, the suction stress can be rewritten as:

$$\sigma^s = -\frac{s}{[1+(\alpha h)^n]^m} \qquad (7.5)$$

Now the effective stress for an unsaturated soil can be expressed as

$$\sigma' = \sigma - u_a + \frac{s}{\left[1+\left(\frac{\alpha s}{g}\right)^n\right]^m} \qquad (7.6)$$

The effective stress is now a function of the total stress, matric suction and the two van Genuchten parameters: α and *n*. As explained previously, the physical meaning of α is that it is a measure of the matric suction at which the pore fluid begins to leave a drying soil (i.e.; it is the inverse of the air entry pressure) while the parameter *n* is an indicator of the pore size distribution of the soil.

The parameter *n* divides the suction stress into two distinct behavior regimes. When $n \leq 2$ (namely clays), σ^s monotonically increases with increasing suction whereas when $n > 2$ (namely silts and sands), σ^s increases with increasing suction, reaches a peak and then decreases with further suction increase (Figure 7.9). The latter ($n > 2$) is more intuitive and can be explained as follows. σ^s is governed by the product χs (or $S_e s$). At low water contents, *s* is high but $\chi \rightarrow 0$ so $\chi s \rightarrow 0$. On the opposite end of the spectrum, when the soil approaches full saturation, $\chi \rightarrow 1$ but $s \rightarrow 0$. So $\chi s \rightarrow 0$ also. Therefore, there must exist some value of degree of saturation in between 0 and 1 at which χs is a maximum. Lu et al. (2010) explained that there is no maximum with clays because the physico-chemical bonding force is significant when *s* is high, which causes σ^s to remain elevated for clays.

For the silt slope analyzed in this research, *n* is less than 2 (Table 6.3) suggesting that the silt behaves more like a clay than a silt. A landslide warning system is more concerned with the wetting behavior. As the soil is wetted, the suction stress decreases regardless of the value of *n*. Besides, the field suction path typically runs along a scanning curve. Since *n* is associated with either the main wetting or the main drying branch only, the value of *n* is unimportant in the stability analysis (i.e.; it is better to estimate σ^s using Eq. 7.9 rather than 7.11.

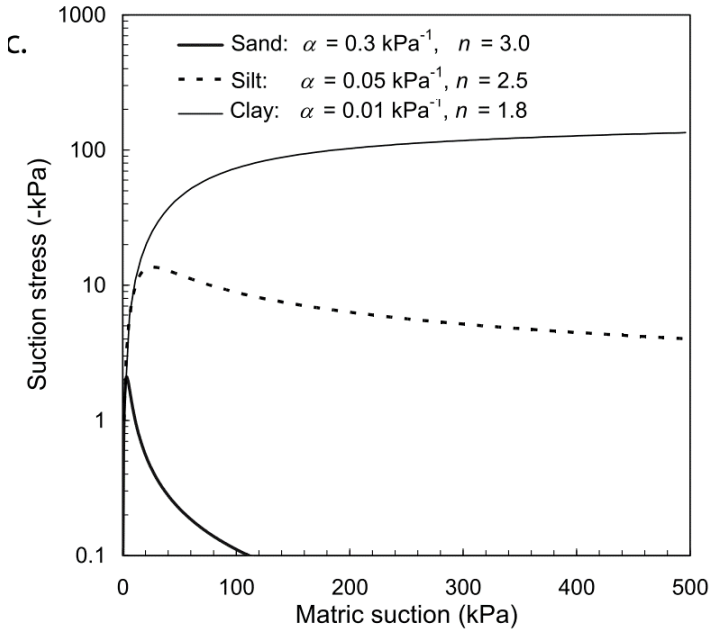

FIGURE 7.9 Soil suction characteristic curve for typical soils with differing n values (from Lu et al., 2010)

The suction stress concept is utilized to estimate the infinite slope analysis factor of safety as a consequence of the 500-year storm. Values of σ^s along vertical lines at the two middle third points of the 63° portion of the slope were estimated from HYDRUS and utilized for infinite slope analyses after both the 5-minute-duration, high intensity and 60-day-duration, lower intensity storms. It was found that the upper of the two middle third portions gave lower factors of safety and only their results are presented below for the sake of brevity.

Rahardjo et al. (2010) observed a time delay of 5 days after the storm for the factor of safety to reach a minimum for a residual soil slope. Zhang et al. (2016) found that it took at most 5 days for the factor of safety to reach a minimum for a residual slope under varying scenarios. Therefore, it is important to investigate the variation of factor of safety with time after a storm.

Figure 7.10 presents factors of safety for the 500-year 5-minute storm at the end of the storm and 60 days after the storm assuming dry initial conditions. It can be seen that the minimum factor of safety occurred at the end of the storm. However, the factors of safety were always greater than 2.0.

Figures 7.11 and 7.12 present the factors of safety for the 500-year 60-day duration storm at the end of storm, 12 hours after the storm, and 3 days after the storm for the initially dry conditions and initially wet conditions, respectively.

For the case of an initially dry slope, the minimum factor of safety occurred at the end of the storm. For this case, the critical depth is about 3.2 m. For the case of an initially wet slope, the minimum factor of

safety did decrease slightly after the end of the storm but not by much. For this case, the sliding plane is at a depth of about 3 m. The time it took for the factor of safety to decrease to a minimum was 3 days.

These analyses utilize Hvorslev's true $\phi'_e \approx 28°$ and $c'_e \approx 18$ kPa. The factor of safety clearly increased compared to the case of the saturated slope suggesting that these values are trending in a reasonable fashion.

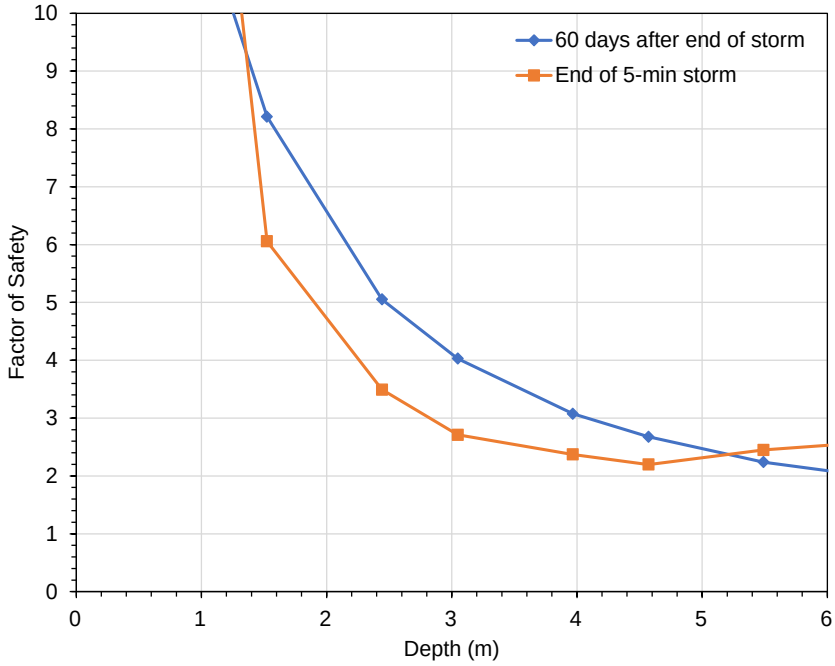

FIGURE 7.10 Factor of safety assuming 63° infinite slope 500-year 5-minute-duration storm

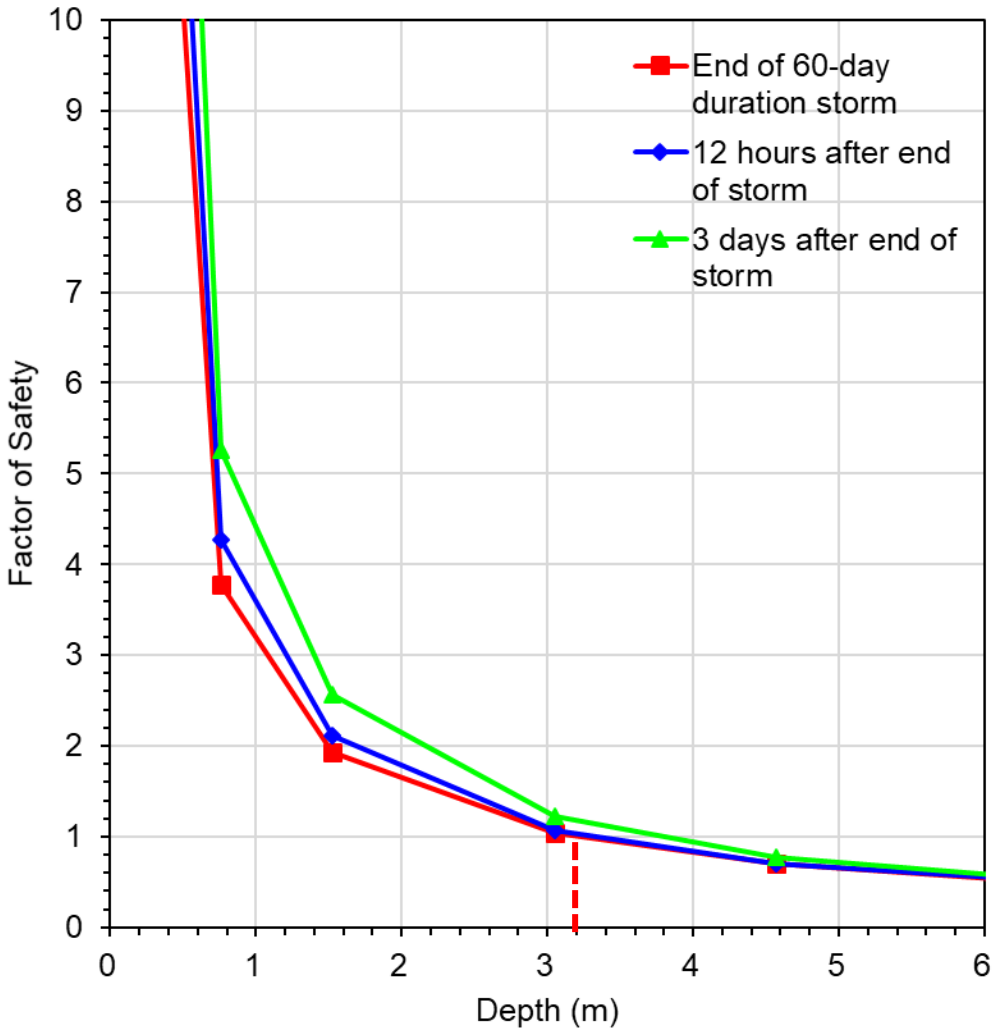

FIGURE 7.11 Factor of safety assuming 63° infinite slope subjected to a 500-year 60-day-duration storm with initially dry conditions

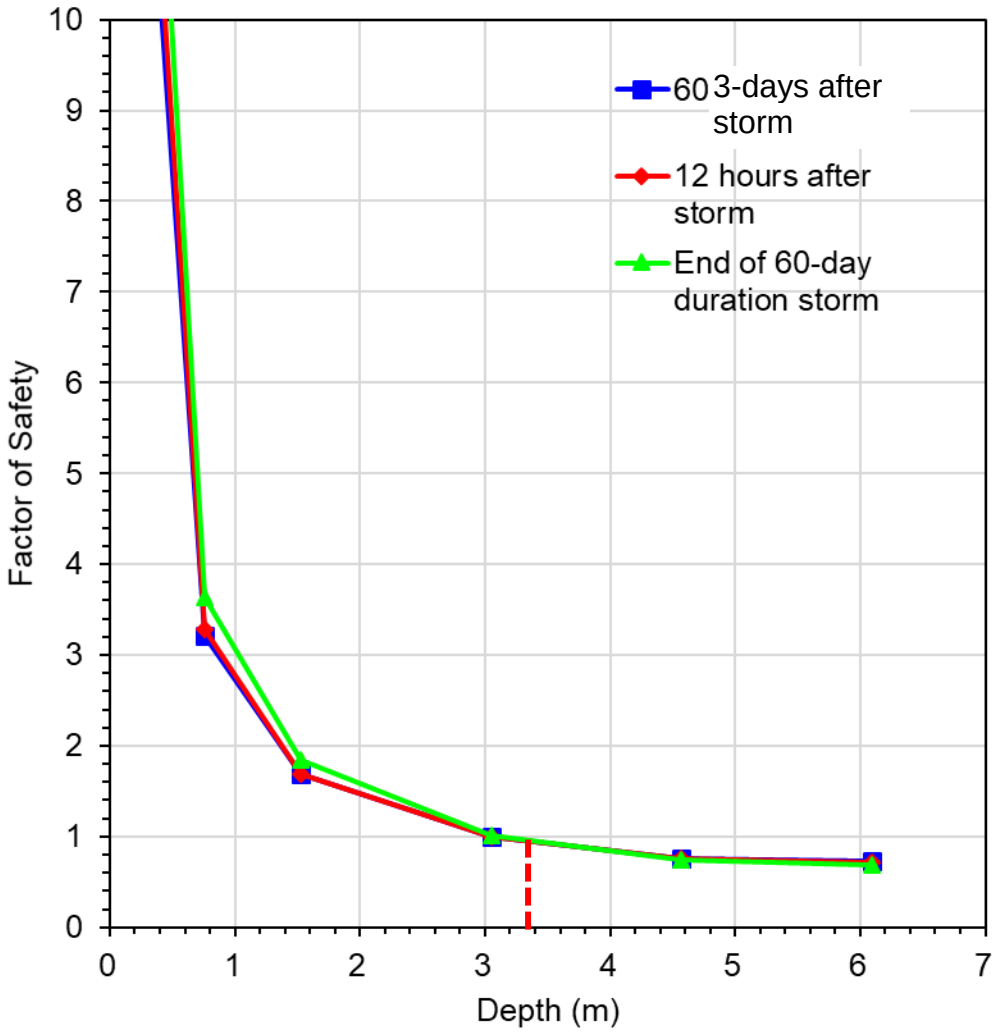

Figure 7.1 Factor of safety assuming 63° infinite slope subjected to a 500-year 60-day-duration storm with initially wet conditions

7.4 2D Slope Stability Analysis During 500-year Storm

Suction values from HYDRUS can be imported into SLOPE/W to perform 2D slope stability analyses for the 500-year storm. SLOPE/W interpolates between suction values to generate equal suction contours, which are then used to estimate the shear strength of the soil. When the slope is unsaturated, SLOPE/W estimates the shear strength of the soil at the bottom of each slice in accordance with the following equation proposed by Vanapalli et al. (1996):

$$\tau = c' + (\sigma - u_a)\tan\phi' + (u_a - u_w)S_e \tan\phi' \quad (7.13)$$

Equation 7.13 can be rewritten as:

$$\tau = c' + \left[(\sigma - u_a) + (u_a - u_w) S_e \right] \tan \phi' \quad (7.14)$$

Since S_e can be expressed in terms of suction using the van Genuchten model (Equation 7.10), therefore the shear strength then becomes:

$$\tau = c' + \left[(\sigma - u_a) + \frac{s}{\left[1 + (\alpha\psi)^n\right]^{(n-1)/n}} \right] \tan \phi' \quad (7.15)$$

which implies that

$$\tau = c' + \left[(\sigma - u_a) + \sigma^s \right] \tan \phi' \quad (7.16)$$

In essence, Vanapalli et al. (1996) had proposed the notion of suction stress about a decade before Lu and Likos (2006) and Lu et al. (2010) without referring to it as suction stress.

When analysing the stability of an unsaturated slope using SLOPE/W, input of suction (*s*), α and *n* throughout the slope is required. However, since the field suction path follows a scanning curve, values of α and *n* from Table 6.3 are inadmissible because they apply either to the main drying or main wetting branches only. This problem can be circumvented in SLOPE/W as follows

1. Use values of *s* and θ from HYDRUS and manually calculate σ^s as follows:

$$\sigma^s = -\left[\frac{\theta}{\theta_s} \right] s \quad (7.17)$$

since θ_r in Equation 7.9 = 0. The beauty of calculating suction stress this way is that θ_s is the same for drying, wetting and scanning (since $\theta_{sd} = \theta_{sw}$) unlike when using α ($\alpha_d \neq \alpha_w$) and *n*.

2. Input the calculated values of σ^s from Equation 7.17 throughout the slope geometry as *s* and assign $\alpha = n = 1$.
3. Calculate the 2D factor of safety for the slope.

This is one of an infinite number of ways to fool SLOPE/W into using the correct value of suction stress for the slope stability analysis.

The same four methods of analyses used for the saturated case (Bishop's simplified, Morgenstern-Price's, Spencer's and Sarma's methods) were utilized to analyse the unsaturated case during the 500-year storm. Summarized in Table 7.1, the results indicate that:

1. The 60-day low-intensity storm on an initially dry slope yielded the lowest factors of safety. The factors of safety increased as the storms trend toward the shorter duration higher-intensity

variety. For the sake of brevity, only the results for the 5-minute and 60-day duration storms are tabulated in Table 7.1;

2. Overall, the factors of safety are greater than 1.19 suggesting that the slope will survive a 500-year storm. For the 60-day low-intensity storm, the lowest factors of safety occur at the end of the storm under initially dry conditions. They were estimated to be 1.196, 1.195, 1.191 and 1.197, respectively using the Bishop's simplified, Morgenstern-Price's, Spencer's and Sarma's methods (see Figs. 7.12, 7.13, 7.14 and 7.15, respectively).
3. The initially dry conditions produced lower factors of safety than the initially wet conditions. Rahardjo et al. (2010) saw similar results where a drier slope "sucked up" more rainfall and decreased in suction much faster than an initially wetter slope during a low intensity rainfall.
4. There was a delayed response for the initially wet slope. The minimum factor of safety occurred three days after the end of the storm. This can be seen by the suction response (Figure 6.34a) at the locations of the 15-ft and 20-ft tensiometers, which continue to decrease after the end of storm. They do not continue to decrease for the initially dry slope (Figure 6.33b).
5. The 60-day duration storm is severe enough to decrease the suctions in the deeper layers to values lower than at shallower depths (Figure 7.16). This has never been observed in the field.
6. Variable rainfall patterns like those proposed by Ng et al (2010) that more resemble real rainfall patterns should be but were not investigated as they are hypothetical scenarios that fall outside the scope of work.

The 2D analyses factors of safety differ from the infinite slope analyses. While the 2D factors of safety indicate that the slope is safe during a 500-year storm, the infinite slope factors of safety especially for the 60-day low-intensity storm do drop below unity. Naturally, the 2D slope analysis is more realistic than the infinite slope analysis, which is accurate only when the slip surface runs roughly parallel to the slope face and is long in comparison to its depth. Despite the fact that the slope is expected to survive this storm, it will be conservative to base threshold values off its seepage pattern. The following section details the background behind the selection of these threshold values.

Table 7-1 500-year 5-minute duration storm 2D factors of safety against slope instability

Analysis Method	Factor of Safety		
	End of storm	3 days after storm	30 days after storm
Simplified Bishop	2.28	2.23	2.21
Morgenstern-Price	2.58	2.40	2.62
Spencer	2.61	2.40	2.65
Sarma	2.34	2.24	2.23

Table 7-2 500-year 60-day duration storm 2D factors of safety against slope instability

Analysis Method	Factor of Safety					
	Initially Wet			Initially Dry		
	End of Storm	12 hours after storm	3 days after storm	End of Storm	12 hours after storm	3 days after storm
Simplified Bishop	1.288	1.286	1.282	1.196	1.208	1.239
Morgenstern-Price	1.287	1.285	1.282	1.195	1.208	1.236
Spencer	1.287	1.285	1.279	1.191	1.204	1.235
Sarma	1.286	1.284	1.281	1.197	1.207	1.238

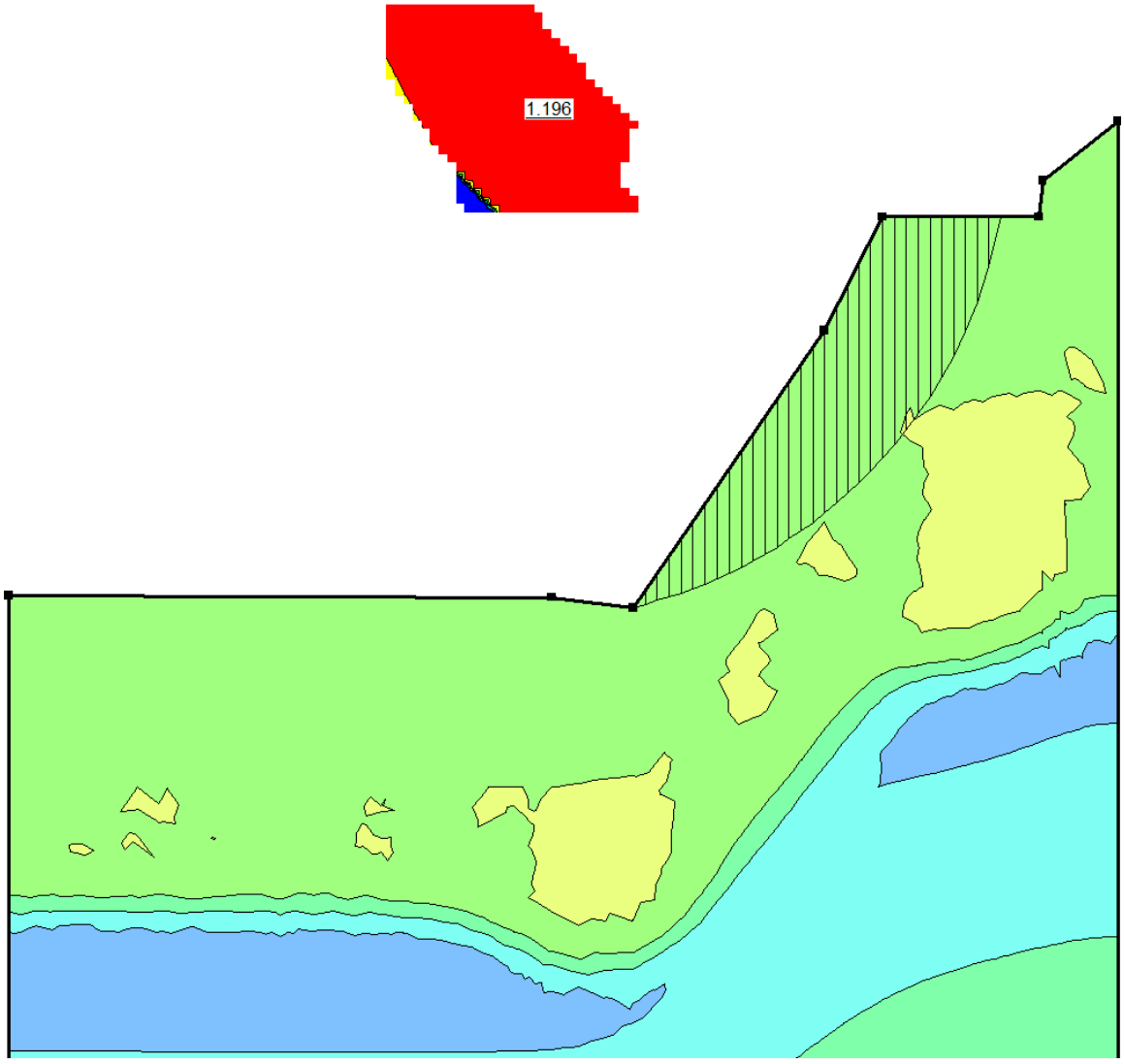

FIGURE 7.12 2D factor of safety using Bishop's simplified method from SLOPE/W for the unsaturated case at the end of a 500-year 60-day low intensity storm with initially dry conditions

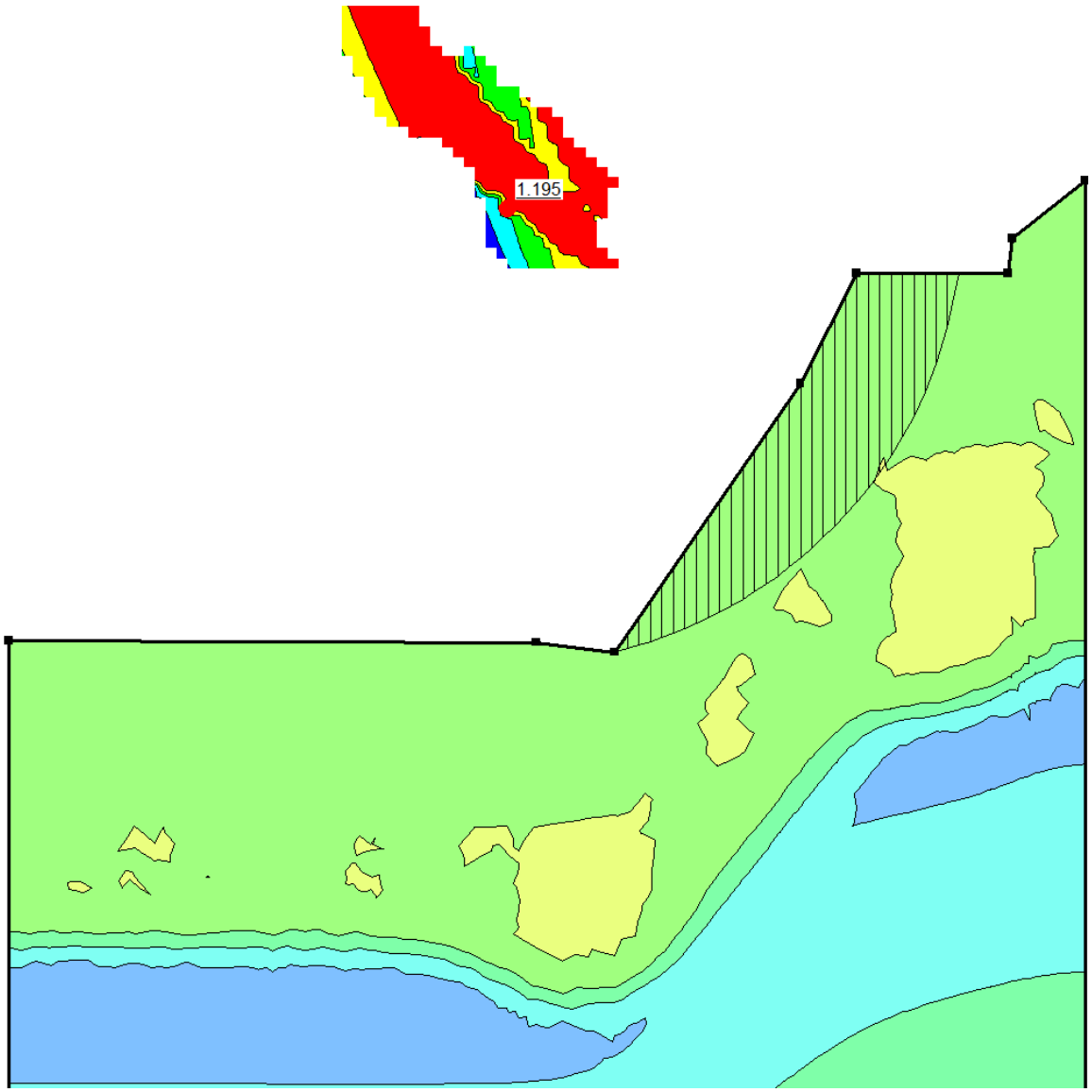

FIGURE 7.13 2D factor of safety using Morgenstern-Price's method from SLOPE/W for the unsaturated case at the end of a 500-year 60-day low intensity storm with initially dry conditions

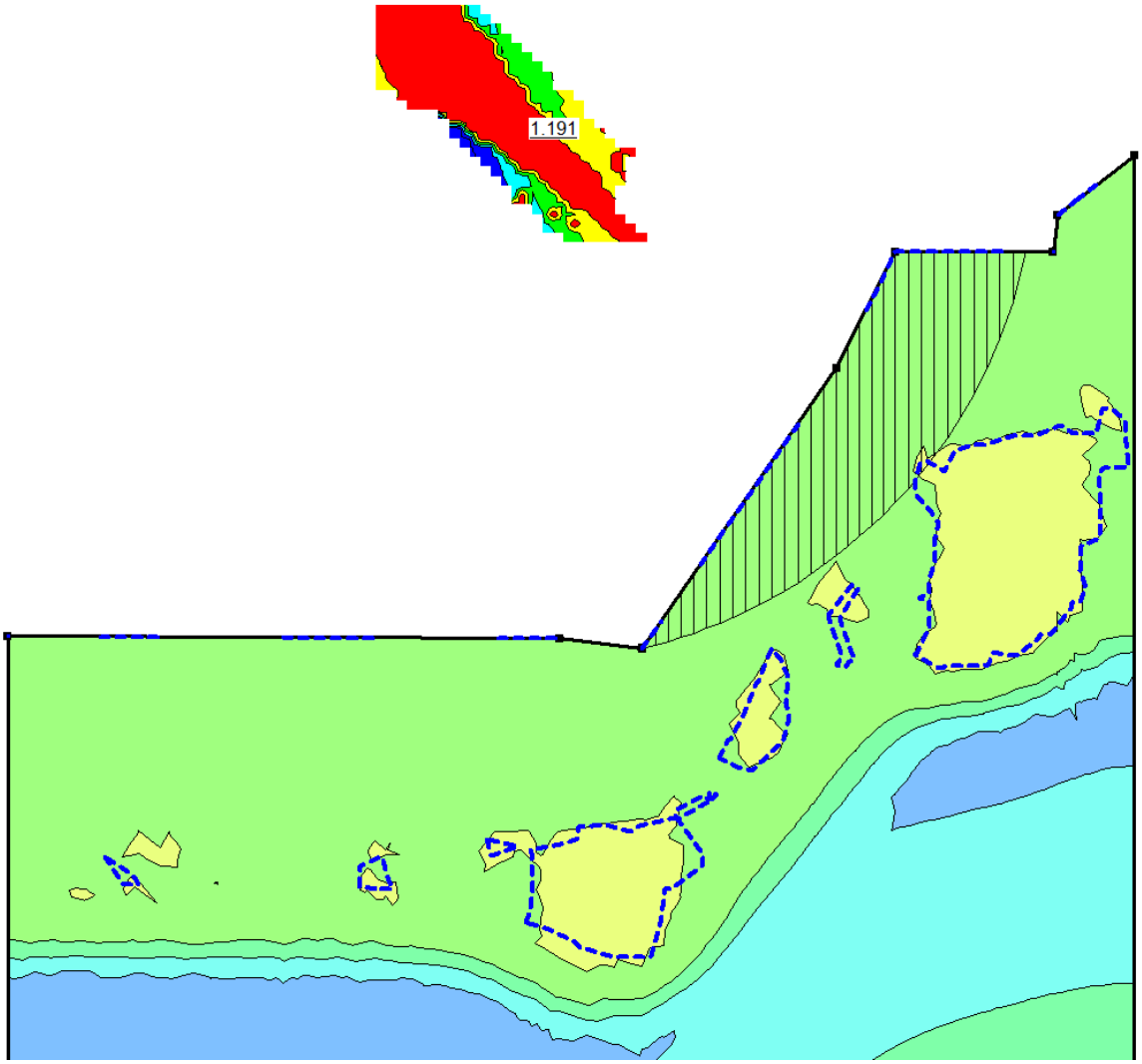

FIGURE 7.14 2D factor of safety using Spencer's method from SLOPE/W for the unsaturated case at the end of a 500-year 60-day low intensity storm with initially dry conditions

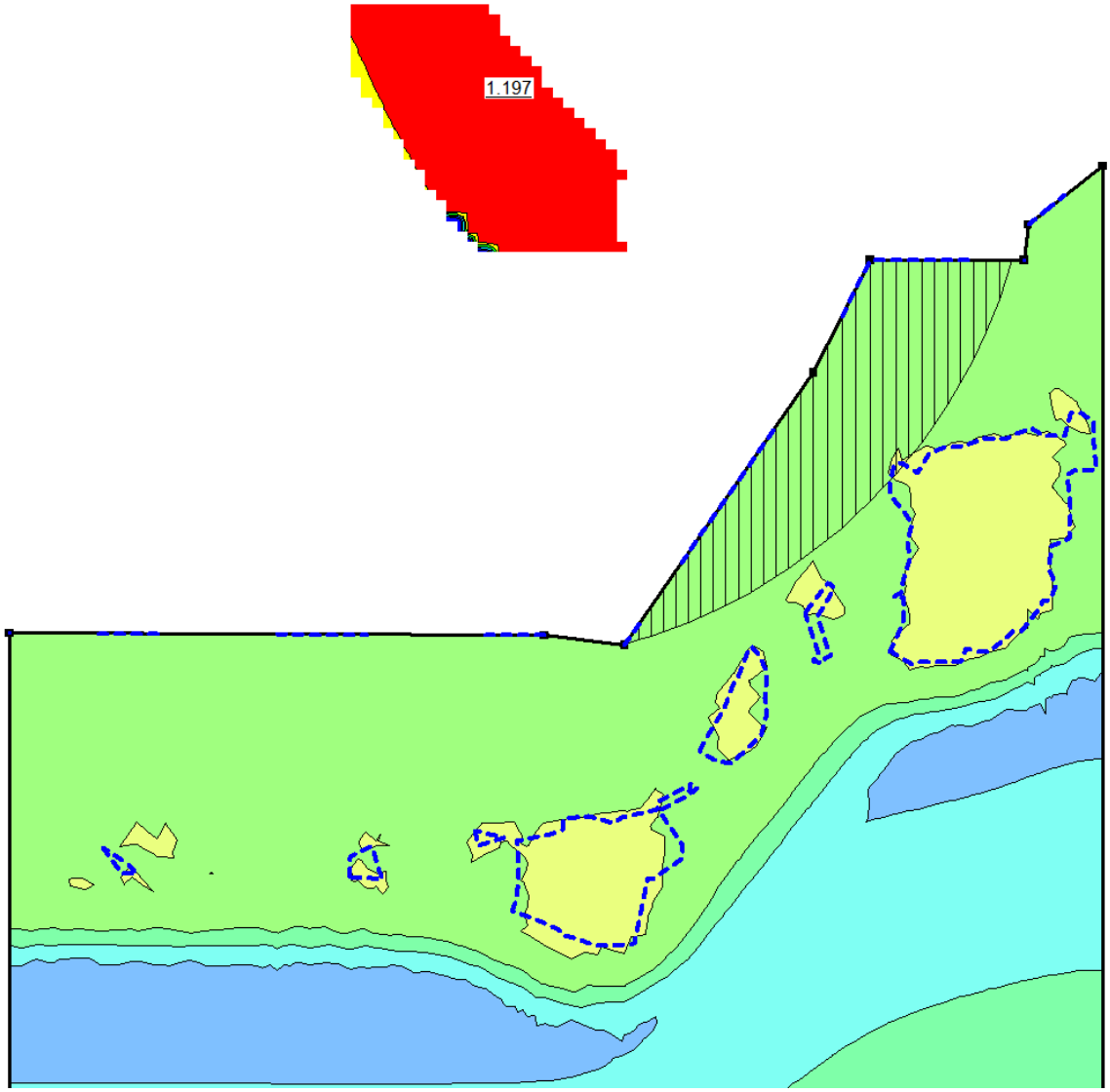

FIGURE 7.15 2D factor of safety using Sarma's method from SLOPE/W for the unsaturated case at the end of a 500-year 60-day low intensity storm with initially dry conditions

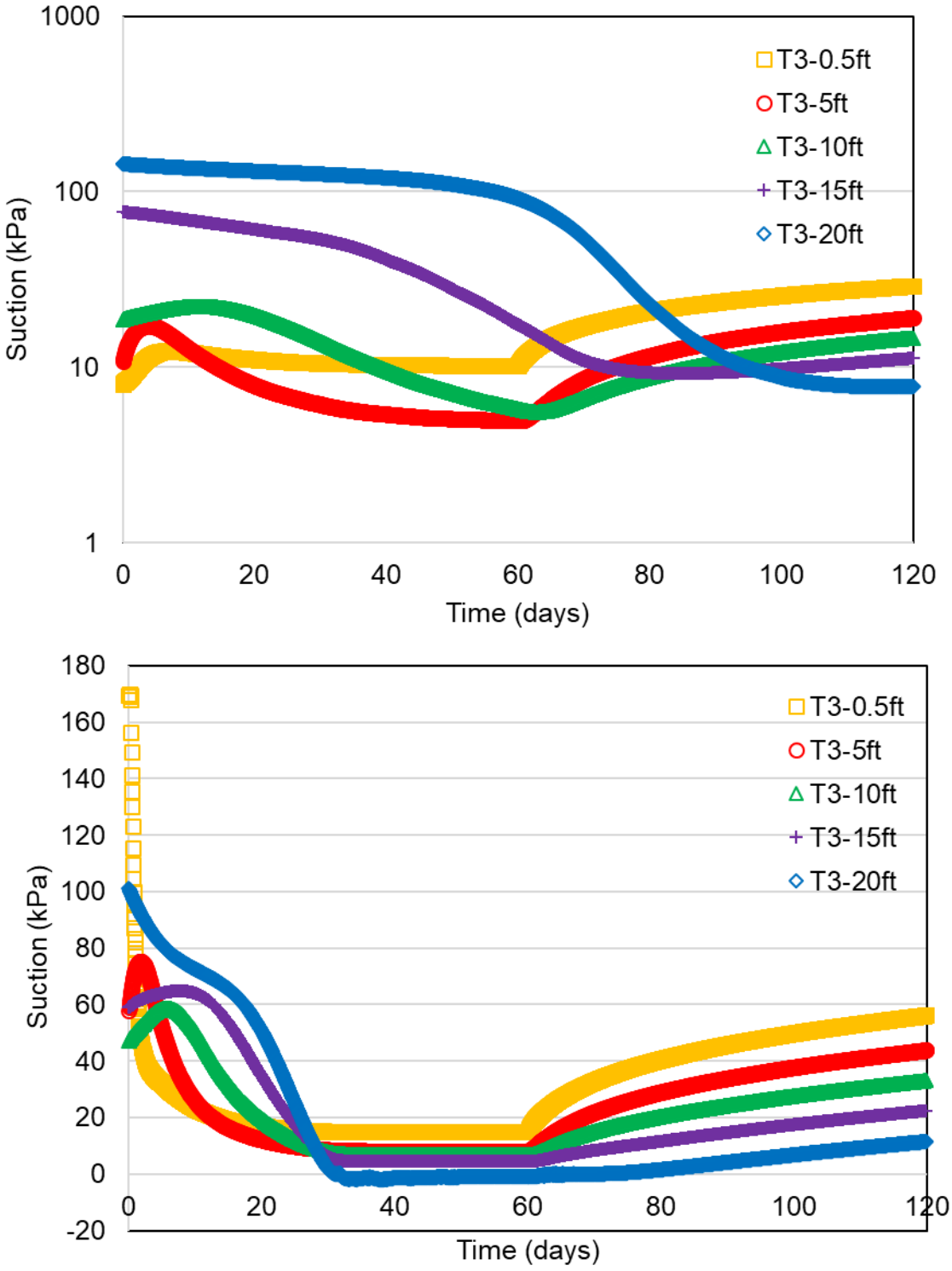

FIGURE 7.16 Suctions predicted using HYDRUS at T3 tensiometers during a 500-year 60-day duration storm for an (a) initially wet slope and (b) initially dry slope

7.5 Threshold Values

A rainfall-induced landslide warning system essentially involves using the observational method (OM) to identify if a slope is rapidly deteriorating. For this particular slope, the "cause" of the rapid deterioration is extreme rainfall and the "symptoms" may include elevated volumetric water content, reduced suction and/or increasing slope movement*. According to Nicholson et al. (1999), the observational method is only applicable if the soil behaves in a ductile fashion; i.e.; significant displacement is required to mobilize the peak strength. If the soil is brittle (i.e.; small displacement to mobilize peak strength which is true for the stiff silt in this slope), then Nicholson et al. (1999) stated that the OM is not applicable. With this slope however, it can be argued that because the hydraulic conductivity of the soil, k, is quite low ($k < k_s = 10^{-6}$ cm/s), there will be ample lead time to forecast whether a slide is impending provided continuous monitoring data of suction/volumetric water content is available.

Nicholson et al. (1999) proposed a traffic-light-based trigger criterion that is useful for establishing instrument thresholds as follows:

1. **Green** = safe site condition
2. **Amber** = decision stage
3. **Red** = implement planned modifications

with the understanding that the monitored value (most likely based on a "symptom" rather than the "cause") follows the trend as shown in Figure 7.16. In light of this figure, plots of the HYDRUS-calculated suction and volumetric water content vs. time values due to the 500-year event at the instrument locations are shown in Figs. 7.17 and 5.18 for the 5-minute, high-intensity storm and Figs. 7.19 and 7.20 for the 60-day, low-intensity storm.

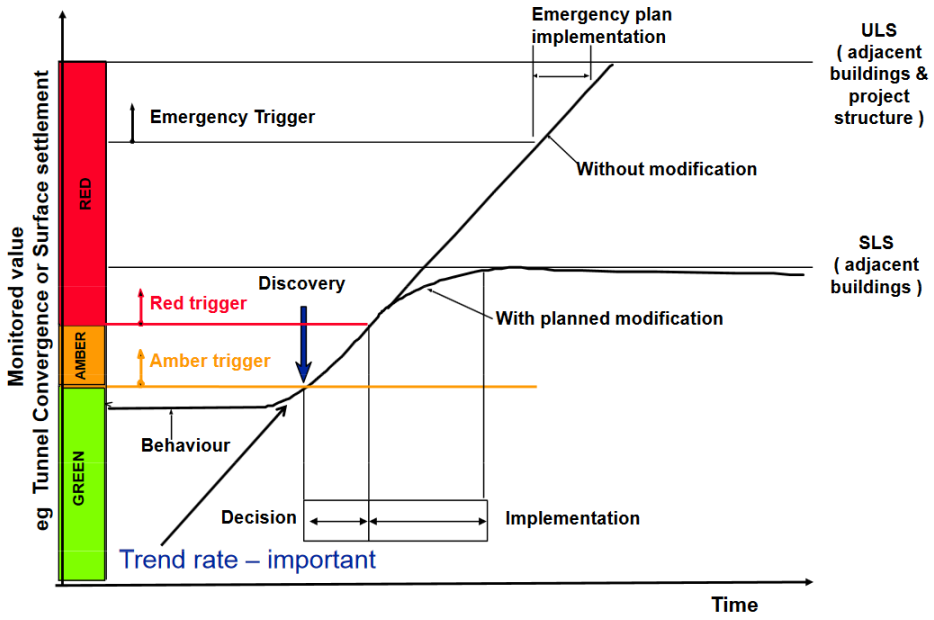

FIGURE 7.17 Traffic-light-based trigger criteria useful for selecting threshold values after (after Nicholson et al., 1999)

For an instrument to be considered a good candidate for use as a threshold indicator, the response has to be in the correct direction; i.e.; as a result of the storm, volumetric water contents should trend upward and suctions should trend downward. Otherwise, there may be ambiguity as the opposite trend is more closely associated with a dry spell.

Based on this criterion and based on the 5-minute storm simulation, all sensors in Borehole 3 trend in the right direction and make good candidates except for T3 tensiometers at 3.05 and 4.57 m (10 and 15 ft). Use of T3 tensiometer at 1.52 m (5 ft) is questionable. Even though there was an episode of a decrease in suction, there were also two episodes of suction increase.

Based on this criterion and based on the 60-day storm simulation, all sensors in Borehole 3 trend in the right direction and make good candidates. Even though the suctions in the T3 tensiometers at depths of 1.52, 3.05 and 4.57 m (5, 10 and 15 ft) increased initially, they eventually decreased as the 60-day storm progressed. Due to the erratic observations in the T3 tensiometers at 1.52, 3.05 and 4.57 m (5, 10 and 15 ft) and due to the fact that the HYDRUS analyses do not predict suctions as well in these instruments (Figure 6.28 through 6.30) compared to the shallower sensors (Figure 6.26 and 6.27), the T3 tensiometers at 1.52, 3.05 and 4.57 m (5, 10 and 15 ft) will not be utilized as triggers for instrument thresholds.

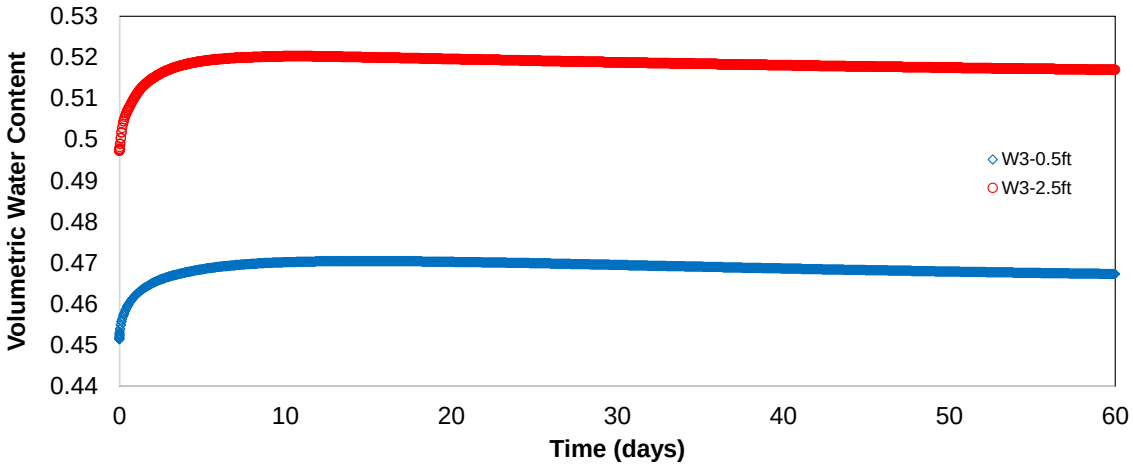

FIGURE 7.18 *Volumetric water content vs time during and after 500-year 5-minute, high-intensity storm at W3 water content sensors*

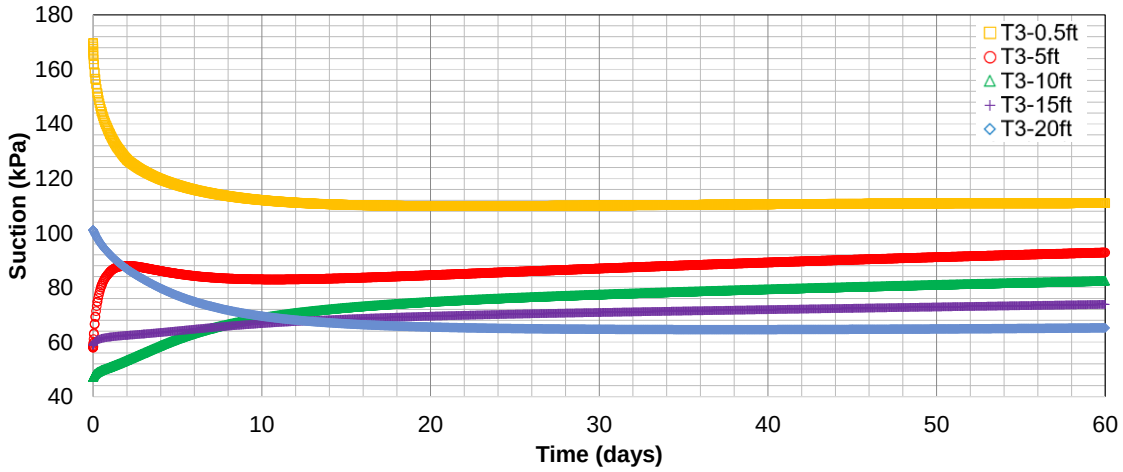

FIGURE 7.19 Matric suction vs time during and after 500-year 5-minute, high-intensity storm at T3 tensiometers

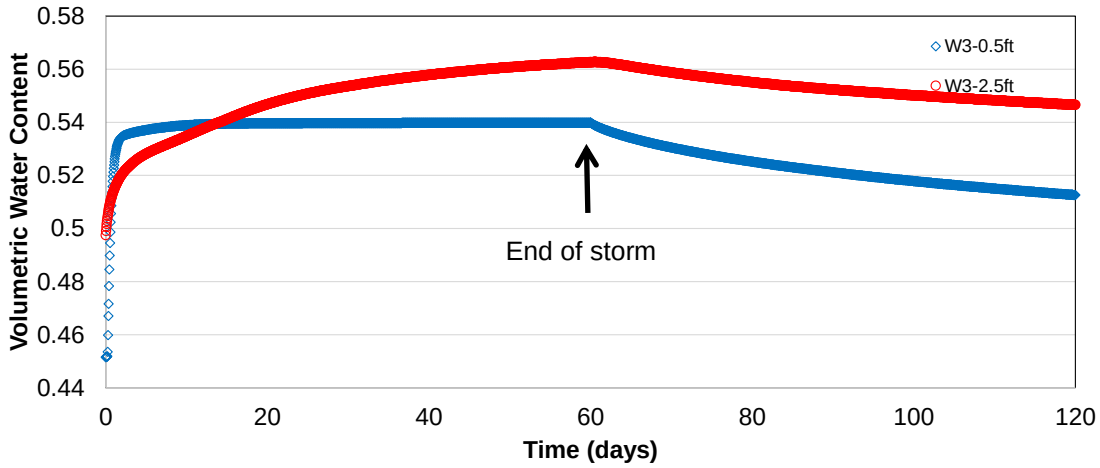

FIGURE 7.20 *Volumetric water content vs time during and after 500-year 60-day, low-intensity storm in W3 water content sensors*

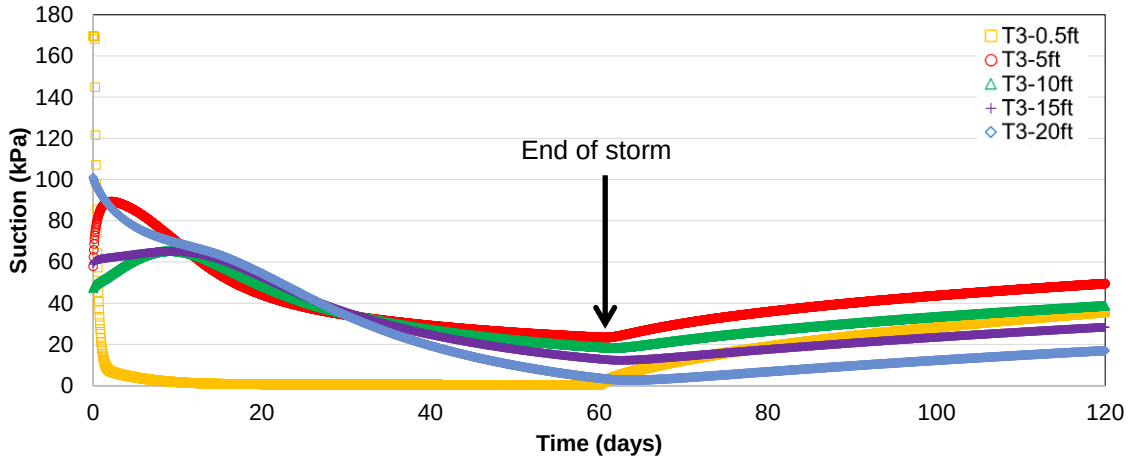

FIGURE 7.21 Matric suction vs time during and after 500-year 60-day, low-intensity storm in T3 tensiometers

A discussion on the assignment of threshold values is best facilitated with the following information:

1. Replots of W3 and T3 instruments to cover the 500-year 60-day, low intensity storm period only (Figs. 7.21 and 7.22);

2. Average, minimum and maximum instrument values recorded during the period of this study (Table 7.2).

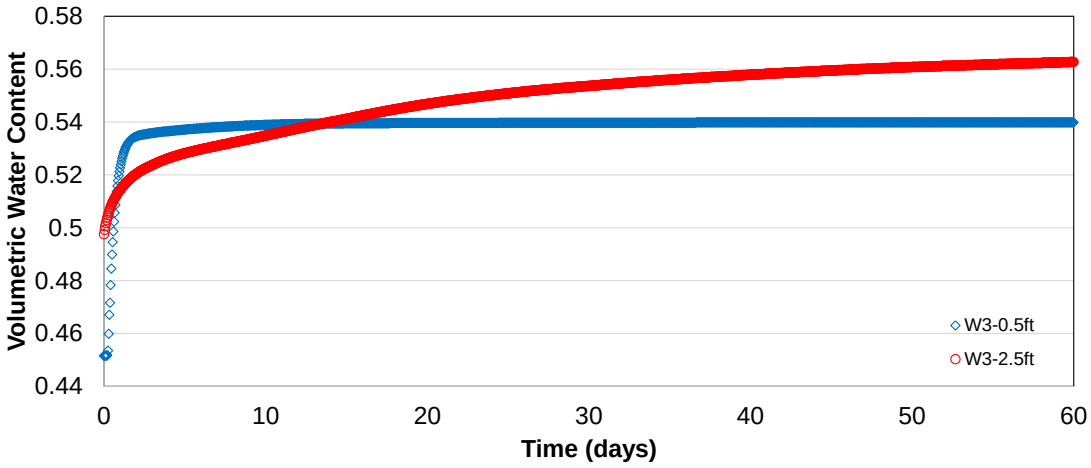

(a)

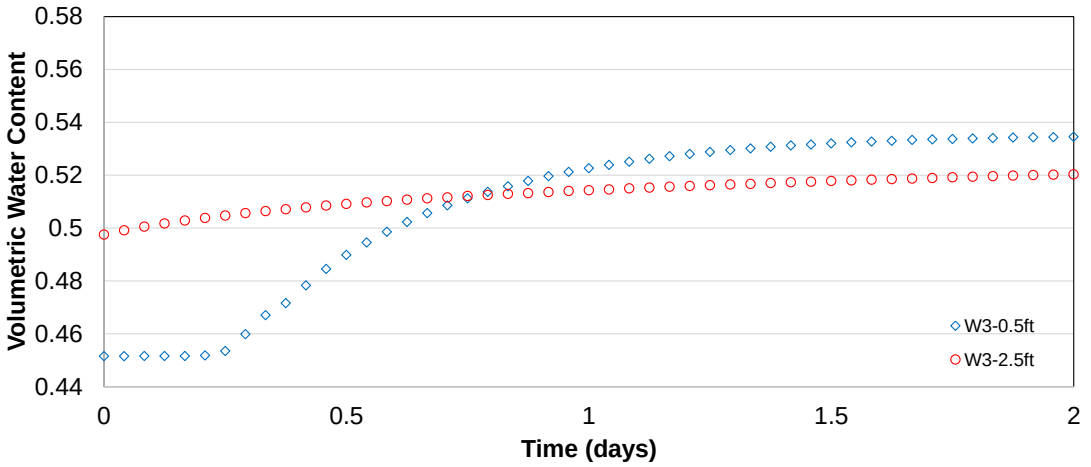

(b)

FIGURE 7.22 (a) Volumetric water content vs time during 500-year 60-day, low-intensity storm in W3 water content sensors and (b) blow-up of the first two days of this plot

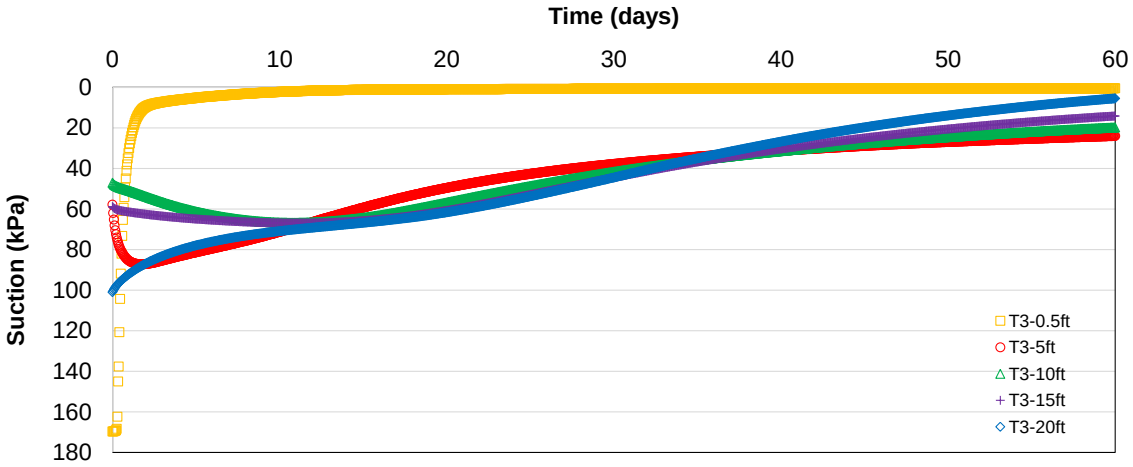

(a)

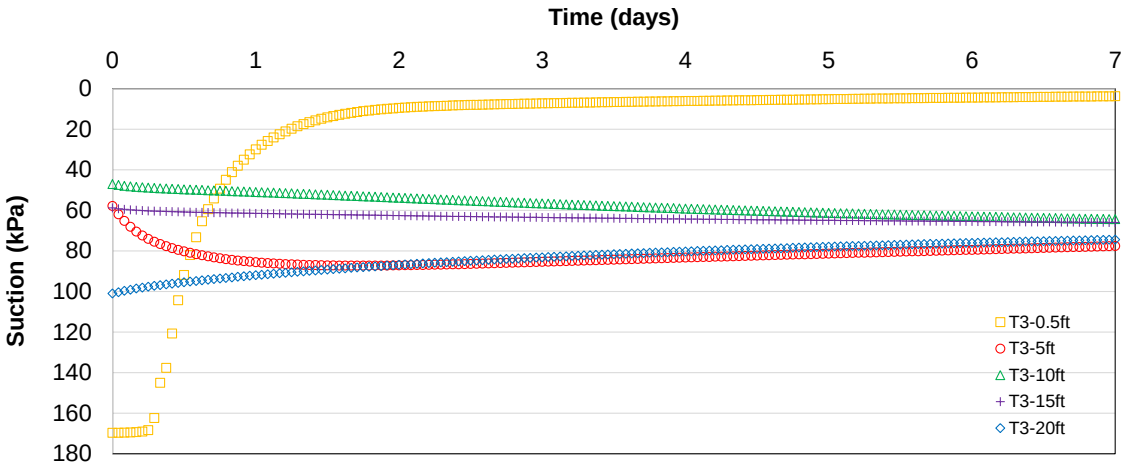

(b)

FIGURE 7.23 (a) Matric suction vs time during 500-year 60-day, low-intensity storm in T3 tensiometers with the vertical axis reversed and (b) blow-up of the first 7 days of this plot

Table 7-3 Mean, minimum and maximum recorded instrument values

Instrument	Depth (m/ft)	Mean Reading	Minimum Reading	Maximum Reading
Water content sensor W3	0.15/0.5	0.46	0.37	0.50
Water content sensor W3	0.76/2.5	0.48	0.40	0.53
Tensiometer T3	0.15/0.5	76.4	9.1	684
Tensiometer T3	1.52/5	43.5	10.8	146
Tensiometer T3	3.05/10	48.9	11.2	79
Tensiometer T3	4.57/15	68.7	51.9	112
Tensiometer T3	6.1/20	115.2	94.1	193

The discussion for each instrument is as follows:

1. W3 at 0.15 m (0.5 ft) – This instrument reacted very rapidly to the 60-day storm. In 2 days, the volumetric water content increased by 0.08 from 0.45 to about 0.54. The threshold values have to be selected in light of the field measured values where the volumetric water content averaged 0.46 with a maximum of only 0.50. The proposed amber and red thresholds are 0.51 and 0.53, which must be accompanied by at least 2 days of rainfall averaging about 1 inch/day (0.043 inches/hr).

2. W3 at 0.76 m (2.5 ft) – This instrument reacted more gradually to the 60-day storm. In 2 days, the volumetric water content increased by 0.02 from 0.5 to about 0.52. The maximum volumetric water content reached was 0.563 at 60.5 days. The threshold values have to be selected in light of the field measured values where the volumetric water content averaged 0.48 with a maximum of 0.53. The proposed amber and red thresholds are 0.54 and 0.55 accompanied by at least 14 days of rainfall averaging about 1 inch/day (0.043 inches/hr).

3. T3 at 0.15 m (0.5 ft) – This instrument reacted very rapidly to the 60-day storm. In 2 days, the suction decreased by 159 kPa from 169 to 10 kPa. The minimum suction reached was 0.5 kPa at 54 days. Realistically, the tensiometer cannot read suctions less than 9 kPa due to the limitation of the sensor. The threshold values have to be selected in light of this sensor limitation and in light of the field measured suctions which averaged 76 kPa and with minimum and maximum readings of 9 and 684 kPa. The proposed amber threshold is 10 kPa accompanied by at least 2 days of rainfall averaging about 1 inch/day (0.043 inches/hr). Due to the limitation of this sensor, it is not reasonable to propose a red threshold.

4. T3 at 6.1 m (20 ft) – This instrument reacted more gradually to the 60-day storm. In 51 days, the suction decreased by 92 kPa from 101 to 9 kPa. The minimum suction reached was 2.6 kPa at

63 days. Realistically, the tensiometer cannot read suctions less than 9 kPa due to the limitation of the sensor. The threshold values have to be selected in light of this sensor limitation, in light of the fact that the HYDRUS analysis for the 500-year, 60-day duration low intensity storm tends to under-predict suctions at this depth (Figure 6.31), and in light of the field measured suctions which averaged 115 kPa and with minimum and maximum readings of 94 and 193 kPa. The proposed amber and red thresholds are 70 and 50 kPa accompanied by at least 14 days of rainfall averaging about 1 inch/day (0.043 inches/hr).

Table 7-4 Proposed threshold values for the various monitoring instruments

Instrument	Amber Threshold Value	Red Threshold Value	Accompanying Threshold
W3 at 0.15 m	0.51	0.53	2 days rain averaging about 1 inch/day
W3 at 0.76 m	0.54	0.55	14 days rain averaging about 1 inch/day
T3 at 0.15 m	10 kPa	-	2 days rain averaging about 1 inch/day
T3 at 6.1 m	70 kPa	50 kPa	14 days rain averaging about 1 inch/day

Planned modifications for the amber trigger can consist of placing tarp or geomembrane on the slope crest to minimize infiltration into the slope. For the red trigger, closing the lane closest to the slope may be prudent until the suctions increase, and the water contents decrease.

7.5.1 Error Analysis

In the development of instrument threshold values, the possible sources of uncertainty include:

1. Error in the instrument readings themselves;
2. Error in the transient hydrological model; and
3. Error in the design storm characteristics.

With respect to 1, the instruments have been factory calibrated. The factory provided accuracy of the tensiometers, water content sensors and rain gage are ±10%, ±3% and ±1%, respectively as summarized in Table 4-1. There is every reason to believe that the calibration of the instruments was not compromised during transport or during installation because the HYDRUS results predicted the hourly response of all seven instruments very well for a period of over 2.5 years as shown in Figures 6.24 through 6.29. The correlation coefficients between the predicted and measured instrument response values are summarized in Table 7-5.

Table 7-5 Improved correlation coefficients between calculated and measured suctions and volumetric water contents for the final calibration run

Depth (m)	Suction	Volumetric Water Content
0.15	0.95	0.93
0.76	-	0.86
1.52	0.89	-
3.05	0.87	-
4.57	0.65	-
6.10	0.74	-

It is unlikely that this level of agreement is fortuitous. So, there must be some credence to the accuracy of the transient hydrological model as well. This level of agreement further justifies the use of: (1) a software that models SWCC and HCF hysteresis; and (2) porosity-dependent SWCC and HCF in the transient hydrological model, which incidentally are two of the biggest takeaways from this research.

Characteristics of the design storm are most likely the greatest level of uncertainty among the 3 sources of error because this was developed or assumed for an event that has not yet occurred. There is uncertainty in the prevailing ground moisture (although both dry and wet initial conditions were analyzed and it was found that the initially dry conditions were more critical for slope stability) prior to the design storm as well as uncertainty in the intensity, duration and time history of the design storm rainfall (a constant precipitation rate with time for a period of 60 days was used because the longer the duration, the more conservative the results with respect to slope stability). The literature has shown that a storm that is front-loaded is more critical but sensitivity analyses of the shape of the precipitation time-history for the design storm is beyond the scope of this work. Besides, it may not be necessary because ultimately, threshold values cannot be categorized as outright right or wrong. There could be a possible range of values that could be utilized without compromising the stability of the slope.

7.5.2 Applicability of Threshold Values to Other Slope Sites

Landslide warning systems can be site specific or regionally based. A site-specific landslide warning system is more reliable than a regional, empirically-based landslide warning system. In this research, a landslide warning system was developed for a specific slope with its own unique geometry, soil properties, hydrological conditions and monitoring instruments. Soil properties vary with location and depth. Therefore, the instrument thresholds, geotechnical properties and transient flow model developed are not applicable to other slopes. Only the principles can be used to develop other site-specific landslide warning systems. A set of guidelines to develop site-specific rainfall-induced landslide warning systems are provided below.

1. Instruments capable of measuring high-resolution suction response from full-saturation to high suction range (past the soil air entry value) should be installed with companion water content sensors at the same depth and as near to the slope face as possible. Near the ground surface,

the instruments should be installed at closer depth increments because the zone of interest is at shallow depths.

2. A total weather station would be useful to install at the slope site. This will avoid reliance on third party weather data that may or may not be representative of the actual site.
3. A geotechnical investigation should be performed with continuous disturbed and undisturbed sampling of the geomaterial.
4. Laboratory tests on undisturbed samples should be performed to obtain the main wetting and drying SWCC and HCFs as a function of porosity. This research shows that pressure-dependent SWCC is of paramount importance to obtain a good fit between predicted and measured instrument response to the applied boundary conditions.
5. To the author's knowledge at the time of writing, HYDRUS 2D/3D is the only commercially available software capable of performing transient hydrological analyses considering SWCC and HCF hysteresis.
6. The transient hydrological analysis must be calibrated to field measured suction and water content response over several dry-wet cycles to gain confidence that the model is reliable.
7. Once calibrated, the transient hydrological flow model should be used to predict the suction and water content response to hypothetical design storms. The estimated suction stresses can then be inserted into a slope stability or numerical model to assess the slope's performance during the design storm.
8. The predicted suction and water content response during the design storm should be compared to the maximum and minimum recorded field measured data, to establish the instrument thresholds.
9. Nicholson et al's (1999) traffic light procedure provides a logical approach to establish instrument thresholds.

8 FEM ANALYSIS

It was originally intended to develop threshold values based on another measured symptom, lateral deflection, in addition to suction and volumetric water content. However, due to the limitations of the software utilized in this research, it was decided that any threshold values of lateral deflection developed based on finite element analyses would be difficult to justify with a great deal of confidence. The reasons can be explained by identifying the software limitations below.

8.1 CODE_BRIGHT

CODE_BRIGHT is an extremely powerful finite element software developed at the Universitat Politecnica de Catalunya (2017) that can be used to solve uncoupled and coupled problems in soils. It can handle hydro-mechanical, thermo-mechanical and hydro-thermal problems in one-, two- and three-dimensions. It uses the Basic Barcelona Model (BBM) as the constitutive model for unsaturated soils. The BBM is an elasto-plastic model that can be considered as state-of-the-art for unsaturated soils at the time of writing. The model was formulated for isotropic and triaxial compression stress states. It can model both collapse and expansive responses of unsaturated soils upon wetting. When the soil reaches saturation, the BBM defaults to the modified Cam-clay model.

After extensive use of this software to solve just hydro- or seepage problems for the unsaturated slope, it was discovered that agreement between the calculated and measured values of suction and volumetric water content was difficult to achieve. When the field suction paths were superimposed on the SWCC, it was realized that the field values of suction and water content do not follow the wetting or drying curves in most instances. Instead, they scan. Since CODE_BRIGHT does not allow scanning, it was recognized as a major limitation that precluded its use to evaluate the slope deformation behaviour.

8.2 Slope Cube Module in HYDRUS

HYDRUS 2D is a finite element software that is renowned for its capability to solve problems involving water flow and solute transport in variably saturated media. This software was utilized after failed attempts with CODE_BRIGHT to simulate scanning because HYDRUS 2D does have a scanning routine for water flow in unsaturated soils. The **S**lope **S**tress and **S**tability (Slope Cube by Lu et al., 2016) framework is a HYDRUS add-on module that combines variably-saturated flow and stress fields to simulate transient hillslope hydrology and stability in response to rainfall. Slope Cube calculates the factor of safety at each point in the slope instead of a single factor of safety for the entire slope that is

traditionally employed in limit equilibrium analysis. The local factor of safety is then quantitatively used to identify stress paths toward failure due to rainfall.

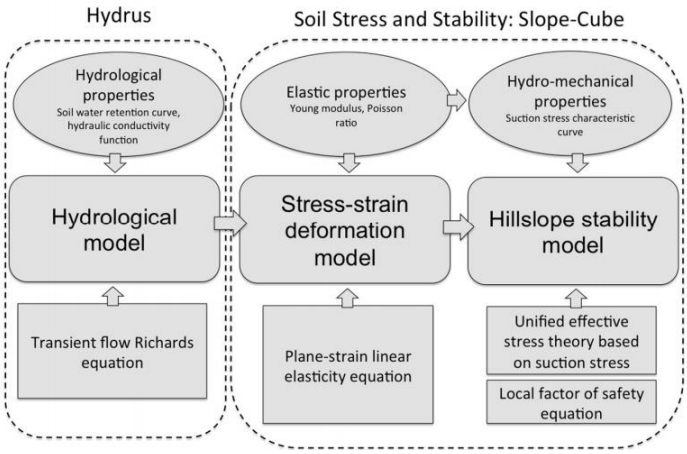

FIGURE 8.1 Flow chart showing Slope Cube analysis methodology (after Lu et al., 2016)

The Slope Cube methodology for plane-strain analysis of a slope is summarized in Figure 8.1. It calculates soil stresses, strains and displacements in the slope using a linear elastic finite element code, FEM2D, originally developed by Reddy (1993). For plane strain problems, the governing differential equations are the force-equilibrium equations in 2D as follows:

$$\frac{\partial \sigma_{xx}}{\partial x} + \frac{\partial \sigma_{xz}}{\partial z} = 0 \tag{8.1}$$

$$\frac{\partial \sigma_{zz}}{\partial z} + \frac{\partial \sigma_{xz}}{\partial x} + Z = 0 \tag{8.2}$$

where σ_{xx} and σ_{zz} are the normal stresses in the horizontal and vertical directions, respectively, σ_{xz} is the shear stress and Z is the body force due to the soil in the slope calculated using field moist unit weights. Stresses are all effective and Slope Cube calculates effective stresses, σ', as follows:

$$\sigma' = \sigma - u_a - \sigma^s \tag{8.3}$$

where σ = total stress, and σ^s = suction stress which is given by Eq. 7.9 or 7.11.

In the context of the Mohr-Coulomb envelope, the physical meaning of the suction stress can be best explained with the aid of Figure 8.2. When the soil is sheared under saturated conditions, the matric suction, $u_a - u_w = 0$ but the suction stress, $\sigma^s = -c'/\tan\phi'$. As matric suction increases, the suction stress and consequently the apparent cohesion increase. Therefore, increasing the matric suction effectively contributes to an increase in the apparent cohesion.

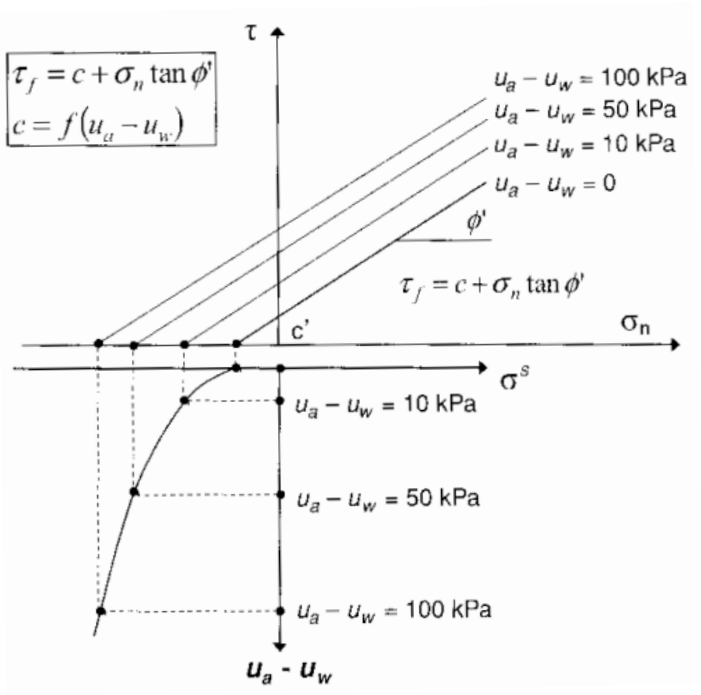

FIGURE 8.2 Determination of suction stress from the apparent cohesion intercept with varying degrees of suction (after Lu and Godt, 2013)

Lu et al. (2016) argues that traditional limit equilibrium slope stability analysis suffers from the following limitations: (1) the failure surface is presumed (usually circular in a 2D analysis); and (2) failure occurs simultaneously along every point on the failure surface. To overcome these limitations, the Slope Cube analysis adopts the shear strength reduction approach with the aid of finite element analysis. In the finite element routine, the soil is assumed to be linear elastic. Linear elasticity may be simple but it suffers from the following shortcomings:

1. Selecting a representative Young's modulus for soils which have a non-linear and stress-dependent stress-strain curve is extremely challenging;
2. A linear elastic soil will not fail unless a yield strength is specified;
3. Soil is not elastic at large strains; e.g.; if a sand is initially sheared in triaxial compression and then the confining stress is decreased, that sand will eventually fail when the confining stress is low enough. However, if Hooke's law is used, the soil will just unload elastically and not fail (Lade, 2007);
4. Hooke's law cannot handle stress path dependency (Lade, 2007);
5. A Hookean soil cannot have a negative Young's modulus and hence cannot strain soften (Lade, 2007);

6. An isotropic elastic soil cannot dilate since Poisson's ratio, μ, is limited by $-1 \leq \mu \leq 0.5$. If a soil dilates, μ must be > 0.5. Use of $\mu > 0.5$ results in negative work; i.e.; energy can be produced along certain stress paths which is clearly incorrect (Lade, 2007);

7. Hooke's law cannot handle normal strain and shear stress or normal stress and shear strain coupling effects in soil as shown in Figure 8.3 (Lade, 2007);

8. With Hooke's law, it is implied that stress and strain directions or stress increment and strain increment directions coincide. However experimental evidence based on simple shear and torsional shear tests indicate that stress directions coincide with strain increment directions at high stress levels as shown in Figure 8.4 (Lade, 2007). This has been observed in materials that behave plastically and forms the basis of Saint Venant's (1870) principle whereby he proposed that the principal axes of stress coincide with the principal axes of incremental plastic strain during stress rotation.

Due to the abovementioned limitations, any deformation analysis using Slope Cube cannot be relied upon to derive meaningful threshold inclinometer deflection values. Without a fundamentally sound finite element routine, no logical and reasonable inclinometer threshold values can be established with a great degree of confidence.

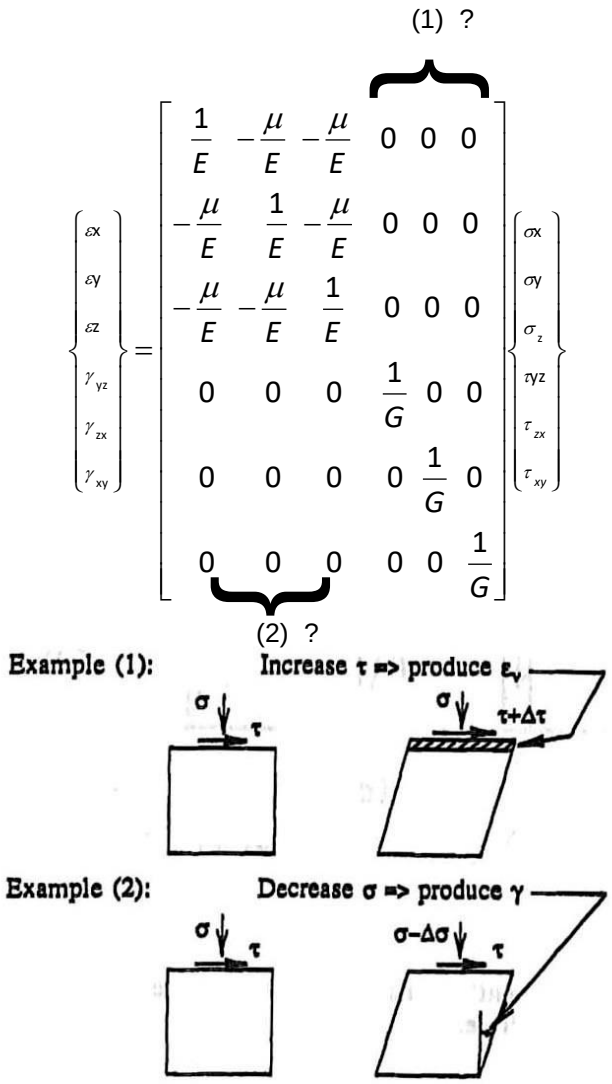

FIGURE 8.3 Normal strain and shear stress or normal stress and shear strain coupling in soils (after Lade, 2007)

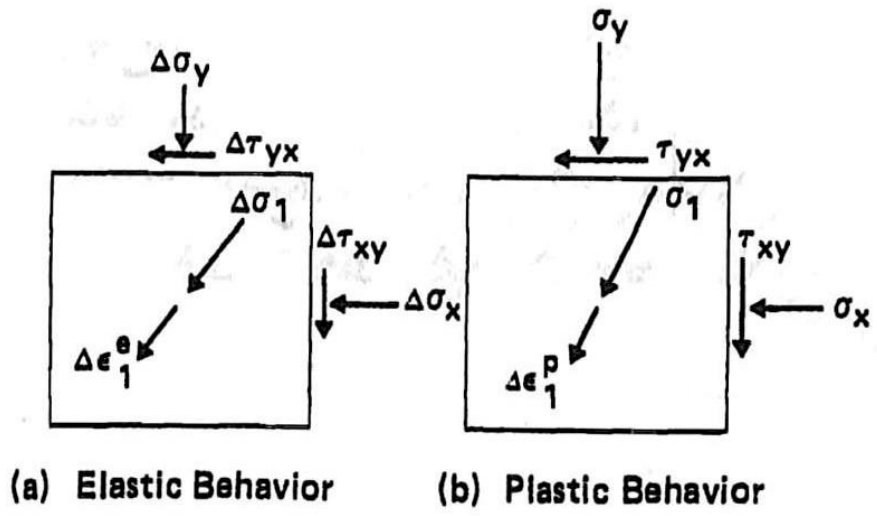

FIGURE 8.4 (a) Elastic and (b) plastic behavior of material during rotation of principal stress axes (after Lade, 2007)

9 SUMMARY AND CONCLUSIONS

9.1 Summary and Conclusions

A landslide warning system was developed for a cut slope along Kalaniana'ole Highway by performing a soil investigation, collecting soil samples, performing laboratory tests, installing monitoring instruments at a soil slope site, collecting field data, developing and calibrating a saturated-unsaturated transient hydrological model, using the calibrated model to predict pore pressure/suction during a design rainfall event (a 500-year storm), inputting these pore pressure/suction values into a slope stability analysis and determining threshold values of these instruments to develop a real-time landslide warning system.

Laboratory test results showed that the soil was a uniform stiff to very stiff high plasticity silt. Field instruments installed included tensiometers to measure in situ suction, water content sensors to measure volumetric water content, in-place inclinometers to measure lateral ground deflections and a rain gage to measure precipitation at the slope site.

A saturated-unsaturated transient hydrological flow model was developed and calibrated using the field data and the lab test data. Calibration was achieved by adjusting the model parameters to match the laboratory measured and calculated SWCC and HCF, and to match calculated and field-measured suctions and water contents. The following conclusions can be made from this research.

1. A field suction path can be drawn by plotting tensiometer and the corresponding water content sensor readings over several drying-wetting events. It usually runs along a scanning curve except during periods of heavy rain or extreme drought when the field suction path could join up and run along the wetting or drying branches, respectively. Therefore, it is important for a saturated-unsaturated transient flow model to allow for scanning in order to predict field behaviour reliably;
2. If scanning is not allowed, the calculated field suction path will run along the main drying or main wetting branches only depending on which is specified. Doing so will result in over-estimated suctions and water contents when the SWCC and HCF are specified for the drying branch only. Conversely, use of the wetting branch only will yield under-predicted suctions and water contents;
3. To the author's knowledge, HYDRUS (Simunek et al., 2006) is the only commercial software that will allow scanning;
4. When using a SWCC constant with depth, the calculated surficial water contents and suctions matched well with the measured values. However, the calculated water contents and suctions

did not match as well deeper. This is because the SWCC is affected by confining stress (Ng and Pang, 2000);

5. Increasing confining stress has a tendency to "squash" or "pancake" the SWCC. This implies that the soil at larger depths tend to have larger changes in suction for the same change in water content as the shallower soils. The SWCC obtained using the pressure plate and VSA was derived under zero confinement and thus are applicable only to surficial soils;

6. To estimate pressure-dependent SWCCs, it is possible to use the results of the isotropic compression triaxial tests. By expressing the van Genuchten parameters as a function of the soil porosity using a model suggested by the Universitat Politecnica de Catalunya (UPC, 2017), separate constants for the drying and wetting portions of the SWCC can be discerned based on the results of isotropic compression tests. These model constants were then used to develop various SWCCs at different depths;

7. When HYDRUS was rerun using pressure-dependent SWCCs, the calculated water contents and suctions matched better with the measured values especially deeper;

8. HYDRUS was used to run this more detailed model to estimate suctions and volumetric water contents within the slope during and after a 500-year storm. These suctions and water contents were then used in infinite slope analyses as well as 2D slope stability analyses with the aid of SLOPE/W;

9. To fool SLOPE/W into using the correct value of suction stress, σ^s, for the slope stability analysis, manual calculations of σ^s and unit dummy values of the van Genuchten parameters (α and n) were input into SLOPE/W;

10. Based on infinite slope analyses, the calculated factors of safety suggest that the slope will survive the 5-minute-duration, high intensity 500-year storm where the lowest factor of safety was > 2.0. For the 60-day-duration, low-intensity 500-year storm, the factors of safety did decrease below 1.0 at the end of the storm. The critical depth was 3.4 m when the factor of safety = 1.0;

11. Based on 2D slope stability analyses, the calculated factors of safety suggest that the slope will survive the 5-minute-duration, high intensity 500-year storm where the lowest factor of safety (> 2.0) occurred about 3 to 30 days after the end of the storm. For the 60-day-duration, low-intensity 500-year storm, the factors of safety were lower than the 5-minute, high intensity variety. The lowest factor of safety was 1.3, which occurred at the end of the storm;

12. Instrument thresholds were established using a traffic-light-based trigger criterion proposed by Nicholson et al. (1999);

13. Instrument threshold values were selected in light of whether the HYDRUS prediction was trending in the right direction during a storm, in light of sensor limitation (e.g.; tensiometers cannot read below 9 kPa), in light of the agreement between calculated and predicted sensor responses during calibration, and in light of the field measured average, minimum and maximum values;
14. Instrument threshold values could be established for 2 water content sensors and 2 tensiometers with confidence;
15. Instrument threshold values were not established for the inclinometers due to no significant observed field movement and due to the limitations of the software utilized in this research. For instance, CODE_BRIGHT did not have the ability to scan and the Slope Cube module in HYDRUS utilized a linear elastic soil constitutive model. Therefore, it was decided that any threshold values for lateral deflection developed based on finite element analyses would be difficult to justify with a great deal of confidence.

9.2 Suggestions for Future Research

The following are suggestions for future research or suggestions if additional research work were to be conducted for this or similar slope site:

1. “Undisturbed” soil samples were collected using modified California samplers. To decrease sample disturbance, Pitcher samplers should be used to collect samples if the soils are stiff and where use of Shelby tubes is precluded.
2. Although this may be challenging and dangerous, instruments to measure suctions and water contents should ideally be installed from the slope face.
3. Water content sensors should be installed to coincide with tensiometers at larger depths now that an installation tool is available from the Miter Group.
4. More consolidation tests at larger depths would have provided a clearer picture of the stress history at the site.
5. Pressure-dependent SWCC tests should be conducted to validate the UPC (2017) porosity-based model used in conjunction with BBM parameters derived from isotropic compression test data.
6. Other models (Gallipoli et al., 2003) for pressure-dependent SWCC should be explored and compared to the approach in Suggestion 5.
7. The variation of hydraulic conductivity with water content of the unsaturated soil should be experimentally derived to verify the HCF computed using the method of Kunze et al. (1968).

8. The triaxial shear apparatus utilized contains only one tensiometer located in the bottom pedestal. Suction measurements at both the top and bottom of the sample should be used to provide a more representative overall value of suction in the sample.
9. Potential evaporation computed using Kohler and Parmele's (1967) modification of Penman's (1948) equation should be compared to values from the Evapotranspiration Atlas (Giambelluca et al., 2014).
10. A numerical software utilizing the BBM (or better) as a constitutive model that allows for scanning should be used to establish inclinometer threshold values.

REFERENCES

1. Baum, Rex L., and Jonathan W. Godt. “Early Warning of Rainfall-Induced Shallow Landslides and Debris Flows in the USA.” *Landslides* 7, no. 3 (2010): 259–272.
2. Bishop, A.W. (1954). The use of pore water coefficients in practice. Geotechnique, 4(4): 148-152.
3. Bishop, A.W. (1955). The use of the slip circle in the stability analysis of slopes. Geotechnique. 5(1): 7-17.
4. Bishop, A.W. and Henkel, D.J. (1962). The measurement of soil properties in the triaxial test. 2nd Edition. Edward Arnold Ltd., London.
5. Bishop, Alan W., I. Alpan, G. E. Blight, and I. B. Donald. “Factors Controlling the Strength of Partly Saturated Cohesive Soils,” 1960.
6. Bishop, Alan W., and I. B. Donald. “The Experimental Study of Partly Saturated Soil in the Triaxial Apparatus.” In *Proceedings of the 5th International Conference on Soil Mechanics and Foundation Engineering, Paris*, 1:13–21, 1961.
7. Blatz, J. A., and J. Graham. “Elastic-Plastic Modelling of Unsaturated Soil Using Results from a New Triaxial Test with Controlled Suction.” *Géotechnique* 53, no. 1 (2003): 113–122.
8. Bolzon, G., Schrefler, B.A. and Zienkiewicz, O.C. (1996). Elastoplastic soil constitutive laws generalized to partially saturated states. Geotechnique. 46(2): 270-289.
9. Borja, R.I. and J.A. White. (2010). Continuum Deformation and Stability Analyses of a Steep Hillside Slope Under Rainfall Infiltration. *Acta Geotechnica*, 5: 1-14. DOI 10.1007/s11440-009-0108-1.
10. Brooks, S., M. Crozier, T. Glade, and M. Anderson. (2004). Towards Establishing Climatic Thresholds for Slope Instability: Use of a Physically-Based Combined Soil Hydrology-slope Stability Model. Pure and Applied Geophysics, 161: 881-905.
11. Brutsaert, W. On a Derivable Formula for Long-Wave Radiation from Clear Skies. *Water Resources Research*, Vol. 11, No. 5, 1975, pp. 742-744.
12. Burman, R.D., M. Jensen, and R.G. Allen. Thermodynamic Factors in Evapotranspiration. In *Irrigation Systems for the 21st Century: Proceedings of a Conference* (James, L.G. and M.J. English, eds.) ASCE, Portland, 1987, pp. 28-30.
13. Cai, F. and K. Ugai. (2004). Numerical Analysis of Rainfall Effects on Slope Stability. *International Journal of Geomechanics*, 4(2): 69-78.
14. Cai, W., Borlace, S., Lengaigne, M., Van Rensch, P., Collins, M., Vecchi, G., Timmermann, A., Santoso, A., McPhaden, M.J., Wu, L. and England, M.H., 2014. Increasing frequency of extreme El Niño events due to greenhouse warming. *Nature climate change*, *4*(2), p.111.
15. Carlquist, S. (1970). Hawaii – A Natural History. The Natural History Press, New York.

16. Casagrande, A. and Fadum, R.E. (1940). Notes on soil testing for engineering purposes, Soil Mechanics Series, Graduate School of Engineering, Harvard University, Cambridge, MA, Vol. 8.
17. Cabarkapa, Zeljko, and Teresa Cuccovillo. “Automated Triaxial Apparatus for Testing Unsaturated Soils.” *Geotechnical Testing Journal* 29, no. 1 (2005): 21–29.
18. Campbell, G.S. (1985). Soil physics with BASIC, Elsivier, New York.
19. Casini, Francesca, Victor Serri, and Sarah M. Springman. “Hydromechanical Behaviour of a Silty Sand from a Steep Slope Triggered by Artificial Rainfall: From Unsaturated to Saturated Conditions.” *Canadian Geotechnical Journal* 50, no. 1 (2012): 28–40.
20. Chow, V., D. Maidment, and L. Mays. *Applied Hydrology.* McGraw-Hill, New York. 1988.
21. Corominas, J., J. Moya, A. Ledesma, A. Lloret, and J. Gili. (2005). Prediction of Ground Displacements and Velocities from Groundwater Level Changes at the Vallcebre Landslide (Eastern Pyrenees, Spain). *Landslides*, 2: 83-96. DOI: 10.1007/s10346-005-0049-1.
22. Cuomo, S. and M. Della Sala. (2013). Rainfall-Induced Infiltration, Runoff and Failure in Steep Unsaturated Shallow Soil Deposits. *Engineering Geology*, 162: 118-127.
23. Deb, S. K., and El-Kadi, A. I. (2009). “Susceptibility assessment of shallow landslides on Oahu, Hawaii, under extreme-rainfall events.” *Geomorphology*, 108(3–4), 219–233.
24. Dingman, S.L. Physical Hydrology. Waveland Press, Long Grove, Illinois, 2008.
25. Duncan, J.M. and Wright, S.G. (1985). Soil Strength and Slope Stability. John Wiley & Sons, Inc., Hoboken, New Jersey.
26. D’Onza, Francesca, D. Galllipoli, Simon Wheeler, Francesca Casini, Jean Vaunat, Nasser Khalili, Lyesse Laloui, M. Null, D. Masin, and Mathieu Nuth. “Benchmark of Constituive Models for Unsaturated Soils.” *Géotechnique* 61 (2011): 283–302.
27. Edlefson NE, and Anderson, A.B.C. (1943). Thermodynamics of Soil Moisture. Hilgardia, 15(2): 31-298.
28. Eichenberger, J., A. Ferrari, L. Laloui. (2013). Early Warning Thresholds for Partially Saturated Slopes in Volcanic Ashes. *Computers and Geotechnics*, 49: 79-89.
29. Eichenberger, J., Mathier, N. and Laloui, L. (2010). Modeling Landslides in Partially Saturated Slopes Subjected to Rainfall Infiltration. In *Mechanics of Unsaturated Geomaterials*. Edited by Lyesse Laloui (Laloui, L., ed.). ISTE Ltd., London, UK and John Wiley & Sons, Inc., Hoboken, NJ. pp. 233-250.
30. Engott, J., A. Johnson, M. Bassiouni, and S. Izuka. *Spatially Distributed Groundwater Recharge for 2010 Land Cover Estimated Using a Water-Budget Model for the Island of O’ahu, Hawai’i*. U.S. Geological Survey Scientific Investigations Report 2015-5010, U.S. Department of the Interior, 2015.
31. Ensoft Inc, (2015). A Program for Slope Stability Analysis. STABLEPRO 2015 – User’s Manual.

32. Ferrari, A., J. Eichenberger, J. Fern, P. Ebeling, and L. Laloui. (2012). Experimental and numerical analysis of an unsaturated volcanic ash deposit for the establishment of an early warning system in a quarry in Costa Rica. In *Geocongress 2012: State of the Art and Practice in Geotechnical Engineering* (Hryciw, R.D., A. Zthanasopoulos-Zekkos, and N. Yesiller, eds.), pp. 2512-2521.
33. Fuchs, M., and A. Hadas. (1972). The Heat Flux Density in a Non-Homogeneous Bare Loessial Soil. *Boundary-Layer Meteorology*, Vol. 3, No. 2: 191-200.
34. Fredlund, D. G., Morgenstern, N. R., and Widger, R. A. (1978). “The shear strength of unsaturated soils.” *Canadian geotechnical journal*, 15(3), 313–321.
35. François, Bertrand, and Lyesse Laloui. “ACMEG-TS: A Constitutive Model for Unsaturated Soils under Non-Isothermal Conditions.” *International Journal for Numerical and Analytical Methods in Geomechanics* 32, no. 16 (2008): 1955–1988.
36. Gallipoli, D., Wheeler, S. J., and Karstunen, M. (2003). “Modelling the variation of degree of saturation in a deformable unsaturated soil.” *Géotechnique.*, 53(1), 105–112.
37. Gens, A. 1996. Constitutive modeling: application to compacted soils. *Unsaturated Soils; Proc., First Intern. Conf.,* Vol. 3: 1179-1200. Paris, France: A.A. Balkema.
38. Georgetti, G. B., O. M. Vilar, and R. A. Rodrigues. “Small-Strain Shear Modulus and Shear Strength of an Unsaturated Clayey Sand.” In *Proceedings of the 18th International Conference on Soil Mechanics and Geotechnical Engineering*, Vol. 11131116, 2013.
39. Geo-Slope International , Ltd. (2012). Stability modeling with SLOPE/W, An engineering methodology, July 2012 Edition.
40. Geo-Slope International Ltd., (2014). Vadose Zone Modeling with VADOSE/W, An engineering methodology, April 2014 Edition.
41. Geo-Slope International Ltd., (2015). Stability Modeling with VADOSE/W, An engineering methodology, April 2014 Edition.
42. Giambelluca, T.W., X. Shuai, M.L. Barnes, R.J. Alliss, R.J. Longman, T. Miura, Q. Chen, A.G. Frazier, R.G. Mudd, L. Cuo, and A.D. Businger. (2014). Evapotranspiration of Hawai‘i. Final report submitted to the U.S. Army Corps of Engineers—Honolulu District, and the Commission on Water Resource Management, State of Hawai‘i.
43. Godt, J., B. Sener-Kaya, N. Lu, and R. Baum. (2012). Stability of Infinite Slopes under Transient Partially Saturated Seepage Conditions. *Water Resources Research*, Vol. 48, W05505, DOI:10.1029/2011WR011408.
44. Harris, S., R. Orense, and K. Itoh. (2016). Site-Specific Warning System for Rainfall-Induced Slope Failure. *Japanese Geotechnical Society Special Publication*, 2(32): 1171-1176.
45. Hazlett, R.W. and Hyndman, D.W. (1996). *Roadside geology of Hawaii*. Mountain Press Publishing Company, Missoula, MT.

46. Hihara, L. and Sugamoto, R. Weather data. Personal communication. *Hawaii Corrosion Laboratory*. Department of Mechanical Engineering, University of Hawaii. 2017.
47. Hilf, Jack W. “An Investigation of Pore Water Pressure in Compacted Cohesive Soils,” 1956.
48. Honolulu Star Advertiser. (2011). http://www.staradvertiser.com/2011/02/28/breaking-news/pali-highway-reopened-after-landslide/ accessed January 22, 2018.
49. Honolulu Star Bulletin. (2003). http://archives.starbulletin.com/2003/08/09/news/story1.html accessed January 22, 2018.
50. Honolulu Star Bulletin. (2006). http://archives.starbulletin.com/2006/11/03/news/art1cx.jpg accessed January 22, 2018.
51. Horel, J., M. Splitt, L. Dunn, J. Pechmann, B. White, C. Ciliberti, S. Lazarus, J. Slemmer, D. Zaff, and J. Burks, (2002). MESOWEST: COOPERATIVE MESONETS IN THE WESTERN UNITED STATES. *Bull. Amer. Meteor. Soc.,* **83**, 211–226,
52. Hvorslev, M.J. (1937). Uber die Festigkeitseigenshaften Gestorter Bindiger Boden. (On the strength properties of remolded cohesive soil), thesis published by Danmarks Naturvidenskablige Samfund, Ingeniorvidenskabelige Skrifter, Series A, No. 35, Kobenhavn, 159 p.
53. Hoyos, Laureano R., Lyesse Laloui, and Roberto Vassallo. “Mechanical Testing in Unsaturated Soils.” *Geotechnical and Geological Engineering* 26, no. 6 (2008): 675.
54. Hu, Ran, Y. F. Chen, H. H. Liu, and C. B. Zhou. “A Water Retention Curve and Unsaturated Hydraulic Conductivity Model for Deformable Soils: Consideration of the Change in Pore-Size Distribution.” *Géotechnique* 63, no. 16 (2013): 1389.
55. Huang, Shangyan, S. L. Barbour, and D. G. Fredlund. “Development and Verification of a Coefficient of Permeability Function for a Deformable Unsaturated Soil.” *Canadian Geotechnical Journal* 35, no. 3 (1998): 411–425.
56. Idso, S., J. Aase, and R. Jackson. (1975). Net-Radiation – Soil Heat Flux Relations as Influenced by Soil Water Content Variations. *Boundary-Layer Meteorology*, Vol. 9: 113-122.
57. Jennings, J.E.B. and Burland, J.B. (1962). Limitation to the use of effective stresses in unsaturated soils. Geotechnique. 12(2): 125-144.
58. Kanjanakul, C. T. Chub-uppakarn, and T. Chalermyanont. (2016). Rainfall Thresholds for Landslide Early Warning System in Nakhon Si Thammarat. *Arabian Journal for Geosciences*, 9(11): 1-11.
59. Karnawati, D., Ibriam, I., Anderson, M. G., Holcombe, E. A., Mummery, G. T., Renaud, J. P., & Wang, Y. (2005). An Initial Approach to Identifying Slope Stability Controls in Southern Java and to Providing Community-Based Landslide Warning Information. In *Landslide Hazard and Risk* (Glade, T., M. Anderson, and M.J. Crozier, eds), John Wiley & Sons, Ltd, Chichester, West Sussex, England, pp. 733-763.

60. Khalili, N. and Khabbaz, M.H. (1998). An effective stress based approach for shear strength determination of unsaturated soils. *Unsaturated Soils; Proc. Second Intern. Conf.*: 84-89. Beijing: International Academic Publishers.
61. Khalili, N. and Loret, B. (2001). An elasto-plastic model for nonisothermal analysis of flow and deformation in unsaturated soils: formulation. International Journal of Solids Structures. Vol. 38: 8305-8330.
62. Khalili, N., Geiser, F. and Blight, G.E. (2004). Effective stress in unsaturated soils: review with new evidence. International Journal of Geomechanics. 4(2): 115-126.
63. Khalili, N., Habte, M. A., and Zargarbashi, S. (2008). "A fully coupled flow deformation model for cyclic analysis of unsaturated soils including hydraulic and mechanical hystereses." *Computers and Geotechnics*, 35(6), 872–889.
64. KHON2 News. (2016). http://khon2.com/2016/07/26/road-crews-clearing-debris-in-pali-highway-kailua-bound-lane/ accessed January 22, 2018.
65. Kirschbaum, D. B., Adler, R., Hong, Y., Hill, S., and Lerner-Lam, A. (2010). "A global landslide catalog for hazard applications: method, results, and limitations." *Natural Hazards*, 52(3), 561–575.
66. KITV4 News. (2015). https://www.facebook.com/KITV4/posts/10153043577611861 accessed August 15, 2017.
67. Kohgo, Y., Nakano, M. and Miyazaki, T. (1993). Theoretical aspects of constitutive modeling for unsaturated soils. Soil Mechanics and Foundation Engineering. 33(4): 49-63.
68. Kohler, M., and L. Parmele. (1967). General Estimates of Free-Water Evaporation. *Water Resources Research*, Vol. 3, No. 4: 997-1005.
69. Kossin, J.P., Emanuel, K.A., and Vecchi, G.A. (2014). The poleward migration of the location of tropical cyclone maximum intensity. Nature, Vol. 509, May, 349-352.
70. Kunze, R.J., G. Uehara, and K. Graham. (1968). Factors Important in the Calculation of Hydraulic Conductivity. *Soil Science Society of America Journal*, Vol. 32, No. 6, pp. 760-765
71. Laloui, L., Charlier, R., Chazallon, C., Erlingsson, S., Hornych, P., Pavsic, P. and Srsen, M. (2008) Chapter 9 – Water influence on mechanical behavior of pavements: Constitutive modeling of water in Road Structures. Edited by Andrew Dawson. Springer.
72. Lateh H, Anderson MG, Ahmad F (2008) CHASM—the model to predict stability of gully walls along the east–west highway in Malaysia: a case study. Proceedings of the First World Landslide Forum. ISDR, Tokyo, Japan, pp. 340–343
73. Li, L. (2015). Evaluate unsaturated soil behavior using constant water content triaxial tests. May, Fairbanks, Alaska. Proquest.
74. Likos, W., Lu, N. and Godt, J. (2014). Hysteresis and Uncertainty in Soil Water-Retention Curve Parameters. *Journal of Geotechnical and Geoenvironmental Engineering*, 140(4): 04013050.

75. Loret, B. and Khalili, N. (2000). A three phase model for unsaturated soils. International Journal for Numerical and Analytical Methods in Geomechanics. 24(11): 893-927.
76. Lu, N., Godt, J. and Wu, D.T. (2010). A closed-form equation for effective stress in unsaturated soil. Water Reseources Research, 72(5): 1-14.
77. Lu, N., Wayllace, A. and Formetta, G. (2016). The Slope Cube Module for HYDRUS (2D) Simulating **S**lope **S**tress and **S**tability in Variably-Saturated Hillslopes. Version 1.0. Soil Water Retention, LLC Madison, Wisconsin, USA.
78. Kunze, R.J., G. Uehara, and K. Graham. Factors Important in the Calculation of Hydraulic Conductivity. *Soil Science Society of America Journal*, Vol. 32, No. 6, 1968, pp. 760-765.
79. Lade, P.V. (2007). Notes for short course on Soil Constitutive Modeling for Engineers: Fundamentals, Evaluation and Calibration.
80. Likos, W., N. Lu, and J. Godt. (2014). Hysteresis and Uncertainty in Soil Water-Retention Curve Parameters. *Journal of Geotechnical and Geoenvironmental Engineering*, Vol. 140, No. 4, DOI: 10.1061/(ASCE)GT.1943-5606.0001071.
81. Lu, N. and Godt, J.W. (2013). Hillside Hydrology and stability. Cambridge University Press, Cambridge, U.K.
82. Lott, J. Neal, and Rich Baldwin. "6.2 THE FCC INTEGRATED SURFACE HOURLY DATABASE, A NEW RESOURCE OF GLOBAL CLIMATE DATA," 2001.
83. Ma, Shao-kun, Mao-song Huang, Ping Hu, and Chao Yang. "Soil-Water Characteristics and Shear Strength in Constant Water Content Triaxial Tests on Yunnan Red Clay." *Journal of Central South University* 20, no. 5 (2013): 1412–1419.
84. Macdonald, G.A., Abbott, A.T. and Peterson, F.L. (1983). Volcanoes in the sea: the geology of Hawaii. 2nd Edition. University of Hawaii Press, Honolulu, HI.
85. Maleki, Mohammad, and Meysam Bayat. "Experimental Evaluation of Mechanical Behavior of Unsaturated Silty Sand under Constant Water Content Condition." *Engineering Geology* 141 (2012): 45–56.
86. Mašín, David. "Predicting the Dependency of a Degree of Saturation on Void Ratio and Suction Using Effective Stress Principle for Unsaturated Soils." *International Journal for Numerical and Analytical Methods in Geomechanics* 34, no. 1 (2010): 73–90.
87. Maswoswe, Justice. "Stress Paths for Compacted Soil during Collapse Due to Wetting." PhD Thesis, University of London London, 1985.
88. Mbonimpa, M., M. Aubertin, A. Maqsoud, and B. Bussière. "Predictive Model for the Water Retention Curve of Deformable Clayey Soils." *Journal of Geotechnical and Geoenvironmental Engineering* 132, no. 9 (2006): 1121–1132.

89. Modaressi, A. and Abou-Berk, N. (1994). A unified approach to model the behavior of saturated and unsaturated soils. Siruwardane (Ed.). Proc. 8th International Conerence in Computer Methods and Advances in Geomechanics, Morgantown, Balkema, Rotterdam: 1507-1513.
90. Monteith, J.L. and M.H. Unsworth. (2008). *Principles of Environmental Physics*. Third Ed. Academic Press, Amsterdam.
91. Morgenstern, N.R. and price, V.E. (1965). The analysis of the stability of general slip surfaces. Geotechnique. 15(1): 79-93.
92. Murakami, H., Wang, B., Li, T., and Kitoh, A. (2013). Projected increase in tropical cyclones near Hawai'I, Nature Climate Change, (3), August, 749-754.
93. Ng, Charles WW, and Abraham CF Chiu. "Behavior of a Loosely Compacted Unsaturated Volcanic Soil." *Journal of Geotechnical and Geoenvironmental Engineering* 127, no. 12 (2001): 1027–1036.
94. Ng, C.W.W. and Menzies, B. (2007). Advanced Unsaturated Soil Mechanics and Engineering. CRC Press.
95. Ng, C. W., and Pang, Y. W. (2000). "Influence of stress state on soil-water characteristics and slope stability." *Journal of geotechnical and geoenvironmental engineering*, 126(2), 157–166.
96. Ng, C., and Q. Shi. (1998). A Numerical Investigation of the Stability of Unsaturated Soil Slopes Subjected to Transient Seepage. *Computers and Geotechnics*, 22(1):1-28.
97. Nicholson, D., Tse, C.M. and Penny, C. (1999). The Observational Method in ground engineering: principles and applications. CIRIA, London, Report 185.
98. NOAA. (2018). NOAA Atlas 14 Point Precipitation Frequency Estimates, National Weather Service precipitation frequency data server. https://hdsc.nws.noaa.gov/hdsc/pfds/pfds_map_hi.html. Accessed February 6, 2018.
99. Novak, M., and T. Black. (1983). The Surface Heat Flux Density of a Bare Soil. *Atmosphere-Ocean*, Vol. 21, No. 4: 431-443. DOI: 10.1080/07055900.1983.9649178.
100. Nuth, M., and Laloui, L. (2008). "Advances in modelling hysteretic water retention curve in deformable soils." *Computers and Geotechnics*, 35(6), 835–844.
101. Penman, H. (1948). Natural Evaporation from Open Water, Bare Soil, and Grass. *Proceedings of the Royal Society of London. Series A, Mathematical and Physical Sciences*, Vol. 193, No. 1032: 120-145.
102. Peterson, D.M., Ellen, S.D., and Knifong, D.L. *Distribution of Past Debris Flows and other Rapid Slope Movements from Natural Hillslopes in the Honolulu District of Oahu*. Open File Report 93-514. U.S. Department of the Interior. U.S. Geological Survey. 1993.
103. Potts, D.M., G.T. Dounias, and P.R. Vaughan. (1990). Finite Element Analysis of Progressive Failure of Carsington Embankment. *Geotechnique*, 40(1): 79-101.
104. Powrie, W. (1997). Soil Mechanics Concepts and Applications. E & FN Spon, London, UK.

105. Rahardjo, Harianto, Alfrendo Satyanaga, and Eng-Choon Leong. “Effects of Flux Boundary Conditions on Pore-Water Pressure Distribution in Slope.” *Engineering Geology* 165 (2013): 133–142.
106. Rahardjo, Harianto, Alfrendo Satyanaga, Eng Choon Leong, Yew Song Ng, Moo Din Foo, and Chien Looi Wang. “Slope Failures in Singapore Due to Rainfall,” 2007.
107. Rahardjo, Harianto, Alfrendo Satyanaga Nio, Eng Choon Leong, and Ng Yew Song. “Effects of Groundwater Table Position and Soil Properties on Stability of Slope during Rainfall.” *Journal of Geotechnical and Geoenvironmental Engineering* 136, no. 11 (2010): 1555–1564.
108. Rampino, C, C Mancuso, and F Vinale. “Laboratory Testing on an Unsaturated Soil: Equipment, Procedures, and First Experimental Results.” *Canadian Geotechnical Journal* 36, no. 1 (August 8, 1999): 1–12. https://doi.org/10.1139/t98-093.
109. Rassam, D., and D. Williams. A Numerical Study of Steady-State Evaporative Conditions Applied to Mine Tailings. *Canadian Geotechnical Journal*, Vol. 36, 1999, pp. 640-650.
110. Rassam, D., Simunek, J. and van Genuchten, M.T. (2003). *Modelling Variably Saturated Flow with HYDRUS-2D*. ND Consult, Brisbane.
111. Reddy, J.N. (1993). An Introduction to the Finite Element Method. 2nd Edition, McGraw Hill, New York.
112. Richards, L.A. Capillary Conduction of Liquids Through Porous Mediums. *Physics.* Vol. 1, No. 5, 1931, pp. 318–333.
113. Rowe, P.W. (1969). The relation between the shear strength of sands in triaxial compression, plane strain and direct shear. Geotechnique. 19(1): 75-86.
114. Rowland, S.K. and Garcia, M. O. (2004). Southeast Oahu Geology Field Trip Guide. Western Pacific Geophysics Meeting, Honolulu, Hawaii, August 16-20, 2004. http://hahana.soest.hawaii.edu/agouroninstitutecourse/EOahuguide.pdf.
115. Saint-Venant, B. de. (1870). Comptes redus Acad. Sci. Paris, 70(473). Journ. Math. pures et app.
116. Sarma, S.K. (1973). Stability analysis of embankments and slopes. Geotechnique. 23(3): 423-433.
117. Satija, Bhim Sen. “Shear Behaviour of Partially Saturated Soils,” 1978.
118. Saxton, K.E. and rawls, W.J. (2006). Soil water characteristic estimates by texture and organic matter for hydrologic solutions. Soil Science Society of America Journal. 5(70):1569-1578.
119. Sharma, Radhey Shyam. “Mechanical Behaviour of Unsaturated Highly Expansive Clays.” PhD Thesis, University of Oxford, 1998.
120. Schmidt, B. (1966). Discussion of “Earth pressures at rest related to stress history,” Canadian Geotechnical Journal, 3(4): 355-358.

121. Sheng, D., and Zhou, A.-N. (2011). “Coupling hydraulic with mechanical models for unsaturated soils.” *Canadian Geotechnical Journal*, 48(5), 826–840.
122. Sheng, Daichao, Delwyn G. Fredlund, and Antonio Gens. “A New Modelling Approach for Unsaturated Soils Using Independent Stress Variables.” *Canadian Geotechnical Journal* 45, no. 4 (2008): 511–534.
123. Simunek, J., M.T. van Genuchten, and M. Sejna. (2006). The HYDRUS Software Package for Simulating Two- and Three-Dimensional Movement of Water, Heat, and Multiple Solutes in Variably-Saturated Media. Technical Manual, Version 1, PC Progress, Prague, p. 241.
124. SoilVision Systems Ltd, (2018). SVOFFICE 5 Help Manual. April 2018.
125. Spencer, E. (1967). A method of analysis of the stability of embankments assuming parallel inter-slice forces. Geotechnique. 17(1): 11-26.
126. Springman, S.M., A. Thielen, P. Kienzler, and S. Friedel. (2013). A Long-Term Field Study for the Investigation of Rainfall-Induced Landslides. *Geotechnique*, 63(14): 1177-1193. https://doi.org/10.1680/geot.11.P.142.
127. Sun, D., Sheng, D., and Xu, Y. (2007). “Collapse behaviour of unsaturated compacted soil with different initial densities.” *Canadian Geotechnical Journal*, 44(6), 673–686.
128. Sun, J.H., L. Jiang, and W. S. Wang. (2011). Study on Landslide Early Warning of Mayanpo Slope at Xiangjiaba Hydropower Station. *Applied Mechanics and Materials*, 90-93: 328-331.
129. Tarantino, Alessandro. “A Water Retention Model for Deformable Soils.” *Géotechnique* 59, no. 9 (2009): 751–762.
130. Taylor, D.W. (1948). Fundamentals of soil mechanics. John Wiley and Sons, New York.
131. Thiebes, B., R. Bell, T. Glade, S. Jager, J. Mayer, M. Anderson, and L. Holocombe. (2014). Integration of a Limit-Equilibrium Model into a Landslide Early Warning System. *Landslides*, 11: 859-875. DOI 10.1007/s10346-013-0416-2.
132. Thu, Trinh Minh, Harianto Rahardjo, and Eng-Choon Leong. “Shear Strength and Pore-Water Pressure Characteristics during Constant Water Content Triaxial Tests.” *Journal of Geotechnical and Geoenvironmental Engineering* 132, no. 3 (2006): 411–419.
133. Tiwari, R.C., N.P. Bhandary, and R. Yatabe. (2015). 3D SEM approach to evaluate the stability of large-scale landslides in Nepal Himalaya. *Geotechnical and Geological Engineering*, 33(4): 773-793.
134. Torikai, J.D. and Wilson, R.C. (1992). Hourly rainfalls and reported debris flows for selected storm periods, 1935-91, in and near the Honolulu District, Hawaii. U.S. Geological Survey, Open File Report 92-486. https://pubs.usgs.gov/of/1992/0486/report.pdf.
135. Turner, A.K. Socioeconomic Significance of Landslides. *Landslides: Investigation and Mitigation (Special Report)*. Transportation Research Board. 1996. pp. 12-35.

136. Universitat Politecnica de Catalunya. (2017). CODE_BRIGHT Users Guide. Version 7.4. https://deca.upc.edu/en/projects/code_bright/downloads/users_guide/view.
137. van Bavel, C. H. M., and D. I. Hillel, Calculating Potential and Actual Evaporation From a Bare Soil Surface by Simulation of Concurrent Flow of Water and Heat, *Agricultural Meteorology*, Vol. 17, 1976, pp. 453-476.
138. van Genuchten, M. (1980). A Closed-Form Equation for Predicting the Hydraulic Conductivity of Unsaturated Soils. *Soil Science Society of America Journal*, Vol. 44, No. 5. pp. 892-898.
139. Vanapalli, S.K., Fredlund, D.G., Pufahl, D.E. and Clifton, A.W. (1996). Model for the prediction of shear strength with respect to soil suction. Canadian Geotechnical Journal, 33: 379-392.
140. Wheeler, S. J., and Sivakumar, V. (1995). “An elasto-plastic critical state framework for unsaturated soil.” *Géotechnique*, 45(1), 35–53.
141. Wilkinson, P., M. Anderson, and D. Lloyd. (2002). An Integrated Hydrological Model for Rain-Induced Landslide Prediction. *Earth Surface Processes and Landforms*, 27: 1285-1297. DOI: 10.1002/esp.409.
142. Wilson, R.C., J.D. Torikai, and S.D. Ellen. (1992). *Development of Rainfall Warning Thresholds for Debris Flows in the Honolulu District, Oahu*. Open-File Report 92-521. U.S. Department of the Interior. U.S. Geological Survey.
143. Wright, S.G. (2004). UTEXASED4 A Computer Program for Slope Stability Calculations. March. Austin Texas.
144. Wu, YM., HX. Lan, X. Gao, LP. Li, and ZH. Yang. (2015). A Simplified Physically Based Coupled Rainfall Threshold Model for Triggering Landslides. *Engineering Geology*, 195: 63-69.
145. Zhang, X., and Lytton, R. L. (2009). “Modified state-surface approach to the study of unsaturated soil behavior. Part I: Basic concept.” *Canadian Geotechnical Journal*, 46(5), 536–552.
146. Zhang, Xiong, and Robert L. Lytton. “Modified State-Surface Approach to the Study of Unsaturated Soil Behavior. Part II: General Formulation.” *Canadian Geotechnical Journal* 46, no. 5 (2009): 553–570.
147. Zhang, X. (2016). “Limitations of suction-controlled triaxial tests in the characterization of unsaturated soils.” *International Journal for Numerical and Analytical Methods in Geomechanics*, 40(2), 269–296.
148. Zhou, A. N., Daichao Sheng, and John P. Carter. “Modelling the Effect of Initial Density on Soil-Water Characteristic Curves.” *Géotechnique* 62, no. 8 (2012): 669.
149. Zhang, Jian, Jiangteng Li, and Hang Lin. “Models and Influencing Factors of the Delay Phenomenon for Rainfall on Slope Stability.” *European Journal of Environmental and Civil Engineering* 22, no. 1 (2018): 122–136.

APPENDIX A – BORING LOGS

PLog

GEOLABS, INC.

Geotechnical Engineering

SLOPE INSTRUMENTATION & DEVELOPMENT OF A LANDSLIDE
Likelike Hwy/Pali Hwy.

Log of Boring **2**

Field										Approximate Ground Surface Elevation (feet MSL): 160 * Latitude:21.37822 Longitude: -157.76973
w% PL LL	Sample Quality	Rec. Length/ Sample Length (inches)	Gs	Blows/ 6"	Pocket Pen. (tsf)	Depth (feet)	Sample		USCS	Description
58 - -	Good	15/18"	2.91	5/9/10	3.5			2	MH	Mottled multi-color brown ~~CLAYEY SILT~~, very stiff, damp to moist (residual soil) ELASTIC SILT
47 52 67	Fair	23/24"	2.92	5/5/6/7						
	Good	14/18"		5/10/13	3.5	5		2		
44 49 64	Fair	16/18"	2.93	6/8/10						
33 48 65	Fair	16/18"	2.87	4/11/13						
43	Good	13/18"	2.83	6/14/21	4.0	10		1		
38 40 60	Fair	14/18"	2.79	6/9/10						Elastic silt with sand
38 42 59	Fair	15/18"	2.87	4/9/11						
	Good	14/18"		10/16/17	4.0	15		2		
53 56 80	Fair	18/18"	2.99	5/8/11						
40 53 73	Fair	14/18"	2.90	4/8/10						
	Good	15/18"		9/15/23	4.0	20		2		grades with remnant rock structure
33 51 69	Fair	17/18"	2.88	7/11/13						
	Good	14/18"		10/19/19	4.0			2		
						25				Boring terminated at 25.5 feet
						30				
						35				

Date/Time Started:	April 13, 2015 12:30	Water Level: ▼	not encountered 04/14/2015 1030 HRS		
Date/Time Completed:	April 14, 2015 10:30				
Logged By:	Steve Latronic	Driller Name:	K. Vongamath	Plate	
Project Engineer:	Clayton Mimura	Drill Rig:	DIEDRICH D-25.3		
Total Depth:	25.5 feet	Drilling Method:	4" Solid Stem Auger	A -	
Work Order:	7130-00	Driving Energy:	140 lb. wt., 30 in. drop		

BORING LOG DRAFT 7130-00.GPJ GEOLABS.GDT 6/17/15

PLog

GEOLABS, INC.
Geotechnical Engineering

SLOPE INSTRUMENTATION & DEVELOPMENT OF A LANDSLIDE
LIkelike Hwy/Pali Hwy.

Log of Boring 3

Approximate Ground Surface Elevation (feet MSL): 160 *
Latitude:21.37823
Longitude: -157.76973

Field									
w% PL LL	Sample Quality	Rec. Length/ Sample Length (inches)	Gs	Blows/ 6"	Pocket Pen. (tsf)	Depth (feet)	Sample	USCS	Description
	Good	14/18"		8/12/17	3.5		2	MH	Mottled multi-color brown ~~CLAYEY SILT~~, very stiff, damp to moist (residual soil) ELASTIC SILT
40 57 82	Fair	17/24"	2.97	5/8/9/12					
	Good	13/18"		7/15/20	3.0	5	2		
40 57 90	Fair	12/18"	2.97	4/8/11					
39 53 65	Fair	15/18"	2.86	7/12/12					
43	Good	13/18"	3.00	5/15/26	4.0	10	2		
39 48 62	Fair	14/18"	2.85	6/12/14					
34 44 55	Fair	17/18"	2.86	7/12/13					
	Good	14/18"		10/15/20	4.0	15	2		
39 55 79	Fair	18/18"	2.92	6/10/12					
56 54 77	Fair	18/18"	2.92	5/7/9					
43	Good	16/18"	2.84	13/20/24	3.5	20	1		
48 53 60	Fair	17/18"	2.97	9/18/43					grades with remnant rock structure
44 61 68	Fair	18/18"	2.95	7/11/17		25			Boring terminated at 25.5 feet
						30			
						35			

Date/Time Started:	April 14, 2015 10:45	Water Level: ▼ not encountered 04/14/2015 1515 HRS			
Date/Time Completed:	April 14, 2015 15:15				
Logged By:	Steve Latronic	Driller Name:	K. Vongamath	Plate	
Project Engineer:	Clayton Mimura	Drill Rig:	DIEDRICH D-25.3		
Total Depth:	25.5 feet	Drilling Method:	4" Solid Stem Auger	A -	
Work Order:	7130-00	Driving Energy:	140 lb. wt., 30 in. drop		

BORING LOG DRAFT 7130-00.GPJ GEOLABS.GDT 6/17/15

APPENDIX B – CONSTANT WATER CONTENT CONSOLIDATION AND DIRECT SHEAR TESTS BY PROF. XIONG ZHANG AND DR. LIN LI TO ESTIMATE THE BASIC BARCELONA MODEL PARAMETERS

HAWAII PROJECT REPORT

By

Xiong Zhang, Ph.D., P.E., Associate Professor

Department of Civil and Environmental Engineering

University of Alaska Fairbanks

And

Lin Li., Ph.D.

Department of Civil and Environmental Engineering

University of Alaska Fairbanks

December 2017

University of Alaska Fairbanks

Fairbanks, AK 99775-5900

TABLE OF CONTENTS

LIST OF FIGURES

LIST OF TABLES

CHAPTER I INTRODUCTION

1. INTRODUCTION

Unsaturated soils extensively existed in the field. The volume change behaviors and shear strength of unsaturated soils play an essential role in the structural design of the road, building, and dam…..etc. that above the saturated soil layer and the slope stability analysis for slopes of unsaturated soils. However, characterizing the volume change and shear strength of unsaturated soils is still challenging issue for researchers and practicing engineers. The conventional suction-controlled triaxial test (SCTX) required sophisticated test equipment. The testing process was very time-consuming and laborious. In addition, the test results are not very accurate. All these problems become the barriers which prevent unsaturated soil mechanics from being used in routine engineering projects. With the recent developments in high-suction tensiometers and theoretical advancements, the constant water content tests can be easily performed by using HST to measure the matric suction simultaneously with the load applied to characterize the unsaturated soil behavior. However, the test results are complicated, and at present, there is no available method to analyze the test results for constitutive modeling purposes. This research modifies the oedometer and shear test apparatus for saturated soils in conjunction with the high-suction tensiometer (HST) to perform tests for unsaturated soils. In addition, methods are also proposed for data reduction. The constant water content test could be useful to get good results and to save time and money of the engineering projects related to unsaturated soils.

In this project, based on modifications on a conventional oedometer, a new oedometer cell with suction measurement ability developed by Li et al. (2015) was adopted for the one-dimensional oedometer compression test on unsaturated soils. In this system, the oedometer cell was equipped with a high-suction tensiometer to measure suction change during constant water content compression tests. Soil volume change was measured by a displacement transducer. With this newly developed oedometer cell, a series of constant water content compression tests on the unsaturated Hawaii soil was conducted.

Besides this, a new direct shear cell with suction measurement ability was developed to investigate the shear strength of the Hawaii soil through constant water content direct shear tests.

A miniature high-suction tensiometer was also developed and applied to measure the soil matric suction during shearing. A series of tests were performed to characterize the shear strength of the unsaturated soils with different water contents under different normal stresses.

After that, based on (Zhang et al. 2016) a new calculation method was used to combine the constant water content oedometer test results as well as the constant water content direct shear test results together to characterize Hawaii unsaturated soil shear strength and stiffness parameters.

2. LITERATURE REVIEW

2.1.Saturated soil testing

Saturated soils considered as a special case of unsaturated soils. The saturated soil is a two-phase soil (water and solid phase) this makes the saturated soils much simpler than unsaturated soils during testing and analysis. Even for saturated soils, there are some laborious unfavorable tests take much time and effort such as consolidated drained triaxial test which is called slow test. In this section, the purpose and limitation of each test will be briefly presented.

It is well known that when materials are loaded or stressed they suffer from deformations or strains. For elastic materials, the strains are entirely reversible. For plastic materials, part of the strains is irreversible when unloaded. Some other types of materials take relatively long time to deform under loads. Materials with stress-strain time factor are called visco-elastic. For soils, the behavior becomes more complicated because of the introduction of another factor which is the stress history (soil has a memory). Which means, when soils are loaded, they deform, and when stresses are released some permanent deformations are remained. The soil deformations could be either change in shape (which is corresponding to shear loading), or a change in volume (which is corresponding to compression loading), or both.

Terzaghi firstly defined the consolidation process as the process which involves a decrease in soil water content without air replacement. When saturated soils are loaded, excess pore water pressure will be generated. If the soil has a relatively low permeability (i.e., clays and silts), the excess pore water pressure dissipation will take a long time, which is called consolidation (Terzaghi (1944). After that, tremendous researches have been done to define and determine the parameters related to consolidation process such as pre-consolidation pressure, OC and NC slopes, the soil OCR and coefficient of consolidation. Oedometer test is the laboratory test that represents the one-dimensional consolidation process. The oedometer test is called K_0 test and, lateral strains

are constrained by the metal ring. The volume change parameters only could be determined from the oedometer test results.

To characterize the shear strength of soils, the direct shear test is usually used. This test is one of the oldest strength experimental tests. Coulomb has used a test like the direct shear box to determine the required shear strength parameters for his equation (Holtz and Kovacs 1981). In this test firstly, normal force is applied to the sample after that the sample is laterally sheared by means of applying a lateral deformation to the lower part of the soil. By applying different normal stresses and measure the corresponding shear strength. The soil shear strength parameters (cohesion and angle of internal friction) can be determined. The soil shear strength is defined by Mohr-Coulomb shear envelope:

$$\tau = \sigma_n' \tan\phi' + C' \tag{1.1}$$

Where, τ=shear strength; σ_n'= normal stress; C'= cohesion; ϕ'=angle of internal friction.

There are several advantages and disadvantages of the direct shear test. The test is fast, inexpensive and straightforward, especially for cohesionless materials. Disadvantages include the difficulty of controlling drainage, especially for fine-grained soils. Consequently, the direct shear test is suitable only for fully drained soil conditions. Also, in the direct shear tests we are forcing the sample to fail on a horizontal plane, maybe this is not the weakest or critical direction. Moreover, there is a severe stress concentration at the sample boundaries, which mean highly no-uniform stress conditions within the specimen. In addition to, there is uncontrolled rotation in the principal stresses and planes at the failure conditions (Holtz and Kovacs 1981). The vertical deformations can be measured during direct shear testing. However, it is not usable. Only the parameters related to the shear strength of soil can be determined from the direct shear test.

To overcome the shortcomings of the direct shear test, A. Casagrande in 1930 began research to develop a cylindrical compression test at M.I.T. Later, the test called triaxial and now is the most popular testing technique in geotechnical engineering. The triaxial test is more complicated than the direct shear test but also much more versatile and reliable. The drainage could be controlled, and there is no rotation in the principal stresses and planes. One of the vital advantages of the triaxial test that the stress path can be controlled. Using triaxial testing, one can model any complex stress bath for the soil in the real conditions. There are different types of triaxial tests such as Unconsolidated Undrained (UU-rapid test), Consolidated Undrained (CU) and Consolidated Drained (CD-slow test). In the triaxial test, we can get many data about the soil such as shear

strength parameters, volumetric strains, pore water pressure, consolidation parameters, and coefficient of consolidation. In the triaxial test, the major and minor principal stresses are known as well as the pore water pressure so that the total and effective stress paths are known. However, the test is laborious, time-consuming and the results are more complicated.

2.2.Unsaturated soil testing

The unsaturated soil is more complicated than saturated soils. Unsaturated soils have three-phases: soil particle, pore water, and pore air (Kohgo et al. 1993). The contractile skin (air-water-solid interface) was introduced by (Fredlund and Morgenstern 1977) as a fourth independent phase of unsaturated soils. However, it is not used in calculations at because it is too thin. Behavior of unsaturated soils is influenced by many factors, and the influences of these factors are usually coupled together: load applied to an unsaturated soil will lead to changes in the matric suction. Changes in matric suction often cause soil moisture and volume to change, and when volume changes are restricted, stresses are generated (Zhang 2016).

The stress state variables are needed to describe the soils mechanical behavior (the volumetric changes and shear strength behavior). The stress state variable should be independent of any material physical properties (Fredlund and Morgenstern 1977). The use of effective stress (σ-u_w) for saturated soils has proven it's satisfactory for engineering practice. In other words, the effective stress is a unique stress state variable to describe the mechanical behavior of saturated soils. Which means, the effective stress state variable could be used to explain and study the mechanical behavior of saturated sands, silts, and clays because it is independent of any soil properties. Firstly, numerous efforts have been made to extend the single effective stress state variable for unsaturated soils. Bishop (1959) suggested the below equation as an effective stress state variable for the unsaturated soil.

$$\sigma' = (\sigma - u_a) + \chi(u_a - u_w) \tag{1.2}$$

Where,

σ'=effective stress

u_w= pore water pressure

u_a= pore-air pressure

σ-u_a= net normal stress

u_a-u_w= matric suction

χ = a parameter related to the degree of saturation of soils.

The magnitude of χ parameter is unity for saturated soils and between one and zero for unsaturated soils. Jennings and Burland (1962) found that the relationship between volume changes of unsaturated collapsible soils cannot be adequately explained by Bishop's equation (1.2). After that, many researchers suggested that the need for two independent stress state variables (mean stress and matric suction) to define the mechanical behavior of unsaturated soils (Fredlund and Morgenstern 1977; Matyas and Radhakrishna 1968), which means, to explain any mechanical behavior of unsaturated soil such as volumetric changes or shear strength, two variables are required. Although there are some different opinions in the use of two stress state variables (Khalili et al. 2004; Lu and Likos 2004). All researchers controlled the two stress state variables (net normal stress and matric suction) when experimentally characterize unsaturated soils.

For saturated soils, the volume changes equal to the water volume flow in or out of the sample when the load is applied, which is easy to measure during testing using a volume gage. However, for unsaturated soils, the volume change is no longer equal to water volume change because of the presence of air phase in soil pores. This makes the use of the conventional triaxial test is no longer sufficient for unsaturated soils. Bishop and Donald (1961) adopted the first double-cell suction controlled triaxial apparatus as schematically shown in Figure 1.1. Two significant modifications were made to change the conventional triaxial test into suction-controlled triaxial apparatus. First one is the use of double cell to measure the volume change of unsaturated soil specimen. The second one is to replace the porous stone at the base pedestal with a high air entry (HAE) ceramic disc to control matric suction with the axis-translation technique (Hilf 1956).The SCTX is the most popular unsaturated soil testing system. Moreover, it allows researchers to control the stress, air, and pore water pressures separately to eliminate the complicated coupling effect. In addition, using SCTX test the soil mechanical behavior under specific (pre-selected) stress paths could be investigated. Since the 1960s the SCTX test used by many researchers to study and investigate constitutive behaviors of unsaturated soils (Bishop and Blight 1963; Fredlund 1979; Fredlund and Morgenstern 1976; Fredlund et al. 1978; Fredlund and Morgenstern 1977; Jennings and Burland 1962; Matyas and Radhakrishna 1968; Sivakumar 1993). However, there are many limitations for the SCTX test, such as the need for sophisticated equipment and sensitivity of measurements to temperature changes. Also, the SCTX test is a consolidated drained test. Because of large sample dimensions and low permeability of unsaturated soils, the SCTX test

is very time consuming, laborious and costly. Usually, to fully characterize one unsaturated soil it takes several years (Hoyos Jr 1998; Sharma 1998; Sivakumar 1993).

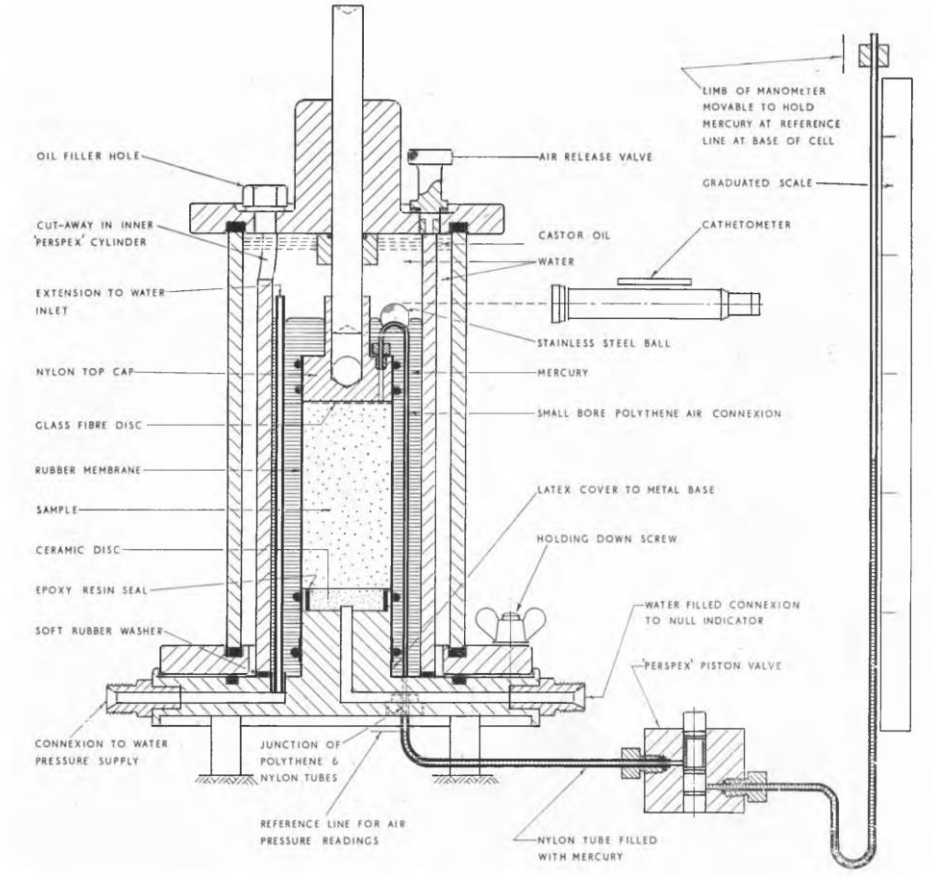

Figure 1.1 Double-cell triaxial apparatus for unsaturated soils (Bishop and Donald 1961).

The SCTX is established based on the divide and conquer approach which implicitly includes an assumption that the unsaturated soil is stress path independent. However, it is well established that the unsaturated soil is elasto-plastic and stress-dependent (Zhang 2016). One significant additional limitation for the SCTX that the results are theoretically not correct. The test theoretical principals were deeply investigated and discussed by Zhang (2016). It was concluded that the soil elastic behavior is stress path independent and the SCTX test results could be accepted. However, the soil plastic behavior is stress path dependent and the test results are only a collection of elastic behaviors of the soil with different pre-consolidation stresses and are always lower than the results from the idealized stress path as shown in Figure 1.2. Moreover, applying continuous load into the drained unsaturated soil will result in non-uniform suction changes within the sample.

As a result, the sample cannot be considered as a representative elementary volume (REV). In other words, using SCTX test we made a good sample representing the field conditions to a non-REV sample. If the soil is not a REV, the test results cannot used for constitutive modeling purpose (Zhang 2016).

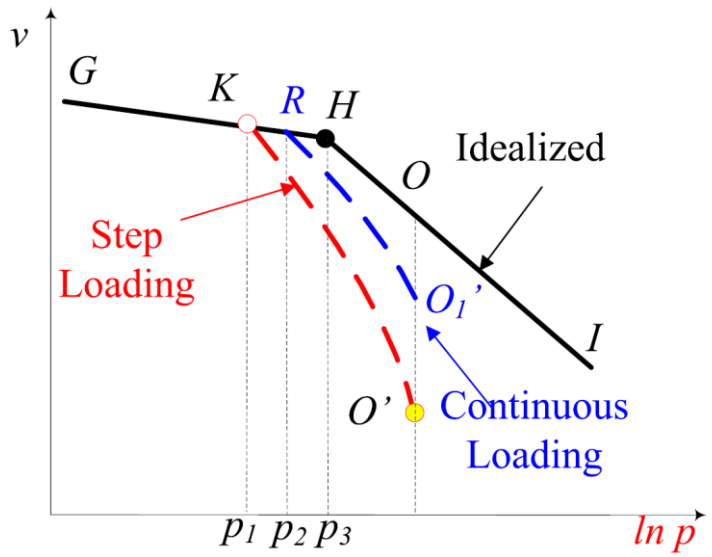

Figure 1.2 Schematic plot of effects of loading procedure on suction-controlled triaxial test results (Zhang 2016).

Because of the limitations mentioned above of SCTX test and the non-availability in most of the universities and research centers due to high cost and time-consuming. There was a great need to develop and modify simple testing equipment for unsaturated soils to be used for common engineering projects.

The suction-controlled direct shear test was firstly proposed by (Gan et al. 1988) to characterize the shear strength parameters of unsaturated soils. Similar to the suction-controlled triaxial test proposed by Bishop and Donald (1961), the axis-translation technique was also used to control soil suction during shearing. The soil specimens shall be conditioned to different suction levels after that sheared. Using different samples at different suction levels, the shear strength parameters could be determined based on (Fredlund et al. 1978) equation. After that, many researchers successfully used the suction-controlled direct shear test to characterize the unsaturated soils shear strength (De Campos and Carrillo 1995; Nam et al. 2011). However, the test required sophisticated modifications to the conventional direct shear test apparatus for suction control purpose and was complicated to operate. Moreover, suction controlled tests are drained tests. As

mentioned previously, due to the extremely low permeability of unsaturated soils, suction-controlled tests could be time-consuming.

The oedometer test is a well-known test in classical geotechnical engineering and typically used to get the soil parameters related to consolidation and stress history. Some researchers have also modified the oedometer test for saturated soils to a suction-controlled oedometer test (SCOD) for unsaturated soils by introducing suction control system through axis-translation or vapor equilibrium technique (Dineen and Burland 1995; Kassiff and Shalom 1971; Maswoswe 1985; Romero et al. 1995). Compared to triaxial test, the suction controlled oedometer is much cheaper, simpler, faster and easier to perform. In the oedometer test, the volumetric changes can be directly calculated from the vertical deformations, which can be easily measured using LVDT. One of the significant limitations of the oedometer test is that the lateral stress is unknown. Another limitation of the suction controlled oedometer test is the required significant modifications to the conventional oedometer cell. Moreover, it takes a fair amount of time to perform a SCOD test because the long time needed for suction equilibrium. In the past, there was no method to use the oedometer test results for constitutive modeling. As a result, most researchers used the oedometer results for only verify their models, based on two assumptions: (a) elastic shear strains are small and negligible and (b) the K_0 consolidation line shares the same slope and is a constant for saturated and unsaturated soils. (Zhang et al. 2016) demonstrated that these two assumptions are problematic.

With the recent developments in high-suction tensiometers, the constant water content tests can be easily used by using HST to measure the matric suction simultaneously with the load applied to characterize the unsaturated soil behavior. Based on this concept of Zhang et al. (2016) modified a constant water content oedometer cell (CWOD) for unsaturated soils which is schematically presented in Figure 1.3. The major advantages of the modified cell are (1) no significant modifications are introduced to the conventional cell and (2) it takes short time (only 4 to 7 hours) to run a CWOD for unsaturated soils, which is 300 to 400 times less than the required for SCTX test. In addition to the modified equipment, Zhang et al. (2016) developed a method to analyze the test results for constitutive modeling based on the conceptual definition of K_0 conditions only. One limitation of Zhang et al. (2016) is that the oedometer test is not a failure test. As a result, the shear strength obtained from Zhang et al. 92016) represent an extrapolation of soil shear strength behavior, which can be inaccurate.

In this report, a constant water content direct shear test will be developed. Similar to the CWOD, the conventional direct shear cell is equipped with a miniature high-suction tensiometer to measure suction changes during normal and shear loading. Knowing the suction value at failure, (Fredlund et al. 1978) equation could be used directly to adopt the unsaturated soil shear strength parameters.

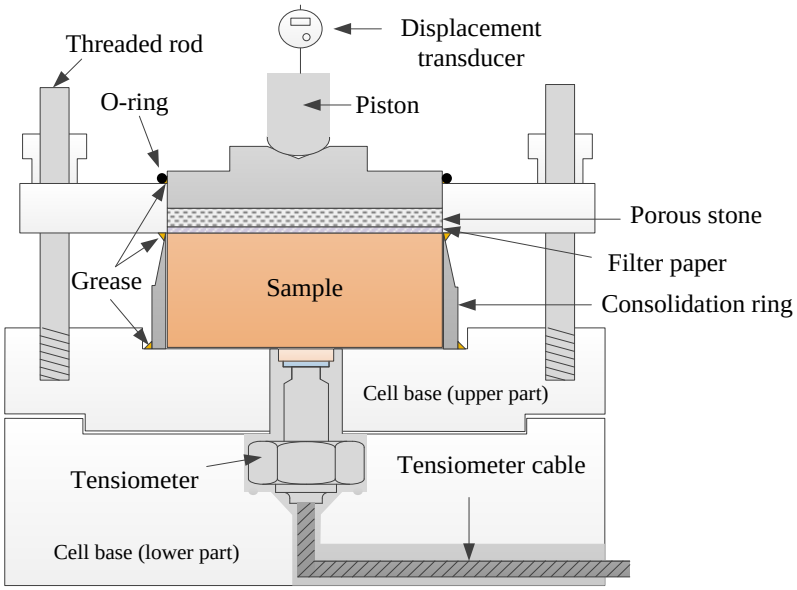

Figure 1.3 Modification on cell base for one-dimensional oedometer compression test.

Besides the developed CWOD and CWDS tests, based on the explicit formulation developed by Zhang et al. (2015), a method was also developed to analyze the results of unsaturated soil SCOD test for constitutive modeling. The developed method combined the modified state surface approach MSSA with the quasi-Newton method to calibrate the Barcelona basic model (BBM) parameters. Zhang et al. (2016) successfully used the developed method to calibrate the BBM parameters based on the results of constant water content oedometer test (CWOD).It worth noting that oedometer tests are representing the at-rest conditions in which the soil shear strength is not mobilized. However, M and k parameters in the BBM are related to the shear strength of unsaturated soils. Which means, M and k values calculated using the proposed method are an extrapolation of the oedometer test results to failure conditions and could be subjected to significant error (Zhang et al. 2016).

To overcome this limitation, Zhang et al. 2016 recommended using another test to introduce the M and K values to the proposed approach as an additional constraint. Here is the role of constant water content direct shear test (CWDS) to provide the shear strength parameters to the process. In other words, the constant water content oedometer test (CWOD) combined with the constant water content direct shear test (CWDS) may be used to replace the suction controlled triaxial test to fully calibrate the BBM parameters using the method developed by (Zhang et al. 2016). Using both results of the CWOD test allow more stress paths and ranges to be included in the analysis so that the prediction will be made on the bases of interpolations instead of extrapolations.

CHAPTER II DEVELOPMENT OF TEST APPARATUS

1. INTRODUCTION

For both saturated and unsaturated soils in the field, most of the time, due to the applied vertical load, the soil deformation is under K_0 (no lateral strain) condition. Moreover, the K_0 condition is critical to include in the numerical modeling and simulation since it represents the soil initial (at rest) conditions. As a result, a one-dimensional oedometer compression test is still very popular for soil behavior investigation and verification of model parameters. For saturated soils, due to the simplicity and equipment availability, oedometer cell is widely used to characterize saturated soil behaviors. However, the conventional oedometer cannot be directly used for unsaturated soil investigation due to the difficulties in measuring soil suction. Ridley and Burland (1993) developed the first high-suction tensiometer for direct suction measurement on unsaturated soils. Since then, more and more high-suction tensiometers have been developed and utilized for both laboratory and field suction measurements (Ridley and Burland 1993; Meilani et al. 2002; Take and Bolton 2003; and Lourenco et al. 2006). In Le et al. (2011), a high-suction tensiometer was equipped in the conventional oedometer for direct suction measurement during undrained testing on unsaturated soils. In this chapter, the development of the modified oedometer cell is presented in detail.

The direct shear test is usually used to characterize saturated soils from which the shear strength properties can be determined. Different from the saturated soils, the suction of unsaturated soils during shearing is also affecting the shear strength characterization of unsaturated soil. However, the conventional direct shear apparatus cannot be directly used for unsaturated soils due to difficulties in soil suction measurement during testing. In the past few decades, several methods had been developed to characterize shear strength properties of unsaturated soils. However, these methods suffered from several limitations such as significant system modification on the existing apparatus and time-consuming testing process. Due to difficulties in measuring suction during a shearing test of unsaturated soils. (Vanapalli and Lane 2002) proposed a method using conventional direct shear test apparatus combined with soil water characteristic curve to determine the soil shear strength and the corresponding suction value. The proposed method was based on the assumption that the suction value does not change significantly during shearing. However, this

assumption is not correct because the volumetric changes in soils during shearing even contraction or dilation will cause suction changes. Moreover, the load application during shearing test either normal loading and shear loading will cause suction changes. All these efforts from researchers around the world were to eliminate the introduction of significant modifications into the direct shear test which will make the simple test more complicated and time-consuming. Nowadays, using the high suction tensiometer the conventional direct shear test could be used with very few modifications will not affect the test simplicity and short time advantage. In this chapter, to characterize the shear strength of the Hawaii unsaturated soil, a modified direct shear cell was developed and described in detail.

2. MODIFIED OEDOMETER CELL

2.1.Literature Review

Conventional triaxial test apparatus designed to test saturated soils cannot be directly utilized for triaxial tests on unsaturated soils due to the difficulties in matric suction and volume change measurements. Bishop and Donald (1961) developed the suction-controlled triaxial test apparatus to characterize unsaturated soil behaviors. Since then, suction-controlled triaxial test, which is a drained test, has been extensively used to characterize unsaturated soil behaviors (Fredlund et al. 1978; Josa et al. 1987; Wheeler 1988; Sivakumar 1993; Romero et al. 1997; Ng et al. 2002; and Thu et al. 2006). However, suction-controlled triaxial tests are too laborious, time-consuming, and costly, and cannot be justified for routine engineering projects. Moreover, the SCTX test results are theoretically incorrect as presented in (Zhang 2016). Usually, it took months to years to characterize the stress-strain behavior of one unsaturated soil (Sivakumar 1993).

One-dimensional oedometer compression test was reported to be utilized for unsaturated soil behavior investigation (Le et al. 2011). However, in this test, due to lack of confining pressure, the test results cannot be used for soil constitutive behavior characterization. In the present study, a similar one-dimensional oedometer compression test system was presented to characterize unsaturated soil behaviors. The confining pressure generated by the oedometer compression ring was back-calculated based on the assumption that there is no lateral deformation during loading. Compared with the conventional suction-controlled triaxial test, suction-monitored one-dimensional oedometer compression test significantly reduced the time required to characterize an unsaturated soil behavior from years to days.

The suction-monitored one-dimensional oedometer compression test equipment was modified based upon a conventional oedometer for a one-dimensional oedometer compression test on saturated soils. Since the one-dimensional oedometer compression test was designed to investigate unsaturated soil behavior, under the undrained condition, soil suction would change due to the applied vertical stress. Thus, it was required to monitor soil suction change during loading. In Le et al. (2011), a high capacity tensiometer was adopted for the matric suction measurement. In this project, a newly designed high-suction tensiometer was utilized for the soil suction measurement.

3. SUCTION MEASUREMENT USING A HIGH-SUCTION TENSIOMETER

In the past few decades, a great effort has been dedicated to measuring matric suction of unsaturated soils. Reviews of conventional suction measurement methods on unsaturated soil are found in Fredlund and Rahardjo (1993), Ridley and Burland (1993), Ridley and Burland (2003), and Rahardjo and Leong (2006). Based on the literature review on existing high-suction tensiometers, a new high-suction tensiometer, as schematically shown in Figure 2.1a, was developed based upon an EPXO pressure transducer. Similar to previously developed high-suction tensiometers (Ridley and Burland 1993; Meilani et al. 2002; Lourenco et al. 2006), the tensiometer developed in this project as shown in Figure 2.1b included three parts: a pressure transducer, ceramic disc, and housing. However, unlike the other high-suction tensiometers, the ceramic disc was glued to a stainless steel ring (Figure 2.1b) instead of directly glued to the housing. To reduce the possibility of water cavitation under negative pressure and provide the room for the transducer diaphragm outward deformation, the thickness of the water reservoir was designed to be 0.2 mm. Ceramic disc with an air-entry value of 15 bar was used as a filter to prevent air from entering the water reservoir. The detailed fabrication process is presented in Li and Zhang (2014).

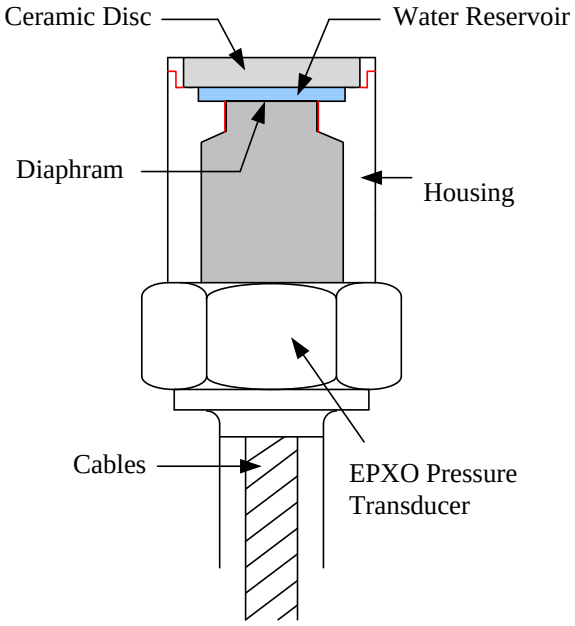

(a) Tensiometer design

(b) Tensiometer picture

Figure 2.1 High-suction tensiometer (Li and Zhang 2014)

4. OEDOMETER MODIFICATION

Since the one-dimensional oedometer compression test is to be performed on unsaturated soils under the undrained condition, the cell wall mounted on the pedestal of the oedometer is no longer required. Due to the use of high-suction tensiometers for matric suction measurement, a new cell base is required to accommodate the high-suction tensiometers. The oedometer modification is presented in Figure 2.2. A new cell base, the schematic design shown in Figure 2.2, was fabricated with a hole inside to hold the high-suction tensiometer in place. The new cell base has two parts. As shown in Figure 2.2, the tensiometer sits on the lower part. The upper part is in direct contact with the tested soil sample. The tensiometer is well aligned with the upper surface of the cell base to ensure a good contact between the tensiometer and soil sample. The upper part of the oedometer is firmly fixed to the cell base through threaded rods as shown in Figure 2.2.

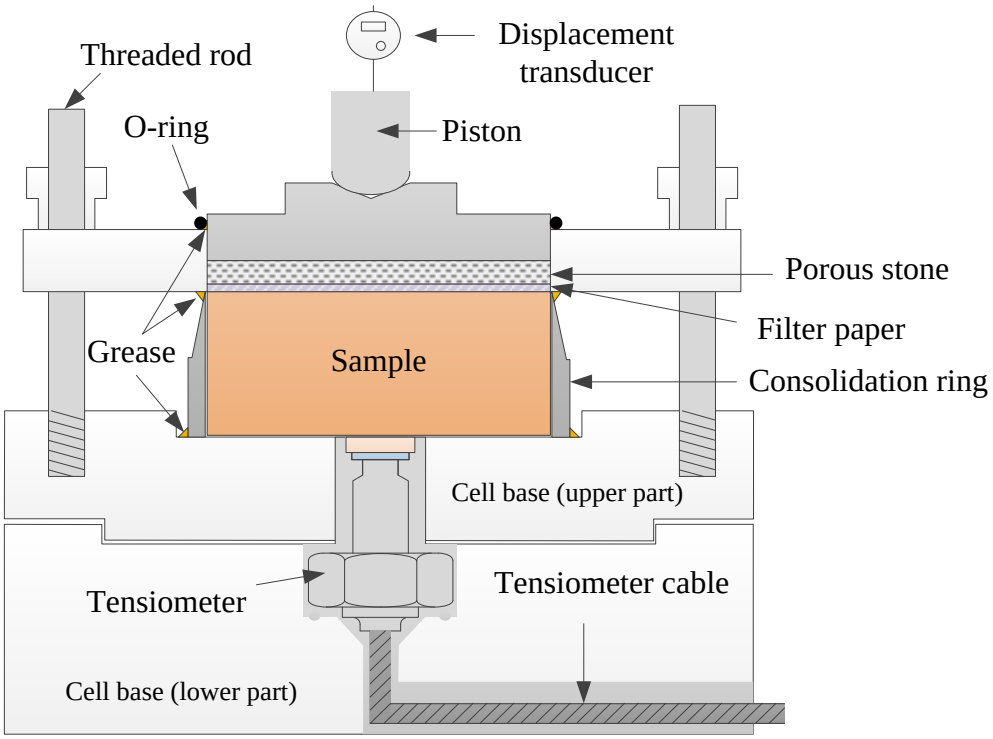

Figure 2.2 Modification on cell base for one-dimensional oedometer compression test

A new cell base was fabricated with a hole inside to hold the high-suction tensiometer (Figure 2.3a) in place. The lower part of the new oedometer cell base is shown in Figure 2.3b. As shown in Figure 2.2, the tensiometer sits on the lower part which is also shown in Figure 3c. The upper part of the cell base as shown in Figure 2.3d is in direct contact with the tested soil sample. The tensiometer is designed to be aligned with the upper surface of the cell base as shown in Figure 2.3d to ensure a good contact between the tensiometer and soil sample. An unsaturated soil sample inside the oedometer compression ring as typically shown in Figure 2.3e sits on the top of the upper part of the cell base. The upper part of the oedometer, which is the same as the conventional oedometer (2.5 inches fixed ring oedometer compression cell from Humboldt), is then firmly fixed to the cell base through threaded rods as shown in Figure 2.3f. The detailed fabrication process is presented in Li et al. (2015) and Zhang et al. (2016).

In this project, the used tensiometer was saturated in a triaxial chamber. To achieve an accurate measurement, high-suction tensiometer was calibrated in a positive pressure range after saturation. Negative pressure range calibration is based on extrapolation which was also used in Lourenco et al. (2006). The accuracy of the calibration can be checked by the water pressure immediately after cavitation, which should be approximate -100 kPa. After saturation and

calibration, the tensiometer was ready for matric suction measurement. The maximum attainable pressure of the high-suction tensiometer was determined to be approximately 1100 kPa through a free evaporation test presented by Guan and Fredlund (1997).

(a) High-suction tensiometer

(b) Cell base (lower part)

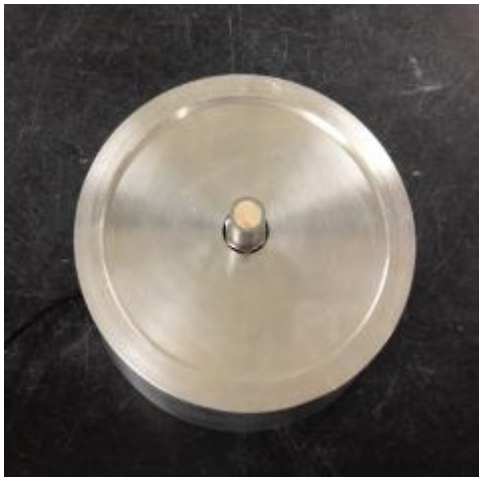

(c) Cell base with tensiometer

(d) Cell base (lower part)

(e) Unsaturated soil in a consolidation ring

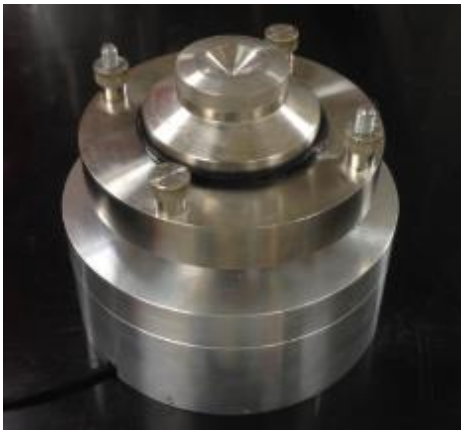

(f) Oedometer cell

Figure 2.3 Assembly for one-dimensional oedometer compression test

5. MODIFIED DIRECT SHEAR CELL

5.1.Literature Review

In geotechnical engineering, the soil shear strength parameters are required for the most man-made earth structures such as highway embankments, earth dams, and foundations. In these man-made earth structures, the compacted unsaturated soils are commonly used. A safe and economic slope or foundation design is highly dependent on an accurate determination of the unsaturated soil shear strength. As we know, the water content is playing a crucial role in advancing understanding of unsaturated soil behavior. The influence of water content on the shear strength and constitutive behavior of unsaturated soils could be found in many research efforts (e.g. Hilf 1956; Fredlund et al. 1978; Feddes et al. 1988; Fredlund and Rahardjo 1993; Fredlund et al. 1996; Thu et al. 2006; Li and Zhang 2015a and 2015b). An increase of water content could cause a decrease in shear strength of unsaturated soils which was one of the primary reasons for the failure of man-made earth structures and natural slopes (when induced to rainfalls). In the past, to be conservative, the unsaturated soils were usually considered as saturated for the design of the man-made earth structures. However, this design (consider unsaturated soils to be saturated) can be over-conservative and wasteful under the following situations: (1) the structure is located in arid areas with limited water access; and (2) the structure is equipped with a well-designed drainage system. On the other hand, studying the stability of natural slopes from unsaturated soils requires to precisely determine the unsaturated shear strength and evaluate the strength loss in case of rainfalls or water leakage. To design reliable and economically efficient structures and study natural slopes, the measurement of unsaturated soil shear strength has gained increasing attention in the past few decades (e.g., Bishop and Donald 1961; Gan et al. 1988; and Li and Zhang 2015a and 2015b).

5.2.Shear Strength of Unsaturated Soils

According to the Mohr-Coulomb failure criteria for saturated soils, a linear relationship exists between the shear strength and the net normal stress applied to the soil. However, different from the saturated soils, besides the net normal stress, the soil suction also plays an important role in the shear strength properties and soil failure criterion (Fredlund et al. 1978 and Khalili and Khabbaz 1998). Fredlund et al. (1978) reported that besides the normal stress, the shear strength of unsaturated soils could be significantly influenced by the soil suction. Subsequently, a new shear

strength equation was proposed for unsaturated soils using two independent stress state variables (net normal stress and matric suction) as shown in Equation 2.1.

$$\tau_f = c' + (\sigma - u_a)_f \tan\phi' + (u_a - u_w)_f \tan\phi^b \quad (2.1)$$

Where, ϕ^b= angle indicating the rate of change in shear strength relative to changes in matric suction. Equation 2.1 was well accepted and widely used to model the shear strength of unsaturated soils (e.g.,(Escario and Saez 1986; Gan et al. 1988; Oloo and Fredlund 1996; Vanapalli et al. 1996),(Li and Zhang 2015; Li and Zhang 2015; Thu et al. 2006). As stated in (Hamid and Miller 2009) the angle ϕ^b is approximately equal to ϕ' while the soil is saturated. However, once the air-entry value is exceeded, ϕ^b tends to decrease with increasing matric suction. As a result, the relationship between matric suction and shear stress becomes nonlinear which cannot be captured by Equation 2.1. To overcome this limitation, Vanapalli et al. (1996) proposed a nonlinear equation to model the shear strength of unsaturated soils (equation 2.2) as a relation with the volumetric water content. The unsaturated soil shear strength prediction models were summarized in Garven and Vanapalli (2006). However, equation 2.1 is more famous for practical use because of simplicity.

$$\tau_f = c' + (\sigma - u_a)\tan\phi' + (u_a - u_w)\left[\tan\phi'\left(\frac{\theta - \theta_r}{\theta_s - \theta_r}\right)\right]$$

where,

θ:soil volumetric water conent

θ_r: residual volumetric water content

θ_s:saturation volumetric water conten (2.2)

5.3.Tests to Characterize Shear Strength of Unsaturated Soils

There are several well-established tests available for the determination of shear strength parameters such as direct shear, triaxial, unconfined compression, and vane shear for saturated soils in both laboratory and field. However, all these conventional methods cannot be directly used to characterize the shear strength properties of unsaturated soils due to the difficulties in soil suction measurement. Bishop and Donald (1961) proposed the use of a consolidated drained test for measuring the shear strength of an unsaturated loose silt using a triaxial equipment. In this system, the soil suction during testing was controlled using the axis-translation technique proposed by Hilf (1956). This suction-controlled triaxial system was adopted by Miao (2002) for shear strength characterization on unsaturated soils. However, since the suction-controlled triaxial test is a consolidated drained test, the suction-controlled triaxial test is very laborious, time-consuming

due to the low permeability of unsaturated soils. In (Li and Zhang 2015) a modified unconfined compression system was developed and used to characterize the stress-strain behavior of unsaturated soils under low net confining stresses through constant water content triaxial tests. In this system, the confining load was applied through vacuum pressure. During testing, the soil suction was measured through two high-suction tensiometers mounted at the middle height of the unsaturated soils sample. With this system, the shear strength property of the tested unsaturated soil was determined. The adoption of constant water content test significantly reduced the time required for the unsaturated soil shear strength characterization when compared with the suction-controlled triaxial test. However, the major disadvantage of this system is the applied confining stress was limited to 100 kPa due to water cavitation when applying confining stress through vacuum pressure. Besides using the unconfined compression system, the constant water content triaxial test (e.g., Thu et al. 2006 and Li and Zhang 2015b) was also developed to characterize unsaturated soils through constant water content triaxial tests (unconsolidated undrained triaxial). With this system, the constitutive behavior and shear strength of unsaturated soils can both be characterized by the constant water content triaxial tests on unsaturated soils with different initial soil suction and confining pressure conditions. Besides the triaxial test as discussed above, similar to saturated soils, the shear strength properties of unsaturated soils can also be determined through direct shear tests.

Gan et al. (1988) developed a suction-controlled direct shear test, as schematically shown in Figure 2.4, to characterize the shear strength characteristics of unsaturated soils. Similar to the suction-controlled triaxial test proposed by Bishop and Donald (1961), the axis-translation technique was also used to control soil suction during shearing. An additional chamber was added to the direct shear cell to facilitate the adoption of the axis-translation technique. Using this system, the shear strength properties of a glacial till was successfully determined. This system was later adopted by Miller and Hamid (2006) and Hamid and Miller (2009) for shear strength characterization on different unsaturated soils. The soil specimens used in this direct shear tests were thin when compared to those used in the triaxial tests. As a result, the time required for direct shear testing was reduced when compared with the suction-controlled triaxial test due to the use of thin specimens. However, as presented in Gan et al. (1988), this testing apparatus required significant modifications on the conventional direct shear testing apparatus for the suction control purpose and was complicated to operate.

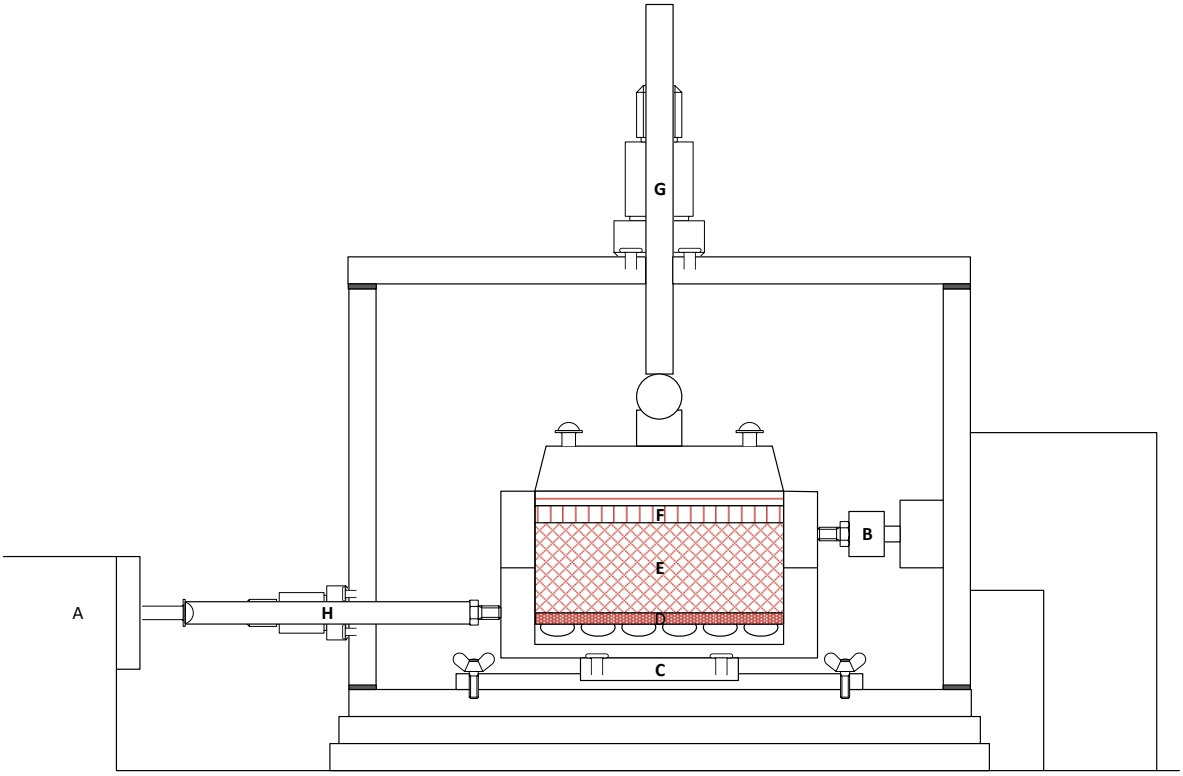

A: Gear Box B: Load cell C: Linear guide D: High air entry ceramic disc (HAID)
E: Soil sample F: Porous stone g: Loading ram H: Shearing ram

Figure 2.4 Suction-controlled direct shear test apparatus.

Besides the experimental methods as discussed above, the shear strength properties of unsaturated soils can be predicted based on the soil shear strength properties at saturated and the soil water retention curve as presented in Fredlund et al. (1996). However, there is a significant limitation which is the hysteresis effect of the soil water retention curve as well as the influence of specific volume and loading history.

Theoretically, as long as the soil suction at failure is known, both suction-controlled and constant water content direct shear tests can be used to characterize the shear strength of unsaturated soils. However, the stress paths for two tests during testing are different which are discussed in detail as follows.

5.4.Suction-Controlled Direct Shear Test

In a typical suction-controlled direct shear test, the soil specimen was required to be saturated in the direct shear chamber first as presented in Gan et al. (1988). Then, the specimen was

conditioned to different target suction levels through the axis-translation technique. After this, the direct shear test could be performed. Using the failure plane defined by Equation 2 as an example, Figure 2.5a shows the stress paths of unsaturated soils during suction-controlled direct shear testing. Point A represents a soil specimen with zero all-around stress and suction of s_1 at the start of a direct shear test. The application of the normal stress, σ_{n1}, caused the stress state moved from A to B on the σ - s plane at a constant suction of s_1. Then, the direct shear load was applied which caused the movement of stress state from B to C and continuous increase of the Mohr Circle diameter until touched the failure plane at F_1 as shown in Figure 2.5a. The failure plane is tangential to the Mohr Circle at the suction of s_1. However, only point F_1 is not sufficient to define a plane. At least two more direct shear tests for soils with different suction (s_2 and s_3) and normal stress (σ_{n2} and σ_{n3}) levels are required to be performed to define the failure plane. With these tests, the corresponding failure points F_2 and F_3 can then be determined. To increase the accuracy of the shear strength parameters (i.e. c', ϕ', and ϕ^b), more direct shear tests are encouraged to be performed. With these test results, a linear regression can be easily performed to find the best combination of the shear strength parameters through best-fit the failure points with a plane represented by Equation 2. Once the failure plane is defined (i.e., specified c', ϕ', and ϕ^b), the shear strength of the unsaturated soil at any combination of stress and suction can be predicted using Equation 2. The above process is straightforward. However, suction controlled tests are drained tests. As mentioned previously, due to the extremely low permeability of unsaturated soils, suction-controlled tests could be time-consuming.

5.5.Constant Water Content Shear Test

Before the direct shear test, the soil specimens were conditioned to different suction levels. Different from the suction-controlled direct shear test, the suction of an unsaturated soil during constant water content direct shear test continuously changing with normal and shear load application. Using the failure plane defined by Equation 2.1 as an example, Figure 2.5b shows the stress paths during constant water content direct shearing testing. Point A represents a soil specimen with zero all-around stress and suction of s_0 at the initial conditions (before the direct shear test). The application of the normal stress, σ_{n1}, caused the movement of stress state from A to B on the σ - s plane during which the soil suction decreased from s_0 to s_1. Then, the direct shear load was applied which caused the continuous movement of stress state from B to C and then to

F_1 at the constant normal stress of σ_{n1}. Meanwhile, the Mohr Circle diameter continuously increased until touched the failure plane at F_1 as shown in Figure 2.5b. Different from the suction-controlled direct shear test, the soil suction continuously varied from s_1 to s_2 and then to s_{1F} during shear loading. With the results from more direct shear tests at different soil suction (s_{2F} and s_{3F}) and normal stress levels (σ_{n2} and σ_{n3}), more failure points such as F_2 and F_3 can be obtained. Then, the shear strength parameters can then be determined through the best-fit linear regression on Equation 2.1. As discussed above, the principle for unsaturated soil strength measurement using the constant water content direct shear test is very simple. However, till now, the constant water content direct shear test has never been reported to characterize unsaturated soil shear strength due to lack of a proper sensor for soil suction measurement during shearing.

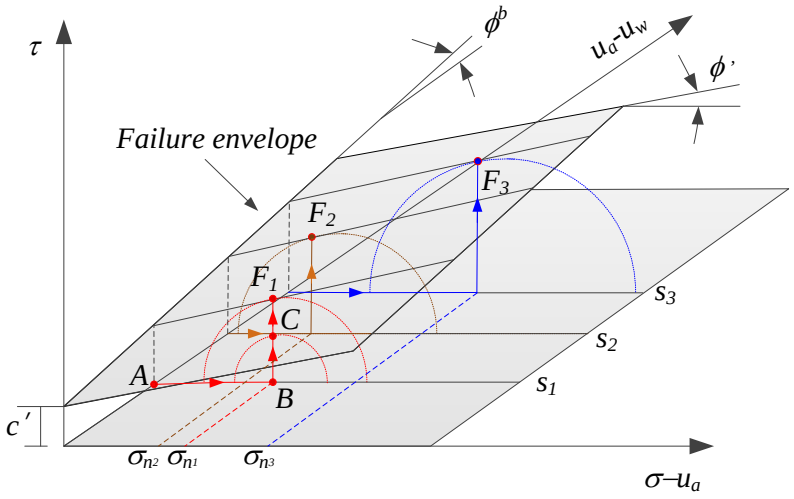

(a) Suction-controlled direct shear test

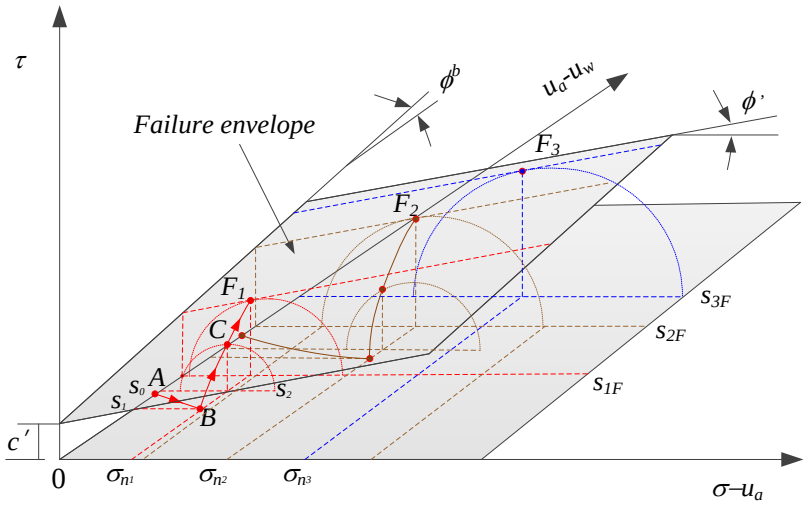

(b) Constant water content direct shear test

Figure 2.5 Stress paths for direct shear test on unsaturated soils

5.6. A Miniature High-Suction Tensiometer

The high-suction tensiometer used in the oedometer cell was too big for the direct shear cell. As a result, a miniature high-suction tensiometer was developed as shown in Figure 2.6a. This high-suction tensiometer comprised (1) a miniature EPB-PW pressure transducer for pressure measurement, (2) a 15 Bar high air-entry disc (6.5 mm in diameter and 1 mm in thickness) as a filter to prevent the tensiometer from cavitation at low pressures (< -100 kPa), and (3) a water reservoir to facilitate the generation of a negative water pressure which is detected by the pressure transducer. For the developed miniature high-suction tensiometer, the clearance between transducer diaphragm and ceramic disk, where the water reservoir was located, was approximately 0.1 mm. Figure 2.6b shows a picture of the miniature high-suction tensiometer developed in this project. After fabrication, the miniature high-suction tensiometer was saturated in a triaxial chamber through repeatedly applied water pressure of 600 kPa. The first saturation usually takes time (approximately a week for the tensiometer developed). This time for first saturation can be reduced through applying a higher chamber pressure and more pressurizing cycles. Besides this, the saturation method using CO_2 presented in Acikel and Mancuso (2009) can also be used to shorten the saturation process. To prevent any possible damage from impact, the miniature high-suction tensiometer was protected by a silicone rubber grommet as shown in Figure 2.6b.

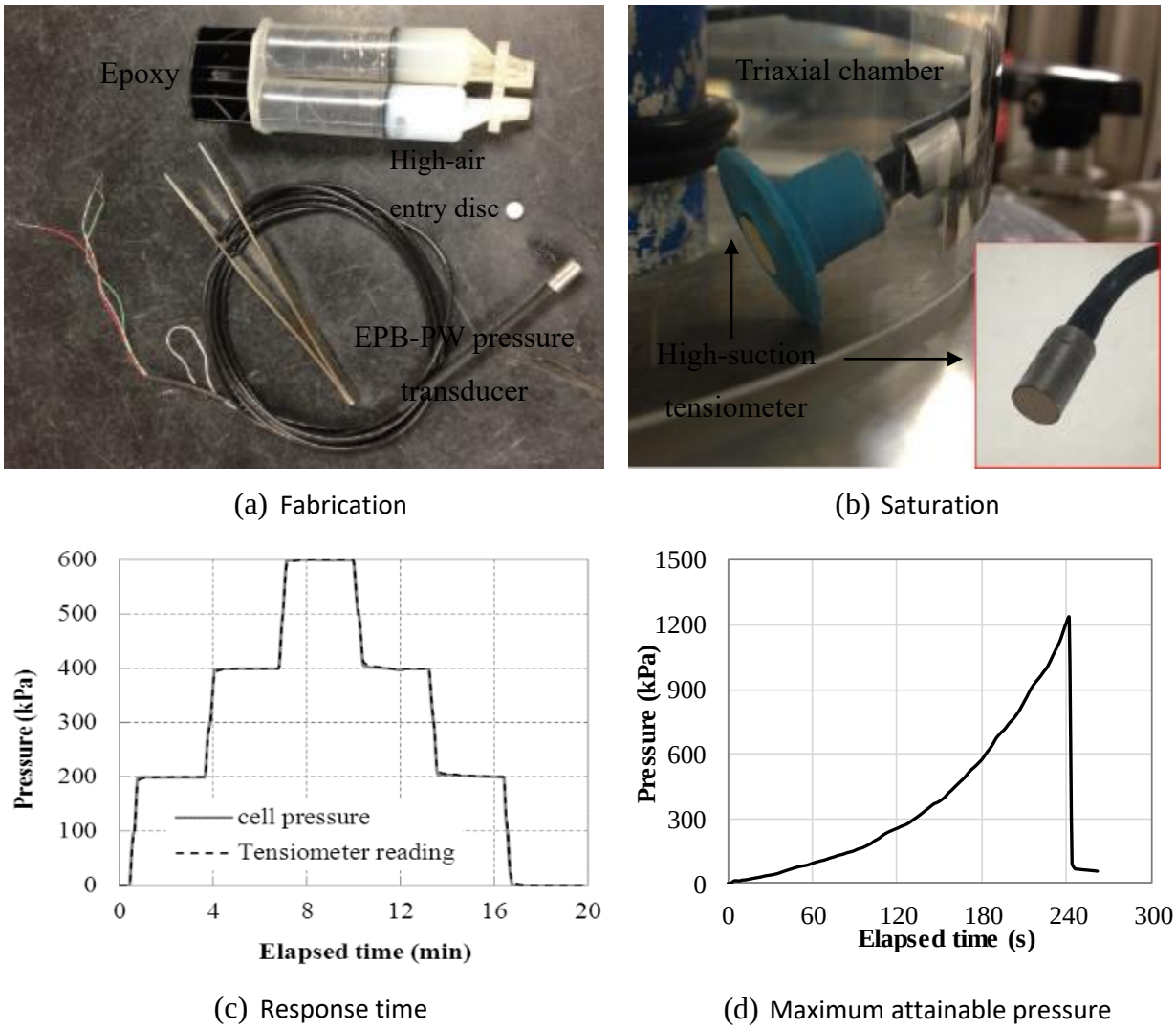

Figure 2.6 A miniature high-suction tensiometer

After saturation, the miniature high-suction tensiometer was calibrated in a positive pressure range. Negative pressure range calibration was based on extrapolation, which was also used by Li and Zhang (2014) and Lourenço et al. (2006). The accuracy of the calibration was examined by the water pressure immediately after cavitation, which should be approximate -100 kPa. After calibration, to evaluate tensiometer response time under a pressure change, a loading-unloading process was performed for the saturated tensiometer in the triaxial cell filled with water applying precise pressures. The scanning interval for the used data logger was set to be 2 seconds during data acquisition. Figure 2.6c shows the responses of the high suction tensiometer. It can be seen that the pressure measured by the miniature high-suction tensiometer was consistent with cell pressure variation with no delay, which means the response of the tensiometer was less than 2

seconds or nearly instantaneous. Free evaporation tests as suggested by Guan and Fredlund (1997) were also performed to evaluate the maximum attainable suction of the new miniature high-suction tensiometer. Figure 2.6d shows the response of the tensiometer during the free evaporation test. The maximum attainable suction of the used tensiometer was found to be 1235 kPa. After cavitation, the tensiometer pressure quickly reduced to nearly -100 kPa as shown in Figure 2.6d which verified that the tensiometer calibration was accurate.

5.7.Direct Shear Cell Modification

In this project, a direct shear cell was modified for direct shear test on unsaturated soils. As shown in Figure 2.7, this new cell comprised three components: (1) a miniature high-suction tensiometer for soil suction measurement during direct shearing under the undrained condition, (2) a top cap for the application of the normal stress during testing, and (3) two separate stainless steel rings to hold the unsaturated soil specimen and create the shear plane. Figure 2.7 shows a schematic plot of the new cell for the constant water content direct shear test on unsaturated soils. To achieve more representative soil suction measurement results, the miniature high-suction tensiometer tip is preferred to be located on the failure plane. However, for a real direct shear test, the failure plane is usually rough due to the non-uniformity of the soil specimen. As a result, in this new cell, the high-suction tensiometer tip was set to be approximately 1 mm above the failure plane as shown in Figure 2.7a. The miniature high-suction tensiometer tip should not be placed “far” away from the failure plane. Otherwise, the measured soil suction would be less representative. The presence of the spring ensured a good contact between the soil and the high-suction tensiometer. This new cell was designed to accommodate the conventional direct shear cell. To characterize the shear strength properties of unsaturated soils, this new cell was placed in the conventional direct shear cell as shown in Figure 2.7b. With this new cell, the conventional direct shear test apparatus could then be performed.

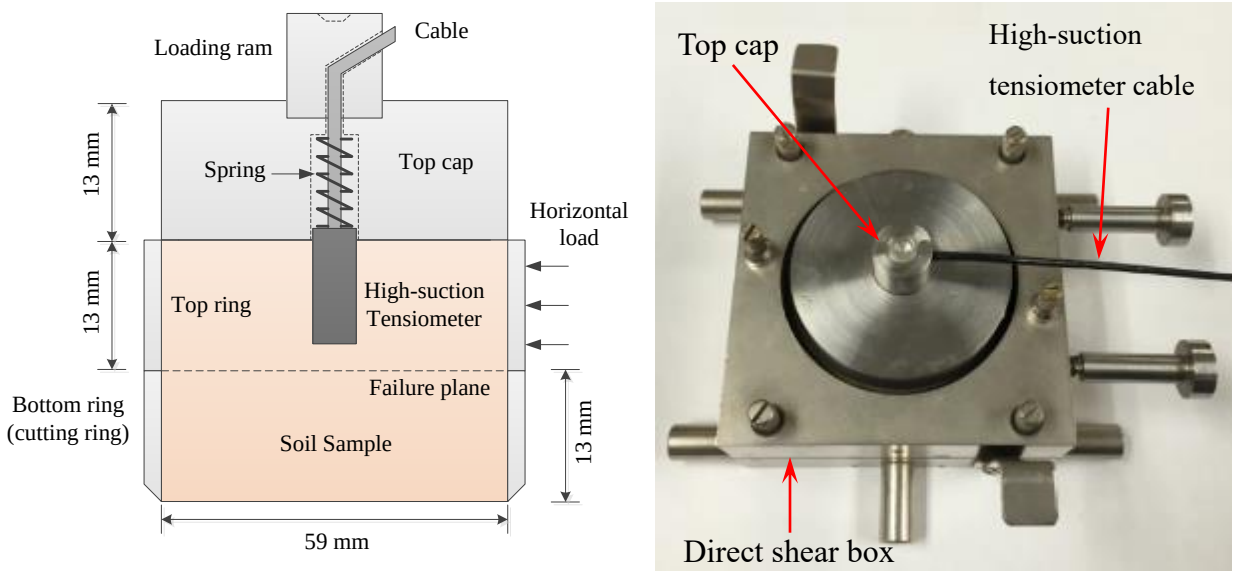

(a) Schematic design (b) New cell in a direct shear box

Figure 2.7 A new direct shear cell

CHAPTER III EXPERIMENTAL PROGRAM

1. SAMPLING

The samples were stored in metal or plastic tubes as shown in Figure 3.1. The original soil samples were not in good shape especially at both ends as typically shown in Figure 3.1. Before testing, the samples were extracted using a hydraulic extruder. To minimize the disturbance during extraction, the soil specimens were directly extracted to the rings for oedometer compression and direct shear test as shown in Figures 3.2a and 3.2b. Then, the soil specimen was cut off from the tube as shown in Figure 3.2c. No obvious disturbance on the sample surface was observed after this extraction. Figure 3.2d shows a picture of the soil specimen in the ring before the oedometer compression or direct shear test. After extraction, the soil specimens were stored in air-tight plastic bags for suction equilibrium or conditioning. The soil specimens were conditioned to different moisture contents by controlling the number of exposures to the atmosphere for about 15 min/day. Finally, the soil specimens were sealed in plastic bags and stored in a moist room for at least one week to ensure suction equilibrium in the whole soil specimen.

Figure 3.1 Soil Samples

Figure 3.2 Sampling process

2. ONE-DIMENSIONAL OEDOMETER COMPRESSION TEST ON UNSATURATED SOILS

After suction equilibrium in the unsaturated soil specimen, the constant water content one-dimensional oedometer compression test can then be performed. Before testing, the weight of the oedometer compression ring, as well as the soil specimen inside as shown in Figure 3.2d, was accurately determined. Then, the saturated high-suction tensiometer was mounted to the oedometer cell base. To avoid cavitation during test preparation, the porous ceramic disc of the tensiometer was covered with a thin layer of Kaolin paste which was also recommended by other researchers (e.g. Colmenares and Ridley 2002 and Le et al. 2011). The unsaturated soil specimen was mounted

to the cell base after tensiometer installation. Due to the self-weight of the upper part of the modified oedometer and the soil specimen, a good contact between the tensiometer and the bottom surface of the specimen was established. System setup for the one-dimensional oedometer compression test is shown in Figure 3.3. The loading device is exactly the same as the conventional oedometer. Since the testing process for the one-dimensional oedometer compression test lasted for several hours, water evaporation during testing is very critical. After system assembling as shown in Figure 3.3, vacuum grease was smeared to the places needed to avoid water evaporation during testing. Also, an O-ring was placed around the loading piston to prevent water evaporation from the top surface of the specimen. Then, the used displacement transducer and tensiometer were connected to a Datalogger. A computer was required to monitor the soil volume and suction change during testing as shown in Figure 3.3.

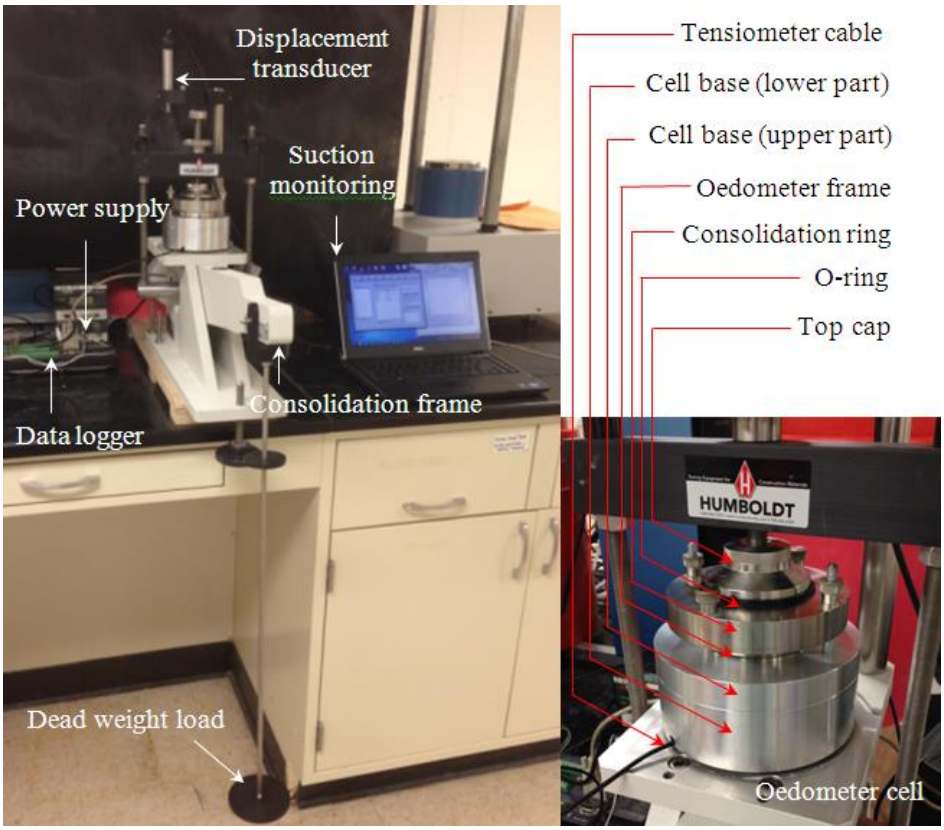

Figure 3.3 One-dimensional oedometer compression test on an unsaturated soil

Usually, before loading, several minutes were required for the high-suction tensiometer readings to reach equilibrium. Then, the vertical load was applied to the unsaturated soil specimen through dead weight come with the oedometer compression system. After each loading step, the

applied vertical stress was maintained to be constant for a certain time. This is because the matric suction in the soil specimen would change due to the applied load and this suction change required some time to reach a new equilibrium (Le et al. 2011). The higher the soil suction, the more time required for suction equilibrium (Oliveira and Marinho 2008). The applied vertical stress gently increased or decreased to a target value and followed by another equilibrium period. After reach equilibrium, the readings of tensiometer and the local displacement transducer were recorded. In this project, the tested soil specimen was gradually loaded to a vertical stress of 800 kPa and then unloaded to 25 kPa. After testing, the weight of the oedometer compression ring, as well as the soil specimen inside after testing, was double checked to make sure that there was no water loss during testing.

3. DIRECT SHEAR TEST ON UNSATURATED SOILS

After conditioning, the specimens were then used for the direct shear test. The rings for the direct shear test, as shown in Figure 3.4a, were 59 mm in diameter and 26 mm in height. Also, the saturated miniature high-suction tensiometer was assembled with the top cap as shown in Figure 3.4b. Before the installation of the high-suction tensiometer, a 6.5 mm in diameter and 12 mm in depth hole was required to be made at the center of the specimen as shown in Figure 3.4c. In order to prevent tensiometer cavitation during installation and maintain a good contact between the high-suction tensiometer and the soil, similar to the oedometer compression test, a thin layer of saturated kaolin was also smeared on the surface of the ceramic disk. The analysis of shear strength data would not be complete without the volume change behavior during testing. In this direct shear test, the soil volume change was monitored through a linear variable differential transformer (LVDT) mounted at the top of the soil as shown in Figure 3.4d. After installation of soil specimen, high suction tensiometer, and LVDT, dead weight was placed on the yoke to apply the normal load on the soil specimen. When the tensiometer reading stabilized, the direct shear load could then be applied at a constant loading rate of 0.05 mm/min. The shearing process was stopped after the soil specimen reached the failure stage. The soil specimen after the direct shear test was then used for moisture content measurement. Figure 3.4e shows a soil specimen after the direct shear test. It was found that the tensiometer was exactly located at the failure plane. In other words, the measured soil suction was representative of the unsaturated soil shear strength characterization.

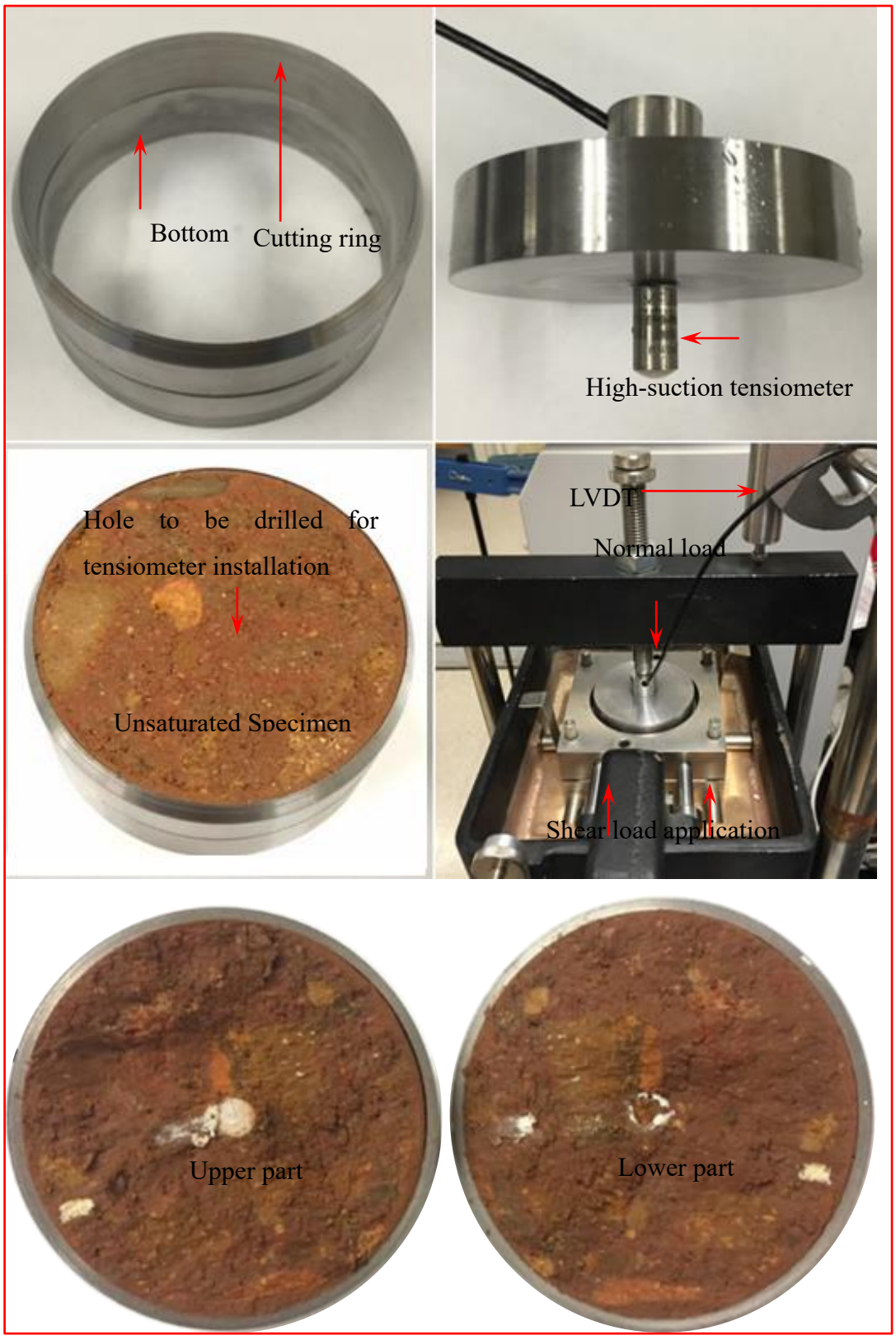

Figure 3.4 Constant water content direct shear test on an unsaturated soil

CHAPTER IV TEST RESULTS AND DATA ANALYSIS

1. TEST RESULTS

The matric suction, water content, and specific volume of the tested soil specimens before the oedometer compression test are summarized in Table 4.1. Besides this, the soil information before the direct shear test and at-failure during shearing are also summarized in Table 4.2. Direct shear test number (3) was excluded from the direct shear test results because of negative suction value. Negative suction value means pore water pressure is generated which is not expected for unsaturated soil sample.

Table 4.1 Summary of specimen initial conditions for oedometer compression tests

Water content	v=1+e	Initial suction (kPa) at 25 kPa normal load
35.81%	2.28	386.3
46.04%	2.485	56.3
34.23%	2.145	136.4
29.84%	2.081	325.7
33.56%	2.116	106.5
30.09%	2.026	224.9
26.19%	2.085	353.6
34.64%	2.153	98.2

Table 4.2 Summary of specimen initial and final conditions for direct tests

Test No.	*Initial condition*			*At failure during shearing*		
	W_c	*v=1+e*	*s (kPa)*	*Matric suction (kPa)*	*Shear strength (kPa)*	*Normal stress(kPa)*
1	30.21%	2.191	58.7	235	310	463
2	29.10%	2.209	403	224.70	171.06	139
3	35.81%	2.132	83.4	-7.0	255.96	463
4	38.34%	2.204	428.7	128.9	185.59	236
5	41.38%	2.228	47.9	18.6	80.87	116
6	41.23%	2.235	87	62.60	79.774	58
7	44.23%	2.313	18.9	24.2	173	232
8	32.00%	1.991	649.4	282	356.8	463
9	32.43%	1.973	81.5	84	132.188	116
10	33.72%	2.006	144.4	110.80	99.708	58

2. ONE-DIMENSIONAL OEDOMETER COMPRESSION TEST

For the constant water content one-dimensional oedometer compression tests, matric suction and vertical displacement were recorded during testing using the high-suction tensiometer and the local displacement transducer, respectively. In this project, soil suctions after equalizations were used as the representative suctions for soil at different loading steps. Based on soil displacement at different loading steps, soil volumes at different loading steps were calculated. Figures 4.1a and 4.1b presented the soil volume and suction variations at different loading steps, respectively. The experimental test results were plotted in different 3D spaces using the Matlab software as presented in Figure 4.2 to be investigated more clearly. Detailed oedometer compression test results are summarized in Appendix A.

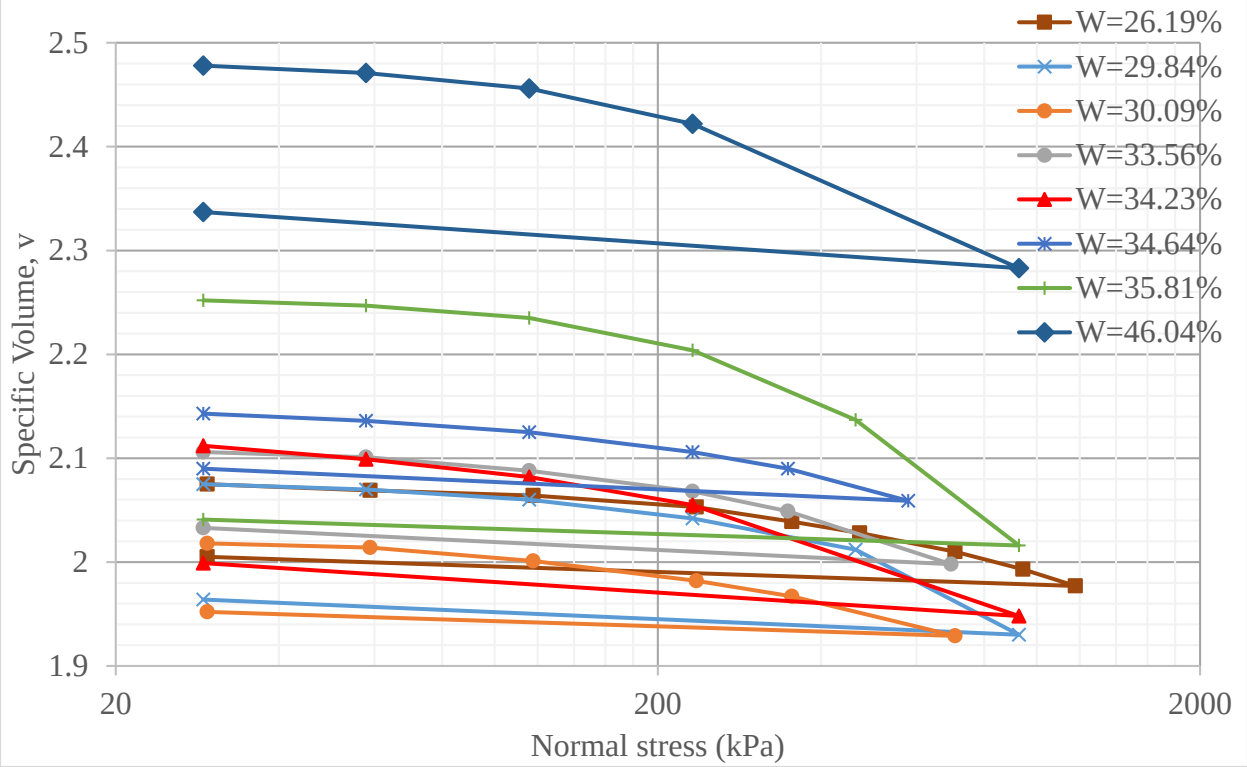

(a)

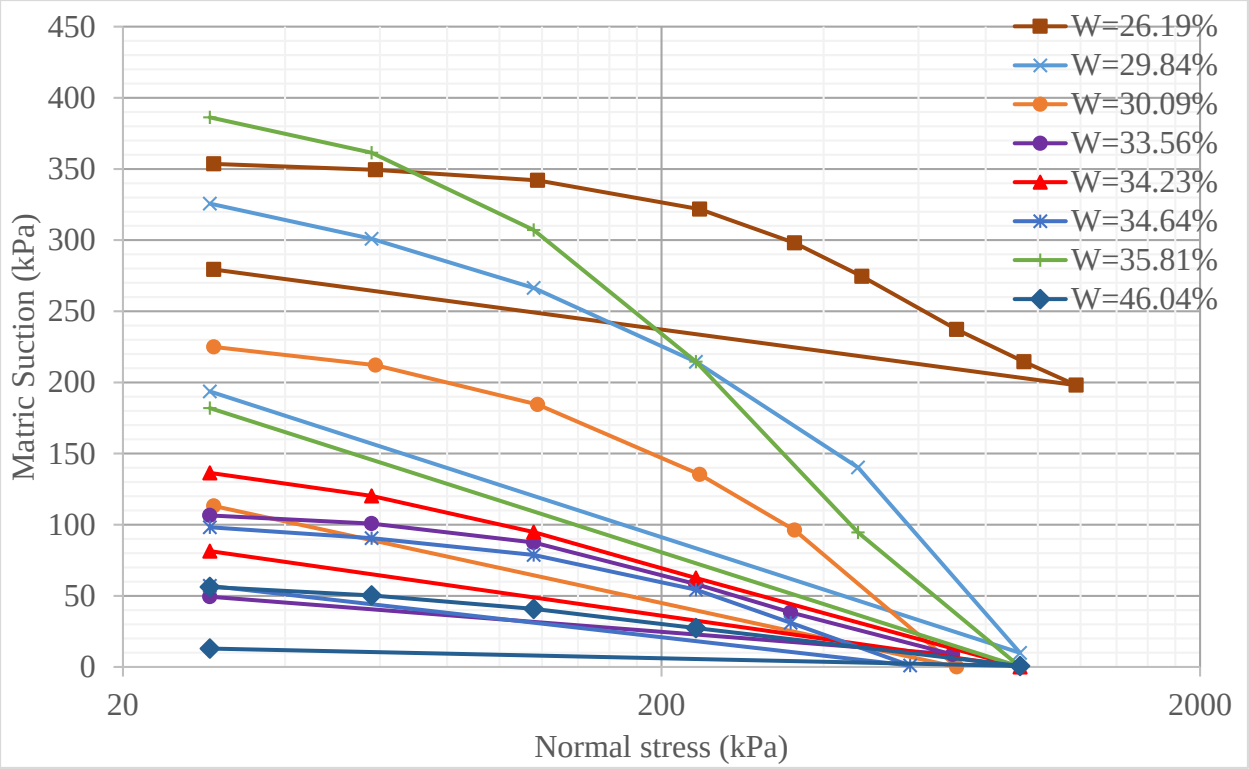

(b)

Figure 4.1 Soil volume and suction variations during oedometer compression.

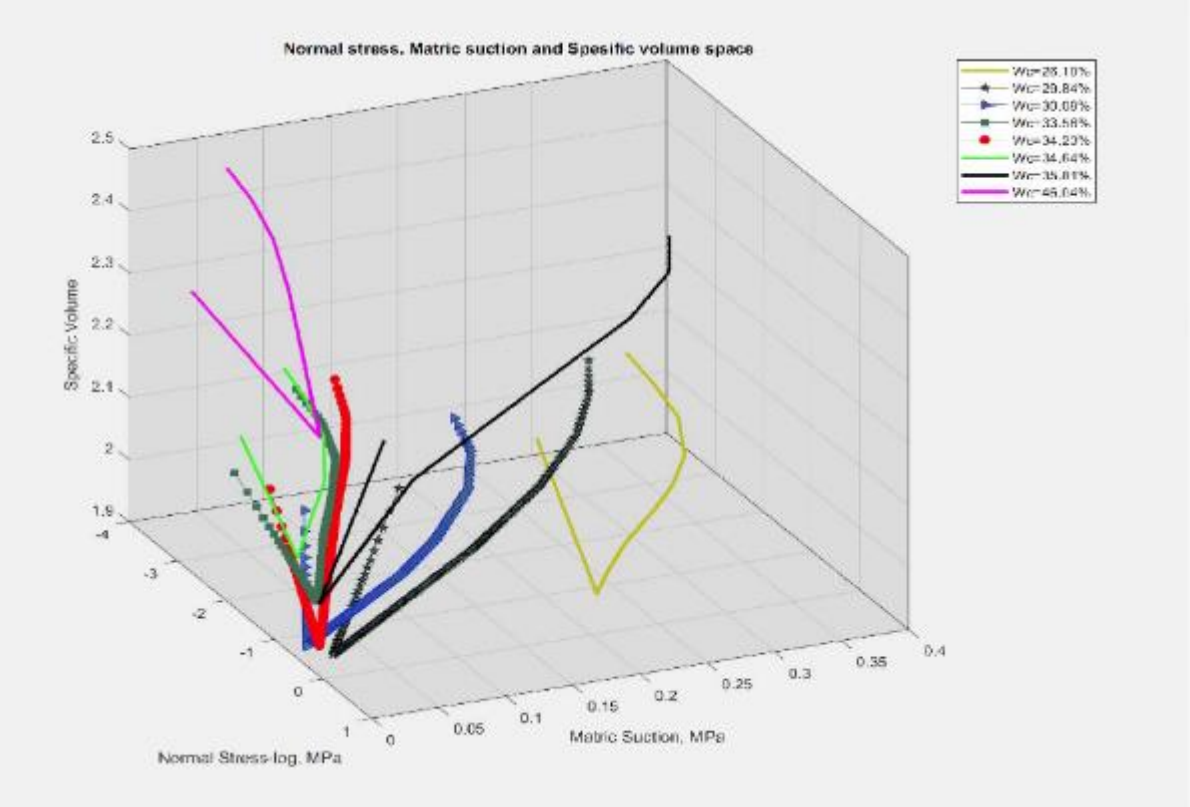

(a) Normal stress-suction-specific volume space

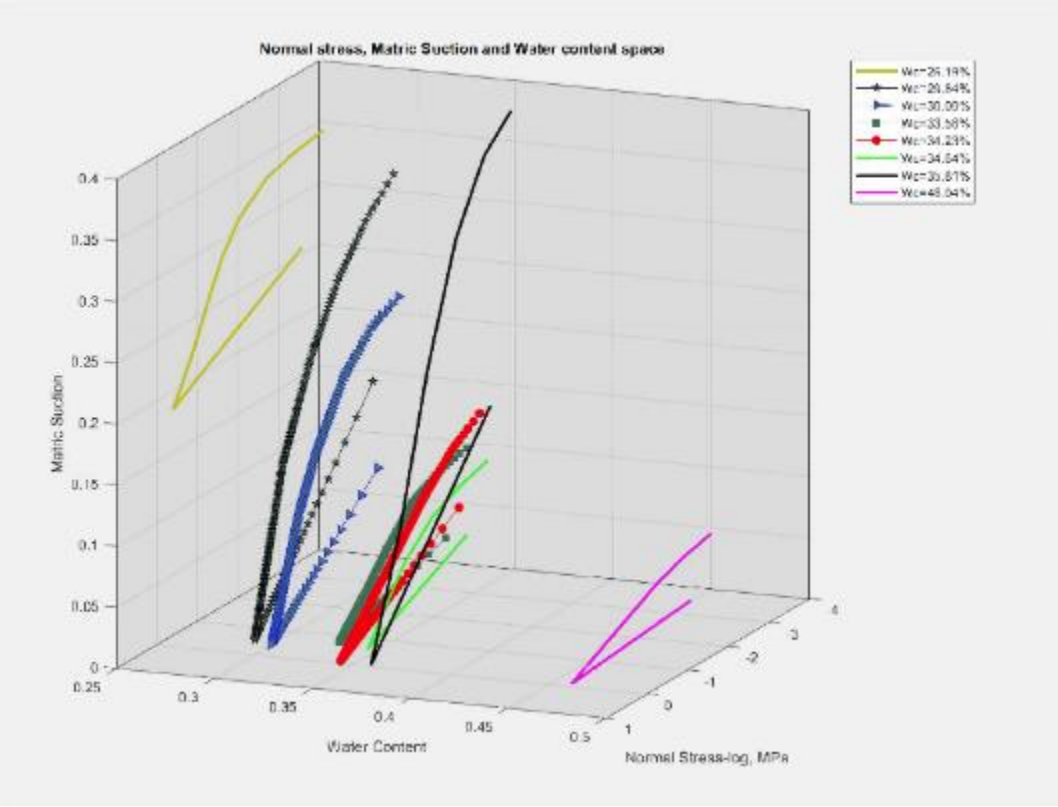

(b) Normal stress-water content-suction space

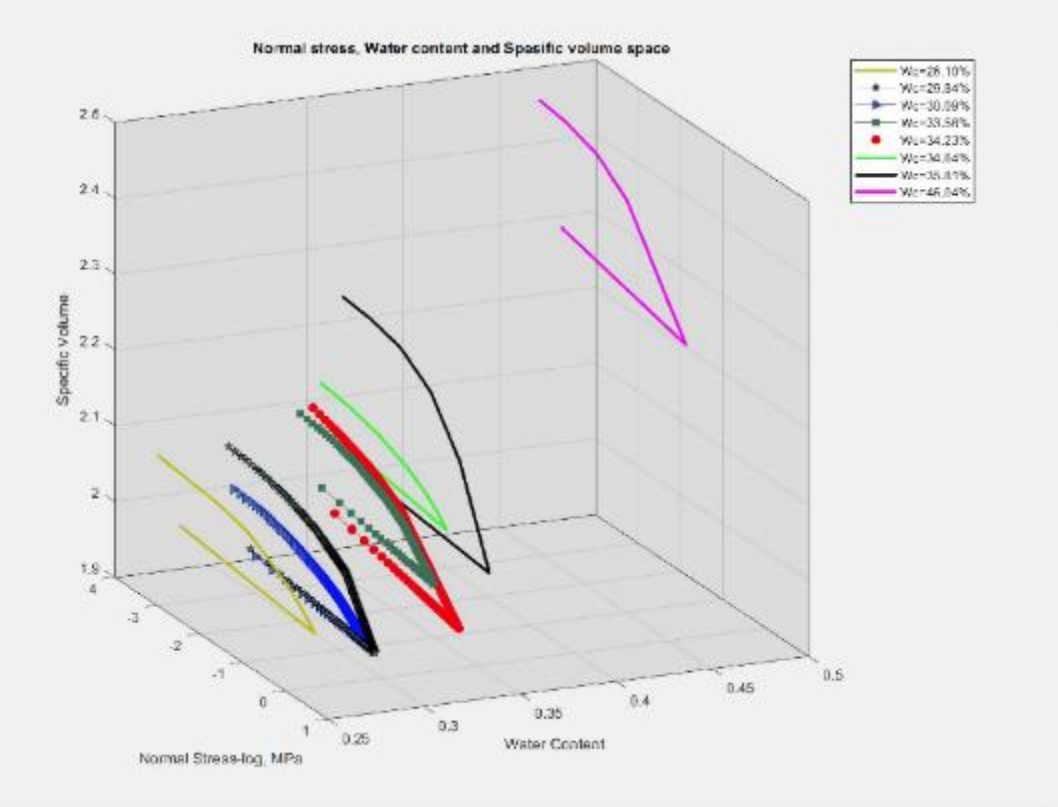

(c) Normal stress-water content-specific volume space

Figure 4.2 Oedometer compression test results in different 3D spaces.

As can be seen in Figure 4.1a and 4.2a, during vertical testing, soil volume decreased with increasing vertical stress. This volume decrease is attributed to the elasto-plastic behavior of unsaturated soils. During unloading, soil volume increased with decreasing vertical load. When comparing the soil volume at a vertical stress of 25 kPa at loading and unloading stages, it could be found the unsaturated soil specimens experienced a significant volume decrease as shown in Figure 4.1a. During vertical testing, as can be seen in Figure 4.1b, soil suction decreased with the increase of vertical stress. It is clear from Figure 4.2a that as the normal stress increases the soil specific volume as well as the matric suction decreases simultaneously. During unloading, soil suction increased with decreasing vertical stress. However, soil suction was not fully recovered at 25 kPa after unloading due to the plastic volumetric deformation.

3. DIRECT SHEAR TEST

After the constant water content, direct shear test on unsaturated soil specimens, matric suction and soil volume changes of the tested specimens during testing were recorded using the miniature

high-suction tensiometer and the local displacement transducer, respectively. Detailed direct shear test results are summarized in Appendix B. The shear stress variations in the soil specimens with different water contents during loading under different normal stresses were presented in Figure 4.3.

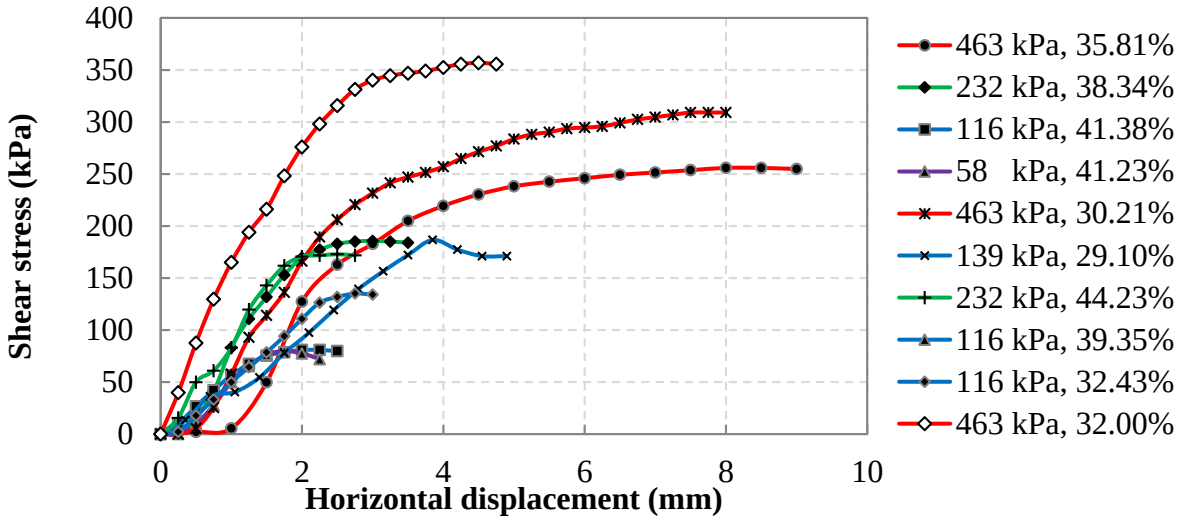

Figure 4.3 Shear stress variations during shearing

As can be seen in Figure 4.3, with increasing horizontal displacement, the shear stress in the soil increased and then reach peaks and then stabilized or decreased. It could be found that the peak shear stresses generally increased with increasing normal stress. Besides the shear stress, soil suction and volume variations versus horizontal displacement during shearing under different normal stress and water content levels were also extracted and presented in Figures 4.4a and 4.4b, respectively.

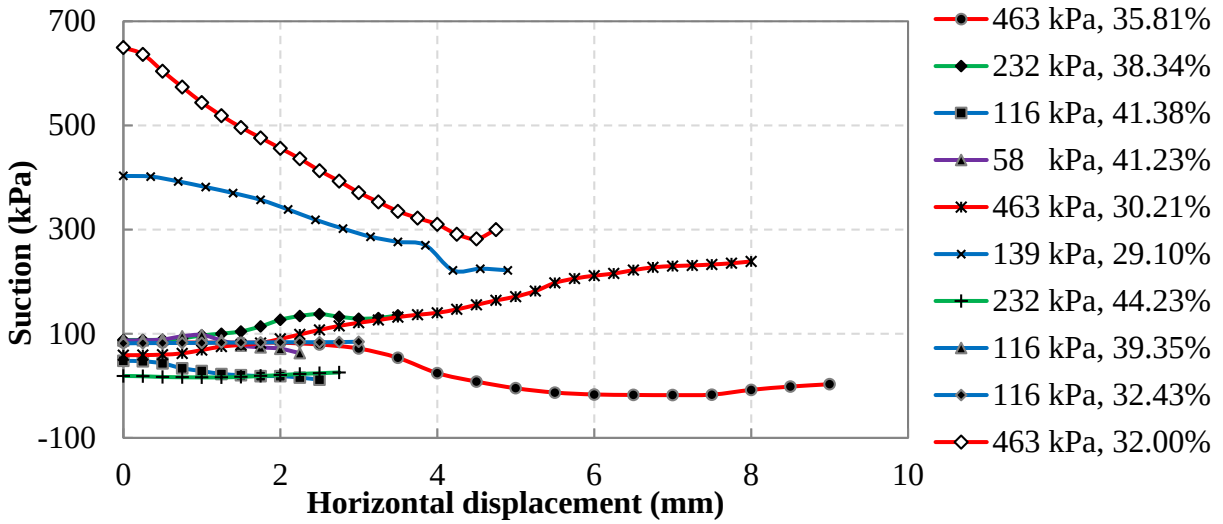

(a)

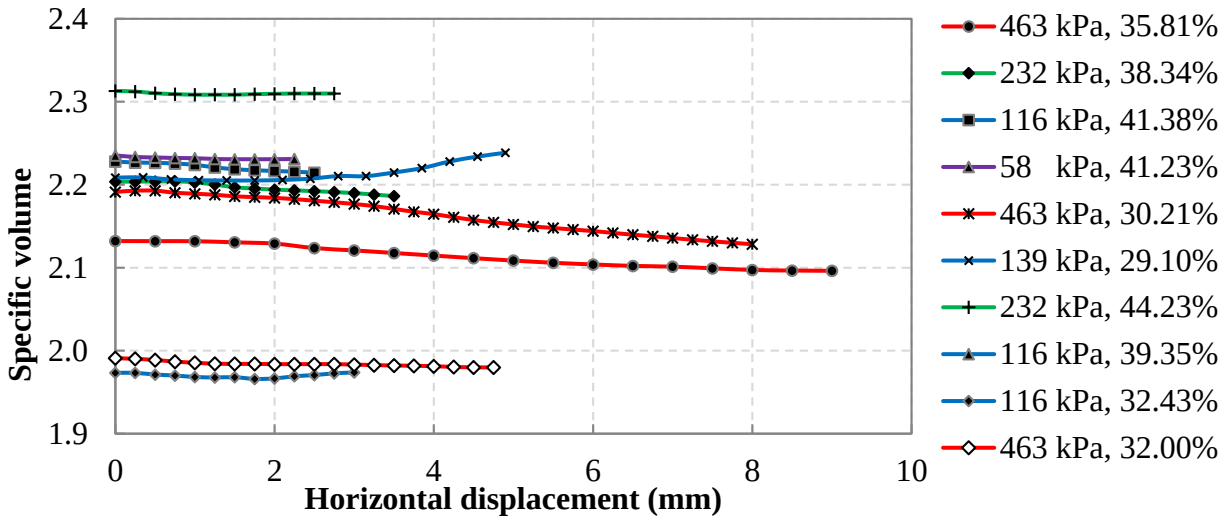

(b)

Figure 4.4 Soil volume and suction variations during shearing

As shown in Figure 4.4a, at high initial soil suction levels, the soil suction usually decreased with increasing shear load/displacement. However, for soil specimens with initial soil suction less than 100 kPa, with increasing shear load/displacement, the soil suctions variations during shearing were different under different normal stress and water content conditions. At different normal stress conditions (e.g., 463 kPa), most of the soil volumes slightly decreased with horizontal displacement during shearing except the specimen with a water content of 29.1% and 32.43 sheared under normal stresses of 139 kPa and 116 kPa, respectively.

4. DATA ANALYSIS

4.1.Shear Strength Characterization

The shear strength equation proposed by (Fredlund et al. 1978) was used to study and analyze the stress states for all soil specimens at failure (σ_{1f}-u_a, σ_{3f}-u_a, s_f). A linear regression was performed on the test results to find the best estimation of the shear strength parameters. To find out the suitable combination of shear strength parameters c', ϕ', and ϕ^b, the below procedure shall be followed:

1- Assume arbitrary values for the shear strength parameters (i.e., c', ϕ', and ϕ^b).

2- Using Fredlund, Morgenstern et al. (1978) equation, calculate the shear strength based on the assumed values in step (1).

3- Calculate the square of differences between the measured and predicted shear strength based on the below equation. The predicted values and the squared errors are presented in table 4.3.

$$F(x)=\sum_{i=1}^{n} w_i\left[(\tau_{fm})_i-(\tau_{fp})_i\right]^2 \qquad (4.1)$$

4- Use SOLVER add-in in Microsoft Excel to guess the best-fit parameters to get the minimum error.

Table 4.3 Predicted shear stress and errors.

Initial condition			At failure during shearing			Predicted	Error^2
W_c (%)	v	s (kPa)	s_f (kPa)	*Shear stress* (kPa)	*Normal stress* (kPa)	*Shear stress* (kPa)	
30.21	2.191	58.7	235	310	463	329.75	390.08
29.10	2.209	403	224.7	171.06	139	169.78	1.64
38.34	2.204	428.7	128.9	185.59	236	188.19	6.75
41.38	2.228	47.9	18.6	80.87	116	97.19	266.35
41.23	2.235	87	62.6	70	58	82.22	149.40
44.23	2.313	18.9	24.2	173	232	155.03	322.80
32.00	1.991	649.4	282	356.8	463	343.76	169.93
32.43	1.973	81.5	84	132.188	116	116.69	240.17
33.72	2.006	144.4	110.8	99.708	58	96.59	9.69
						Sum of errors =	1556.81

The calculated best-fit shear strength parameters c', ϕ', and ϕ^b were 35.47 kPa, 25.84°, and 16.60°, respectively. As shown in Figure 4.5, the coefficient of determination (i.e., R^2) was 98% which indicates a strong relationship between the independent variables (i.e. c', ϕ', and ϕ^b) and the dependent variables (i.e., $_{1f}$-u_a, σ_{3f}-u_a, $_{sf}$). Figure 4.6 shows the Mohr circles at failure and the Mohr-Coulomb failure envelope based upon the calibrated model parameters in the $\tau - (\sigma - u_a) - (u_a - u_w)$ space.

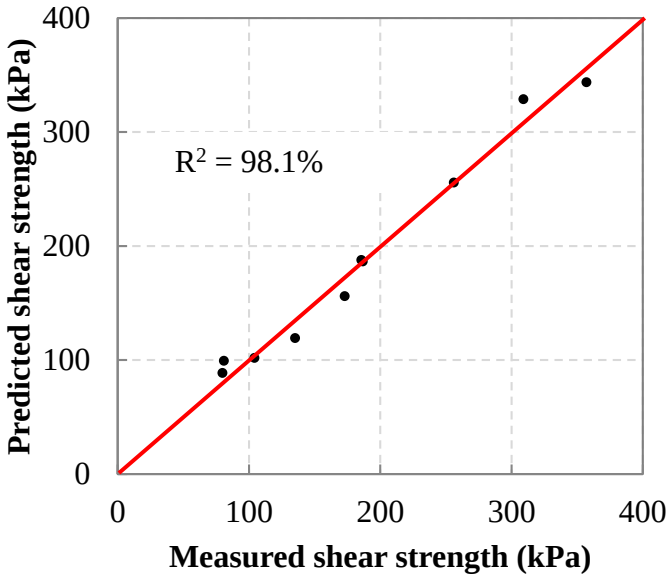

Figure 4.5 Measured and predicted shear strength

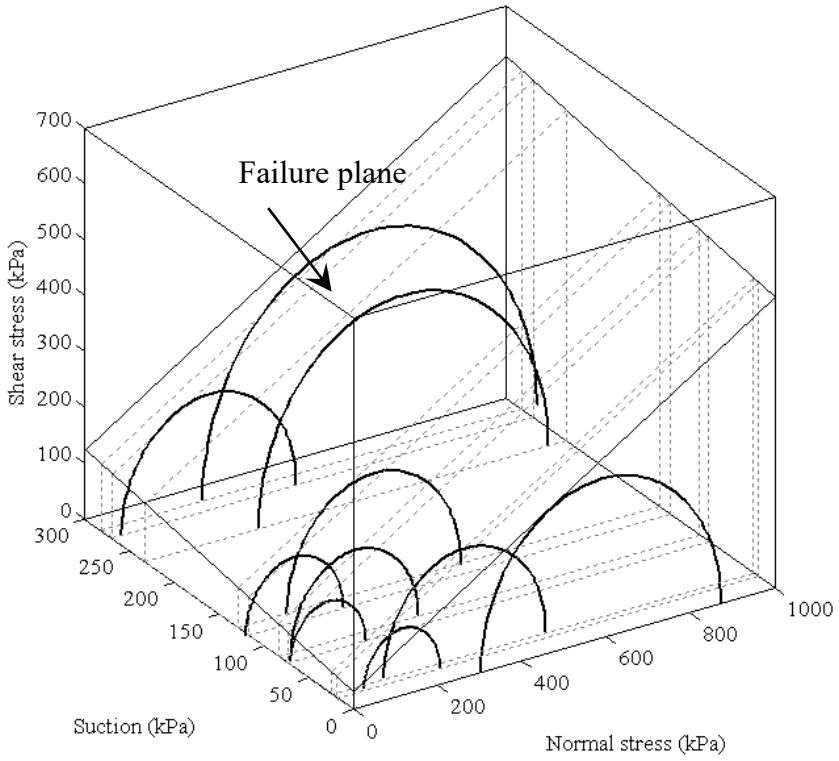

Figure 4.6 Mohr-Coulomb circles at failure and the failure envelopes

5. CONSTITUTIVE MODELING

5.1.General

Unsaturated soils are exhibit irrecoverable volumetric changes (elasto-plastic) when subject to loading and wetting or drying cycles. (Alonso et al. 1990) proposed the first unsaturated soil model that considers the elasto-plastic behavior of unsaturated soils, which later called Barcelona Basic Model (BBM). The BBM successfully explained many features related to the unsaturated soils behavior. One of the most important features of the BBM is the introduction of LC yield curve (Loading Collapse) concept in the p-s plane on which the yield stress increases with the suction increase. The BBM was proposed using incremental form following the conventional theories of soil plasticity. This makes the calibration of the model parameters extremely difficult, even if SCTX used (Gallipoli et al. 2010; Zhang and Lytton 2009; Zhang and Lytton 2009; Zhang and Lytton 2011; Zhang and Xiao 2013). The concept of state surface approach (SSA) was firstly proposed by Matyas and Radhakrishna in 1968 to relate the void ratio and degree of saturation to the suction and mean stress. However, the SSA is an elastic analysis of the unsaturated soils

(Alonso et al. 1987; Alonso et al. 1990). In 2009, Zhang and Lytton proposed the modified state surface approach (MSSA) which considers the elasto-plastic behavior of unsaturated soils. The MSSA used to explain the BBM using the integrated form to generate surfaces for the elastic and plastic behavior of soils (Zhang and Lytton 2009; Zhang and Lytton 2009; Zhang and Lytton 2011).

(Zhang et al. 2016) derived and explicit formulation for at-rest coefficient based on k_0 definition without any additional assumptions. In addition to, a procedure to calibrate the BBM parameters under triaxial stress conditions based on the results of oedometer test only. After that, the same procedure used to calibrate the BBM parameters under triaxial loading conditions based on constant water content oedometer tests (Zhang et al. 2016). However, it was recommended by the author that the BBM shear strength parameters shall be introduced from additional test related to soil shear strength at failure. This was based on the concept that no failure is related to the oedometer test which means that the shear strength parameters calibrated using only oedometer test results are just extrapolations to the oedometer test results. In Hawaii project, the procedure described by (Zhang et al. 2016) to calibrate BBM parameters will be used and the shear strength parameters will be introduced to the procedure from constant water content direct shear test. The calculations will be explained in detail in the following sections.

5.2.BBM Shear Strength Parameters

In this section, the BBM parameters related to shear strength (i.e. M and K) will be calculated from the constant water content direct shear test results (CWDS). In the CWDS, the suction at failure measured using miniature HST equipped in the conventional direct shear cell. A derivation is provided to calculate M and K from the unsaturated soil shear strength properties (i.e. c', ϕ', and ϕ^b) based on C'=0.0 which is assumed by the first author of modified Cam-Clay model and addressed by Alonso et al., 1990.

Starting from Fredlund et al. (1978) shear strength equation.

$$\tau_f = c' + (\sigma - u_a)_f \tan\phi' + (u_a - u_w)_f \tan\phi^b \quad (4.2)$$

The suction effect may be considered as a cohesion effect and can be added to the cohesion.

$$\tau_f = \left[c' + (u_a - u_w)_f \tan\phi^b \right] + (\sigma - u_a)_f \tan\phi' \quad (4.3)$$

Denoting the suction and cohesion term as C.

$$\tau_f = C + (\sigma - u_a)_f \tan\phi' \quad (4.4)$$

Below is the shear strength of the soil as a function of the major and minor principal stresses.

$$(\sigma_1 - u_a)_f = (\sigma_3 - u_a)_f \tan^2\left[\frac{\pi}{4} + \frac{\phi'}{2}\right] + 2C\tan\left[\frac{\pi}{4} + \frac{\phi'}{2}\right] \tag{4.5}$$

The deviatoric and mean effective stresses are defined as follows:

$$q = (\sigma_1 - u_a) - (\sigma_3 - u_a) \tag{4.6}$$

$$p = \frac{(\sigma_1 - u_a) + 2(\sigma_3 - u_a)}{3} \tag{4.7}$$

From that one can get σ_1 and σ_3 as functions in q and p,

$$(\sigma_1 - u_a) = \frac{3p + 2q}{3} = p + \frac{2q}{3} \tag{4.8}$$

$$(\sigma_3 - u_a) = \frac{3p - q}{3} = p - \frac{q}{3} \tag{4.9}$$

Substituting equations (4.8) and (4.9) into equation (4.5),

$$\left(p + \frac{2q}{3}\right)_f = \left(p - \frac{q}{3}\right)_f \tan^2\left[\frac{\pi}{4} + \frac{\phi'}{2}\right] + 2C\tan\left[\frac{\pi}{4} + \frac{\phi'}{2}\right] \tag{4.10}$$

Inserting C back to equation (4.10), one has

$$\left(p + \frac{2q}{3}\right)_f = \left(p - \frac{q}{3}\right)_f K_p + 2\left[c' + (u_a - u_w)_f \tan\phi^b\right]\sqrt{K_p} \tag{4.11}$$

Where, $K_p = \tan^2\left[\frac{\pi}{4} + \frac{\phi'}{2}\right]$

Expressing equation (4.11) in terms of q, on has

$$\begin{aligned} q &= \frac{3(K_p - 1)}{2 + K_p} p + \frac{6\left[c' + (u_a - u_w)_f \tan\phi^b\right]\sqrt{K_p}}{2 + K_p} \\ &= \frac{3(K_p - 1)}{2 + K_p} p + \frac{3(K_p - 1)}{2 + K_p} \frac{2\left[c' + (u_a - u_w)_f \tan\phi^b\right]\sqrt{K_p}}{K_p - 1} \\ &= \frac{3(K_p - 1)}{2 + K_p}\left[p + \frac{2\left[c' + (u_a - u_w)_f \tan\phi^b\right]\sqrt{K_p}}{K_p - 1}\right] \\ &= M\left[p + \frac{2\left[c' + (u_a - u_w)_f \tan\phi^b\right]\sqrt{K_p}}{K_p - 1}\right] = M\left[p + \frac{2\left[c' + (u_a - u_w)_f \tan\phi^b\right]\sqrt{K_p}}{K_p - 1}\right] \\ &= M\left[p + \frac{2\tan\phi^b\sqrt{K_p}}{K_p - 1}(u_a - u_w)_f + \frac{2c'\sqrt{K_p}}{K_p - 1}\right] \end{aligned} \tag{4.12}$$

Where, $M = \frac{3(K_p - 1)}{2 + K_p} = \frac{3\left\{\tan^2\left[\frac{\pi}{4} + \frac{\phi'}{2}\right] - 1\right\}}{2 + \tan^2\left[\frac{\pi}{4} + \frac{\phi'}{2}\right]}$, the cohesion is assumed to be equal to zero in BBM and Cam-clay models (Roscoe and Burland 1968), putting C'=0 in equation (4.12),

$$q = M\left[p + \frac{2\tan\phi^b\sqrt{K_p}}{K_p - 1}(u_a - u_w)_f\right] \tag{4.13}$$

When one can get the original BBM shear failure equation:

$$q = M(p + ks) \tag{4.14}$$

Finally, from the above derivation, BBM parameters related to shear strength M and K can be calculated from the soil parameters C and ϕ using the below equations:

$$M = \frac{3(K_p - 1)}{2 + K_p} = \frac{3\left\{\tan^2\left[\frac{\pi}{4} + \frac{\phi'}{2}\right] - 1\right\}}{2 + \tan^2\left[\frac{\pi}{4} + \frac{\phi'}{2}\right]} \tag{4.15}$$

$$k = \frac{2\tan\phi^b\sqrt{K_p}}{K_p - 1} \tag{4.16}$$

Using the same criterion described in section 4.1. The shear strength parameters were re-guessed forcing C' to be zero. The corresponding shear strength properties ϕ' and ϕ^b were 28.13 and 22.26 degrees, respectively. Table 4.4 presents the predicted shear strength values and the errors. Based on C'=0, ϕ' and ϕ^b, the BBM shear strength parameters K and M were calculated using equations 4.15 and 4.16, and the values are 0.74 and 1.13, respectively. Figure 4.7 presents the coefficient of determination between the measured and predicted shear strength (R^2=94%) which indicates a strong relationship.

Table 4.4 Predicted shear stress and errors in case of forcing C' to zero.

Test No.	Initial condition			At failure during shearing			Predicted	Error^2
	W_c (%)	v	s (kPa)	s_f (kPa)	*Shear stress* (kPa)	*Normal stress* (kPa)	*Shear stress* (kPa)	
1	30.21	2.191	58.7	235	310	463	344.24	1172.55
2	29.10	2.209	403	224.7	171.06	139	165.10	35.52
3	38.34	2.204	428.7	128.9	185.59	236	179.12	41.87
4	41.38	2.228	47.9	18.6	80.87	116	70.11	115.75
5	41.23	2.235	87	62.6	70	58	56.41	184.74
6	44.23	2.313	18.9	24.2	173	232	135.01	1442.87
7	32.00	1.991	649.4	282	356.8	463	363.07	39.32
8	32.43	1.973	81.5	84	132.188	116	96.31	1287.16
9	33.72	2.006	144.4	110.8	99.708	58	75.72	575.56
						Sum of errors =		4895.36

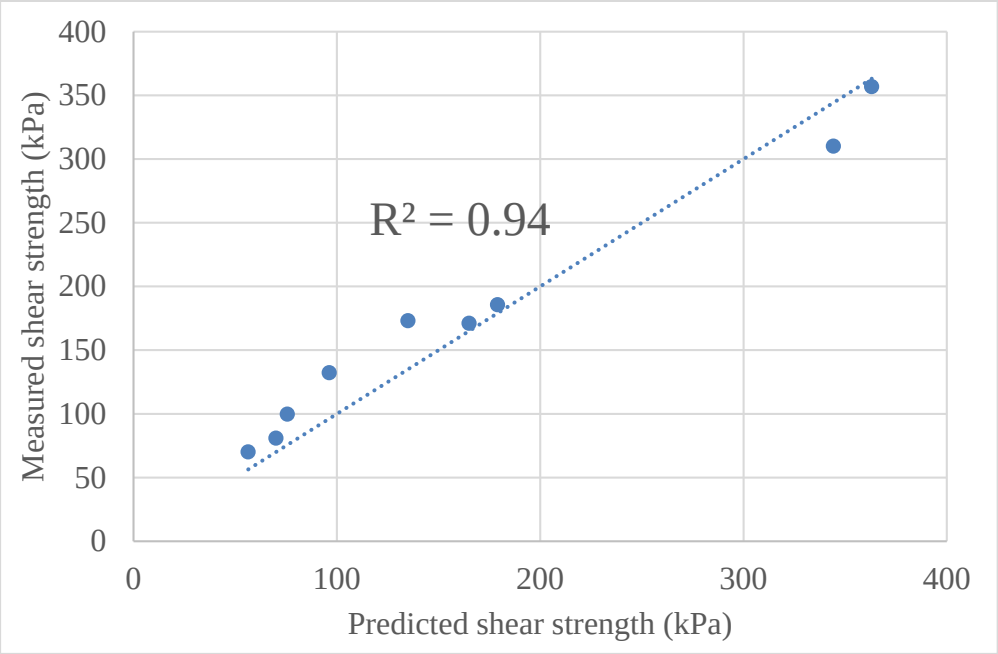

Figure 4.7 Measured and predicted shear strength in case of C' forced to zero.

5.3.BBM Stiffness Parameters

The at-rest conditions, k_0, commonly used to verify the model parameters by many researchers. Zhang, Alonso et al. (2016) proposed an explicit formulation to calculate the lateral stress from oedometer test results. The formulation was derived based on the definition of the K_0

without any additional assumptions. Once the lateral stress at K_0 test is known, the oedometer test becomes a triaxial test with a well-defined stress path. After that, the procedure was successfully used by (Zhang et al. 2016) to calibrate the BBM parameters from a set of six constant water content oedometer test. In this section, the procedure proposed by Zhang, Alonso et al., 2016 will be used for the analysis of Hawaii data from eight constant water content oedometer tests and nine constant water content direct shear tests.

The MSSA summarizes the BBM under triaxial loading conditions into two surfaces: (1) Elastic surface and (2) plastic surface as presented in equations 4.18 and 4.19, respectively. While the elastic surface is easy to determine by calculating the constant (C_1) from the soil initial conditions. After that, the elastic BBM parameters (κ and κ_s)can be calibrated by using solver in Microsoft Excel to make the squared difference between measured and predicted specific volumes minimum. The major challenge is to determine the eight parameters related to soil plastic behavior, which are N(0), $\lambda(0)$, β, r, p^c, M, K and α. It worth note that in the original BBM (Alonso et al. 1990), it was suggested that α is chosen in such a way that the flow rule predicts zero lateral strain for stress states, corresponding to Jaky's equation K0=1-sin ϕ'. Two assumptions were made to derive α : (a) the elastic shear strain is small and negligible and (b) for saturated and unsaturated conditions, the K0 consolidation line shares the same slope and is a constant. (Zhang et al. 2016) found that neither assumption holds true for unsaturated soils and suggested that α be used as an additional constant for the modified BBM. These BBM parameters have physical meanings and constrained, as follows in equation 4.17:

$$N(0)>0,\ \lambda(0)>0,\ \beta>0,\ r>0,\ p^c>0,\ M>0,\ K>0 \text{ and } \alpha>0 \tag{4.17}$$

$$v = C_1 - \kappa \ln p - \kappa_s \ln\left(s + p_{at}\right) \tag{4.18}$$

$$v = N(0) - \kappa \ln \frac{p}{p^c} - \kappa_s \ln\left(\frac{s+p_{at}}{p_{at}}\right) - \left(\lambda(s) - \kappa\right)\left[\ln\left(p + \frac{q^2}{M^2\left(p+ks\right)}\right) - \ln p^c\right] \tag{4.19}$$

Where,

ν = specific volume,

p = mean net stress,

q = deviatoric stress,

s = suction,

C_1 = Constant related to initial specific volume of the soil,

κ = slope of unloading reloading line in the p-e space,

κ_s = slope of unloading reloading line associated with soil suction,

p_{at} = atmospheric pressure,

p^c = reference stress,

M = slope of theoretical critical state line,

k = parameter describing increase in cohesion with suction,

$\lambda(s)$ = slope of virgin expansion line at different suction values associated with mean net stress, and

$N(0)$ = constant representing virgin specific volume at zero suction value and mechanical stress.

Mathematically, the calibration problem can be described as follows: the calibration of the BBM parameters under K_0 condition is to find the appropriate combination of $N(0), \lambda(0), \beta, r, p^c$, M, K and α , which can minimize the overall difference between the measured and predicted specific volumes (using equation 4.19) for all oedometer test stress paths under the constraints of equation 4.17.

The eight CWOD tests (with water content of 26.19%, 29.84%, 30.09%, 33.56%, 34.23%, 34.64%, 35.81%, 46.06%) are used to demonstrate the proposed approach. The procedures for BBM parameter calibration are as follows:

1- Prepared the experimental data for each test, each point has three entries ($(\sigma_1 - u_a)_i$, S_i and measured specific volume v_{mi}).
2- Find the yield stress (pre-consolidation stress) from Figure 4.1-a for each CWOD test using Casagrande method (Casagrande 1936).
3- The poisons ratio (μ) was assumed to be constant for the soil and equal to 0.35.
4- Assume arbitrary initial parameters for the BBM taking into account the constraints in equation 4.17. In addition, the BBM shear strength parameters M and K will be introduced from the constant water content direct shear tests results.

5- Starting from the initial condition where the vertical and lateral stresses are zero, assume a small increase in the vertical stress $d(\sigma_1 - u_a)$, find the corresponding suction change ds from Figure 4.1-b, and calculate the increase in lateral stress $d(\sigma_3 - u_a)$ as follows:

$$d(\sigma_3 - u_a) = \frac{\mu}{1-\mu} d(\sigma_1 - u_a) - \frac{\kappa_s}{\kappa} \frac{1-2\mu}{1-\mu} \frac{p}{s + p_{at}} ds \tag{4.20}$$

6- Update the stress state using the following equations:

$$(\sigma_1 - u_a)_{i+1} = (\sigma_1 - u_a)_i + \Delta(\sigma_1 - u_a) \tag{4.21}$$

$$(\sigma_3 - u_a)_{i+1} = (\sigma_3 - u_a)_i + \Delta(\sigma_3 - u_a) \tag{4.22}$$

$$S_{i+1} = S_i + \Delta S \tag{4.23}$$

7- Starting from $(\sigma_1 - u_a)_{i+1}, (\sigma_3 - u_a)_{i+1}$ and S_{i+1}, repeat steps 5 and 6 until the yield point is reached.

8- Calculate p and q for the same point using the following equations:

$$p = \frac{(\sigma_1 - u_a) + 2(\sigma_3 - u_a)}{3} = \frac{\sigma_1 + 2\sigma_3}{3} \tag{4.24}$$

$$q = (\sigma_1 - u_a) - (\sigma_3 - u_a) = \sigma_1 - \sigma_3 \tag{4.25}$$

9- At initial conditions, calculate the elastic surface constant (C_1) using the arbitrary κ and κ_s values and the measured specific volume as inputs in equation 4.18. Similarly, calculate the unloading-reloading elastic surface constant.

10- For the plastic part based on the firstly assumed arbitrary BBM parameters and assuming a small increase in vertical stress $d(\sigma_1 - u_a)$ and the corresponding change in suction *ds* from Figure 4.1-b, calculate the incremental change in lateral stress $d(\sigma_3 - u_a)$ using the following equation:

$$d(\sigma_3-u_a)=\frac{[(D-EB)-(\frac{2\kappa}{3p}+\frac{EA}{3})]d(\sigma_1-u_a)-(\frac{2\kappa_s}{s+p_{at}}-EC)ds}{2(\frac{2\kappa}{3p}+\frac{EA}{3})+(D-EB)}$$

Where,

$$A=\frac{\lambda(s)-\kappa}{q^2+M^2(p+ks)p}$$

$$B=\frac{M^2(p+ks)^2-q^2}{p+ks}$$

$$C=\frac{Aq^2K}{p+ks}+\lambda(0)(1-r)\beta\exp(-\beta s)\left[\ln(\frac{\lambda(s)-\kappa}{AM^2(p+ks)})-\ln p^c\right]$$

$$D=\frac{2(1+\mu)}{3(1-2\mu)}\frac{\kappa}{p}$$

$$E=(2-\frac{6q(p+ks)\alpha}{M^2(p+ks)^2-q^2})$$

(4.26)

11- Update the stress state variables using the following equations:

$$(\sigma_1-u_a)_{i+1}=(\sigma_1-u_a)_i+\Delta(\sigma_1-u_a) \quad (4.27)$$

$$(\sigma_3-u_a)_{i+1}=(\sigma_3-u_a)_i+\Delta(\sigma_3-u_a) \quad (4.28)$$

$$p_{i+1}=p_i+\Delta p \quad (4.29)$$

$$q_{i+1}=q_i+\Delta q \quad (4.30)$$

12- Repeat steps 10 and 11 to calculate the stress path for the entire oedometer K_0 loading conditions.

13- Repeat steps 1 through 9 for all the eight CWOD tests.

14- Calculate the void ratio based on the exact solution from equations 4.18 and 4.19 each for the corresponding surface (elastic or plastic).

15- Calculate the square of differences between the measured and predicted specific volumes.

16- Sum all the squares of differences between measured and predicted values.

17- Use the solver add-in in Microsoft Excel to search the minimum of the sum of the squares of the difference between measured and predicted values by changing the BBM parameters (κ, κ_s, N(0), $\lambda(0)$, β, r, p^c, and α) based on the below equations. Solver

stop is internally set that the variation between the current and previous iteration for each parameter is less than 0.001.

For plastic: $F(X)=\sum_{i=1}^{n} w_i\left(v_{mi}-v_{pi}\right)^2=$

$$=\sum_{i=1}^{n} w_i\left\{v_{mi}-\left[\begin{array}{l} N(0)-\kappa\ln\dfrac{p}{p^c}-\kappa_s\ln\left(\dfrac{s+p_{at}}{p_{at}}\right) \\ -\left(\lambda(s)-\kappa\right)\left[\ln\left(p+\dfrac{q^2}{M^2\left(p+ks\right)}\right)-\ln p^c\right] \end{array}\right]\right\}^2 \tag{4.28}$$

For elastic: $F(X)=\sum_{i=1}^{n} w_i\left(v_{mi}-v_{pi}\right)^2=$

$$=\sum_{i=1}^{n} w_i\left\{v_{mi}-\left[C_1-\kappa\ln p-\kappa_s\ln\left(s+p_{at}\right)\right]\right\}^2 \tag{4.29}$$

Table 4.5 presents the yield stress and elastic surfaces constants for each CWOD test.

Table 4.5 Summary of yield stress, first and second elastic surface constant for each test.

Test No.	Water content (%)	Yield stress (kPa)	Loading elastic surface constant (C_1)	Maximum applied vertical stress (kPa)	Unloading-reloading elastic surface constant (C_1)
1	26.19	300.0	2.024	1178.0	1.962
2	29.84	325.0	2.012	925.0	1.901
3	30.09	300.0	1.964	700.0	1.878
4	33.56	270.0	2.038	695.0	1.969
5	34.23	160.0	2.045	875.0	1.924
6	34.64	250.0	2.083	575.0	2.018
7	35.81	75.0	2.190	925.0	2.014
8	46.04	115.0	2.408	925.0	2.272

As explained in the chapter (3) the samples seem to have some disturbance during transportation. This makes the initial conditions of the samples not consistent with each other. Therefore, $N(0)$ for each test will be different. This will not make any significant difference since the BBM incremental approach will be used. Only the slopes of the surfaces are required. However, this might make some difficulties if the MSSA surface needs to be generated.

It is well-known that the direct shear test results are not precise enough because of rotation of principal axes and the shear failure forced to be in a preselected plane may be not the weaker plane the sample supposed to fail on in the field. Because of that, the BBM shear strength parameters were allowed to change by 5% and 10% when guessing using solver. Summary of the set of iterations for BBM parameters is illustrated in Table 4.6. Following the described procedure and considering the three iterations summarized in Table 4.6, the calculations were repeated three times based on each iteration and the guessed parameters using solver are presented in table 4.7. Comparison between the iterations results and the experimental measurements are illustrated in Figure 4.8 through 4.15. It is clear from these figures that the predictions for all the iterations are very close to the experimental results and a good match has been reached except for two tests (30.09% and 34.64%) this may be due to the mentioned disturbance in chapter three. In order to judge the results of the three iterations the soil shear strength parameters c', ϕ', and ϕ^b were back-calculated from the guessed M and K values using equations 4.15 and 4.16 and the results shown in Table 4.8. The original (fixed) BBM shear strength parameters (i.e. M=1.13 and K=0.74) will be used since it gave the lowest soil shear strength parameters to be on the conservative side. Which means that the BBM parameters corresponding to iteration three, the fixed iteration, are recommended after that to be used for any further numerical modeling.

Table 4.6 Summary of yield stress, first and second elastic surface constant for each test.

Parameter	Iteration number		
	1	**2**	**3**
Description	**10% allowed for M&K**	**5% allowed for M&K**	**M&K Fixed**
N(0)	**Changing for each test**	**Changing for each test**	**Changing for each test**
κ_s	Constant for the entire set of tests		
κ	Constant for the entire set of tests		
$\lambda(0)$	Constant for the entire set of tests		
r	Constant for the entire set of tests		
β	Constant for the entire set of tests		
p^c	Constant for the entire set of tests		
α	Constant for the entire set of tests		
M	10% allowed	5% allowed	Fixed
k	10% allowed	5% allowed	Fixed
μ	Constant for the entire set of tests		

Table 4.7 BBM strength and stiffness parameters.

Parameter		Iteration number		
		1 (10%)	2 (5%)	3 (Fixed)
N(0)	Wc=26.19%	2.129	2.138	2.119
	Wc=29.84%	2.132	2.131	2.131
	Wc=30.09%	2.097	2.095	2.097
	Wc=33.56%	2.183	2.181	2.182
	Wc=34.23%	2.156	2.154	2.155
	Wc=34.64%	2.223	2.221	2.224
	Wc=35.81%	2.251	2.250	2.249
	Wc=46.04%	2.508	2.507	2.507
κ_s		0.0069	0.0055	0.0066
κ		0.0155	0.0151	0.0147
$\lambda(0)$		**0.077**	**0.076**	**0.075**
r		**0.453**	**0.612**	**0.158**
β		**5.413**	**8.626**	**3.182**
p^c		**0.046**	**0.046**	**0.046**
α		**0.742**	**0.796**	**0.802**
M		**1.177**	**1.185**	1.13
k		**0.814**	**0.777**	0.74
μ		0.350	0.350	0.350
Standard deviation		0.128	0.128	0.128
Coefficient of determination R^2		99.72%	99.71%	99.73%

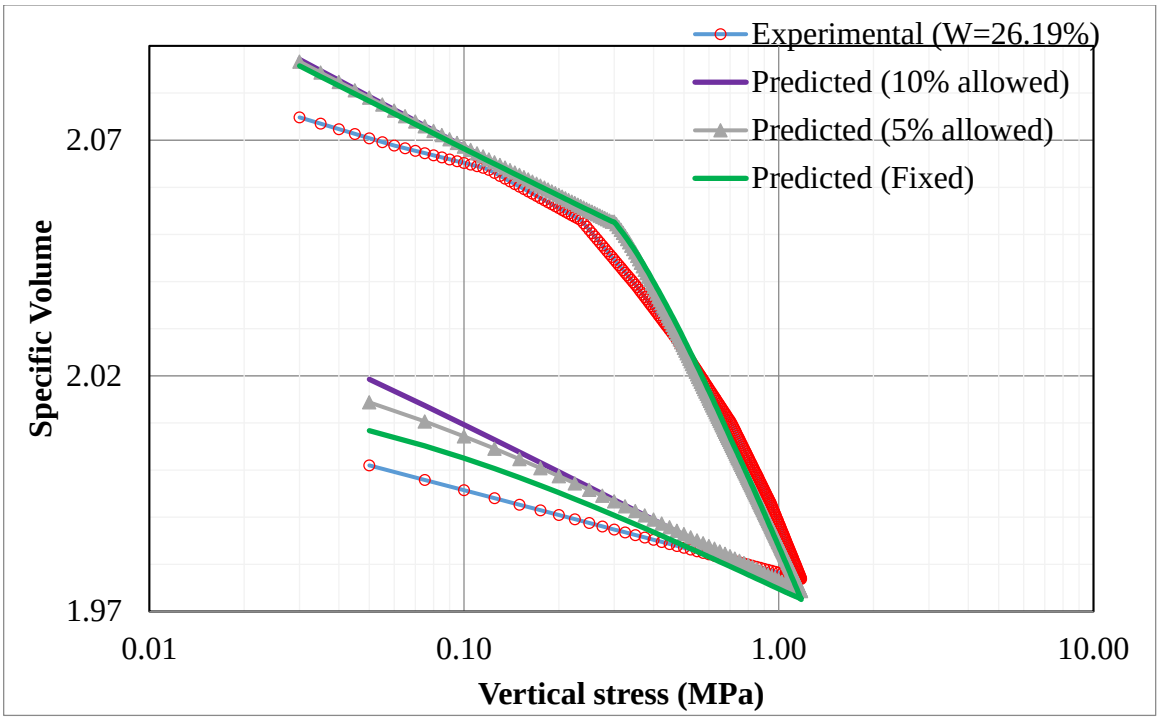

Figure 4.8 Comparison between predictions and experimental results for oedometer at Wc=26.19%.

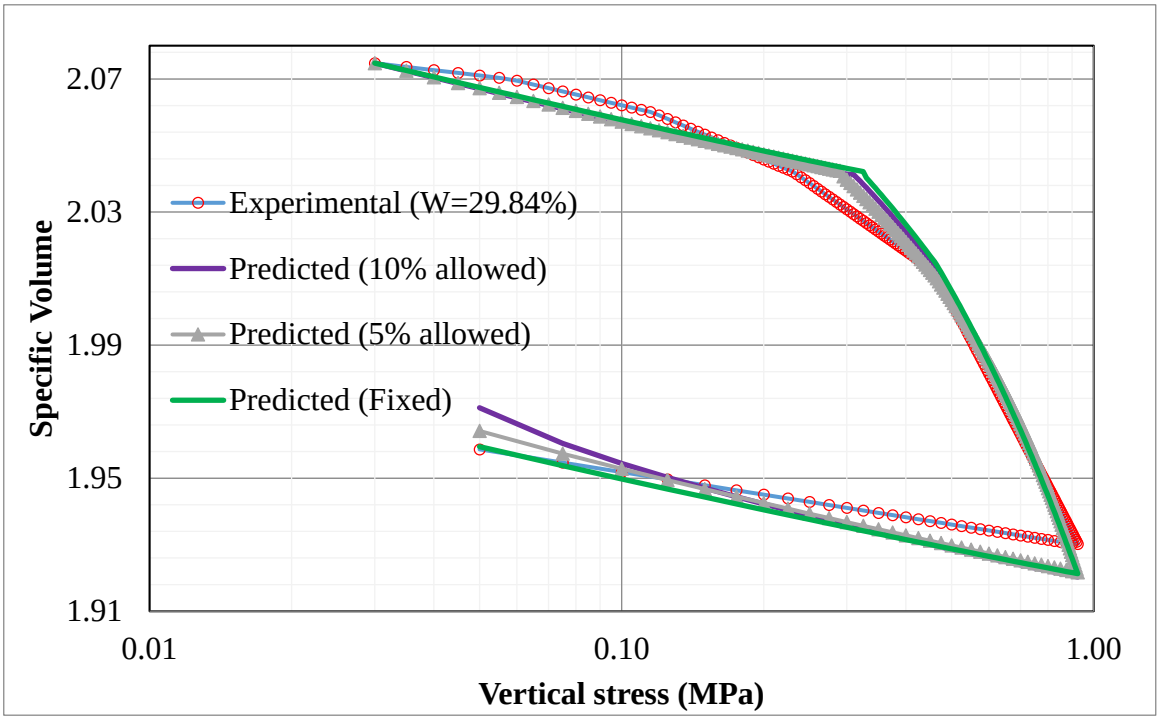

Figure 4.9 Comparison between predictions and experimental results for oedometer at Wc=29.84%.

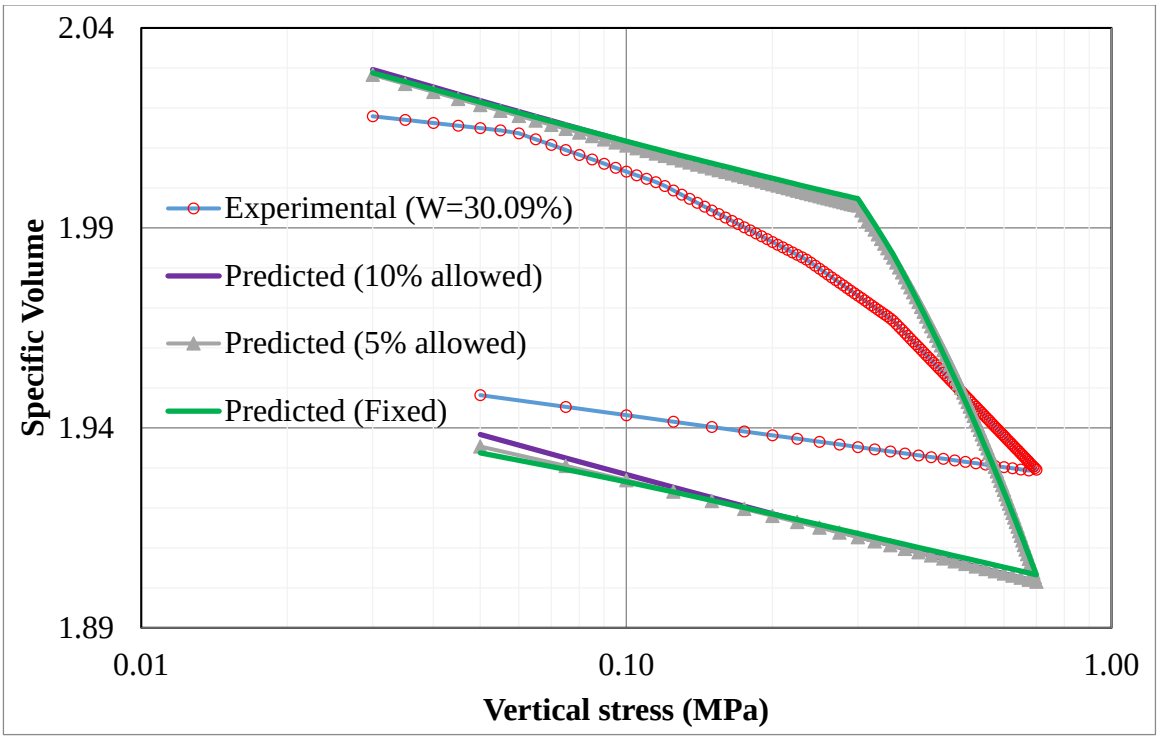

Figure 4.10 Comparison between predictions and experimental results for oedometer at Wc=30.09%.

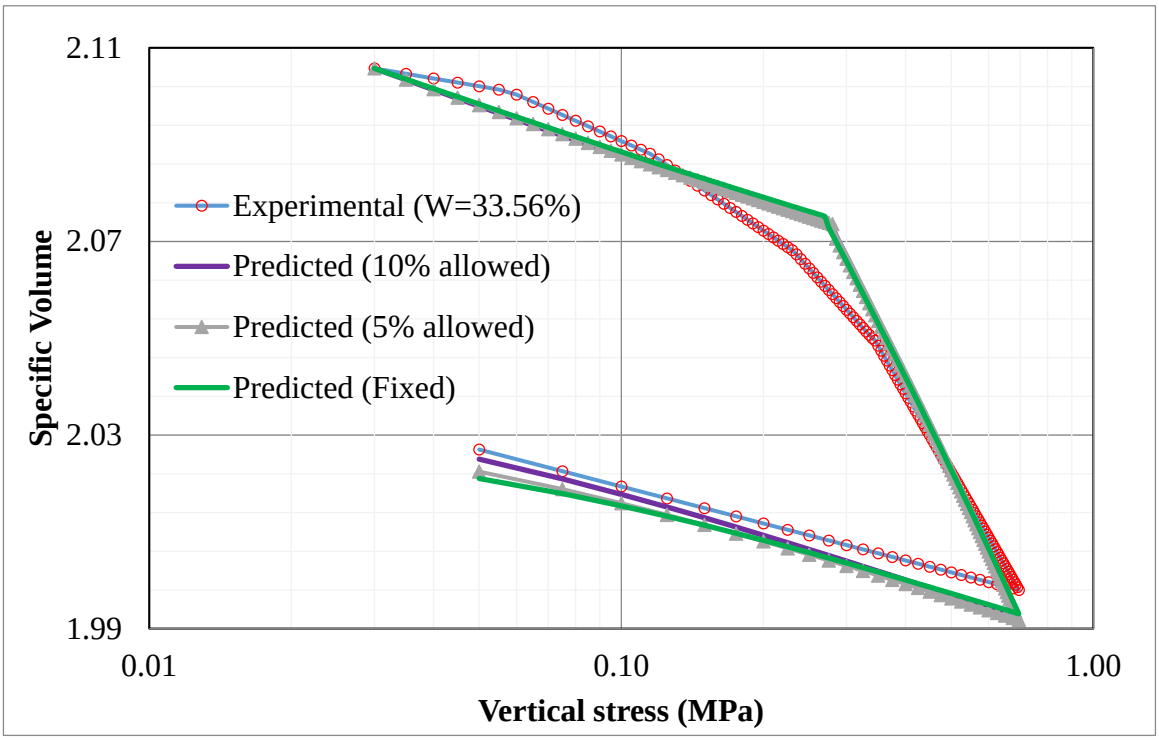

Figure 4.11 Comparison between predictions and experimental results for oedometer at Wc=33.56%.

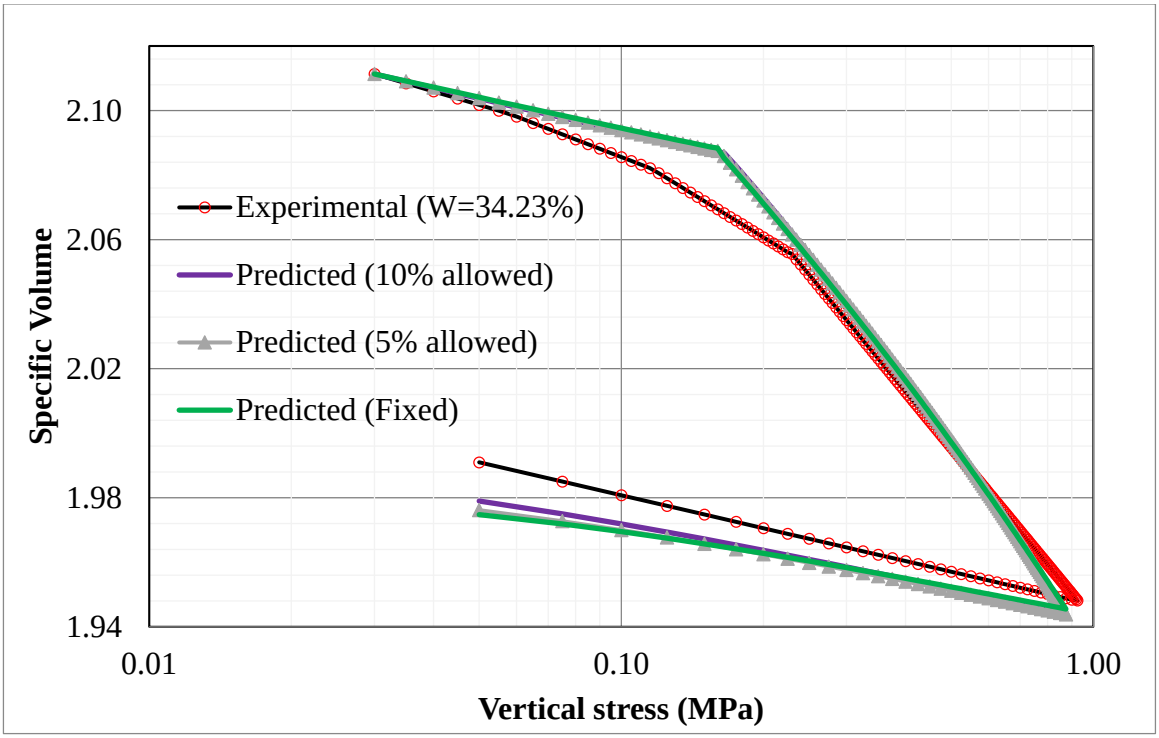

Figure 4.12 Comparison between predictions and experimental results for oedometer at Wc=34.23%.

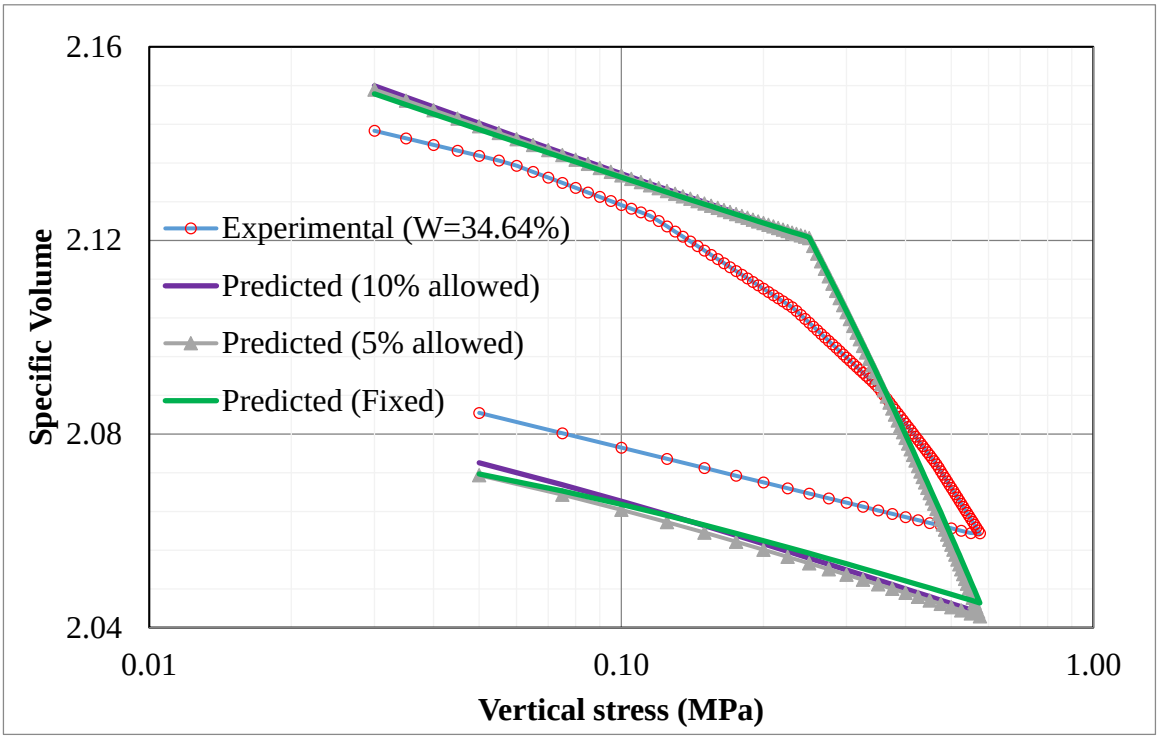

Figure 4.13 Comparison between predictions and experimental results for oedometer at Wc=34.64%.

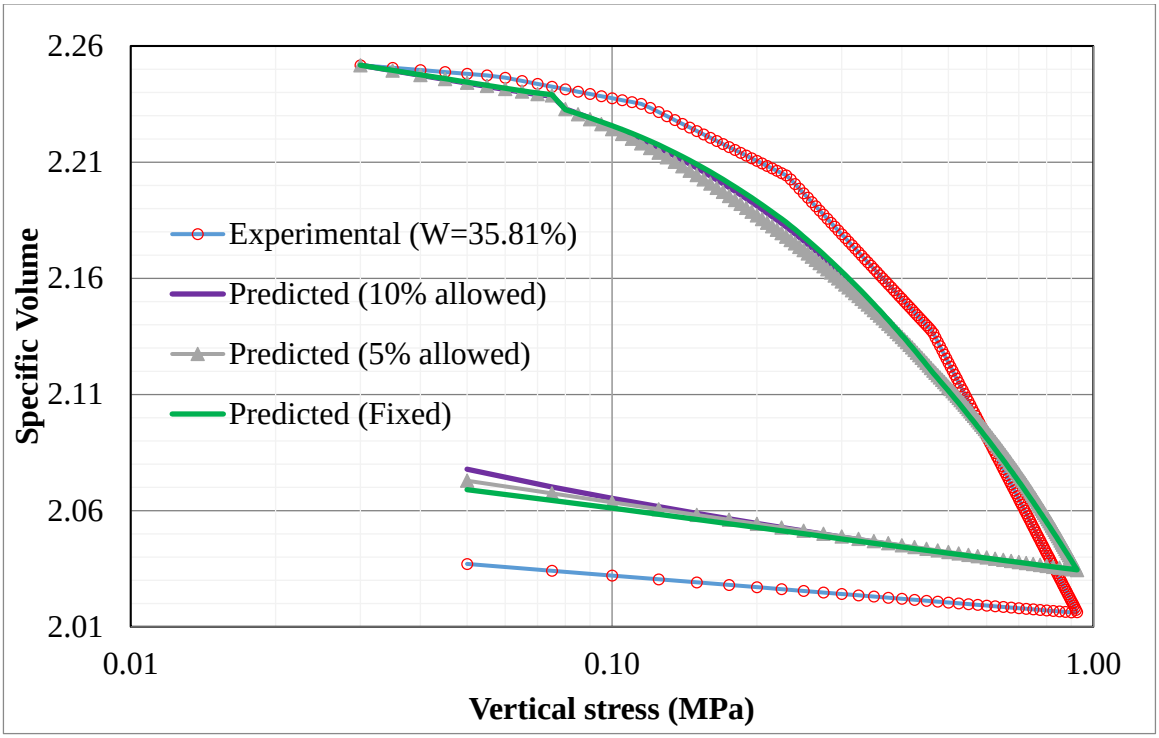

Figure 4.14 Comparison between predictions and experimental results for oedometer at Wc=35.81%.

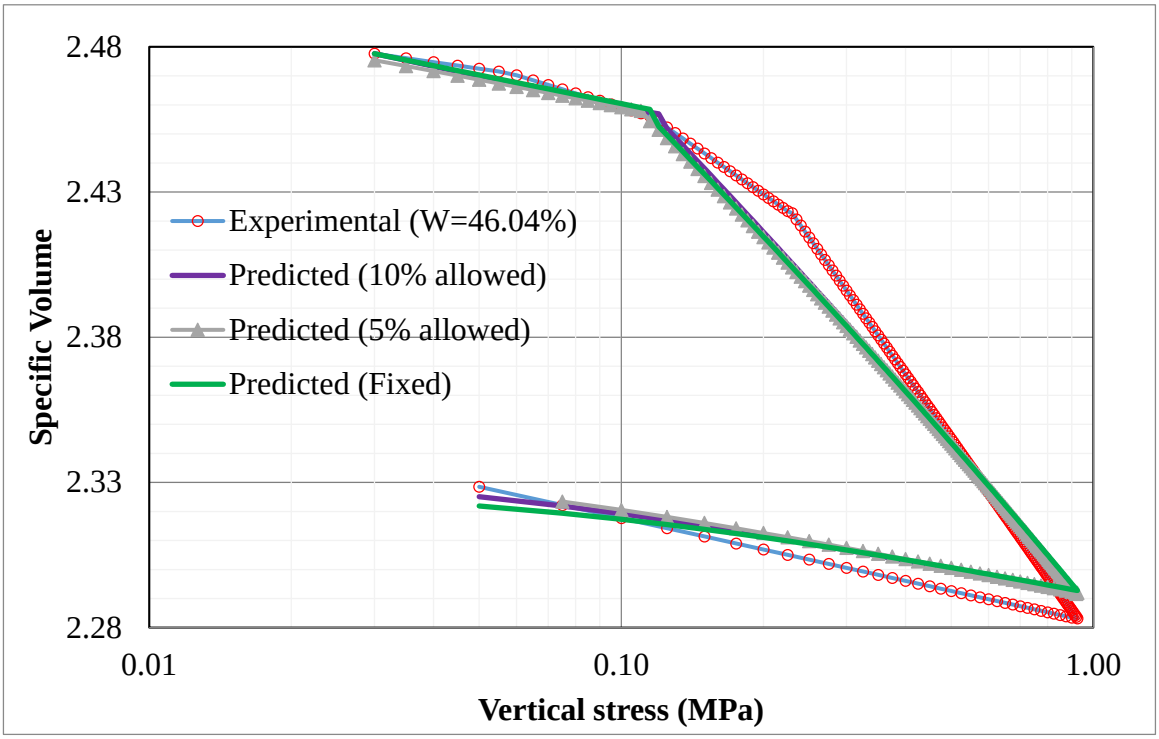

Figure 4.15 Comparison between predictions and experimental results for oedometer at Wc=46.04%.

Table 4.8 Soil shear strength parameters corresponding to BBM parameters for each iteration.

Iteration	BBM Strength parameters		Corresponding Shear Strength Parameters		
	M	K	C	Φ'	Φ^b
1 (10%)	1.177	0.814	0.0	29.47	24.70
2 (5%)	1.185	0.777	0.0	29.66	23.86
3 (Fixed)	1.13	0.74	0.0	28.38	21.83

As previously discussed, during the optimization process, the values of the BBM parameters (κ, κ_s, N(0), $\lambda(0)$, β, r, p^c, and α) were changing to minimize the overall difference between the measured and predicted test results. As shown in Table 4.7 that the coefficient of determination (R^2) is higher than 99.70%, indicating a very strong relationship between the measured and predicted test results. It can be clearly seen from Figures 4.8 through 4.15 that the predicted results match the measured ones very well in the elastoplastic zone. In the above procedure tow tests (CWOD and CWDS) were combined together to calibrate the model parameters. The idea is to include more types of stress paths and covers as much as possible of stress ranges so that the predictions are based on interpolations instead of extrapolations of oedometer test results.

Based on the MSSA, the intercept of the elastic surface and the plastic surface in the ν-p-q-s space is the yield hypersurface. The expression of the yield surface could be obtained by letting equation 4.18 equal to equation 4.19 according to Criterion 4 in the MSSA:

$$p_0 = p + \frac{q^2}{M^2(p+ks)} = P^C \exp\left(\frac{N(0) - C_1 + \kappa \ln(P^C) + \kappa_s \ln\left(p_{at}\right)}{\lambda(s) - \kappa}\right) \tag{4.30}$$

The size of the yield surface is controlled by the value of the constant (C_1) in equation 4.30. Figure 4.16 shows the initial shapes of the yield curves (in s-p plane) for specimens in each oedometer test with different C_1 corresponding to each test as shown in Table 4.5. Figure 4.16 indicates that when the mean net stress is greater than 0.1 MPa, suction increases with the increase of mean net stress on the yield curves, which is similar to the original BBM assumption (Alonso et al. 1990). This behavior could be explained based on (Zhang 2016; Zhang and Lytton 2009), Hawaii soils have a collapsible behavior when the mean net stress is greater than 100 kPa. Figure 4.16 shows different yield curve for each CWOD test. If the tested specimens in oedometer test at

different water contents have the same stress history, the saturation pre-consolidation stress shall be the same. There will be one yield curve for all the tests. The results indicate that the specimens used in the eight oedometer tests have different stress histories. This implies that there was soil yielding due to drying and wetting the samples during preparation for testing (different water content values). This proves the strength of the MSSA to determine the shapes of the LC yield curves. When soil specimens with identical stress histories are available, one LC yield curve could be generated using MSSA. When soil specimens with identical stress are available, using MSSA we still can get correct shapes for LC yield curves.

Figure 4.17 shows the predicted lateral stress as a function of the applied vertical stress during eight CWOD tests. It can be clearly seen that generally for all test, firstly the lateral stresses increased at a faster rate with the increase of the vertical stresses. After that, there was a sudden decrease in the rate of lateral stress increase with the applied vertical stress. Figure 4.18 shows the calculated K_0 stress paths for the CWOD test at different water content levels in the p-q plane. As shown, the stress paths are consist of two straight lines connected by a transition curve. In the elastic zone, the ratio between deviatoric stress and mean net stress (slope of the line) is 0.667 which is corresponding to a Poisson's ratio of 0.35. When, the mean net stress passes the yield stress the K_0 value reaches almost a constant value for the eight CWOD of 0.574 in average (the behavior is consistent with (Zhang et al. 2016) and (Zhang et al. 2016) findings).

Figure 4.19 presents the calculated lateral strain increments at different vertical stresses for the CWOD tests at different water contents. The lateral strains calculated based on the calibrated BBM parameters (Fixed case) and the stress paths in Figure 4.18. The lateral strains increments in the range of 10×10^{-5}, indicating that the predicted K_0 stress paths according to this approach are very accurate.

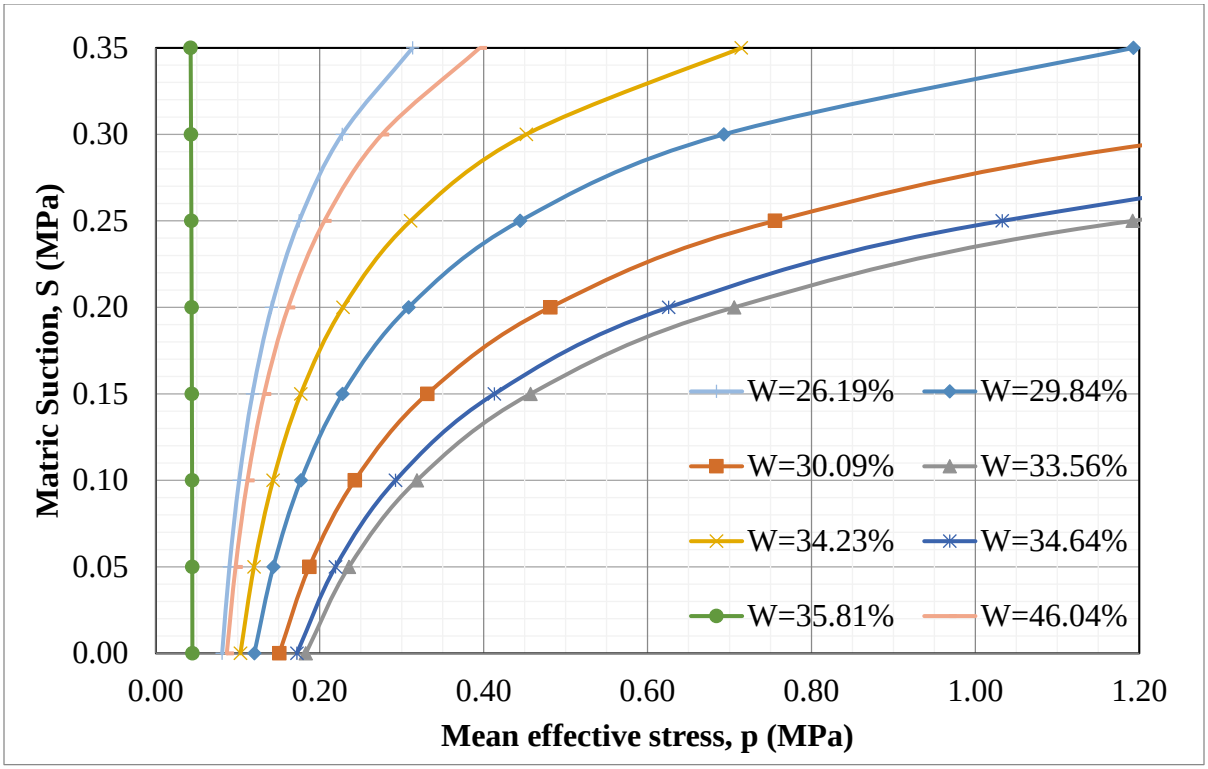

Figure 4.16 Yield curves for tested samples with different water contents.

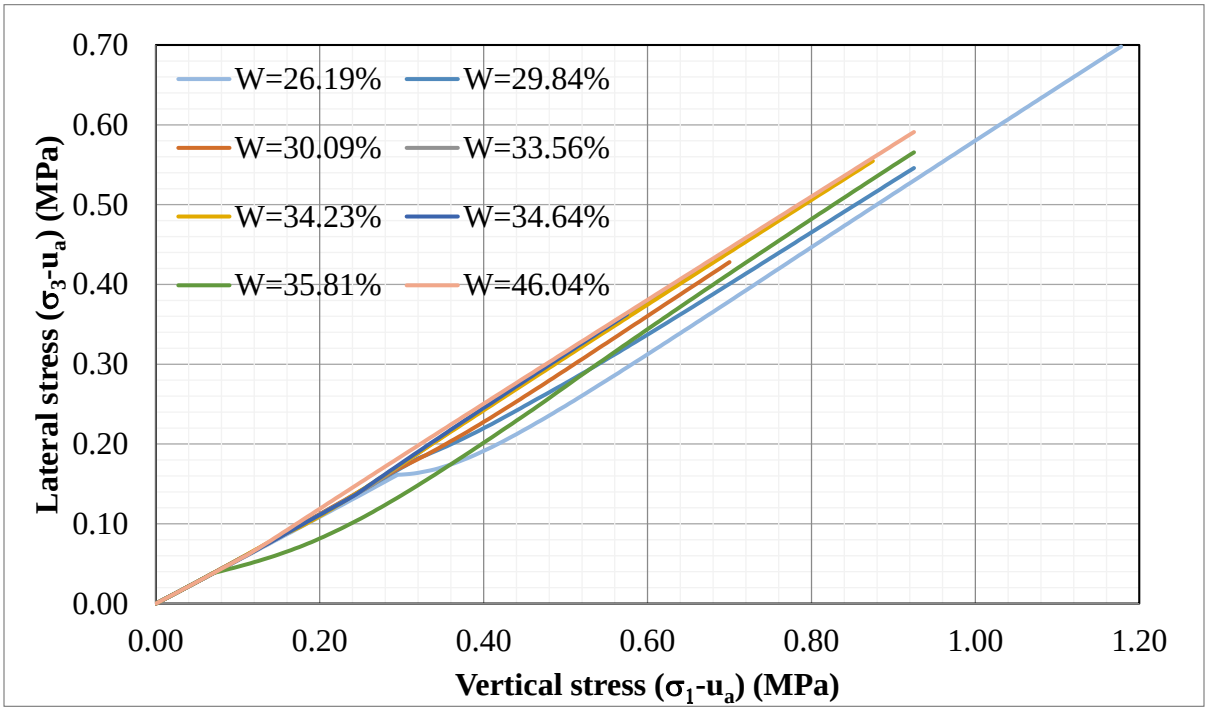

Figure 4.17 Predicted lateral stress as a function of applied vertical stress during CWOD tests.

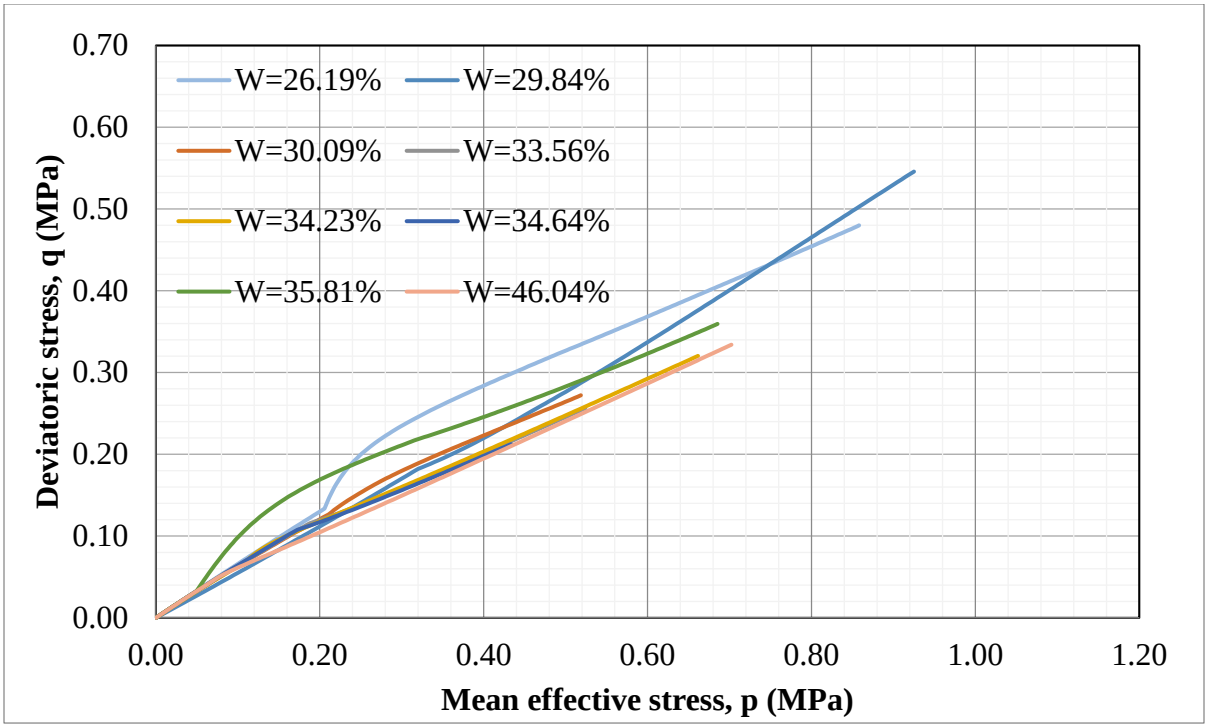

Figure 4.18 K_0 stress paths in the p-q space for the CWOD tests.

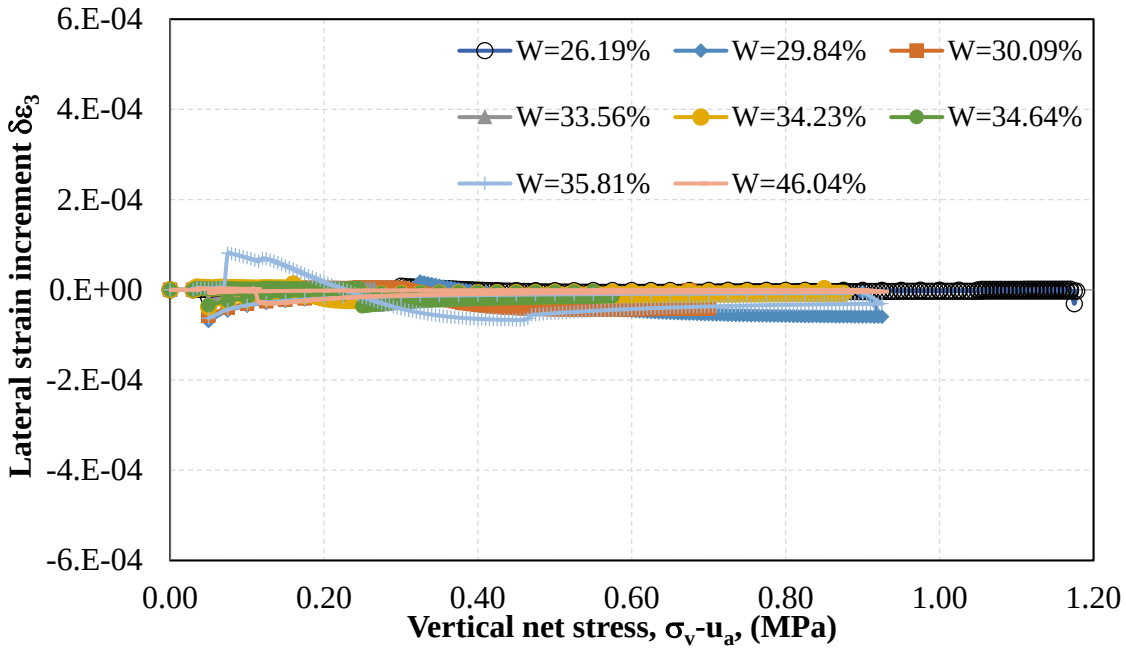

Figure 4.19 Predicted lateral strain increments at different vertical stresses.

CHAPTER V CONCLUSIONS

In this project, a new system, based on modification on a conventional oedometer apparatus for saturated soils, was adopted for the constant water content one-dimensional oedometer compression tests on unsaturated soils. A high-suction tensiometer was utilized to monitor matric suction variation during testing. Results from the constant water content test using the newly developed one-dimensional oedometer compression test equipment were then used to characterize the constitutive behavior of the unsaturated soils. In addition to the one-dimensional oedometer compression test, a method with the modified state surface approach developed by Zhang et al. (2016) was adopted to analyze the one-dimensional oedometer compression test results for the constitutive modeling purpose.

Besides the oedometer compression test, a new direct shear cell was developed to investigate the shear strength properties of unsaturated soils. In this cell, a miniature high-suction tensiometer was used to directly measure the soil suction variation during shearing which was significantly different from the conventional suction-controlled direct shear test. Also, since the soil suction was directly measured at the failure plane, the measured soil suction was more representative when compared with the other tests for shear strength determination methods. The direct soil suction measurement at the failure plane eliminated the problem of the suction representativeness due to possible non-uniformity during testing in the other methods. With the newly developed direct shear cell, a series of tests were performed on the unsaturated soil to characterize the shear strength through constant water content direct tests.

Finally, in this project instead of using the suction controlled triaxial test (SCTX) which is a time-consuming test and requires sophisticated and expensive equipment. Instead of the controlled suction oedometer and direct shear tests which requires significant modifications to the conventional test apparatuses. A new approach wish is the constant water content oedometer and the direct shear test is proposed.

The direct shear test results combined with the oedometer test results are used to calibrate the BBM strength and stiffness parameters based on the modified state surface approach developed by (Zhang and Lytton 2009) and using the procedure described by (Zhang et al. 2016) to calculate the lateral stress from oedometer test results and BBM parameters calibration. The calibrated BBM parameters after that used to predict the specific volumes for the set of constant water content

oedometer test results and a very close match was reached. The final adopted BBM parameters to be used for any further analysis are summarized in the below table. In addition, the results indicated that Hawaii soils might experience collapsible behavior at mean net stress greater than 100.0 kPa. This behavior shall be taken into account in the further studies related to slope stability analysis. When the soil collapses, the shear strength will be reduced, and excessive plastic deformations will be experienced.

Parameter	Unit	Best Fit BBM Parameters							
Test (Wc, %)		26.19%	29.84%	30.09%	33.56%	34.23%	34.64%	35.81%	46.04%
N(0)	---	2.119	2.131	2.097	2.182	2.155	2.224	2.249	2.507
κ_s	---	0.0066							
κ	---	0.0147							
$\lambda(0)$	---	**0.075**							
r	---	**0.158**							
β	MPa-1	**3.182**							
p^c	MPa	**0.046**							
α	---	**0.802**							
M	---	**1.130**							
k	---	**0.740**							
μ	---	0.350							

REFERENCES

Acikel, A. S., & Mancuso, C. (2009). Use of CO2 gas to improve saturation of high capacity tensiometer (HCT). In Proceedings of the 4th Asian Pacific Conference on Unsaturated soils, Newcastle, Australia (pp. 23-25).

Bishop, A. W., and Donald, I. B. The experimental study of partly saturated soil in the triaxial apparatus. In: Proc., 5th Int. Conf. Soil Mech., 1, 1961, pp.13–21.

Colmenares, J. E. and Ridley, A. M., 2002, "Stress–Strain and Strength Relationships for a Reconstituted Clayey Silt," Proceedings of the Third International Conference on Unsaturated Soils. Unsat 2002, Recife, Brazil, March 10–13, Vol. 2, pp. 481–484.

Escario, V., and Saez, J. 1986. The shear strength of partly saturated soils. Geotechnique, 36: 453–456.

Feddes, R. A., Kabat, P., Van Bakel, P., Bronswijk, J. J. B., and Halbertsma, J. (1988). Modelling soil water dynamics in the unsaturated zone-state of the art. Journal of Hydrology, 100(1), 69-111.

Fredlund, D. G., and Rahardjo, H. (1993). Soil Mechanics for Unsaturated Soils. New York: John Wiley and Sons.

Fredlund, D. G., Morgenstern, N. R., and Widger, R. A., 1978, "The Shear Strength of Unsaturated Soils," Can. Geotech. J., Vol. 15, No. 3, pp. 313–321.

Fredlund, D. G., Xing, A., Fredlund, M. D., and Barbour, S. L. (1996). The relationship of the unsaturated soil shear to the soil-water characteristic curve. Canadian Geotechnical Journal, 33(3), 440-448.

Gan, J. K. M., Fredlund, D. G., and Rahardjo, H. (1988). Determination of the shear strength parameters of an unsaturated soil using the direct shear test. Canadian Geotechnical Journal, 25(3), 500-510.

Garven, E. A., and Vanapalli, S. K. (2006). Evaluation of empirical procedures for predicting the shear strength of unsaturated soils. In Unsaturated Soils 2006 (pp. 2570-2592). ASCE.

Guan, Y. and Fredlund, D.G. (1997). "Use of Tensile Strength of Water for the Direct Measurement of High Soil Suction." Canadian Geotechnical Journal 36, pp. 604–614.

Hamid, Tariq B., and Gerald A. Miller. "Shear strength of unsaturated soil interfaces." Canadian Geotechnical Journal Vol. 46. No.5 (2009): 595-606.

Hilf, J. W. (1956). An investigation of pore water pressure in compacted cohesive soils.

Josa, A., Alonso, E. E., Lloret, A., and Gens, A., 1987, "Stress-Strain Behaviour of Partially Saturated Soils," Proc. 9th European Conz Soil Mech. Fdn Engng, Dublin, 2, pp. 561-564.

Khalili, N., and Khabbaz, M. H. (1998). A unique relationship of chi for the determination of the shear strength of unsaturated soils. Géotechnique, 48(5).

Le, T. T., Cui, Y. J., Muñoz, J. J., Delage, P., Tang, A. M., and Li, X. L., 2011, "Studying the Stress-suction Coupling in Soils Using an Oedometer Equipped with a High Capacity Tensiometer," Frontiers of Architecture and Civil Engineering in China, Vol. 5, No. 2, pp. 160-170.

Li, L. and Zhang, X. (2015a). "Modified Unconfined Compression Testing System to Characterize the Stress-Strain Behavior of Unsaturated Soils at Low Confining Stresses Journal of the Transportation Research Record, No. 2510: 54-64.

Li, L. and Zhang, X. (2015b). "A New Triaxial Testing System for Unsaturated Soil Characterization." ASTM Geotechnical testing Journal, 38(6), 823-839.

Li, L. and Zhang, X., 2014, "Development of a New High-Suction Tensiometer," Soil Behav. Geomech., Proceedings of Geo-Shanghai 2014, Shanghai, China, May 26–28, pp. 416-425.

Li, L., Zhang, X., and Lin, C. (2015) Development of an Oedometer Cell with Suction Measurement Ability. Innovative Materials and Design for Sustainable Transportation Infrastructure: pp. 179-188. doi: 10.1061/9780784479278.017.
Lourenco, S.D.N., Gallipoli, D, Toll, D.G, and Evans, F.D. (2006) "Development of a commercial tensiometer for triaxial testing of unsaturated soils." Proceedings of 4th international conference on unsaturated soils, Phoenix, Geotechnical Special Publication 147, vol. 2. pp. 1875–1886.
Meilani I., Rahardjo H., Leong E.C., and Fredlund D.G. (2002). "Mini suction probe for matric suction measurements." Canadian Geotechnical Journal 39. pp. 1427-1432.
Miao, L.C., 2002. Research of soil–water characteristics and shear strength features of Nanyang expansive soil. Engineering Geology 65, 261–267
Oliveira, O. M., and Marinho, F. A. M., 2008, ".Suction Equilibration Time for a High Capacity Tensiometer," Geotech. Test. J., Vol. 31, No. 1, pp. 1-5.
Oloo, S.Y., and Fredlund, D.G. 1996. A method for determination of ϕb for statically compacted soils. Canadian Geotechnical Journal, 33: 272–280. doi:10.1139/t96-006.
Rahardjo, H. and Leong, E. C. (2006). "Suction measurements." In: Proc. of the 4th International Conference on Unsaturated Soils, April 2006, Carefree, AZ, Geotechnical Special Publication No.147, pp. 81–104.
Ridley, A.M. and Burland, W.K. (1993). A new instrument for the measurement of soil moisture suction, Géotechnique 43, No. 2, pp. 321-324.
Romero, E., Facio, J. A., Lloret, A., Gens, A., and Alonso, E. E., 1997, "A New Suction and Temperature Controlled Triaxial Apparatus," Proceedings of the 14th International Conference on Soil Mechanics and Foundation Engineering, Hamburg, Vol. 1, pp. 185-188.
Sivakumar, V. A., 1993, "Critical State Framework for Unsaturated Soil," Ph.D. Thesis, University of Oxford.
Take, W. A., and Bolton, M. D., (2003). "Tensiometer Saturation and the Reliable Measurement of Matric Suction," Géotechnique, 53(2), 159-172.
Alonso, E., Gens, A., and Hight, D. "Special problem soils. General report." *Proc., Proceedings of the 9th European conference on soil mechanics and foundation engineering, Dublin*, 1087-1146.
Alonso, E. E., Gens, A., and Josa, A. (1990). "A constitutive model for partially saturated soils." *Géotechnique*, 40(3), 405-430.
Bishop, A., and Donald, I. "The experimental study of partly saturated soil in the triaxial apparatus." *Proc., Proceedings of the 5th international conference on soil mechanics and foundation engineering, Paris*, 13-21.
Bishop, A. W., and Blight, G. (1963). "Some aspects of effective stress in saturated and partly saturated soils." *Geotechnique*, 13(3), 177-197.
Casagrande, A. "The determination of preconsolidation load and its practical significance. p. 60–64. Proc Int. Conf. on Soil Mechanics and Foundation Eng., 1st, Cambridge, MA. Vol. 3." *Proc., The determination of preconsolidation load and its practical significance. p. 60–64. In Proc Int. Conf. on Soil Mechanics and Foundation Eng., 1st, Cambridge, MA. Vol. 3.*, -.
De Campos, T., and Carrillo, C. "Direct shear testing on an unsaturated soil from Rio de Janeiro." *Proc., PROCEEDINGS OF THE FIRST INTERNATIONAL CONFERENCE ON UNSATURATED SOILS/UNSAT'95/PARIS/FRANCE/6-8 SEPTEMBER 1995. VOLUME 1*.
Dineen, K., and Burland, J. "A new approach to osmotically controlled oedometer testing." *Proc., PROCEEDINGS OF THE FIRST INTERNATIONAL CONFERENCE ON UNSATURATED SOILS/UNSAT'95/PARIS/FRANCE/6-8 SEPTEMBER 1995. VOLUME 2*.

Escario, V., and Saez, J. (1986). "The shear strength of partly saturated soils." *Geotechnique*, 36(3).
Fredlund, D. (1979). "Second Canadian Geotechnical Colloquium: Appropriate concepts and technology for unsaturated soils." *Canadian Geotechnical Journal*, 16(1), 121-139.
Fredlund, D., and Morgenstern, N. (1976). "Constitutive relations for volume change in unsaturated soils." *Canadian Geotechnical Journal*, 13(3), 261-276.
Fredlund, D., Morgenstern, N. R., and Widger, R. (1978). "The shear strength of unsaturated soils." *Canadian geotechnical journal*, 15(3), 313-321.
Fredlund, D. G., and Morgenstern, N. R. (1977). "Stress state variables for unsaturated soils." *Journal of Geotechnical and Geoenvironmental Engineering*, 103(ASCE 12919).
Gallipoli, D., D'Onza, F., and Wheeler, S. J. (2010). "A sequential method for selecting parameter values in the Barcelona basic model." *Canadian Geotechnical Journal*, 47(11), 1175-1186.
Gan, J., Fredlund, D., and Rahardjo, H. (1988). "Determination of the shear strength parameters of an unsaturated soil using the direct shear test." *Canadian Geotechnical Journal*, 25(3), 500-510.
Hamid, T. B., and Miller, G. A. (2009). "Shear strength of unsaturated soil interfaces." *Canadian Geotechnical Journal*, 46(5), 595-606.
Hilf, J. W. (1956). "An investigation of pore water pressure in compacted cohesive soils."
Holtz, R. D., and Kovacs, W. D. (1981). *An introduction to geotechnical engineering*.
Hoyos Jr, L. R. (1998). "Experimental and computational modeling of unsaturated soil behavior under true triaxial stress states." Georgia Institute of Technology.
Jennings, J., and Burland, J. (1962). "Limitations to the use of effective stresses in partly saturated soils." *Géotechnique*, 12(2), 125-144.
Kassiff, G., and Shalom, A. B. (1971). "Experimental relationship between swell pressure and suction." *Géotechnique*, 21(3), 245-255.
Khalili, N., Geiser, F., and Blight, G. (2004). "Effective stress in unsaturated soils: review with new evidence." *International journal of Geomechanics*, 4(2), 115-126.
Kohgo, Y., Nakano, M., and Miyazaki, T. (1993). "Theoretical aspects of constitutive modelling for unsaturated soils." *Soils and foundations*, 33(4), 49-63.
Li, L., and Zhang, X. (2015). "Modified Unconfined Compression Testing System to Characterize Stress–Strain Behavior of Unsaturated Soils at Low Confining Stresses." *Transportation Research Record: Journal of the Transportation Research Board*(2510), 54-64.
Li, L., and Zhang, X. (2015). "A New Triaxial Testing System for Unsaturated Soil Characterization."
Lu, N., and Likos, W. J. (2004). *Unsaturated soil mechanics*, Wiley.
Maswoswe, J. (1985). "Stress paths for compacted soil during collapse due to wetting." Imperial College London (University of London).
Matyas, E. L., and Radhakrishna, H. (1968). "Volume change characteristics of partially saturated soils." *Géotechnique*, 18(4), 432-448.
Nam, S., Gutierrez, M., Diplas, P., and Petrie, J. (2011). "Determination of the shear strength of unsaturated soils using the multistage direct shear test." *Engineering geology*, 122(3), 272-280.
Oloo, S., and Fredlund, D. (1996). "A method for determination of φ b for statically compacted soils." *Canadian Geotechnical Journal*, 33(2), 272-280.
Romero, E., Lloret, A., and Gens, A. "Development of a new suction and temperature controlled oedometer cell." *Proc., PROCEEDINGS OF THE FIRST INTERNATIONAL*

CONFERENCE ON UNSATURATED SOILS/UNSAT'95/PARIS/FRANCE/6-8 SEPTEMBER 1995. VOLUME 2.

Roscoe, K. H., and Burland, J. (1968). "On the generalized stress-strain behaviour of wet clay."

Sharma, R. S. (1998). "Mechanical behaviour of unsaturated highly expansive clays." University of Oxford.

Sivakumar, V. (1993). "A critical state framework for unsaturated soil." University of Sheffield.

Terzaghi, K. (1944). *Theoretical soil mechanics*, Chapman And Hali, Limited John Wiler And Sons, Inc; New York.

Thu, T. M., Rahardjo, H., and Leong, E.-C. (2006). "Shear strength and pore-water pressure characteristics during constant water content triaxial tests." *Journal of Geotechnical and Geoenvironmental Engineering*, 132(3), 411-419.

Vanapalli, S., Fredlund, D., Pufahl, D., and Clifton, A. (1996). "Model for the prediction of shear strength with respect to soil suction." *Canadian Geotechnical Journal*, 33(3), 379-392.

Vanapalli, S., and Lane, J. "A simple technique for determining the shear strength of finegrained unsaturated soils using the conventional direct shear apparatus." *Proc., Proc. Second Canadian Specialty Conference on Computer Applications in Geotechnique, Winnipeg*, 245-253.

Zhang, X. (2016). "Limitations of suction-controlled triaxial tests in the characterization of unsaturated soils." *International Journal for Numerical and Analytical Methods in Geomechanics*, 40(2), 269-296.

Zhang, X., Alonso, E. E., and Casini, F. (2016). "Explicit formulation of at-rest coefficient and its role in calibrating elasto-plastic models for unsaturated soils." *Computers and Geotechnics*, 71, 56-68.

Zhang, X., Lu, H., and Li, L. (2016). "Use of Oedometer Equipped with High-Suction Tensiometer to Characterize Unsaturated Soils." *Transportation Research Record: Journal of the Transportation Research Board*(2578), 58-71.

Zhang, X., and Lytton, R. L. (2009). "Modified state-surface approach to the study of unsaturated soil behavior. Part I: Basic concept." *Canadian Geotechnical Journal*, 46(5), 536-552.

Zhang, X., and Lytton, R. L. (2009). "Modified state-surface approach to the study of unsaturated soil behavior. Part II: General formulation." *Canadian Geotechnical Journal*, 46(5), 553-570.

Zhang, X., and Lytton, R. L. (2011). "Modified state-surface approach to the study of unsaturated soil behavior. Part III: Modeling of coupled hydromechanical effect." *Canadian Geotechnical Journal*, 49(1), 98-120.

Zhang, X., and Xiao, M. (2013). "Using modified state surface approach to select parameter values in the Barcelona basic model." *International Journal for Numerical and Analytical Methods in Geomechanics*, 37(12), 1847-1866.

Thu, T. M., Rahardjo, H., and Leong, E. C., 2006, "Shear Strength and Pore-Water Pressure Characteristics during Constant Moisture content Triaxial Tests," Journal of Geotechnical and Geoenvironmental Engineering, Vol.132, No.3, pp. 411-419.

Wheeler, S.J., 1988, "The Undrained Shear Strength of Soils Containing Large Gas Bubbles," Geotechnique, Vol. 38, No. 3, pp. 399-413.

Zhang, X., H., Lu, and L., Li. "Use of Oedometer Equipped with High-Suction Tensiometer to Characterize Unsaturated Soils." Transportation Research Record: Journal of the Transportation Research Board 2578 (2016): 58-71.

APPENDIX A OEDOMETER COMPRESSION TEST RESULTS

Sample 5, Oedometer compression specimen 3, w=26.19%			
Normal stress (kPa)	H (mm)	Suction (kPa)	Specific v
1.2	25.50	-	2.085
29.5	25.38	353.6	2.075
58.9	25.30	349.4	2.069
117.8	25.25	342	2.064
235.6	25.10	321.7	2.053
353.5	24.94	298	2.039
471.3	24.81	274.5	2.028
706.9	24.59	237.2	2.010
942.6	24.38	214.5	1.993
1178.2	24.18	198.1	1.977
29.5	24.52	279.3	2.005

Sample 4, Oedometer compression specimen 2, w=29.84%			
Normal stress (kPa)	H (mm)	Suction (kPa)	Specific v
1.0	25.30	-	2.081
29.0	25.22	325.7	2.075
57.9	25.17	300.9	2.070
115.8	25.04	266.4	2.060
231.7	24.83	214.5	2.042
463.3	24.46	140.2	2.012
926.7	23.46	9.9	1.930
29.0	23.88	193.7	1.964

Sample 5, Oedometer compression specimen 2, w=30.09%			
Normal stress (kPa)	H (mm)	Suction (kPa)	Specific v
1.2	25.50	-	2.026
29.5	25.40	224.9	2.018
58.9	25.34	212.1	2.014
117.8	25.18	184.4	2.001
235.6	24.94	135.3	1.982
353.5	24.76	96.2	1.967
471.3	24.58	62.5	1.953
589.1	24.42	31.7	1.941
706.9	24.28	0	1.929
29.5	24.57	113.1	1.952

Sample 5, Oedometer compression specimen 1, w=33.56%			
Normal stress (kPa)	H (mm)	Suction (kPa)	Specific v
1.2	26.00	117.2	2.116
29.0	25.88	106.5	2.106
57.9	25.81	100.8	2.101
115.8	25.66	87.5	2.088
231.7	25.40	58.3	2.068
347.5	25.17	38.4	2.049
463.3	24.95	17.7	2.031
695.0	24.55	8.8	1.998
29.0	24.98	49.4	2.033

Sample 4, Oedometer compression specimen 1, w=34.23%			
Normal stress (kPa)	H (mm)	Suction (kPa)	Specific v
1.0	26.00	155.2	2.145
29.0	25.60	136.4	2.112
57.9	25.45	120.2	2.099
115.8	25.23	94.8	2.082
231.7	24.90	62.6	2.055
463.3	24.41	7.6	2.014
926.7	23.61	0	1.948
29.0	24.23	81.5	1.999

Sample 6, Oedometer compression specimen 1, w=34.64%			
Normal stress (kPa)	H (mm)	Suction (kPa)	Specific v
1.2	26.00	108.8	2.153
29.0	25.87	98.2	2.143
57.9	25.79	90.6	2.136
115.8	25.66	78.7	2.125
231.7	25.43	54.3	2.106
347.5	25.23	31.1	2.090
463.3	25.04	6.6	2.074
579.2	24.86	-1	2.059
29.0	25.24	57.1	2.090
1.2	26.00	108.8	2.153

Sample 2, Oedometer compression specimen 1, w=35.81%			
Normal stress (kPa)	H (mm)	Suction (kPa)	Specific v
1.0	24.40	-	2.280
29.0	24.10	386.3	2.252
57.9	24.05	361.4	2.247
115.8	23.92	307.1	2.235
231.7	23.59	214.6	2.204
463.3	22.87	94.6	2.137
926.7	21.58	0.2	2.016
29.0	21.85	182	2.041
1.0	21.92	205	2.048

Sample 3, Oedometer compression specimen 1, w=46.04%			
Normal stress (kPa)	H (mm)	Suction (kPa)	Specific v
1.0	26.00	-	2.485
29.0	25.93	56.3	2.478
57.9	25.86	50.3	2.471
115.8	25.70	40.9	2.456
231.7	25.34	27.4	2.422
463.3	24.79	1.68	2.369
926.7	23.89	0.7	2.283
29.0	24.46	13	2.337

APPENDIX B DIRECT SHEAR TEST RESULTS

Sample 1, direct shear specimen 1, w=30.32%, normal load = 463 kPa					
Displacement (mm)	H (mm)	Suction (kPa)	Shear load (N)	Stress (kPa)	Specific v
0	25.28	58.7	0	0.0	2.191
0.25	25.30	58.9	0	0.0	2.193
0.5	25.30	59.8	15.1	5.5	2.193
0.75	25.27	62.2	69.7	25.5	2.190
1	25.26	68.6	157.5	57.6	2.189
1.25	25.24	75.3	254.5	93.1	2.188
1.5	25.22	78.4	312.0	114.1	2.186
1.75	25.21	82.1	372.6	136.3	2.185
2	25.20	90	454.4	166.2	2.184
2.25	25.18	98.6	518.0	189.5	2.183
2.5	25.16	107.3	563.4	206.1	2.181
2.75	25.14	115	602.8	220.5	2.179
3	25.11	121	633.1	231.6	2.177
3.25	25.08	126.2	660.4	241.5	2.174
3.5	25.04	132	675.5	247.1	2.171
3.75	25.01	136.4	687.7	251.5	2.167
4	24.97	140.2	702.8	257.1	2.165
4.25	24.93	146.8	724.0	264.8	2.161
4.5	24.89	155.5	742.2	271.5	2.157
4.75	24.86	164	757.3	277.0	2.155
5	24.83	171.3	775.5	283.7	2.152
5.25	24.80	182	787.6	288.1	2.150
5.5	24.78	197.7	793.7	290.3	2.148
5.75	24.76	206	802.8	293.6	2.146
6	24.74	211.5	805.8	294.7	2.144
6.25	24.71	215.6	808.8	295.8	2.142

6.5	24.69	222.2	817.9	299.2	2.140
6.75	24.67	227.5	827.0	302.5	2.138
7	24.64	230	833.1	304.7	2.136
7.25	24.62	231.2	839.1	306.9	2.134
7.5	24.60	233	845.2	309.1	2.132
7.75	24.58	235.4	845.2	309.1	2.130
8	24.56	238.9	845.2	309.1	2.128

Sample 1, direct shear specimen 2, w=29.10%, normal load = 139 kPa					
Displacement (mm)	H (mm)	Suction (kPa)	Shear load (N)	Stress (kPa)	Specific v
0	25.48	403	0	0.0	2.209
0.35	25.48	401.7	36.9	13.5	2.209
0.7	25.46	392.5	99.2	36.3	2.206
1.05	25.44	381.5	110.6	40.4	2.205
1.4	25.44	370.1	148.8	54.4	2.205
1.75	25.44	357	212.6	77.8	2.205
2.1	25.45	338.5	266.5	97.5	2.206
2.45	25.47	318.7	326.0	119.3	2.207
2.8	25.50	301.7	381.3	139.5	2.210
3.15	25.50	286.2	428.1	156.6	2.210
3.5	25.55	276.3	470.6	172.1	2.215
3.85	25.61	269.8	510.3	186.7	2.220
4.2	25.71	221.6	484.8	177.3	2.228
4.55	25.77	224.7	467.8	171.1	2.234
4.9	25.83	221.6	467.8	171.1	2.239

Sample 2, direct shear specimen 1, w=35.81%, normal load = 463 kPa					
Displacement (mm)	H (mm)	Suction (kPa)	Shear load (N)	Stress (kPa)	Specific v
0	22.82	83.4	0	0.0	2.132
0.5	22.82	83.2	6.1	2.2	2.132
1	22.82	83.2	15.1	5.5	2.132
1.5	22.80	83.1	136.3	49.9	2.131
2	22.79	82.8	348.4	127.4	2.129
2.5	22.73	79.3	445.3	162.9	2.124
3	22.70	71.64	499.8	182.8	2.121
3.5	22.67	53.7	560.4	205.0	2.118
4	22.63	24.4	599.8	219.4	2.115
4.5	22.60	8.12	630.1	230.5	2.111
5	22.57	-4.7	651.3	238.2	2.109
5.5	22.54	-13	663.4	242.7	2.106
6	22.52	-16.7	672.5	246.0	2.104
6.5	22.50	-17.6	681.6	249.3	2.102
7	22.49	-17.9	687.7	251.5	2.101
7.5	22.47	-17	693.7	253.7	2.099
8	22.45	-7.8	699.8	256.0	2.097
8.5	22.44	-1.5	699.8	256.0	2.097
9	22.44	3	696.7	254.8	2.096

Sample 2, direct shear specimen 2, w=38.34%, normal load = 236 kPa					
Displacement (mm)	H (mm)	Suction (kPa)	Shear load (N)	Stress (kPa)	Specific v
0	25.45	87.9	0	0.0	2.204
0.25	25.45	87.9	9.1	3.3	2.204
0.5	25.45	88.4	42.4	15.5	2.204
0.75	25.45	91.1	112.1	41.0	2.204
1	25.44	96.7	227.2	83.1	2.203
1.25	25.41	100	302.9	110.8	2.200
1.5	25.37	104.3	360.5	131.9	2.197
1.75	25.36	113.9	418.0	152.9	2.195
2	25.34	126.7	463.5	169.5	2.194
2.25	25.33	134	484.7	177.3	2.193
2.5	25.32	137.7	499.8	182.8	2.192
2.75	25.31	132.5	505.9	185.0	2.191
3	25.29	128.9	507.4	185.6	2.190
3.25	25.27	130	505.9	185.0	2.188
3.5	25.25	135.3	502.9	183.9	2.186

Sample 2, direct shear specimen 3, w=41.38%, normal load = 116 kPa					
Displacement (mm)	H (mm)	Suction (kPa)	Shear load (N)	Stress (kPa)	Specific v
0	25.74	47.9	0	0.0	2.228
0.25	25.73	47.2	27.3	10.0	2.227
0.5	25.72	43	72.7	26.6	2.226
0.75	25.71	33.6	115.1	42.1	2.225
1	25.69	28.4	154.5	56.5	2.224
1.25	25.66	22.6	184.8	67.6	2.221
1.5	25.63	20.4	206.0	75.3	2.219
1.75	25.62	18.6	215.1	78.7	2.217
2	25.61	18.6	221.1	80.9	2.216
2.25	25.60	15.77	221.1	80.9	2.216
2.5	25.58	11.73	218.1	79.8	2.214

Sample 2, direct shear specimen 4, w=41.23%, normal load = 58 kPa					
Displacement (mm)	H (mm)	Suction (kPa)	Shear load (N)	Stress (kPa)	Specific v
0	25.84	87	0	0.0	2.235
0.25	25.82	87.2	0.0	0.0	2.233
0.5	25.81	88.8	27.3	10.0	2.233
0.75	25.80	94.9	75.7	27.7	2.232
1	25.80	97.6	136.3	49.9	2.232
1.25	25.79	87	178.7	65.4	2.231
1.5	25.79	77.1	209.0	76.5	2.231
1.75	25.79	73.7	218.1	79.8	2.231
2	25.79	71.1	212.1	77.6	2.231
2.25	25.79	62.6	196.9	72.0	2.231

Sample 3, direct shear specimen 1, w=44.23%, normal load = 232 kPa					
Displacement(mm)	H (mm)	Suction (kPa	Shear load (N)	Stress (kPa)	Specific v
0	24.21	18.9	0	0.0	2.313
0.25	24.20	18.4	42.4	15.5	2.312
0.5	24.18	16.99	136.3	49.9	2.310
0.75	24.17	16.5	166.6	60.9	2.309
1	24.16	16.22	227.2	83.1	2.309
1.25	24.16	16.3	327.2	119.7	2.309
1.5	24.16	17.2	390.8	142.9	2.309
1.75	24.17	19	442.3	161.8	2.309
2	24.17	20.5	466.5	170.6	2.310
2.25	24.18	22.8	469.5	171.7	2.310
2.5	24.18	24.2	472.6	172.9	2.310
2.75	24.18	25.6	469.5	171.7	2.310

Sample 3, direct shear specimen 3, w=32.00%, normal load = 463 kPa					
Displacement (mm)	H (mm)	Suction (kPa)	Shear load (N)	Stress (kPa)	Specific v
0	25.50	649.4	0.0	0.0	1.991
0.25	25.49	636.3	109.1	39.9	1.990
0.5	25.47	604.1	239.3	87.5	1.989
0.75	25.45	573.6	354.4	129.6	1.987
1	25.43	544	451.4	165.1	1.985
1.25	25.41	518.7	530.1	193.9	1.984
1.5	25.41	496	590.7	216.1	1.984
1.75	25.41	476.1	678.6	248.2	1.984
2	25.41	456	754.3	275.9	1.984
2.25	25.41	436	814.9	298.1	1.984
2.5	25.41	413	863.4	315.8	1.984
2.75	25.41	393	905.8	331.3	1.984
3	25.40	371	930.0	340.2	1.983
3.25	25.39	353	942.1	344.6	1.983
3.5	25.39	335	948.2	346.8	1.982
3.75	25.38	322	954.2	349.0	1.982
4	25.38	310	963.3	352.4	1.981
4.25	25.36	291	972.4	355.7	1.980
4.5	25.36	282	975.4	356.8	1.980
4.75	25.36	300	972.4	355.7	1.980

Sample 4, direct shear specimen 1, w=32.43%, normal load = 116 kPa					
Displacement (mm)	H (mm)	Suction (kPa)	Shear load (N)	Stress (kPa)	Specific v
0	23.94	81.5	0	0.0	1.973
0.25	23.94	81.9	6.1	2.2	1.973
0.5	23.92	82.1	48.5	17.7	1.971
0.75	23.90	82.3	90.9	33.2	1.970
1	23.88	82.5	136.3	49.9	1.968
1.25	23.87	82.9	175.7	64.3	1.968
1.5	23.88	83.1	215.1	78.7	1.968
1.75	23.85	83.2	257.5	94.2	1.966
2	23.86	83.6	302.9	110.8	1.966
2.25	23.89	83.7	345.3	126.3	1.969
2.5	23.91	83.7	360.5	131.9	1.971
2.75	23.93	84	369.6	135.2	1.973
3	23.95	84.6	366.5	134.1	1.974

Sample 4, direct shear specimen 2, w=33.72%, normal load = 58 kPa					
Displacement (mm)	H (mm)	Suction (kPa)	Shear load (N)	Stress (kPa)	Specific v
0	25.50	144.4	0.0	0.0	2.006
0.25	25.50	144.7	9.1	3.3	2.006
0.5	25.48	146.2	45.4	16.6	2.005
0.75	25.47	147.2	112.1	41.0	2.004
1	25.46	135.3	175.7	64.3	2.003
1.25	25.45	126.8	218.1	79.8	2.002
1.5	25.46	127.1	263.5	96.4	2.003
1.75	25.47	122	272.6	99.7	2.004
2	25.48	117.2	284.8	104.2	2.005
2.25	25.49	114	284.8	104.2	2.006
2.5	25.50	110.8	272.6	99.7	2.006
2.75	25.50	144.4	0.0	0.0	2.006